New Drug Discovery Approaches to target undruggable oncogenic targets

Ainoa Sánchez Arfelis

UNIVERSITAT DE BARCELONA
FACULTAT DE FARMÀCIA I CIÈNCIES DE L'ALIMENTACIÓ
PROGRAMA DE DOCTORAT EN QUÍMICA ORGÀNICA

NEW DRUG DISCOVERY APPROACHES TO TARGET UNDRUGGABLE ONCOGENIC TARGETS

NOVES ESTRATEGIES EN EL DESCOBRIMENT DE FÀRMACS DIRIGIDES A DIANES ONCOGÈNIQUES INTRACTABLES

AINOA SÁNCHEZ ARFELIS
2025

UNIVERSITAT DE BARCELONA
FACULTAT DE FARMÀCIA I CIÈNCIES DE L'ALIMENTACIÓ
PROGRAMA DE DOCTORAT EN QUÍMICA ORGÀNICA
DEPARTAMENT DE FARMACOLOGIA, TOXICOLOGIA I QUÍMICA TERAPÈUTICA

NEW DRUG DISCOVERY APPROACHES TO TARGET UNDRUGGABLE ONCOGENIC TARGETS

NOVES ESTRATEGIES EN EL DESCOBRIMENT DE FÀRMACS DIRIGIDES A DIANES ONCOGÈNIQUES

Memòria presentada per Ainoa Sánchez Arfelis, sota la dirección de la Prof Carmen Escolano Mirón i el Dr Carles Galdeano Cantador per optar al títol de Doctora per la Universitat de Barcelona en el Programa de Doctorat en Química Orgànica.

Carles Galdeano Cantador	**Carmen Escolano Mirón**	**Ainoa Sánchez Arfelis**
(Director i tutor de tesi)	(Director de tesi)	(Doctoranda)

AINOA SANCHEZ ARFELIS - DNI 48058667Y

Firmado digitalmente por AINOA SANCHEZ ARFELIS - DNI 48058667Y
Fecha: 2025.05.12 16:56:19 +02'00'

AINOA SÁNCHEZ ARFELIS

2025

This thesis was developed in the Laboratory of Medicinal Chemistry, Department of Pharmacology, Toxicology and Therapeutic Chemistry, Faculty of Pharmacy and Food Sciences, University of Barcelona, and in the Institute of Advanced Chemistry (IQAC- CSIC) from October 2020 to July 2024. Also, the experimental work was carried out at the Galdeano's Lab at the Departament de Farmàcia i Tecnologia Farmacèutica i Fisicoquímica de la Facultat de Farmàcia i Ciències de l'Alimentació de la Universitat de Barcelona. Part of this work was performed at Centre for Targeted Protein Degradation (CeTPD), University of Dundee (Dundee, Scotland) at the laboratory of Prof Alessio Ciulli. This work was supported by the Ministerio de Ciencia e Innovación (PID2021-127693OB-100, PID2022-1380790B-I00, 2021 SGR 00357 and PDC2022-133441-I00). To conduct this thesis, the candidate Ainoa Sanchez Arfelis was granted with a fellowship funded by Agència de Gestió d'Ajuts Universitaris I de Recerca (AGAUR) (Ajuts per a la contractació de personal investigador novell FI-DGR PID2019-107991RB-I00). Part of this work benefited from the access to the Centre for Targeted Protein Degradation (CeTPD), University of Dundee (Dundee, Scotland). Financial support was provided by Short-Term Scientific Mission Grant (STSM) from ProteoCure Cost Action CA20113.

A vosaltres: pares, germà, familia i Carlitos.
A les persones que estimo,
em fan feliç i estan sempre al meu costat.

The endeavor to work on the unknown.

ACKNOWLEDGEMENTS

Encara recordo el primer dia que em vaig reunir amb vosaltres, Carmen i Carles, quan em vau presentar el que seria el meu projecte d'investigació durant els pròxims quatre anys. Sempre havia volgut estar involucrada, d'alguna manera, en la recerca contra el càncer, i en aquell moment vaig tenir clar que aquest era el projecte en què volia posar tot el meu esforç, amb l'esperança de poder aportar, encara que fos una petita llavor, a la investigació en aquest camp. Gràcies a vosaltres, per ser els meus tutors, per confiar en mi des del primer moment i haver-me format com a científica i professional. Gràcies per la vostra guia i suport incondicional al llarg d'aquest projecte, no només com a supervisors, sinó també com a mentors i, en molts moments, gairebé com a "pares" en aquest camí. Gràcies per donar-me l'oportunitat de créixer al vostre costat, per fer-me sentir com a casa i per inculcar-me valors que van més enllà de la recerca.

Com he estat codirigida, he tingut la sort de poder treballar conjuntament amb dos laboratoris, el de Química Mèdica i el de Fisicoquímica, i, gràcies a això, he pogut formar part de dues grans famílies. Especialment, volia agraïr al Yerma, amb qui he compartit més hores del dia i dinars durant els últims quatre anys. Gràcies per aguantar-me cada dia, pels caps de setmana purificant junts, per les teves sessions de música, pels riures i pels moments de suport incondicional. També a la Celia, que tot i arribar més tard, t'has convertit en un pilar molt important per a mi. Gràcies per ser-hi sempre. A l'Eugenia, que tot i que només vam coincidir al laboratori quan feia el treball dirigit, després t'has convertit en una amistat indispensable i persona exemplar per a mi. La teva taquilla sempre m'ha donat sort! També vull agraïr l'Andrea Bertran per haver-me introduït i compartit els seus coneixements en el camp de la biologia cel·lular, i les técniques biofísiques. La teva ajuda i mentoria han estat fonamentals en el meu aprenentatge, i sempre t'estaré agraïda per la teva dedicació.

Finalment, i molt important, vull expressar el meu més sincer agraïment als meus companys i família de laboratori, on m'emporto grans amistats. Gràcies Noemi, Anna, Mayonesa, Tuo, Fer, Carlita, Andrea Bagán, Albertito, Sergi Rodríguez, Maria, Elsa, Andreea, Sandra, Uli, Javi, Alba, Bea, Anna Shoef, Alejandra, Roger, Patricia, Álvaro i Varbina. Gràcies per tots els moments compartits, per l'ajuda incondicional al laboratori, ciència i congressos, riures, en definitiva, per fer que el dia a dia fos més especial. Ha estat un privilegi treballar al vostre costat, heu fet aquest camí més fàcil i molt més enriquidor!

També volia agrair als professors i professores del meu departament, especialment al Diego Muñoz-Torrero, Santi Vázquez, Rodolfo Lavilla i Núria Llor, per tot el vostre suport i ensenyaments durant aquests anys. Gràcies per l'acompanyament dins del laboratori, els coneixements, pels consells personals i per tots els dinars compartits. Als professors

del departament de Fisicoquímica, en especial a en Jordi Juárez, la Salomé i en Xavier Barril. Jordi, gràcies per totes les converses compartides i per la teva predisposició a ajudar-me i aconsellar-me tant a nivell professional com personal. Dins de la meva agenda estructurada, sempre hi haurà temps per un cafè! Xavier Barril, gràcies pels coneixements i per permetre'm formar part de la col·laboració d'un projecte iniciat durant el treball dirigit, continuat al llarg de la tesi doctoral i que ha donat fruit a una publicació i un gran nombre de comunicacions.

Als professors i investigadors del departament de Farmacologia, Toxicologia i Química Terapèutica, Mercè Pallàs, Christian Griñán i Aina Bellver, per compartir, col·laborar i contribuir a l'obtenció de grans resultats en un projecte d'Alzheimer tan ambiciós. Ha estat un privilegi formar part d'aquest treball conjunt. A tots els col·laboradors i col·laboradores, incloent-hi a Belén Pérez, pels assajos de PAMPA, i a Elies Molins, pels assajos de cristal·lografia que van donar llum a molts mesos de treball. Als professors i investigadors de l'IQAC-CSIC, per acollir-nos al centre i ajudar-nos durant el primer any de la tesi, especialment a la Gemma Fabrias, Gemma Arsequell, Antonio Delgado i José Luis Abad. També a en Lateef i l'Alex, pel vostre companyerisme i per totes les hores compartides purificant amb la PuriFlash al ritme de la música d'en José Luis Abad.

Finalment, vull agraïr a la Comissió de Seguiment, Xavier Salvatella i Antoni Riera, per tots els vostres consells i orientacions durant les comissions, així com per animar-me a seguir treballant amb dedicació en la meva tesi doctoral.
L'activa participació en congressos i *summer schools* organitzats per la Societat Espanyola de Química Terapèutica (SEQT) va despertar en mi un gran interès per promoure la divulgació científica i la creació de xarxes dins de la comunitat de química mèdica. Tant és així que vaig tenir l'oportunitat de contribuir a l'organització de quatre *Young Researchers Symposiums* i, el 2023, formar part de la creació del grup SEQT-ECS com a secretària. És per tot això que estic molt agraïda a tots els membres de la junta directiva de la SEQT per creure en mi i donar-me suport en aquest camí com a científica, especialment a Beatriz de Pascual-Teresa Fernández, Jose Bartolomé, Marta Gutiérrez, Mercedes Martín, Sara Preciado i Joaquín Calixto. També al gran equip que formem a la SEQT-ECS: Laia Josa, Bárbara Noverges, Vanesa Nozal i Kike Gómez; als antics membres, Paula Morales i Dario; i als nouvinguts, Ángela, Lauri, Anna i Celia. A més, vull donar les gràcies a tots els companys amb qui he compartit la organització dels Young Researchers Symposiums i que, amb la seva dedicació i entusiasme, han fet possible que fossin un gran èxit. Gràcies a aquests simposis, m'emporto una persona molt especial per a mi, la Carol. Perquè, tot i la distància, sempre tindrem una *turulis* interminable i, les nostres abraçades, on tot es para. T'espero a la platja de la Costa Brava!

Durant el quart any de la tesi doctoral vaig tenir l'oportunitat de fer una estada al *Centre for Targeted Protein Degradation* a Dundee, Escòcia, una experiència inolvidable que em

va enriquir d'una ciència excepcional i d'un grup de científics increïbles. Vull expressar el meu agraïment a l'Alessio Ciulli per donar-me la oportunitat de formar-me al seu centre, per acollir-me i permetre'm créixer com a científica, aprenent noves tècniques innovadores i nous coneixements en el camp del TPD. Gràcies també a la Maria, Alejandro, Aitana, Aina, Jack, Calum, Manon, Conner, Diane, Alex, Ryan, Ilaria, Alessandra i tot l'equip de secretaria, per fer-me sentir part de la família des del primer moment, per compartir els *runs* dels dijous, per introduir-me al *hiking*, ensenyar-me els preciosos paisatges escocesos, pels karaokes i pels *after-work*. També vull donar les gràcies a la Isobel, per fer-me sentir cada dia, com a casa.

Finalment, vull expressar el meu agraïment més profund a les persones que han estat el meu suport incondicional durant tot aquest camí: els meus amics i la meva família.

Gràcies Victor, per estar al meu costat des del primer dia de carrera fins ara, per tot el teu suport i moments inolvidables. Gràcies Laura, per tots els *rides*, reptes i aventures juntes, i les que ens queden. Gràcies Toni, Marçal, Equip Trienjoy i Picornell, per acompanyar-me durant tantes hores d'entrenament i comepticions, i per ajudar-me a creure més en mi. Gràcies Diana, per acompanyar-me i estar al meu costat durant aquests dos anys. Gràcies Carles, Albert i Neus, pels runs dels matins que tanta energia m'han donat, pels riures i kilòmetres compartits, jo només us dic que ja estic pensant el proper repte.

I la familia, el meu pilar d'amor i valors més important. Gràcies, papa i mama, per educar-me amb tants bons valors, per inculcar-me el treball, l'esforç, la constància i l'educació, però, per sobre de tot, l'amor. Gràcies per estimar-me d'una manera tan única, per acompanyar-me i recolzar-me sempre, de manera incondicional. Al meu germà, la meva meitat i la meva persona vitamina. Perquè només ens cal una mirada per saber com estem, què pensem i què sentim. Tota la vida junts, aprenent l'un de l'altre i estimant-nos incondicionalment. Gràcies per ensenyar-me que la vida al teu costat és més bonica, divertida i feliç. Gràcies Odena, per fer-lo feliç, formar part de la familia i compartir tants moments juntes. Gràcies padrins, per donar-nos sempre tot el vostre amor. Planero m'agradaria mirar-te als ulls i dir-te "la teva neta ja és doctora". Gràcies Tieta Elena, Glorieta, Frangisquito, Mangels, Tío Jesús i Fusanta, per tot el vostre amor, suport i compartir-me tant coneixements durant tots aquests anys de formació professional i, sobretot, personal. Gràcies als qui hi sou sempre, des de dalt, Patri, Padrí, Magdita, Pepix i Tío Emilio.

Carlos, tant de temps buscan-te i per fi has aparegut. Gràcies per tot el teu amor, fer-me tant feliç cada dia, per fer-ho fàcil, pel teu suport quan més ho he necessitat i per compartir amb mi el que tant ens agrada, el triatló (encara que, a vegades, ens separem per minuts i segons). Gràcies per voler compartir aquest projecte de vida junts. I com sé que mai deixaràs de sorprendre'm, et vull seguir preguntant*, hi ha alguna cosa que et preocupa?*

Fer una tesi doctoral ha estat un viatge ple de reptes, moments de dubte i molta dedicació, però també d'aprenentatge, creixement i experiències inoblidables. Aquesta tesi m'ha ensenyat a crèixer com a persona, a formar-me professionalment i a seguir el camí que, des de ben petita, havia volgut recòrrer. Però, per sobre de tot, m'ha fet veure la sort d'haver estat envoltada de persones i professionals excepcionals, que estimen, impulsen i et fan millor persona.

Ara toca continuar endavant i aquesta etapa sempre quedarà plasmada en la persona que sóc i en la que seré.

Gràcies a tots els qui n'heu format part!

SUMMARY

Modern drug discovery has focused on developing selective small molecules that bind enzymatic active sites to modulate protein function. However, over 80% of human proteins remain "undruggable" due to their lack of defined binding pockets and dynamic and / or unstructured surfaces.

This PhD thesis addresses this gap by exploring innovative chemical strategies to target undruggable cancer-related proteins, focusing on cMyc, Cyclin E / CDK2, and Brd4, which indirectly affect cMyc. The first objective targets the undruggable cMyc using PROTAC technology. Two generations of PROTACs were developed: the first, based on 10058-F4 derivatives and PEG linkers, showed limited degradation efficacy. In contrast, the second generation, incorporating 28RH ligand and alkyl linkers, significantly improved degradation efficiency. Among these, ASA_MDEG-542 demonstrated potent, dose-dependent cMyc degradation, highlighting the critical role of linker design and providing a foundation for further development of cMyc degraders. The second objective addresses Cyclin E, another elusive oncogenic driver, through a "bridged PROTAC" strategy that hijacks its natural partner CDK2 for dual degradation. Six first-generation Cyclin E / CDK2 PROTACs have been synthesized, using ARG-91 as a warhead. Among them, CYC-3 has demonstrated the most promising CDK2 degradation, providing proof-of-concept for this indirect degradation strategy and setting the stage for further optimization with higher-affinity ligands like ARG-15. The final chapter explores a FBDD to develop novel inhibitors targeting Brd4(BD1), a key epigenetic regulator. Using an automated fragment evolution platform and the NAOMInext computational tool, the SSR4 scaffold has been identified and evolved into potent derivatives. Despite synthetic challenges, the optimized compound SSR12 achieved a 650-fold improvement in affinity compared to the original fragment, reaching potency comparable to (+)-JQ1.

Overall, this thesis presents innovative methodologies to expand the druggable proteome, offering new therapeutic strategies against cancers driven by undruggable targets through the combined use of PROTAC technology, computational drug design, and fragment-based discovery.

Keywords: *PROTACs; Targeted Protein Degradation; Fragment – Based Drug Discovery; cMyc; Cyclin E; CDK2; Brd4; undruggable proteome; oncogenes.*

RESUM

La descoberta moderna de fàrmacs s'ha centrat en desenvolupar petites molècules selectives capaces d'unir-se a les cavitats actives enzimàtiques per modular la funció proteica. No obstant això, més del 80% de les proteïnes humanes continuen sent intractables per la manca de cavitats definides i la presència de superfícies dinàmiques o no estructurades.

Aquesta tesi doctoral explora estratègies químiques innovadores per abordar proteïnes relacionades amb el càncer considerades intractables, amb especial focus en cMyc, Cyclin E/CDK2 i Brd4, el qual afecta indirectament cMyc. El primer objectiu se centra en la degradació de cMyc mitjançant la tecnologia PROTAC. S'han desenvolupat dues generacions de PROTACs: la primera, basada en derivats de 10058-F4 i enllaços PEG, va mostrar una eficàcia limitada. En canvi, la segona generació, amb el lligand 28RH i enllaços alquilats, va millorar significativament els perfils de degradació. D'entre aquests, ASA_MDEG-542 ha demostrat una degradació potent i dependent de la dosi, ressaltant el paper crític del disseny de l'enllaçant i proporcionant una base sòlida per a futurs degradadors de cMyc. El segon objectiu aborda Cyclin E mitjançant una estratègia de "PROTAC pont", aprofitant la seva interacció amb CDK2 per a la seva degradació dual. Es van sintetitzar sis PROTACs de primera generació amb ARG-91 com a lligand, i CYC-3 ha mostrat el perfil de degradació més prometedor cap a CDK2, establint la primera prova de concepte i obrint la via a optimitzacions futures amb lligands com ARG-15. L'últim capítol explora la descoberta de fàrmacs basada en fragments per desenvolupar nous inhibidors dirigits a Brd4(BD1), un regulador epigenètic clau per desenvolupar nous inhibidors de Brd4(BD1). Utilitzant la plataforma automatitzada d'evolució de fragments i l'eina NAOMInext, s'ha identificat l'estructura SSR4, fins a obtenir SSR12, amb una millora d'afinitat de 650 vegades respecte al fragment inicial, assolint una potència similar a (+)-JQ1.

En conjunt, aquesta tesi presenta metodologies innovadores per expandir el proteoma tractable oferint noves estratègies terapèutiques contra càncers impulsats per dianes tradicionalment considerades intractables, combinant la tecnologia PROTAC, el disseny computacional de fàrmacs i la descoberta basada en fragments.

Paraules clau: PROTACs; Degradació dirigida de proteïnes; Descoberta de fàrmacs basada en fragments; cMyc; Cyclin E; CDK2; Brd4; proteoma intractable; oncogens.

THESIS ORGANIZATION

This thesis is dedicated to the early stages of a drug discovery campaign, addressing the challenge of identifying ligands capable of targeting either traditionally undruggable or otherwise critical proteins involved in human cancers. The core of the work is structured into three main research chapters, each focused on a specific protein target of interest. These chapters encompass the chemical synthesis and biological evaluation of the compound series, aiming to identify the most potent one in each case.

The thesis begins with an introductory chapter that outlines key concepts relevant to the research, with particular emphasis on current unmet clinical needs and the major challenges in drug discovery that this work aims to address.

Chapter 2 presents an overview of the research objectives, introducing the biological targets selected for investigation and the rationale behind their selection.

Chapters 3 through 5 form the main body of the thesis and present the results of three independent research projects. Each chapter focuses on a specific target and begins with a concise introduction that provides context for the study, highlighting the biological relevance of the target and summarizing the preliminary data that inspired the initial hypothesis. Each chapter concludes with a discussion of the key findings and a summary of conclusions. Specifically, Chapter 3 explores strategies to degrade the undruggable transcription factor cMyc, Chapter 4 focuses on targeting the cell cycle regulators Cyclin E and CDK2, and Chapter 5 addresses the epigenetic reader Brd4(BD1), which indirectly modulates cMyc activity.

Chapter 6 contains the full experimental section, detailing the chemical synthesis, cellular biology protocols, and biophysical assays employed throughout the thesis.

The thesis concludes with a comprehensive bibliography.

STATEMENT OF CONTRIBUTORS

The research outlined in this thesis is the result of collaborative efforts involving several researchers whose contributions were essential at various stages of the different projects. To thank all those who played a role in this work, in the following sections, I outline their specific involvement across the relevant chapters.

Chapter 3: Degrading cMyc with Low-Affinity Small Molecule-Based PROTACs

Dr. Sergi Rodríguez-Arévalo (SRA), initiated the project with the synthesis of the first PROTAC series at the Laboratory of Medicinal Chemistry of the University of Barcelona. Dr. Andrea Bertran-Mostazo (ABM) conducted the initial biological assays at the Scientific and Technical Services of the University of Barcelona (CCTiUB) of the Barcelona Science Park. Prof. Elies Molins (EM) performed the X-ray crystallography studies at the Institute of Materials Science of Barcelona (ICMAB-CSIC). The work was designed and supervised by Prof. Carmen Escolano (CE) and Dr. Carles Galdeano (CG).

Chapter 4: Targeting Cyclin E/CDK2 with a Novel Dual PROTAC Molecule

Dr. Alejandra Ruiz-Gimeno (ARG) led the computational studies and virtual screening campaign. Also, ARG conducted the SPR studies and biological assays at the CCTiUB of the Barcelona Science Park. Additionally, ARG proposed the design of the chemical synthesis of the PROTACs presented in this chapter, and synthesized the ligands ARG-9 and ARG-91 at the Laboratory of Medicinal Chemistry of the University of Barcelona.The biological experiments were conducted at the Centre for Targeted Protein Degradation (CeTPD) during the Short-Term Scientific Mission (STSM) internship stay under the supervision of Prof. Alessio Ciulli (AC), Prof. Adrian Saurin (AS), and Dr. Alejandro Correa-Sáez (ACS). The work was also supervised and planned by CE, CG, and ARG.

Chapter 5: Discovering Brd4(BD1) Inhibitors via Fragment-Based Drug Discovery

Serena G. Piticchio (SGP) developed the fragment evolution platform with support from Moira Rachman (MR). SGP applied the platform to the 1XA fragment and, together with MR, contributed to the development and computational work around the NAOMInext software. Salvatore Scaffidi (SS) and SRA were in charge of the chemical synthesis of the SSR1 to SSR6 compound series. Míriam Martínez-Cartó (MMC) and SS conducted the corresponding TR-FRET biophysical assays. Additionally, SRA further advanced the project by synthesizing the SSR11 and SSR12 compounds, while ABM performed the TR-FRET assays for these later-stage compounds. MMC, Sarah Picaud (SP), Tobias Krojer (TK), Panagis Filippakopoulos (PF), and Frank von Delft (FvD) completed the crystallographic and structural refinement of SSR4 at the University of Oxford. Chemical synthesis was supervised by CE, while Prof. Xavier Barril (XB) and CG coordinated the overall study design and experimental planning.

TABLE OF CONTENTS

ABBREVIATIONS

ADME	Absorption, distribution, metabolism and elimination
AI	Artificial intelligence
AcOEt	Ethyl acetate
AR	Androgen receptor
ASOs	Antisense oligonucleotides
AUTACs	Autophagy- targeted chimeras
BAF	Brg1 / Brm-associated factor
Baf-A1	Bafilomycin A1, reversible inhibitor of vacuolar H+-ATPase
BCA	Bicinchoninic acid assay
BCL6	B-cell lymphoma 6 TF
BCP	Bromodomain containing protein
BET	Bromo and extraterminal domain protein
bHLH-ZIP	Basic- helix- loop- helix- Leucine zipper
BRD	Bromodomain protein
BRET	Bioluminescence resonance energy transfer
bRo5	Beyond the “rule of five”
CADD	Computer- aided drug design
Cas9	CRISPR- associated protein 9
CBFβ	Core binding factor beta
CDK	Cyclin-dependent kinase
CEF	Chicken embryo fibroblast
CHAMP	Chaperone-mediated protein degradation
CH_3CN	Acetonitrile
CI_{95}	95% confidence Interval
cMyc	Myc proto-oncogene protein
CO_2	Carbon dioxide
CRBN	Cereblon E3 ligase
CRISPR	Clustered regularly interspaced short palindromic repeats
CRLs	Cullin-RING ligases
Cs_2CO_3	Cesium carbonate
Cu	Copper
DBD	DNA-binding domain
DCM	Dichloromethane
DC_{50}	50 % degradation concentration
ddH_2O	Double-distilled water
DEL	DNA-encoded libraries
DEPT	Distortionless enhancement by polarization transfer
DIPEA	*N,N*-Diisopropylethylamine
DMEM	Dulbecco’s modified eagle medium
DMF	Dimethylformamide
DMSO	Dimethyl sulfoxide
DUBTACs	Deubiquitinase-targeting chimeras
DPPF	Bis(diphenylphosphino) ferrocene

eBo5	Extended the “rule of five”
eq	Equivalent
EMSA	Electrophoretic mobility shift assay
ER	Estrogen receptor
EtOH	Ethanol
EWG	Electronic withdrawal group
E-box	Enhancer-box
FBBD	Fragment- based drug discovery
FBS	Fetal bovine serum
FBXW7	F-box/WD repeat-containing protein 7
FDA	Food and drug administration
FOXO	Forkhead box O
FP	Fluorescence polarization
F2L	Fragment-to-lead
HAT	Histone acetyltransferases
HATU	O-(7-Azabenzotriazol-1-yl)-*N,N,N′,N*'-Tetramethyluronium hexafluorophosphate
HBA	Hydrogen bond acceptors
HDAC	Histone deacetylases
HBD	Hydrogen bond donors
HCO_2H	Formic acid
HCT 116	MYC-amplified colon cancer cell line
HEK 293	Human embryonic kidney cells
HIF	Hypoxia- inducible factor
HPLC / MS	High-performance liquid chromatography-mass spectrometry
HRMS	High-resolution mass spectrometry
HTS	High-throughput screening
IAP	Inhibitor of apoptosis protein E3 ligase
IC_{50}	50 % inhibition constant
IDP	Intrinsically disordered protein
IGF1R	Insulin like growth factor 1 receptor human
IKZF	Ikaros zinc- finger
IMiDs	Immunomodulatory drugs
IR	Infrared
IRF3	Interferon regulatory factor 3
JohnPhos	(2-Biphenyl)di-*tert*-butylphosphine
KAc	Acetyl lysine pocket
Kd	Equilibrium dissociation constant
*KD*a	Kilodalton
KF	Potassium fluoride
K_i	Inhibitory constant
KOAc	Potassium acetate
KRAS	Kirsten rat sarcoma viral oncogene homolog
K_2CO_3	Potassium carbonate
K_3PO_4	Potassium phosphate
LBD	Ligand- binding domain
LC-MS	Liquid chromatography – mass spectrometry
LE	Ligand efficiency
LogP	Partition coefficient
LTR	Lysosome-targeting receptor

LYTAC	Lysosomal-targeting chimera technologies
Max	Myc-associated factor X
MDM2	Mouse double minute 2 E3 ligase
MG	Molecular glue
MG-132	Z-Leu-Leu-Leu-al, proteasome inhibitor
miRNAs	MicroRNAs
MLN-4924	Pevonedistat, NAE inhibitor
MoA	Mechanism of action
MQW	Milli-Q water
MW	Molecular weight
M/W	Microwave conditions
NAE	NEDD8-activating enzyme
NaCl	Sodium chloride
Na_2SO_4	Sodium sulfate
NMR	Nuclear magnetic resonance
NOTCH	Neurogenic locus notch homolog
PAS-B	Per-ARNT-Sim domain B
PBS	Phosphate-Buffered Saline
Pd	Palladium
$Pd(OAC)_2$	Palladium acetate
$Pd[P(o\text{-}tolyl)_3]_2Cl$	Dichlorobis(tri-*o*-tolylphosphine) palladium (II)
Pd_2dba_3	Tris(dibenzylideneacetone)dipalladium(0)
PEG	Polyethylene glycol
$POCl_3$	Phosphorus oxychloride
POI	Protein of interest
PPh_3	Triphenylphosphine
PPI	Protein-protein interaction
ppm	Chemical shift

PROTAC	Proteolysis targeting chimeras
PROTAB	Proteolysis-targeting antibodies
pPROTAC	Peptide- based PROTAC
PTM	Post-translational Modification
p53	Tumor protein
rac-BINAP	Racemic 2,2'-Bis(diphenylphosphino)-1,1'-binaphthyl
RNAi	RNA interference
Ro5	Rule of five
RUNX1	Runt-related transcription factor 1
R2	R squared correlation coefficient
SAR	Structure-activity relationship
SCF	Skp, cullin, F-box containing complex
SD	Standard deviation
SH2	Src homology 2
siRNAs	Small interference RNAs
SKP2	S-phase kinase-associated protein 2
SNIPERs	Specific and non-genetic IAP-dependent protein erasers
SPR	Surface plasmon resonance
STAT	Signal transducer and activator of transcription
TE	Target engagement
TF	Transcription factor
TFA	Trifluoroacetic acid
THF	Tetrahydrofuran
TLC	Thin-layer chromatography

TPD	Targeted protein degradation
TPSA	Topological polar surface area
VHL	Von Hippel-Lindau E3 ligase
vMyc	Avian myelocytomatosis virus
VS	Virtual screening
WB	Western blot
WPF shelf	Tryptophan, proline, phenylalanine shelf
XantPhos	4,5-Bis(diphenylphosphino)-9,9-dimethylxanthene

CHAPTER 1

Introduction

1. CHAPTER 1: INTRODUCTION

1.1 An overview of the drug discovery and development process

Drug discovery involves an array of multidisciplinary sciences working in concert to identify and characterize molecules with the potential to therapeutically modulate a disease or clinical condition, to address clinical needs, whether suitable medical products currently exist. [1] Developing a new drug from the initial idea to the launch of the finished product is a complex process that can take 12 to 15 years and cost over 1 billion dollars (Figure 1). Optimizing this process is of great interest to the pharmaceutical industry, as the efficient identification and selection of suitable drug candidates can have a dramatic impact on the cost and profitability of new medicines. [2]

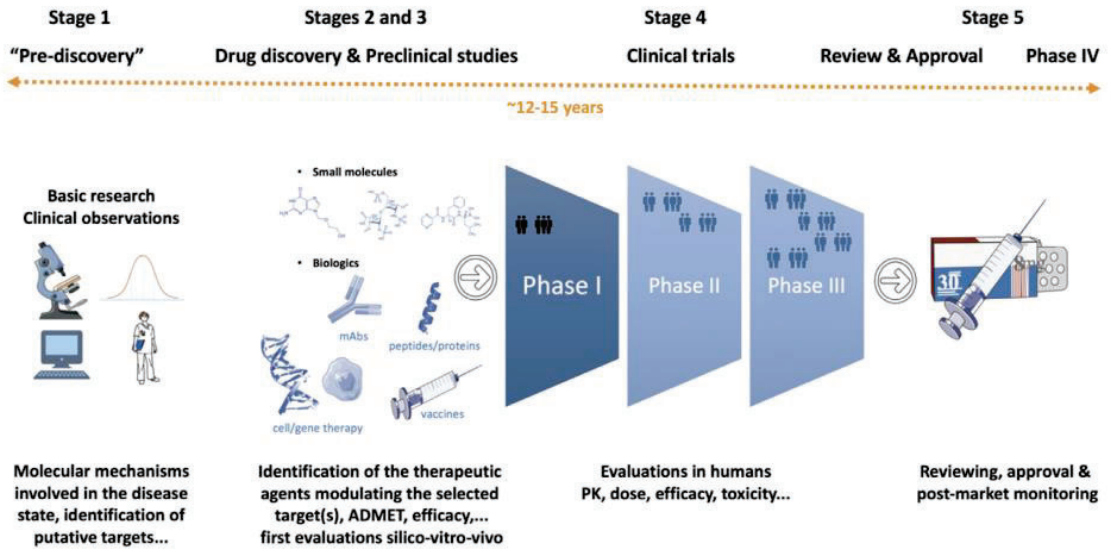

Figure 1: Overview of the drug discovery and development process. From [3].

Nowadays, the drug discovery pipeline [4] begins with the identification and validation of a potential therapeutic target, which can be applied to a range of biological entities (*e.g.,* proteins, genes and RNA), linked to a disease state. A good target should be effective, safe, and able to meet both clinical and commercial requirements. Most importantly, it must be "druggable" meaning it should be accessible to potential drug molecules, whether small compounds or larger biologics, can trigger a measurable biological response upon binding, both *in vitro* and *in vivo*. The process continues with the search of therapeutic agents, able to modify the function or the amounts of the target and restore and / or improve health. We can classify these agents into two big classes: small-molecules (small-chemical compounds, modified short peptides, etc.) and biologics (antibodies, siRNAs, long peptides, etc).

Focusing on the small-molecule drug modality, high-throughput screening [5], fragment-based techniques [6] and other computer-aided drug design approaches [7], as well as structure-activity-relationship (SAR) studies, are developed during the *hit-to-lead* discovery program [8] to optimize and improve the potency, selectivity and drug-like properties of the initial hit series. During the lead discovery phase, molecules are screened in cell-based assays that mimic the disease state and in animal models to evaluate both their efficacy and potential safety profile. The discovery phase concludes with a potent lead that will be advanced into a drug candidate during the preclinical phase, using various assays *in silico*, *in vitro*, and *in vivo* animal models. At the same time, more detailed profiling of physicochemical and pharmacokinetic, and *in vitro* ADME (absorption, distribution, metabolism and elimination) properties are performed. [9]

All information gathered about the molecule at this stage enables the development of a clinical candidate profile, which, along with toxicological data and chemical manufacturing and control considerations, forms the basis of a regulatory submission to advance to human clinical trials. This stage comprises four different phases (I-IV). [10] Phase I focuses on safety and dosage, testing a small group of healthy volunteers to establish safe dosage ranges and identify side effects. Phase II evaluates efficacy and further assesses safety in a larger patient group with the target condition, helping to refine dosing. Phase III trials are large-scale studies comparing the drug's effectiveness to standard treatments while monitoring side effects, providing the data needed for regulatory approval. Upon completion of this phase, the drug is submitted to the regulatory agencies to demonstrate drug safety and efficacy. For approval, the drug must have adequate pharmaceutical quality, therapeutic effectiveness and safety, as well as have a favorable "risk-benefit ratio". In many cases, additional follow-up studies often referred to as phase IV or post-marketing surveillance and/or pharmacovigilance, are required by the regulatory agencies to monitor long-term adverse effects in the general population, ensuring the drug's continued safety and exploring potential new uses.

1.2 Addressing the enduring challenge of drugging the *undruggable*

An assessment of the number of molecular targets that represent an opportunity for therapeutic intervention is crucial to the drug discovery and development campaigns within both academia and pharmaceutical industry. [11] With the human genome now mapped [12], it is intriguing to consider how many molecular targets this breakthrough might offer. However, although biological systems contain four types of macromolecules with which we can interfere using small-molecule therapeutic agents, successful drugs have been inherently limited in binding and modifying the activity of proteins and nucleic acids This limits the molecular targets for which drug candidates can be developed, leading to the concept of the "druggable genome", the subset of the ~ 30,000 genes in

the human genome characterized by the presence of well-defined small-molecule binding pockets. Druggability, termed over fifteen years ago, [13] is currently defined as the ability of a protein to be modulated by small drug-like molecules. Moreover, it is estimated that nearly 60 % of drug discovery failures are a result of invalid or inappropriate identification of drug targets. [14]

The total chemical space of drug discovery is estimated to be 10^{60} possible compounds which can be alleviated somewhat with chemical fragment libraries and physiochemical thresholds reducing this number to roughly 10^{23} possible drugs. [15,16] Conventional screening typically relies on a library of drug-like compounds chosen based on their likelihood of oral absorption, in terms of solubility and permeability, as outlined by "Rule of five" (Ro5) [17], with sufficient affinity and specificity *in vivo* to create a therapeutic effect in a relevant cellular pathway. [18] Nowadays, the interest in exploring the chemical space by driving the search for alternative drug discovery strategies has led to the investigation of approaches like "beyond the Rule of fiv" (bRo5) and "extended Rule of five" (eRo5), which focus on drug-like molecules that do not strictly adhere to the traditional Ro5 but still show promise in terms of pharmacokinetic properties and therapeutic potential. By incorporating additional factors such as polar surface area, the number of rotatable bonds, larger molecular weights, and more polar functional groups, bRo5 and eRo5 help broaden the scope of potential chemical space for drug development. [19-21]

In practice, most of the drug-like compounds following Ro5 fount to bind to molecular targets fall into just six major families: G-protein coupled receptors (GPCRs), zinc metallopeptidases, serine/threonine and tyrosine protein kinases, erine proteases, phosphodiesterases and nuclear hormone receptors (Figure 2). [13]

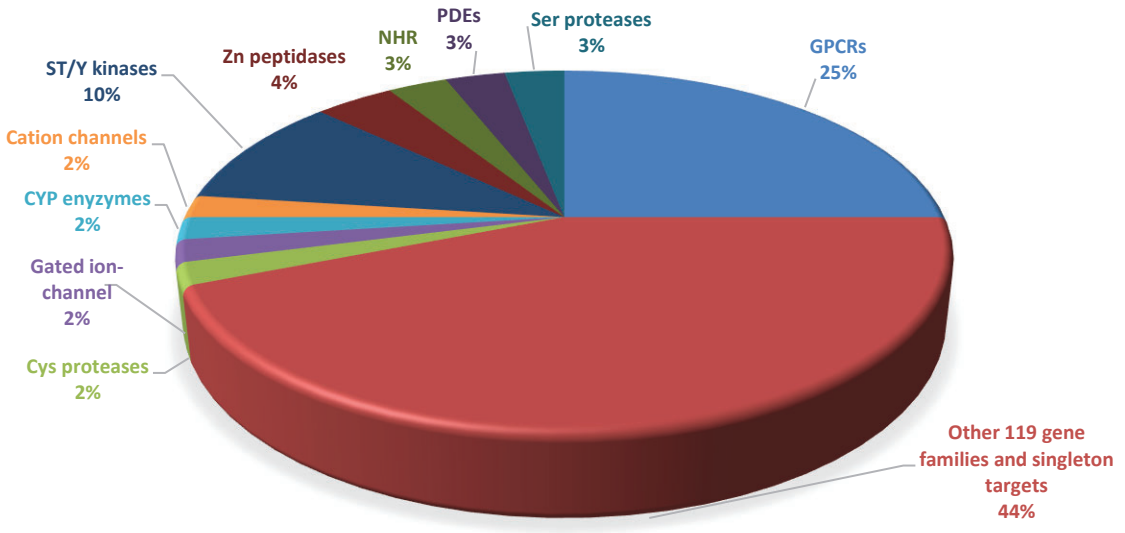

Figure 2: Gene-family distribution of the molecular targets of current Ro5 compliant experimental and marketed drugs. *Serine (Ser)/Threonine and tyrosine protein kinases are grouped as one gene family (ST/Y kinases)as are class 1 and 2 GPCRs; CYP, cytochrome P450; NHR, nuclear hormone receptor; Cys, cysteine; PDE, phosphodiesterase, Zn, zinc*. From [13].

Some proteins are considered “druggable”, while others are termed “ligandable”. Ligandability refers to a protein's ability to bind a small, drug-like molecule without necessarily trigger a pharmacological response. [11, 22] In contrast, the term “undruggable” describes proteins that present flat functional interfaces and lack of well-defined pockets for ligand interaction, resulting in ration drug design a big challenge. [23-25]

Studies indicate that around 10 % of proteins have an identified small-molecule binder. Approximately 3 % of proteins are associated with at least one approved drug, while 7 % are known to bind small molecules with high potency. Proteins that have verified bioactivity and clinical relevance but lack developed small-molecule therapies make up 55 % of the proteome. The remaining 35 % of proteins belong to the "dark proteome", with minimal characterization or known function (**Figure 3**). [26]

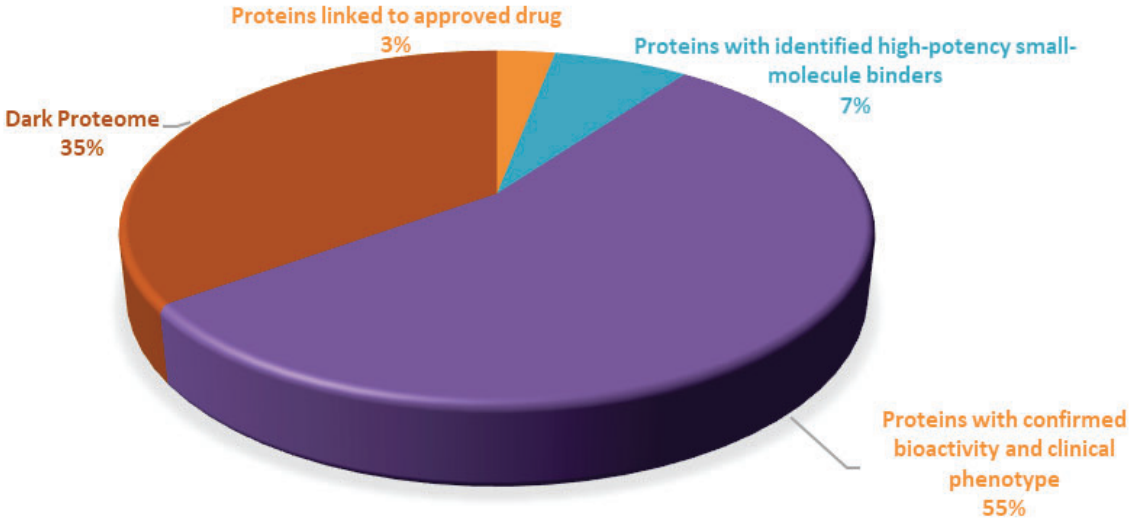

Figure 3: Percentage of the whole ligandable proteome regarding the described data from [26].

Targeting such undruggable proteins is seen as a significant opportunity for treating human diseases like cancer, a critical unmet medical need that causes millions of deaths annually, leading to the pressing urge for research in this area to develop novel therapeutic approaches. [27,28] In fact, we still lack clinically validated treatments for the vast majority of the so- called cancer genes, including many of those that are most frequently altered. A notable example is Kirsten rat sarcoma virus (KRAS) [25], an oncogene protein considered undruggable due to its varying mutation in different solid tumors. In 2021, a significant milestone was reached when the Food and Drug Administration (FDA) approved **sotorasib**, [29] a $KRAS^{G12C}$ inhibitor, for a specific subgroup of patients with non- small cell lung cancer, demonstrating that targeting "undruggable" proteins is very valuable. Therefore, broadening the druggable proteome to develop new treatments for the most frequently activated genes in human cancer could imply a huge benefit.

1.3 Drug modalities for targeting transcription factors

In the early 20th century, the rapid discovery of oncogenes, mutated genes that allow unregulated cell growth, revealed many proteins involved in cell signaling. Proteins in these pathways can be made oncogenic by mutation or overexpression. [30,31] DNA-binding transcription factors (TFs) are among the most essential classes of proteins within the eukaryotic proteome. [32] TFs play foundational roles in the identity and fate of individual cells in multicellular organisms by guiding gene expression and regulation, as well as being responsible for quickly orchestrating responses to internal and external signals, acting as key endpoints in cellular signaling networks. [33] It is estimated that the human genome contains at least 1600 TFs, with approximately 19 % linked to disease

phenotypes (*e.g.*, cancer, autoimmunity, diabetes and cardiovascular disease) and only a handful have been successfully targeted by small molecules. [34] The fundamental challenge not only remains on its undruggability properties but on their function through dynamic interactions with DNA and proteins, complicating the identification of effective modulation site. [35, 36] Moreover, the complex regulation of TFs domains' and evolving insights into gene regulation further challenge their targeting, making TFs some of the most challenging targets in the proteome to address in drug discovery.

Understanding the assembly of TFs in different configurations to recognize binding sites and regulate transcription is crucial for comprehending their functionality (**Figure 4**). A minimal TF is defined by just the presence of two key elements: a DNA-binding domain (DBD) that binds to specific DNA regulatory sequences, and an effector domain that recruits members of transcriptional activation or repression machinery. [37, 38] Many TFs also contain one or more regulatory domains, which typically serve to regulate TFs localization and functional activity (*e.g.,* STAT family regulation to the nucleus is controlled by homodimerization or heterodimerization with other STAT TFs by a SH2 domain). [39] Nuclear receptors, [40] the most druggable family of TFs, feature a ligand-binding domain (LBD) that works with a disordered transactivation domain to recruit transcriptional machinery upon binding to small-molecule ligands. Others such as basic helix-loop-helix family require dimerization with other members to create functional DBDs. [41] These diverse regulatory domains and mechanisms have provided the most promising opportunities for drug discoverers to create effective transcription factor modulators.

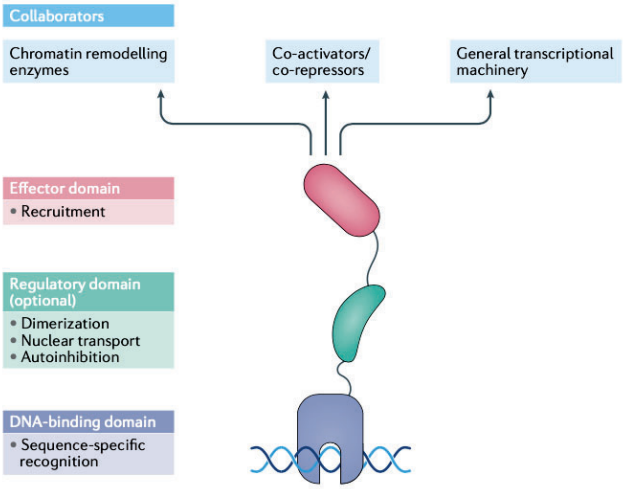

Figure 4: General structure of a TF. All TFs have two primary protein domains: a DBD (in purple), which attaches to specific DNA regulatory sequences (in green), and an effector domain (in light red) that attracts various transcriptional collaborators to control chromatin accessibility and transcriptional output. Additionally, many TFs include one or more regulatory domains (in light blue) that generally modulate their localization and functional activity. From [42].

TFs functionality at a specific binding site, which is highly complex and dynamic, often yielding counterintuitive outcomes, is influenced not only by the thermodynamic stability of the TF-DNA complex but also by various factors, including the multidimensional architecture of DNA and chromatin, the cooperative actions of other TFs and co-activators at nearby or overlapping sites, as well as the kinetics of TF binding to DNA. [43,44] The highly dynamic binding of TFs to DNA has surprising implications. Modern imaging, which contradicts the traditional belief in prolonged binding, revealing that TF only binds to target sites for a few seconds. This dynamism highlights the fast turnover of TFs as a regulatory mechanism and prevents staying at non-specific sites for extended periods. [45] Altogether, the unexpected outcomes of the three-dimensional and dynamic nature of TFs may indicate that many general assumptions about TFs action have significant potential to be misleading, highlighting the importance of continued effort to understand TF- mediated gene regulation. [33]

TFs, as essential regulators of selective gene expression, are deeply involved in the disrupted transcriptional programs critical to pathogenesis, positioning them as prime targets for disease intervention. [46] In fact, dysregulated transcription is a hallmark of cancer and TFs can be responsible for causing a diverse variety of oncogenic phenotypes via overactivation and/or overexpression as well as aberrant inactivation of tumor suppressor. [47, 48] Many cancers rely on TFs for growth, a phenomenon known as "oncogenic addiction". [49] One prominent example is cMyc, a basic-helix-loop-helix-leucine zipper (bHLH-ZIP) TF, that acts as a general transcriptional "amplifier". It enhances gene expression by recruiting the transcriptional elongation machinery, thereby driving onocogenic programs across multiple cancer types. [50] TFs represent a substantial portion of targets identified in cancer genetic dependency databases like DepMap, [51] endorsing that oncogenic addiction to TFs is a common weakness across myriad cancers.

Preventing functional interactions between the nuclear TF protein and DNA or coregulatory proteins with small molecules, has proven remarkably difficult until recently, as the interaction sites on TFs are typically large and flat, unlike the deep, druggable binding pockets common in enzymes and receptors. [28] Emerging medicinal chemistry, biophysics and chemical biology are putting all their efforts to address these challenges and modulate TF activity by small molecules as a therapeutic approach in cancer treatment (Figure 5). [27, 42, 52] Among the different opportunities to indirectly or directly target a transcription factor are the following:

i. Effector domain modulators

In general, one of the most successful and oldest approach in drug discovery for inhibiting transcription factors is the development of ligand-derived drugs, taking advantages of a well-folded LBD that acts as a second effector domain and can serve as intrinsically

ligandable control points to develop structural derivatives of the natural ligands. This is the case of nuclear hormone receptors [53] which binding to specific signaling molecules (*e.g.*, estrogen, androgens, glucocorticoids) to the LBD, activates the TF through various mechanisms such as nuclear localization, homo- or hetero- oligomerization, among others. Accordingly, numerous drugs and chemical probes have been developed targeting nuclear receptors. An example is **enzalutamide** (**Figure 5**), [54, 42] FDA-approved antagonist androgen receptor (AR), which demonstrates the potential of using folded effector domains with conserved small-molecule pockets as handles for expanding the druggability of TFs.

However, most oncogenic transcription factors lack natural ligand-binding pockets, necessitating alternative approaches that leverage, for instance, the dynamics of DNA binding. [55] These dynamics may reveal structural pockets that could serve as targets for selecting or designing well-fitting compounds. This approach is exemplified by two morpholine derivatives, **VPC-14428** and **VPC-14449**, two compounds specifically engineered to bind a pocket within the DNA-binding domain of the AR, a novel target site proposed as an alternative to the traditional androgen-binding pocket. [56] Another is the targeting of Signal Transducer and Activator of Transcription (STAT) with **InS3-54** compound which interacts non-covalently with STAT3 DNA binding domain, without affecting STAT3 homodimerization and phosphorylation. [57]

ii. Regulatory domain modulators: protein- protein interaction (PPI) inhibitors

An alternative approach to targeting TFs involves disrupting their interactions with other proteins, which can lead to various outcomes depending on the modulation of the interacting partner and context. PPI inhibitors come in several types: small molecules, antibodies, peptides, and recombinant proteins, each with unique advantages and limitations. [58] Small molecules are often favored for their pharmacokinetic benefits, including cell penetration and oral availability, and they are also more cost-and time-efficient. However, their limited selectivity and fit for narrow PPI interfaces can constrain their use.

The discovery of “hot spots” has enabled more effective targeting of PPIs. [59] It also allows modulators to be classified as either orthosteric inhibitors or allosteric modulators. Orthosteric inhibitors target PPI interfaces directly at the hot spots, while allosteric modulators act on non-catalytic regions, normally inducing structural changes in the proteins.

Inhibiting these PPI may cause protein sequestration, stabilization, or degradation. Some examples are: targeting the TF itself forming homodimers (STAT), [60]) PPI with another TF (cMyc/Max, [61] RUNX1/CBFβ) [62] from the basal transcription machinery, co-

factor/co- activator/mediator or repressor (HIF2α/PAS-B)[63] or proteins sequestrating the TF in cytoplasm often associated with degradation process (such as MI-77301, as p53/MDM2 inhibitor) [64]) (Figure 5). [42]

iii. Collaborator modulators

Recent studies reveal that chemical inhibition of certain general transcriptional co-factors, like transcriptional kinases, epigenetic proteins, and co-activators, can exhibit cell- type specificity, particularly affecting cell-identity transcriptional programs. This specificity is attributed to the presence of *superenhancers,* regions that regulate critical cell-identity genes and are more sensitive to disruption than typical enhancers. Superenhancers have a highly cooperative structure, making them more susceptible to inhibition of general co-factors, which leads to selective modulation of transcription in a cell-type-dependent manner. One example is bromodomain inhibitors, like ABBV-744, which blocks Brd4(BD2) chromatin reader (Figure 5). [65, 66, 42] Also, transcriptional kinases, such as CDK7, CDK9, and CDK12; [67,68] histone-modifying enzymes, like HDACs and HATs [69]; and chromatin remodelers, like BAF [70], can selectively disrupt superenhancer-associated genes. This insight opens opportunities for more targeted therapeutic approaches by leveraging the unique vulnerabilities of superenhancer-driven gene expression in various cell types of cancer.

iv. Degraders

This strategy exploits pathways like the ubiquitin-proteasome system (UPS) to selectively eliminate TFs that are already expressed, thereby reducing their impact on gene expression. Chapter 1.4 is exclusively dedicated to this approach.

v. Other strategies: gene editing

Targeting RNA has emerged as a promising approach for therapeutically modulating cellular processes linked to previously “undruggable” protein targets. [71, 72] RNA-based therapeutics, which regulate proteins at the genetic and transcriptional level, have developed significantly since their inception in the 1970s. These therapeutics include antisense oligonucleotides (ASOs), RNA interference (RNAi), including small interference RNAs (siRNAs) and microRNAs (miRNAs), and CRISPR-based genome editing.

Some examples of these emerged therapeutic applications are: a reported ASO that showed potential activity in downregulation KRAS mRNA *in vitro* and *in vivo* cancer cells without any delivery agent [73], a siRNA-based therapy that targets mutant-specific p53 developed by Quark Pharmaceuticals for the treatment of kidney acute renal failure and has entered phase II clinical trials (NCT00683553) [74], and engineered exosomes have

been explored as non-viral delivery systems for CRISPR/Cas9, successfully targeting mutant KRAS in pancreatic cancer cells, suppressing tumor growth *in vivo.* [75]

Although genetic therapies have proven effective in indirectly targeting undruggable proteins, these approaches are limited by off-target effects and side effects, which highlights the need for further research. Meanwhile, novel drug discovery approaches, including biological display technologies, DNA-encoded libraries (DEL), fragment-based drug discovery, and gene editing, along with advancements in computing such as AI, computer-aided drug design (CADD), machine learning, and deep learning, can enhance efficiency and conserve resources. Therefore, with continued advancements in understanding disease pathogenesis and the development of improved strategies, it is hopeful that these once unreachable proteins are now emerging as prominent therapeutic targets, representing the forefront of drug discovery.

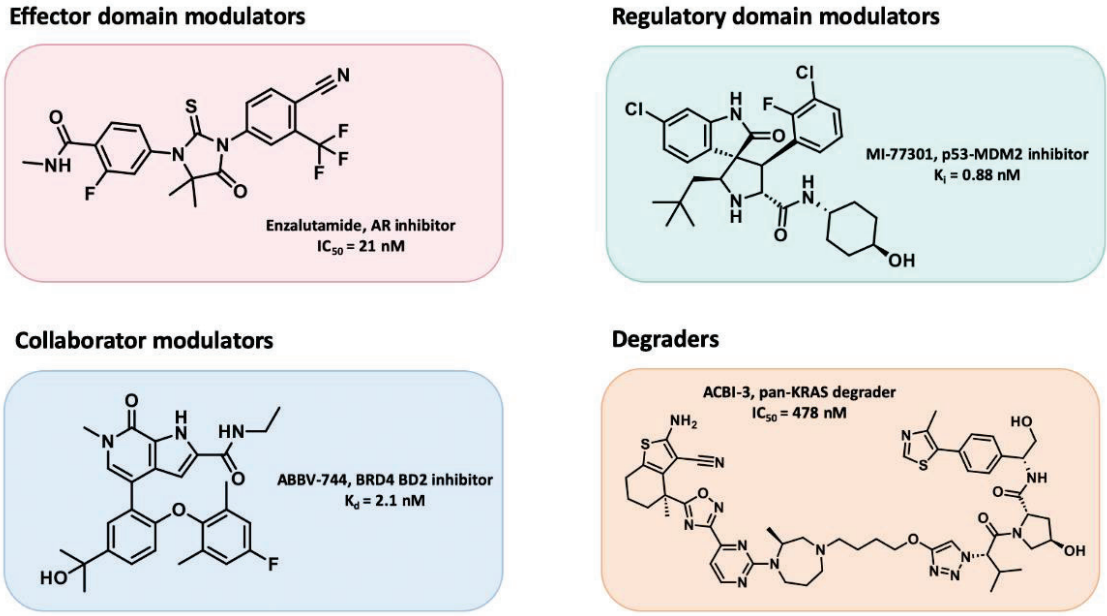

Figure 5: Overview of representative chemical structures of four different current strategies for TF targeting. From [42].

1.4 Hijacking the UPS with small molecule degraders

Proteins in the human body are continually degraded and replaced by newly synthesized molecules. The UPS pathway is a highly regulated proteolytic cell system, responsible for the controlled degradation of around 80 % of the proteome *via* ubiquitination. This process occurs through a cascade of enzymatic reactions, involving an E1 ubiquitin-activating enzyme, an E2 ubiquitin- conjugating enzyme and, finally, an E3 ubiquitin-

ligase (of which > 650 are known in humans) complex that covalently binds ubiquitin to the side chain of a lysine of the given substrate. [76] Repeated iterations of this ubiquitination process result in long chains of ubiquitin repeats and posterior recognition and degradation by the proteasome (Figure 6). [77]

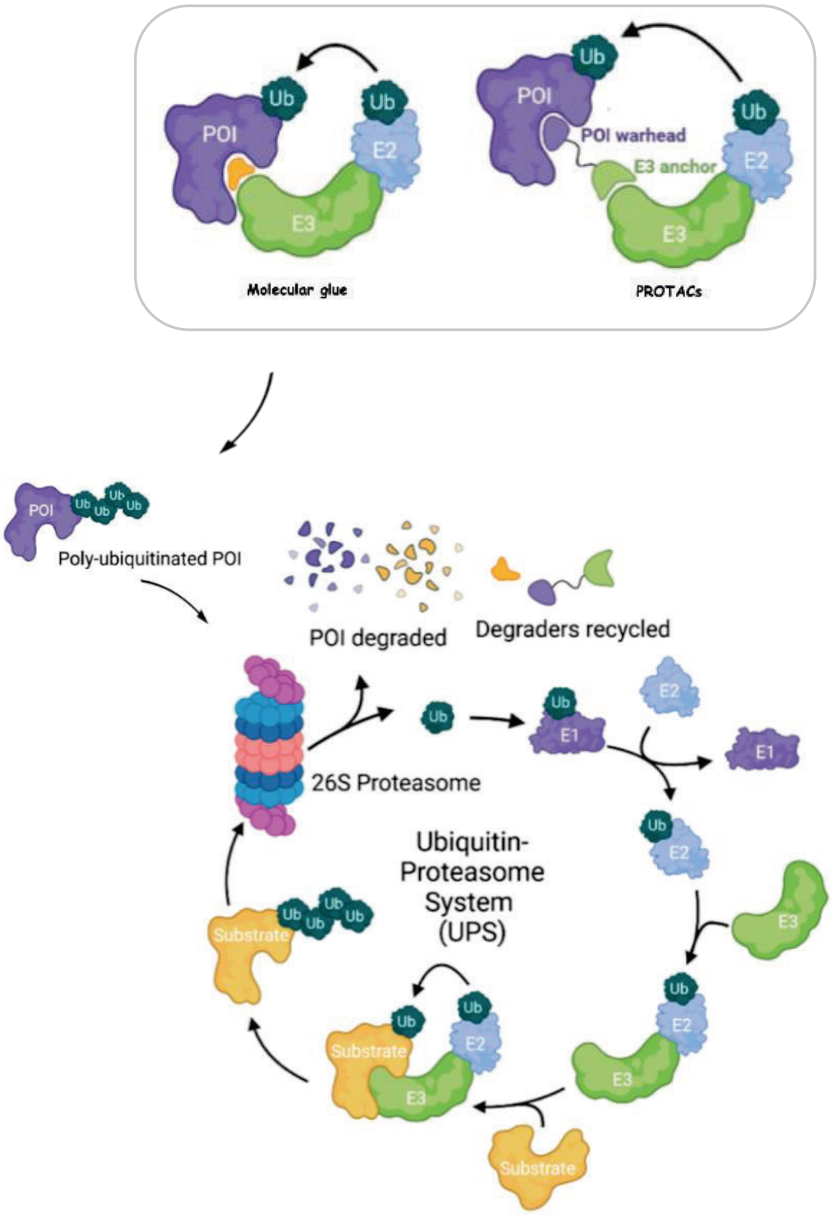

Figure 6: Overview of MG and PROTAC-based TPD technology along with in a graphical representation of the natural pathway for protein ubiquitination and consequent degradation in eukaryotic cells: The E1 enzyme (purple) first activates a ubiquitin molecule (yellow), which is then transferred to an E2 enzyme (white). Following this, the E3 enzyme (green) recruits the substrate protein (yellow) while simultaneously binding to the ubiquitin-loaded E2 enzyme. The E2 then transfers the ubiquitin to the substrate protein. Repeated cycles of this process result in polyubiquitination of the substrate, tagging it for degradation by the proteasome. Created with BioRender.com and adapted from [77].

The therapeutic potential of intervention in the UPS has been demonstrated by the development of peptide inhibitors of the proteasome (bortezomib and carfilzomib), and deubiquitinanting enzyme inhibitors, E1, E2 and E3 inhibitors have been tested in preclinical and clinical phase studies. [78] Only three immunomodulatory drugs, thalidomide, lenalidomide and pomalidomide, have been approved by the FDA for the treatment of hematologic malignancies (*e.g.*, multiple myeloma and del(5q) myelodysplastic syndrome), which work by promoting nonnative interactions between the Ikaros Zing Finger (IKZF) TF and the cerebron E3 ligase (CRBN), resulting in IKZF degradation via the UPS system. [79-82] Therefore, alternative small- molecule modalities are required to expand the range of proteins being targeted for drug discovery. More importantly, unlike E1 or E2, E3 ligases exhibit high specificity to the ubiquitination of certain substrates and, therefore, represent appealing targets in drug discovery. [83] To date, however, the development of small molecules has been rewarded with limited success, partly because modulating their activity requires targeting PPI.

In 2001 and 2004, the field of TPD blossomed when the groups of Profs. C. Crews and R. Deshaies (Caltech) explored a new modality of chemical tools and potential therapeutics to understand and treat human disease: PROTACs. [84] The use of PROTACs led TPD, highlighting the potential of these molecules as both biological tools and therapeutic agents.

During the past few years, the field of PROTACs has experienced rapid advancement, as evidenced by the growing number of publications on the topic (Figure 7). Thus, efforts have resulted in improved small-molecules able to bind to different E3 ligases such as CRBN, VHL and inhibitors of apoptosis proteins (IAPs), to achieve the degradation of various types of interesting proteins. Indeed, in 2012, the laboratories of Profs. C. Crews and A. Ciulli developed novel peptidomimetics pVHL ligands. [85,86] Subsequently, in 2014, Profs. A. Ciulli, C. Galdeano and co-workers described the first nanomolar binder of VHL (VH032). [52]

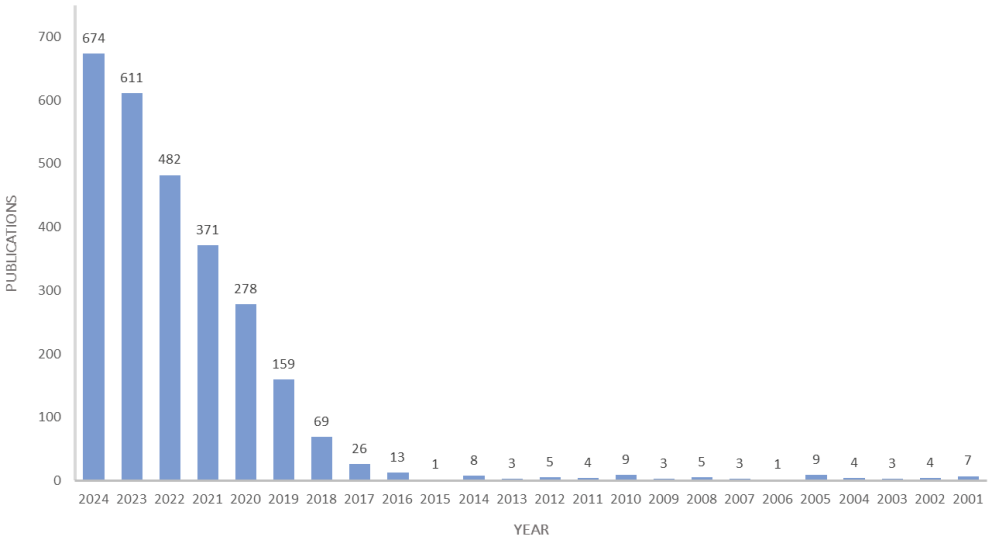

Figure 7: The number of publications on PROTAC field (Y axis) from 2001 to 2024 (X axis), extracted from PubMed (Keyword PROTAC).

In May and June 2015, three teams led by Profs. A. Ciulli, J. Bradner (from Dana Farber Cancer Institute) and C. Crews, published several independent studies describing active PROTAC molecules with drug like properties using VHL and CRBN as E3 ligases. [87-89] Finally, in 2019, Arvinas, Inc. represented the catalyst in taking TPD from the bench to the clinic by presenting interim results of a Phase 1/2 clinical trials of two candidate PROTAC drugs (**ARV-110** and **ARV-471**) for the treatment of male metastatic castrate-resistant prostate cancer and for advanced or metastatic ER+/ HER2-locally advanced or metastatic breast cancer, respectively. [90-92] These findings offered the first clinical proof- of-concept for this new drug modality when targeting two well- established cancer markers, ER and AR, which consequently gained special attention from academia and other pharmaceutical and biotechnology companies. In the past 20 years, the field of PROTACs has ushered in a period of rapid development due to its unique mode of action to possible treatment of cancers, immune disorders, etc.

PROTACs, despite exceeding the Ro5 criteria commonly applied in small-molecule drug design, are regarded as a promising technology for targeting TFs. They provide the following several significant advantages over occupancy- based modulators:

- They can **target any protein regions** (*i.e*. allosteric sites), including inactive ones, through the recruitment of E3 ligases, conceding a superior level of selectivity and allowing them to degrade rather than simply inhibit TFs. This degradation approach impacts all protein functions, not just single domains, making PROTACs especially suitable for complex TFs with multiple functional sites. [93-94]
- The effect induced by PROTACs relies heavily on **cooperativity,** which arises from the formation of a **ternary complex** involving the POI, PROTAC, and E3 ligase. High cooperativity, resulting from the ability to form optimal, specific, and compatible

ternary complexes, enhances PROTAC-mediated degradation of the POI, even when the interaction between the POI and / or E3 ligase and the PROTAC is weak. [95,96] Therefore, the formation of the ternary complex is a critical step for efficient POI degradation. Also, a well-described property of PROTACs is their capacity to form binary complexes with both the POI and E3 ligase when used at saturating concentrations. As a result, a "hook effect" is observed in concentration- response curves, where degradation efficiency decreases at higher concentrations due to this competitive binding, which limits the formation of the desired ternary complex. [97]

- PROTACs operate through a **sub-stoichiometric catalytic mechanism**, allowing them to recycle and repeatedly induce POI degradation by polyubiquitination. This mechanism not only extends the duration of the therapeutic effect by consistently removing the target protein but also minimizes potential side effects from POI accumulation within cells. Moreover, PROTACs require only moderate binding affinity between the ligand and POI, making them less vulnerable to resistance mutations that can compromise ligand- target affinity- unlike traditional small -molecule inhibitors that require a strong, sustained interaction with the target protein. This event- driven pharmacology of PROTACs thus enables effective results at lower drug dosages. [89, 98, 99]

These advantages of PROTACs open the possibility of targeting proteins hitherto considered to be undruggable, [100] TFs, and proteins with druggable yet non-functional binding sites, *e.g.,* cMyc.

1.4.1 Targeting TF with TPD strategies

In recent years, the targeted degradation of TF has emerged as a novel therapeutic approach, particularly for treating disease by aberrant undruggable TFs. Selective protein degradation approaches using small molecules, molecular glues degraders (MGs) and/or monomeric degraders [101, 102], offer the potential to target certain cancer-associated TFs that were previously considered not tractable, leveraging compounds that induce degradation by promoting PPIs, a mechanism observed in many natural and synthetic bioactive molecules (**Figure 6**). In this context, innovative hybrid molecules have been developed to link specific TFs to proteins involved in degradation using peptide-coupled ligands, such as **MVI** SNIPER compound, a peptide-based degrader that stabilizes NOTCH with the E3 ligase Inhibitor of Apoptosis Protein (IAP), facilitating its targeted degradation [103]. Additionally, while developing inhibitors to block homodimerization of the BTB domain of the TF BCL6, researchers found that the most effective compounds worked as monomeric degraders, significantly reducing BCL6 protein levels. [104] These findings illustrate the potential versatility of MGs in modulating TF function by promoting either

stabilization or degradation, depending on the interaction context. The development of effective monomeric degraders gained traction with the discovery of fulvestrant, an FDA-approved Estrogen Receptor (ER) antagonist, which binds to the LBD of the receptor promoting its proteolytic degradation. [105]

PROTACs have been used to target high-profile TFs such as Hypoxia-Inducible Factor 1 subunit alpha (HIF1α),[52, 85, 106] as well as KRAS, by ACBI-3 (Figure 5), the latest KRAS-specific PROTAC degrader. [107] Other reported PROTACs for TFs and their co-regulators have been developed including MDM2, [108], STAT3, [109] and Brd4. [87]

Overall, PROTACs and MGs are redefining how small molecules act. Their activity does not rely on inhibiting a functional site in the target protein; instead, their activity depends on the presence of a suitable molecule that binds to any target protein surface. Moreover, the degradation capability of these molecules is not solely dependent on the ligand's affinity for the target, but also on the ability of the proteins involved to form favourable interactions, a phenomenon known as cooperativity.

1.4.2 Other targeted protein degradation approaches

Although more than 20 small molecule-based PROTAC drugs are currently in clinical trials, researchers are actively investigating the potential of PROTACs, leading to the creation of new variants with related technologies.

As relevant techniques, peptide-based PROTACs (pPROTAC), which uses peptide physicochemical properties to access challenging binding sites such as β-catenin; [110] Proteolysis-Targeting Antibodies (PROTAB), bispecific antibody-based approach that promotes selective protein degradation such as IGF1R; [111] and Chaperone-Mediated protein degradation (CHAMP), [112] using molecular chaperones to assist protein degradation although it has not yet been applied to any undruggable target.

Protein degradation *via* the lysosomal pathway has advanced significantly, [113] providing a complementary mechanism to the proteasome- based PROTAC system. While the proteasome mainly targets short-lived, soluble, or misfolded proteins, the lysosomal system is specialized in degrading long-lived proteins, protein aggregates, and damaged organelles. Both systems rely on ubiquitination to label substrates for degradation and can work together on certain intracellular proteins. Leveraging the lysosomal pathway broadens the range of targetable substrates, making it possible to also degrade traditionally untreatable targets. The field encompasses two primary classes of technologies: autophagy-lysosome pathways, such as Autophagy- Targeted Chimeras (AUTACs), which use autophagy to degrade intracellular and aggregate- prone proteins;

[114] and endocytosis-lysosome pathways, such as Lysosomal- Targeting Chimera Technologies (LYTACs). [115, 116] Focusing on the last class, LYTACs are bifunctional chimeric molecules designed to simultaneously bind an extracellular POI and a cell-surface lysosome- targeting receptor (LTR). This dual binding triggers the internalization of the POI into lysosomes, where it undergoes degradation (Figure 8). Once the POI is directed to the lysosomes, the receptor can be recycled and reused for additional cycles of POI degradation. At Stanford University, Prof. C.R. Bertozzi's team created the first LYTAC molecule, Ab-2, by combining cetuximab, a monoclonal antibody that targets EGFR, with an M6P-modified peptide that binds to the CI-M6PR protein, showing EGFR reduction in HeLa cells. [125]

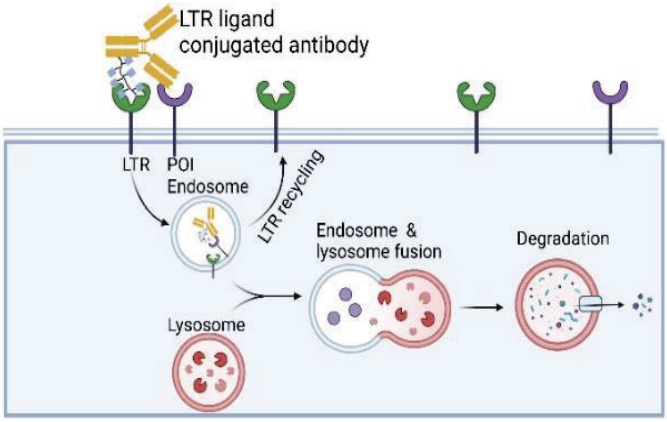

Figure 8: Representation of LYTACs mechanism which use antibodies modified with LTR binder to direct the transmembrane POI to the lysosome for degradation; LTR is recycled to the cell membrane. From [118].

While TPD is highly effective for treating certain diseases, excessive protein degradation can sometimes be harmful, creating a need for targeted protein stabilization drugs. Inspired by PROTACs, Prof. D. Nomura's team developed Deubiquitinase-Targeting Chimeras (DUBTACs) for protein stabilization. [119] Building on this, Prof. W. Wei's team introduced the TF-DUBTAC platform, capable of stabilizing oncoproteins like FOXO3A, p53, and IRF3. Through the Click reaction, they linked EN523 covalent ligand with FOXO-specific DNA motifs to selectively stabilize FOXO3A, inhibiting cMyc expression and demonstrating significant therapeutic promise. [120]

In sum, TPD technologies, including PROTACs and their innovative derivatives, represent a transformative advancement in drug discovery, poised to become indispensable in both research and drug development. Despite ongoing challenges, such as achieving selectivity and minimizing off-target effects, these technologies provide novel solutions and pathways for addressing complex biological challenges. By enhancing the capabilities of TPD and offering fresh perspectives on drug discovery, they pave the way for groundbreaking therapeutic approaches to meet critical unmet medical needs.

CHAPTER 2

Objectives

2. CHAPTER 2: OBJECTIVES

The ability to target transcription factors (TFs) could usher in a new era in drug discovery and medicine. However, the majority of TFs have long been considered undruggable. This perception stems primarily from two factors: (i) the lack of well-defined functional binding sites or the presence of intrinsically disordered regions in these proteins, and (ii) the traditional reliance on occupancy-driven pharmacology, where therapeutic efficacy and meaningful inhibition are typically achieved only when more than 90% of the target is engaged. This approach, which depends on high-affinity binding, has historically dominated drug development.

Recent breakthroughs, such as the approval of drugs targeting the oncogenic form of KRAS (KRASG12C), including sotorasib and adagrasib, have demonstrated that novel drug modalities can effectively target even the most paradigmatically "undruggable" proteins. Within this evolving landscape, the general objectives of this thesis are:

- To develop low-affinity, small-molecule-based PROTACs capable of degrading the TF cMyc (Chapter 3). The intrinsically disordered nature of cMyc poses a significant challenge to conventional structure-based drug discovery. In this context, PROTACs offer a promising alternative strategy by leveraging UPS to selectively degrade cMyc and similar undruggable transcription factors. This work aims to serve as a proof-of-concept that TFs can be targeted for degradation using low-affinity ligands fragment-sized ligands (in the two-digit micromolar range), which are often the only available binders for such proteins. Additionally, the nuclear localization of cMyc and similar TFs introduces another layer of complexity. Considering all of that, we propose the development of several drug-like PROTAC series based on the low-molecular-weight, low-affinity cMyc inhibitor 10058-F4. Additionally, with this Thesis, we aimed to demostrate that cMyc could be degraded using a small-molecule PROTAC, a fact that was not demostrated when the Thesis was initiated.

- To degrade the Cyclin E/CDK2 complex with a novel dual PROTAC approach (Chapter 4). The Cyclin E/CDK2 complex is a key regulator of cell cycle progression at the G1/S transition. Its hyperactivation is frequently observed in a variety of cancers, contributing to uncontrolled cell proliferation. Several CDK2 inhibitors are already in the clinic targeting the ATP binding site of this protein. However, they suffer lack of selectivity. In parallel, despite its clinical relevance, Cyclin E remains largely undruggable due to the absence of suitable ligandable surfaces. In this context, the lab of Dr. Galdeano has recently discovered small molecules that bind in a PPI surface between both proteins. Based on these molecules, for

this Thesis, we envisage a novel approach where both proteins CDK2 and cyclin E can be degraded with a single PROTACs molecules, degrading the full complex, since the ligands discovered interact with both proteins.

- To design and synthesis of novel Brd4- targeting molecules with computer assisted FBDD (Chapter 5). Fragment-Based Drug Discovery (FBDD) is a leading approach for assessing protein-protein interactions, complex multi -targets, intrinsically disordered proteins, and other unconventional targets. FBDD involves screening smaller libraries composed of small compounds (<300 Da). However, the main challenge remains with the optimization process to achieve more potent compounds. Our laboratory developed a computational fragment evolution platform able to generate new chemical entities by exploring the chemical space, given the binding mode of a fragment. The platform raises the possibility to obtain new entities as starting point for lead optimization or with better physicochemical properties compared to the identified fragments. In this Thesis, we have developed compounds proposed bt the platform able to inhibit the epigenetic target Brd4.

Results & Discussion

CHAPTER 3

Degrading cMyc with low-affinity small molecule-based PROTACs

3. CHAPTER 3: Degrading cMyc with low-affinity small molecule-based PROTACs

3.1 Background: cMyc the transcriptional driver in human cancer

cMyc is a master TF regulator that belongs to the bHLH-ZIP family present in the cell nucleus where it acts regulating cell growth, differentiation, metabolism and death, among other functions, which expression is estimated to be upregulated or deregulated in up to 70 % of human cancers. [121]

cMyc is a 62 *KD*a protein of 439 residues which locates in Chromosome 88q24 (region amplified in 18.92 % cancers) which was discovered in the late 1970s as a cellular homolog of the oncogene sequence of avian myelocytomatosis virus (vMyc) that caused leukemia and sarcoma. [122] Myc has two other paralogues that belong to the Myc family, N-Myc and L-Myc, all of which are highly homologous but distributed differently. To fold and become transcriptionally active, cMyc heterodimerizes with Max, forming the cMyc / Max complex which acts as a transcriptional regulator by binding to a specific DNA consensus sequence known as the Enhancer-box (E-box: 5′-CACGTG-3′), [123] and activates (or suppresses) transcription, primarily through RNA polymerase II pause release and transcriptional elongation. Additionally, to transcriptional regulation of cMyc expression, the post- transcriptional modification of cMyc such as phosphorylation and ubiquitination plays an important regulatory role in downstream gene expression. cMyc can be recruited by the Fbxw7 E3 ligase complex as well as SKP2 ubiquitin ligase complex, which both engages its degradation and inhibit its transcriptional activity. [124-126]

Many studies have highlighted the tumorigenesis of cMyc overexpression. In fact, its activation promotes cancer progression by triggering mechanisms that either lead to the intrinsic acquisition of cancer hallmarks within cells or cause dysregulation of the tumor microenvironment and host immune responses. Despite decades of effort in developing any clinically useful drug against cMyc, to date, it still has not been successfully targeted therapeutically, although promising candidates are in development or even in clinical trials, *i.e*. the miniprotein Omomyc (OMO-103). [127] The challenge remains on its unique properties: lack of defined three-dimensional structure, it is considered an intrinsically disordered protein (IDP) with a large and flat interaction surface; nuclear localization; and the lack of a targetable enzymatic pocket, as it does not possess hydrophobic pockets or grooves suitable for small-molecule binding [128].

3.1.1 Challenges and approaches to find cMyc inhibitors

cMyc possess no intrinsic enzymatic activity which limits the number of ways to target it. Several approaches have been explored, including disrupting PPIs between cMyc and Max (direct inhibitors) or interfering with interactions between the cMyc/Max complex and other regulatory proteins (indirect inhibitors). [129] In this thesis, we will focus on the direct inhibition strategy.

The first direct cMyc-inhibitors were described by Berg *et al.*, who screened a small (7000-member) peptidomimetic library and identified four active compounds by monitoring the dissociation of purifies recombinant MycCFP and MaxYFP fusion proteins using FRET-based assays. At the end, two active compounds, IIA6B17 (IC_{50}= 50 µM, Electrophoretic Mobility Shift Assay (EMSA)) and IIA4B20, showed at the highest concentrations tested (IC_{50}= 30-35 µM), growth reduction of chick embryo fibroblasts (CEFs) in response to cMyc over-expression (Figure 9). [130] Nevertheless, as described by other cMyc inhibitors, imperfect correlations between assays were common and likely due to factors such as cellular uptake, distribution, and stability.

Following on these studies, Shi *et al.* derived 120 analogs from each IIA6B17 and IIA4B20 compounds and screened them at a single concentration of 20 µM for their ability to inhibit colony formation by cMyc-transformed CEFs. [131] Two of the compounds, Mycmycin-1 and Mycmycin-2 were found to be very specific (IC_{95} = 20 µM) and prevented the recombinant cMyc/Max proteins association as well (Figure 9).

In a structure-based rational approach, Xu *et al.* hypothesized that small regions within IPDs interfaces, particularly those enriched by His, Tyr and Trp amino acids and other hydrophobic residues, can be considered regions in which the insertion of a planar molecule would be a potentially effective way to block the PPI. After a screening a small size library (250 structures) following the same TR-FRET approach as Berg *et al.*, compound NY2267 (IC_{50}= 37 µM, EMSA) showed significant selectivity for cMyc transformed CEFs (Figure 9). [132]

To identify small molecule inhibitors, Kiessling *et al.* developed a fluorescence polarization (FP) assay that quantified the cMyc - Max bHLH-ZIP heterodimer binding to a fluorophore-tagged. After performing a screening of a 17,298 compounds library, two compounds with a pyrazolo[1,5-*a*]pyrimidine structure were identified: Mycro1, and its analog, Mycro2, which both inhibited DNA binding (IC_{50}= 30 µM and 23 µM, EMSA, respectively) (Figure 9). [133]

Unfortunately, all these cMyc direct inhibitors while being effective and preventing cMyc/Max heterodimerization, would not be considered as chemotherapeutic candidates because of their non-specific toxicity and/or poor cell penetration.

In 2003, Yin *et al*. reported the identification of a set of cMyc inhibitors by using a yeast two- hybrid assay where the bHLH-ZIP domains of cMyc and Max were fused to parts of the yeast Gal4 transcription factor. This approach was of high relevance as it allowed the identification of cMyc/Max dimerization molecule inhibitors, rather than just DNA binding. When screening a ~ 10,000 small molecules, seven compounds were identified, all of which followed well Lipinski's rules, and inhibited cMyc/Max dimerization by ≥ 75 % without any cellular toxicity. Indeed, **10058-F4** (K_d= 42 µM, binding to cMyc by Surface plasmon resonance (SPR)) and **10074-G5** (K_d= 20 µM, EMSA) showed complete specificity for cMyc- Max. [134] From the last compound, a SAR study was performed from which compound **JY-3-094** [135] was discovered, and although being five times more potent (IC_{50}= 33 µM, EMSA) than **10074-G5** (IC_{50}= 147 µM, EMSA), the ionizable carboxylic acid blocked cell permeation. However, compound **SF-4-017**, the phenol ester analogue, proved to be as potent as **JY-3-094** *in vitro* and a new lead cMyc inhibitor (**Figure 9**).

Throughout published inhibitors, **KJ-Pyr-9** has shown the strongest binding affinity to cMyc (K_d= 6.50 nM), which was identified from a Kröhnke pyridine library using FP to screen for cMyc/Max dimerization inhibitors (**Figure 9**). [136] In addition, it exhibited anti-cancer activity *in vivo* by suppressing tumor growth in a human triple- negative breast cancer model without causing acute toxicity.

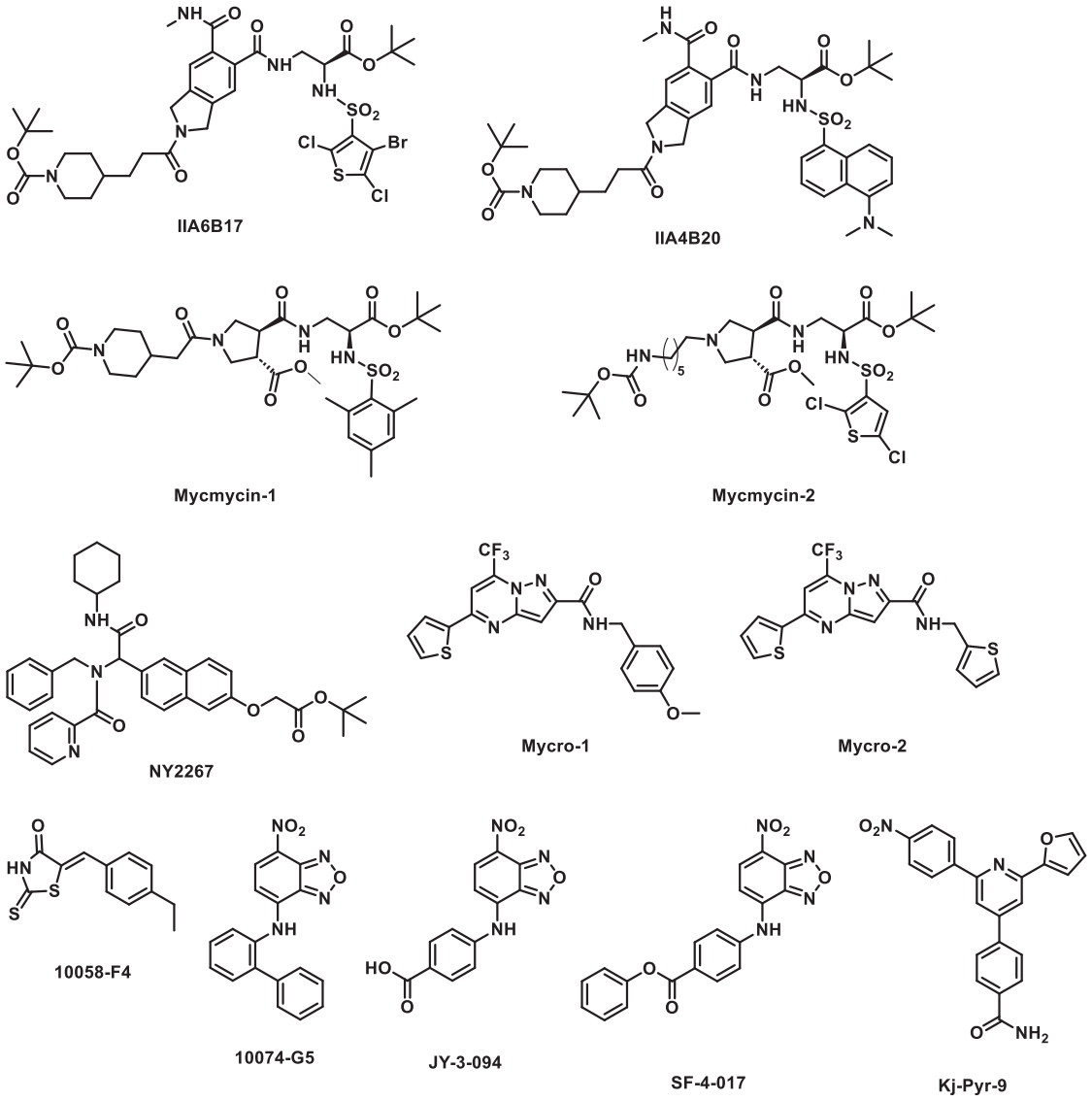

Figure 9: Structures of cMyc / Max dimerization inhibitors: IIA6B17, IIA4B20, Mycmycin-1, Mycmycin-2, NY2267, Mycro-1, Mycro-2, 10058-F4, 10074-G5 and its analogue JY-3-094, SF-4-017, and KJ-Pyr-9.

Focusing on 10058-F4, Wang *et al.* demonstrated that 10058-F4 and its analogs directly bound to the cMyc bHLH-ZIP domain using a FP assay, which leveraged the natural fluorescence of many of these small molecules. [137] Considering these studies, Follis *et al.* used a series of deletion and point mutations within the cMyc bHLH-ZIP domain to identify the exact binding sites of 10058-F4 and 10074-G5. They found that 10058-F4 binds to the Helix 2-ZIP junction (residues 402–412), while 10074-G5 binds to a centered region near the N-terminal part of Helix 1 (residues ~363–381). These findings were validated using synthetic peptides that contained only a single binding site; and structural changes were monitored through circular dichroism and NMR studies. [138, 139]

Additionally, Cuchillo and Michel also confirmed with molecular dynamics that 10058-F4 primarily interacts with Tyr402, Ile402, and Leu404, located in the most hydrophobic segment of the bHLH-ZIP domain, marking a sharp transition to a more hydrophilic region. [140, 141 In contrast, no such segment was found in Max, suggesting that 10058-F4's specificity may stem from its ability to recognize these distinct hydrophobic-hydrophilic transition points. To date, several studies have confirmed the specificity of 10058-F4 on cMyc protein as well as its mechanis of action (MoA).

Multiple library screenings have revealed small molecules that bind directly to cMyc and disrupt its heterodimerization with Max. However, these compounds exhibit only moderate potency (in the micromolar range) and/or have shown limited success *in vivo*. Peptomyc's novel cMyc inhibitor OMO-103, based on the Omomyc membrane penetrating peptide, is a promising candidate that has shown activity in preclinical models of cMyc-driven cancers and has entered phase I/ II clinical trials (NCT04808362) to assess its safety and efficacy, promoting cMyc degradation as another viable therapeutic strategy. [127] Similarly, IDP-121 is a potent and selective peptidomimetic designed to simultaneously block the formation of the cMyc/Max complex and enhance cMyc degradation via the cell's intrinsic machinery. It is currently being investigated in the CASSANDRA open-label phase I/II study (NCT05908409) for hematologic malignancies dependent on cMyc, evaluating its safety, tolerability, pharmacokinetics, pharmacodynamics, and preliminary clinical activity. [142]

Interestingly, in the past years, important developments in the PROTACs field have provided an excellent opportunity to target difficult transcription factors such as KRAS and cMyc, for proteasomal degradation, restoring or even enhancing their ubiquitination and subsequent degradation to inhibit their effects on tumor cells. Presently, PROTACs development has focused on targeting cMyc activity indirectly by degrading bromodomain and extraterminal (BET) proteins. In 2021, Hu's team found that ARV-825 degrades Brd4, inhibited proliferation, and induced apoptosis in T-ALL cells, reducing cMyc expression. [143] Similarly, Prof Crews' team developed ARV-771, a PROTAC molecule that also degrades Brd4 in prostate cancer cells, with high potency in degrading Brd2/3/4 proteins and downregulating cMyc at low concentrations. [144] However, the use of small molecules that bind to cMyc and link them via PROTAC technology to target cMyc for proteasomal degradation remains unexplored.

3.2 Specific objectives of Chapter 2

The following specific objectives were established:

i. First, the **design, synthesis and evaluation of a 1st series of cMyc-based PROTACs**. This series will incorporate:
   - The cMyc inhibitor **10058-F4**, through its *N-alkylated* and *S-alkylated* derivatives, **ASA-5** and **ASA-6**, as cMyc warheads.
   - **VH032** and **Lenalidomide** as E3 ligase- recruiting ligand, targeting VHL and CRBN, respectively.
   - PEG linkers of two different lengths (n=2 and n=4).

   To assess the degradation efficiency of this first series, *in vitro* degradation studies will be conducted using kidney cells HEK 293 and MYC-amplified colon cancer line HCT 116. These studies will include:
   - Single-dose, time-course, and dose-response assays.
   - MoA confirmation through pre-treatment with the proteasome inhibitor **MG-132** and NEDD8-activating enzyme inhibitor **MLN-4924**.

The most promising PROTAC from this series will be used as the basis for the development of a second-generation PROTAC series. The following specific objectives were stablished during the development of the project and includes:

ii. Second, the **design, synthesis and evaluation of a 2nd series of cMyc- based PROTACs**, incorporating insights from the recently reported, potent cMyc degrader **MDEG-541**, to further enhance degradation efficiency and deepen understanding of structure- activity relationships. This 2nd series aims to investigate:
   - Modification of the warhead ligand by comparing **10058-F4** (used in the 1st series) with **28RH**, the warhead used in **MDEG-541**. The reported **MDEG-541** will be synthesized *in house* and used as a control in the *in vitro* assays.
   - Evaluation of the impact on the linker type, comparing PEG and alkyl linkers of equivalent carbon lengths to assess their influence on degradation activity.

To assess the degradation efficiency of this second series, *in vitro* studies will again be conducted in kidney cells HEK 293 and MYC- amplified colon cancer line HCT 116, including:

- Direct benchmarking against ASA_MDEG-541 as a control.
- Dose-response assays with the synthesized 2nd series of PROTACs compared to the control.
- MoA confirmation through pre-treatment with the proteasome inhibitor MG-132, NEDD8-activating enzyme inhibitor MLN-4924 and autophagy inhibitor Baf-A1.

With these last objectives, we aim to identify the most potent cMyc degrader of this last series and contribute to the rational development of effective PROTACs for targeting this challenging TF.

3.3 Design of 1st series of cMyc - based PROTACs

The development of effective cMyc-targeting PROTACs relies on the careful selection and optimization of three essential components:

i. Selecting an appropriate warhead ligand capable of binding cMyc.
ii. Choosing a suitable E3 ligase ligand to facilitate ubiquitination.
iii. Optimizing the linker to enable efficient ternary complex formation.

This section outlines the rationale behind the selection of each element, warhead, E3 ligase and linker, used in the 1st -generation PROTACs targeting cMyc.

cMyc warheads

As previously discussed, several studies have identified small molecules capable of interfering with cMyc function, primarily by disrupting its interaction with Max, which is essential for its transcriptional activity. Among the cMyc/Max inhibitors reviewed, **ASA-5** and **ASA-6**, two isomers resulting from the *N*-alkylation of the low-affinity fragment-sized inhibitor **10058-F4** (Chapter 3.4.1), were chosen as warhead ligands for the synthesis of the 1st series of cMyc-based PROTACs (**Scheme 1**).

Selecting the E3 ligase key players: VHL and CRBN ligands

Although there are about ~ 600 E3 ligases available for targeting PROTACs, only a few have proven effective so far. To date, VHL and CRBN ligands are the most commonly employed in PROTAC design, leading the field due to their strong, specific binding affinities and well-characterized binding structures with their respective E3 ligases. [145]

For the design of the 1st series of VHL-based PROTACs, Dr. Galdeano and Prof. Ciulli previously reported second-generation VHL ligands. [52] Leveraging this expertise, one of the most potent hydroxyproline- based VHL ligand derivatives, **VH032** (K_d = 185 nM), was selected as the anchor ligand for the E3. Regarding CRBN-based PROTACs, **lenalidomide**, an IMID, is chosen as the anchor ligand due to its well-established ability to bind the CRBN ubiquitin ligase activity (**Scheme 1**).

Linkerology of PROTACs and ternary complex formation

In PROTAC molecules, E3 ligases and POI ligands are linked by a carefully designed chemical linker, which plays a crucial role in modulating their physicochemical and pharmacokinetic properties. This linker not only facilitates productive ternary complex formation but also directly influences degradation efficiency and target selectivity in both cellular and *in vivo* settings. Furthermore, linker-mediated binding cooperativity can

enhance the overall affinity of PROTACs, particularly when weak-affinity warheads are utilized, thereby improving their effectiveness in targeting and degrading the POI. [146]

To date, there is currently no generally accepted strategy for de novo PROTAC linker design rather than iterative trial and error, often using simply alkyl or polyethylene glycol (PEG) chains as starting points. The choices of linker chemical composition, length and rigidity/flexibility are often referred as "linkerology" in the field. Alkyl, PEG, and extended glycol chains are the most initially frequently used linker motifs in degraders programs due to their synthetic feasibility, flexibility; and their ability to fine-tune their length and composition via orthogonal conditions or deprotection sequences. Also, the commercial availability of such functionalized linkers enables rapid assembly to the warhead of interest. [147] Additionally, combining PEG and alkyl motifs enables the adjustment of lipophilicity and critical physical properties such as topological polar surface area (TPSA).

In this Thesis, for the design of the PROTAC molecules, a PEG linker motif with two different lengths (n=2 and n=4) is selected as a starting point. This strategy enables us to investigate the influence of linker length on degradation efficiency, optimizing the spatial arrangement for productive ternary complex formation and maximizing target protein degradation.

Therefore, the final design of the 1st series of cMyc-based PROTAC involved conjugating lenalidomide or VH032, as E3 ligase- recruiting ligands, to ASA-5 or ASA-6, as cMyc warheads, via PEG linkers. In total, eight PROTAC molecules were synthesized, from which four are based on ASA-5 and four on ASA-6 as the cMyc- binding ligands (Scheme 1).

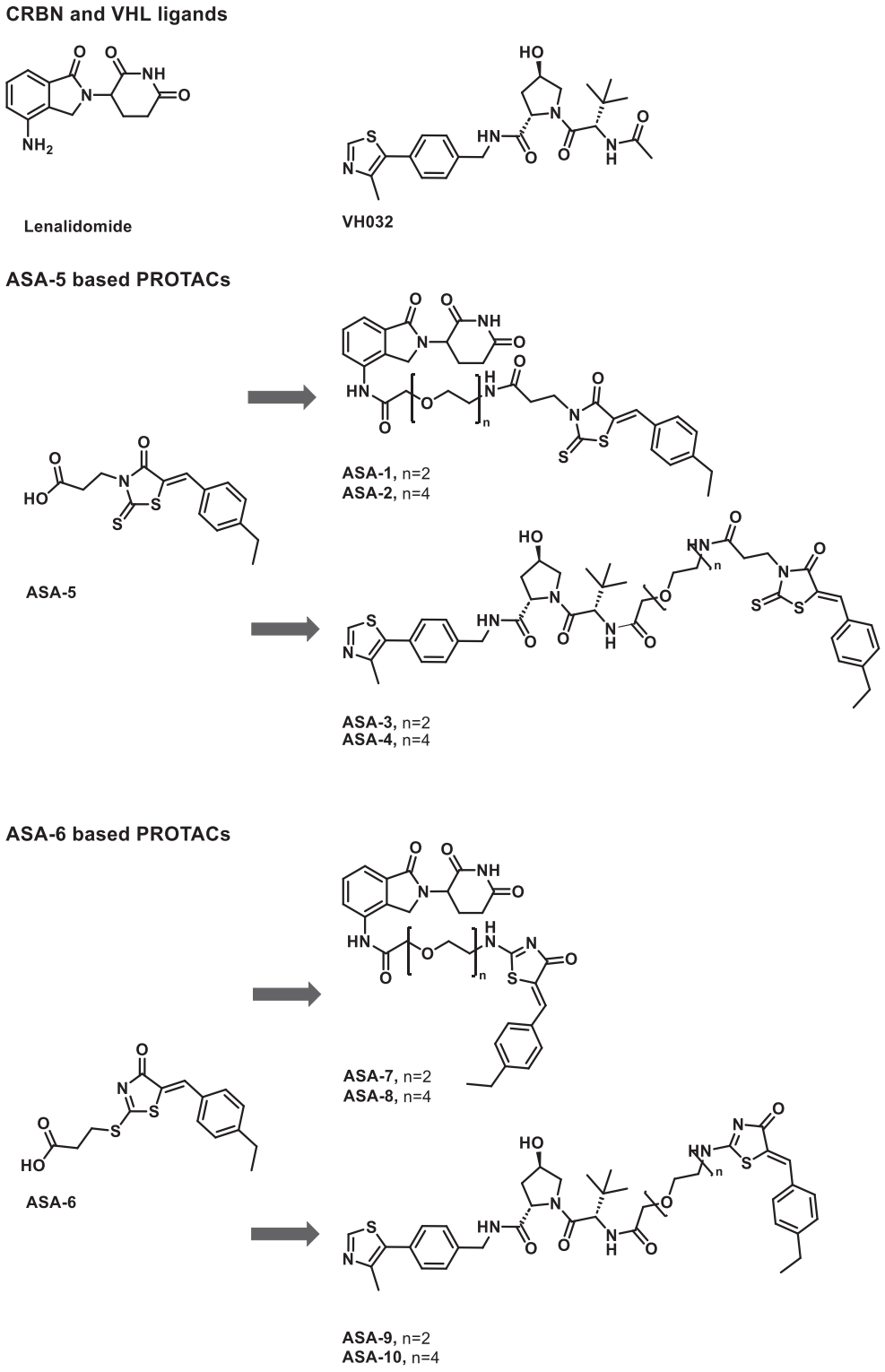

Scheme 1: Chemical structures of the 1st series of cMyc- based PROTAC molecules: ASA-5 based (ASA-1, ASA-2, ASA-3, ASA-4) and ASA-6 based (ASA-7, ASA-8, ASA-9, ASA-10).

3.4 Synthesis of 1st series of cMyc PROTACs

3.4.1 Synthesis of cMyc warheads

Although cMyc inhibitor **10058-F4** (**3**) is commercially available, we decided to synthesize it *in-house* due to synthetic feasibility. The synthesis was based on a Knoevenagel-like condensation between **1** and 4-ethylbenzaldehyde **2** [148] which gave **3** with a high yield of 98 % after filtration of the reaction mixture (**Scheme 2, A**). [149] To note, only *Z* configuration in the doble new formed bond was detected as reported in literature and further confirmed by X-ray crystallographic studies of a monocrystal of **3** prepared by recrystallization in methanol by Prof. Elies Molins (**Scheme 2, C**).

As an initial chemical approach to synthesize cMyc warhead, **ASA-5** was proposed as a derivative of **10058-F4** cMyc inhibitor, which was planned to be obtained after the ***N*-alkylation** of **3**, by using *tert*-butyl 3-bromopropanoate **4** under basic conditions followed by deprotection of the Boc group in acid conditions (TFA). However, the rhodanine ring contains two nucleophilic sites, including the nitrogen atom within the thiazolidine ring and the sulfur atom of the thiocarbonyl group, that when deprotonated, *e.g*. under basic conditions and in the presence of alkyl halides, these centers can undergo alkylation reactions. Hence, the formation of **ASA-5** is due to the ***N*-alkylation** of the rhodanine ring as the nitrogen atom is the more basic site. Alternatively, the sulfur atom of the thiocarbonyl is softer than the nitrogen atom and can be a more favorable nucleophile, [150] especially towards softer electrophiles like alkyl halides and softer bases like K_2CO_3, resulting in ***S*-alkylation** and preferential formation of **6** (**Scheme 2, B**). Therefore, two compounds were obtained and purified during alkylation of **3**, in a 2:5 ratio, giving **5** and **6**, with a yield of 18 % and 46 %, respectively, [149, 151, 152] leading to a non-regioselective reaction. To note, due to their similar polarity, reverse-phase column chromatography was employed to separate them, as **6** is slightly more polar and elutes first. After purification, deprotection of the Boc group was performed under acidic conditions (TFA) to afford **ASA-5** and **ASA-6** in quantitative yields. [52, 153]

To inequivocally elucidate the structures of **5** and **6,** and further characterize them from a stereochemical perspective, X-Ray crystallographic analysis were performed by Prof. Elies Molins (**Scheme 2, C**). This structural confirmation provides key insights into the reactivity profile of the rhodanine ring under the proposed synthetic conditions. Additionally, with the successful synthesis and purification of both products, **ASA-5** and **ASA-6** structures were further validated through NMR spectroscopy. The ^{13}C and ^{1}H NMR spectra, along with the ^{1}H NMR spectra of the crude mixture, are presented (**Figure 46**, Chapter 6.1.1.2.).

Key observations from these spectra are highlighted and discussed, which not only confirm the expected presence of the functional groups but also validate the structural integrity of the two compounds (Scheme 2, D):

^{1}H NMR Spectra (Figure 59, A-B):

- Aromatic and vinyl region (A): the vinyl group C*H* of ASA-5 (7.80 ppm) is slightly more deshielded (downfield shift) than ASA-6 (7.85 ppm).
- Alkyl chain region (B): regarding the alkyl chain, nitrogen is more electronegative than sulfur, leading to a greater deshielding in the N-CH_2 of ASA-5 (4.23 ppm, upfield shift), compared to the S-CH_2 of ASA-6 (3.55 ppm, downfield shift) due to sulfur's weaker electron-withdrawing effect. Additionally, the thiocarbonyl group C=S further deshields the protons adjacent to the N-alkyl group shifting them downfield.

^{13}C NMR Spectra (Figure 59, C):

- Thiocarbonyl and thiol variability: The observed shifts in the thiocarbonyl C=S for ASA-5 (193.3 ppm) and the thiol linkage C-S for ASA-6 (191.7 ppm) highlight their structural differences and characteristic group signals.
- Conjugated ketone: The difference in the conjugated ketone chemical shifts between ASA-5 (171.8 ppm) and ASA-6 (179.0 ppm) is primarily due to the *N-alkyl chain*, which donates electron density, thereby reducing the electron-withdrawing effects on the conjugated ketone, leading to a lower chemical shift. Conversely, the thiol linkage C-S leads to a higher electron-withdrawing effect, reflected in the higher chemical shift for its C=O signal. These differences are a direct consequence of variations in their electronic environments, and the *N*-alkyl group provides a significant steric and inductive distinction between the two compounds.

A)

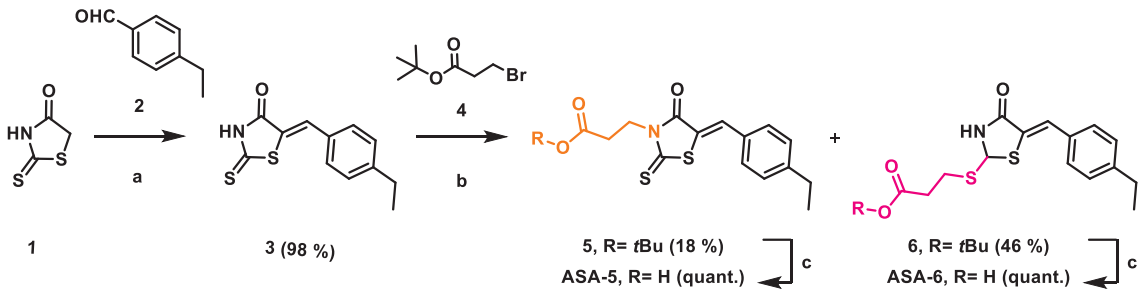

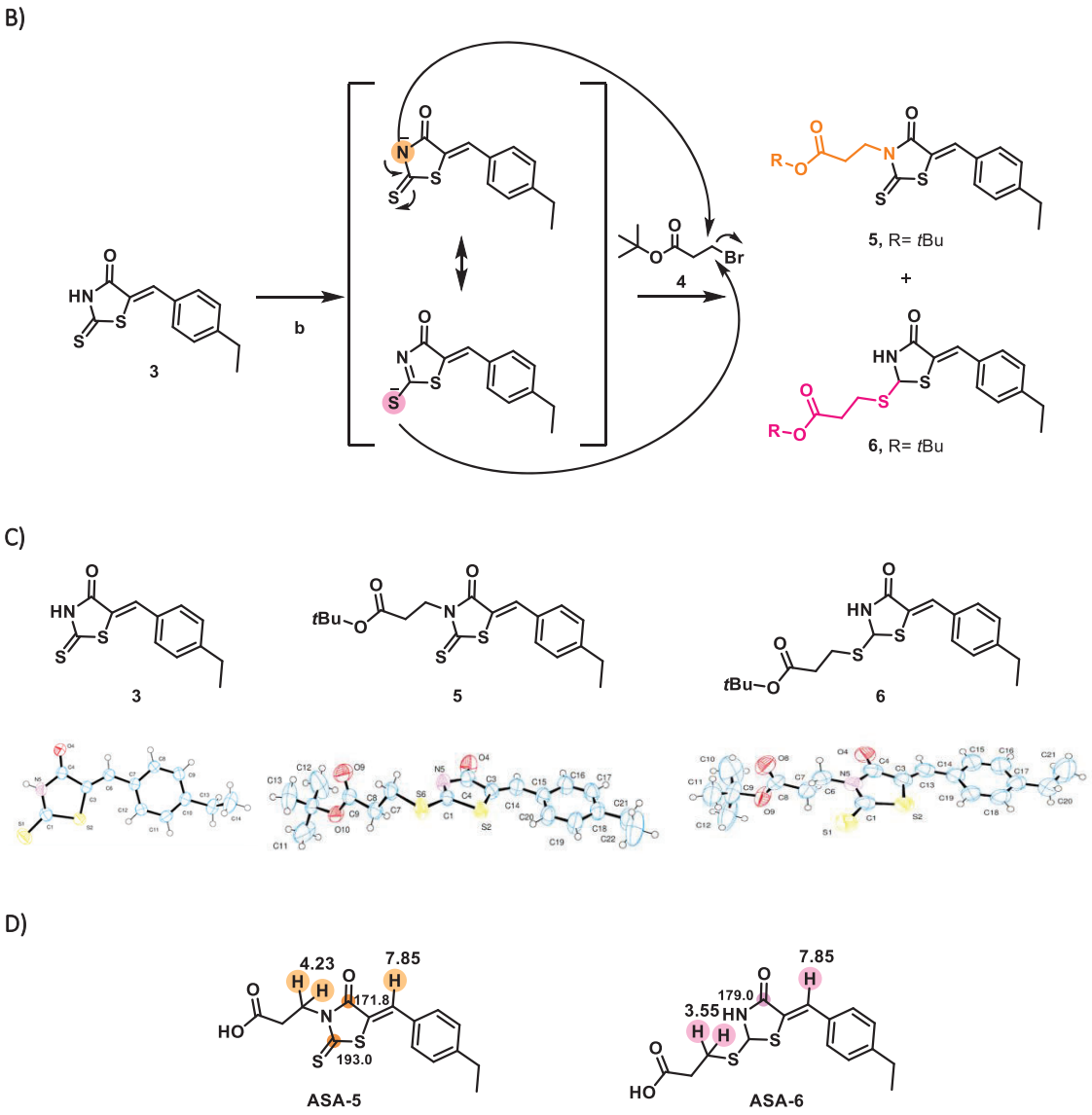

Scheme 2: A) Synthesis of cMyc warheads: **ASA-5**, and **ASA-6**[a]. **B)** Putative mechanism for the ***N*-alkylation** and ***S*-alkylation** of **3**. **C)** X- Ray crystallographic structure of **3**, **5**, and **6**. **D)** Representative NMR data of **ASA-5** and **ASA-6**.

[a]*Reagents and conditions*: (a) glacial acetic acid, ammonium acetate, 117 ºC, 3 h; (b) K_2CO_3, acetone, 56 ºC, 3 h; (c) TFA: DCM (1:1), r.t., 30 min.

Alternative synthetic approach of ASA-5

Due to the structural similarity and comparable polarity of **5** and **6,** their purification presented a significant challenge. To enhance the selectivity in the synthesis and yield of **5**, alternative synthetic strategies were explored.

The initial approach, which relied on the ***N*-alkylation** of **3**, lacks regioselectivity, resulting in formation of **5**, with a low yield of just 18 %. To address this limitation, a modified

strategy was proposed, ensuring that the methylene group acts as the sole nucleophilic site (**Scheme 3, A**). This new approach involved a one-pot microwave-assisted reaction between **2** and 3-(4-oxo-2-thioxothiazolidin-3-yl)propanoic acid **7,** resulting in a high yield of 90 % for **ASA-5**, without requiring further purification (**Scheme 3, B**). [154]

To prevent undesired byproducts during rhodanine ring alkylation, literature widely recommends performing Knoevenagel-type condensations on pre-substituted 5-arylidene rhodanines**.** In alignment with this strategy, instead of first alkylating compound **3** followed by the Knoevenagel reaction, the reaction was initiated using the commercially available compound **7**, which underwent Knoevenagel condensation directly to afford **ASA-5** in high yield. [155, 156]

A)

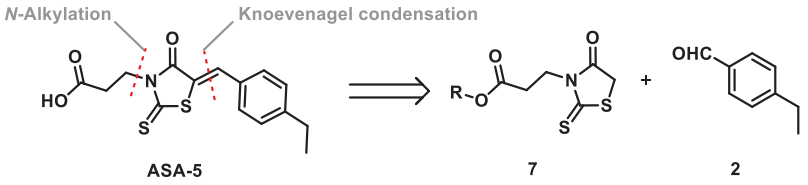

B)

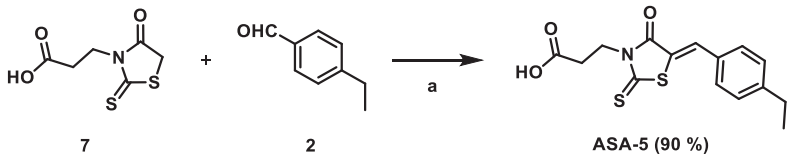

Scheme 3: A) Proposed retrosynthetic approach to synthesize **ASA-5**. **B)** Synthesis of **ASA-5**[a].
[a]*Reagents and conditions*: (a) solvent free, M/W conditions, 90 ºC, 10 min.

3.4.2 Synthesis of ASA-5 and ASA-6 based PROTACs

Synthesis of CRBN-based PROTACs

For the synthesis of the CRBN-based PROTACs, the PEG linkers of varying length, **9a** and **9b**, were coupled to **8**, using HATU and DIPEA as coupling reagents, to give **10a** and **10b** with a yield of 78 % and 53 %, respectively. Then, the deprotection of the Boc group was performed in acidic conditions (TFA) to achieve **11a** and **11b**, in quantitative yields (**Scheme 4, A**). [52, 157]

Focusing on the 1st series of the **ASA-5** CRBN-based PROTACs using **ASA-5** as the cMyc warhead, the synthesis followed the previous coupling conditions between **11a** and **11b,** allowing the reaction to proceed overnight and giving **ASA-1** and **ASA-2** with a yield of 49 % and 36 %, respectively. [52]

Following the same approach, the ASA-6 CRBN-based PROTACs, using ASA-6 as the second cMyc warhead, were synthesized with the same intermediates 11a and 11b, under coupling conditions. [52, 158] However, rather than a coupling reaction leading to amide bond formation between the amine of the intermediates and the carboxylic acid of ASA-6, the reaction occured *via* an *N-C* nucleophilic substitution, proceeding by an addition- elimination mechanism. This resulted in the formation of ASA-7 and ASA-8 with yields of 45 % and 19 %, respectively, instead of the expected ASA-11 and ASA-12 (Scheme 4, A). [52]

Looking into the mechanism of action and considering the chemical structure of ASA-6, helps explain the formation of ASA-7 and ASA-8. The thiopropionic acid acts as a good leaving group, while the amine nucleophile attacks the carbon attached to the thiopropionic acid, enhancing its electrophilicity. This leads to the formation of a tetrahedral intermediate, where the thiolate anion departs due to sulfur's ability to stabilize the negative charge, resulting in the formation of the *N-C* bond and the final product. Additionally, the use of DMF, a polar aprotic solvent, likely enhances the nucleophilicity of the nitrogen and stabilizes the intermediate thiolate anion (Scheme 4, B). [158]

A)

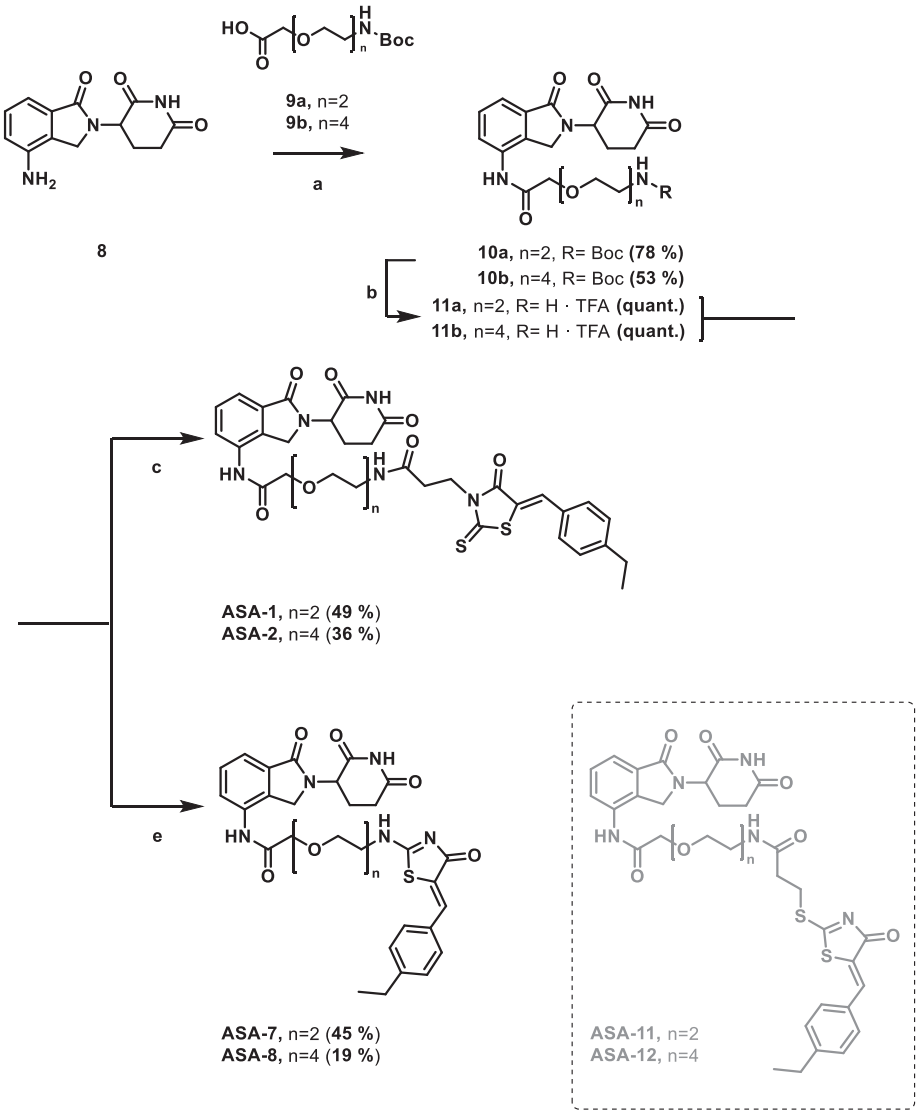

B)

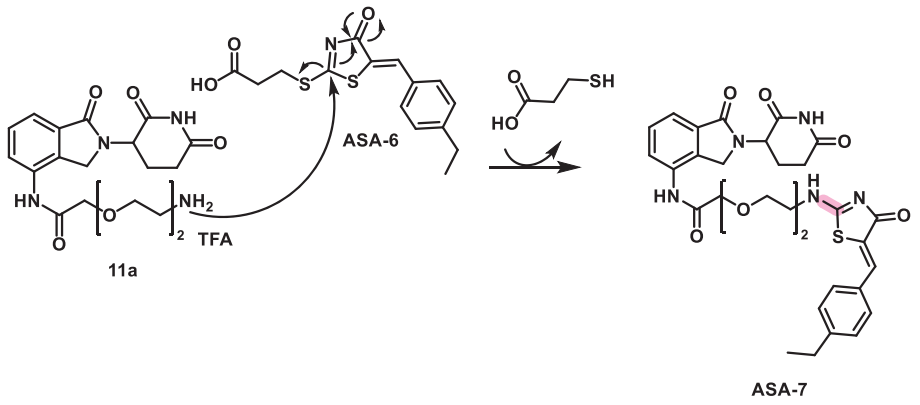

Scheme 4: A) Synthesis of CRBN anchor ligands and ASA-5 and ASA-6 PROTACs (ASA-1, ASA-2, ASA-7 and ASA-8) and the expected ASA-6 PROTACs (ASA-11 and ASA-12, doted squared in grey)[a]. B) Overview of the putative *N-C* nucleophilic substitution mechanism[a].

[a] *Reagents and conditions:* (a) HATU, DIPEA, DMF, r.t., overnight; (b) TFA: DCM (1:1), r.t., 30 min; (c) ASA-5 (R= H), HATU, DIPEA, DMF, r.t., overnight; (d) ASA-6 (R= H), HATU, DIPEA, DMF, r.t., overnight.

Synthesis of VHL- based PROTACs

For the VHL- based PROTACs, the synthesis started with a Heck reaction of **12** and 4-methylthiazole **13**, resulting in **14** with a 71 % yield (**Scheme 5**). [159] It should be mentioned that several approaches have been reported to synthesize **14.** [160] The most common ones have been a Suzuki- coupling reported by Kymera Therapeutics [161], between Boc-protected benzyl amine boronic acid and 5-bromo-4-methylthiazole; and a Heck reaction reported by Han et *al.*, between **12** and **13** [162]. In this case, the Heck reaction (or Mizoroki-Heck reaction) [163] based on the palladium-catalyzed *C-C* coupling between aryl halides (or vinyl halides) and activated alkenes in the presence of a base, was preferred due to the low cost of the starting materials and catalysts, as well as the reaction's short reaction time and high yield.

The Boc group of **14** was deprotected under acidic conditions (TFA) to yield **15** (TFA). This intermediate was subsequently coupled to **16** (R = Boc) using HATU and DIPEA as coupling reagents, resulting in **17** with a 71 % yield. Following this, deprotection of the Boc group in acidic conditions (TFA) affords **18**, in quantitative yield. Finally, **18** underwent coupling with **19** under standard coupling conditions, yielding **20** with a 69 % yield. Subsequent deprotection of the Boc group in acidic conditions (TFA) led to the formation of **21**, also known as the **VH032** ligand, as a TFA salt, in quantitative yield (**Scheme 5**). [52, 159, 164, 165] The synthesis of the **VH032** ligand achieved high yields in key steps, including a 71 % yield in the Heck reaction, a complex Pd-catalyzed transformation, and subsequent coupling reactions. The efficiency of these steps is enhanced by expertise in the purification process, which ensured favorable yields.

PEG linkers of varying lengths, **9a** and **9b**, were reacted with **21** under coupling conditions to yield **22a** and **22b** with yields of 68 % and 69 %, respectively. Boc deprotection under acidic conditions (TFA) then afforded **23a** and **23b**, in quantitative yields. [52, 166, 167]

For the synthesis of the VHL-based PROTAC with **ASA-5**, **23a** and **23b** werere coupled to **ASA-5**, yielding **ASA-3** and **ASA-4** with yields of 21 % and 53 %, respectively. [52] In contrast, and consistent with previous observations using CRBN-based PROTACs, the synthesis of **VHL-based PROTACs** from **ASA-6** under coupling conditions resulted in an *N-C* nucleophilic substitution reaction. Thus, instead of yielding **ASA-13** and **ASA-14**, the reaction gave **ASA-9** and **ASA-10**, with yields of 31 % and 21 %, respectively (**Scheme 5**). [52, 158]

Although the intended PROTACs derived from ASA-6, specifically ASA-11, ASA-12, ASA-13 and ASA-14, were not obtained under the applied coupling conditions, the unexpected formation of ASA-7, ASA-8, ASA-9 and ASA-10 led to structurally novel derivatives. This outcome highglights the role of nucleophilic substitution pathways influenced by the specific chemical environment of ASA-6. While these compoundsoffer new opportunities for structural and functional exploration, future efforts will focus on optimizing reaction conditions or employing alternative synthetic approaches to achieve the successful synthesis of the originally designed PROTACs.

Overall, the synthesis of these PROTACs achieved good yields, despite some challenges in purification that resulted in slightly lower yields in certain cases. Reverse- phase column chromatography was used to address issues related to compound polarity and limited quantities, ensuring effective isolation of pure compounds (>95%). As expertise in PROTAC synthesis grows, reaction conditions have been optimized, leading to improved yields and higher product purity.

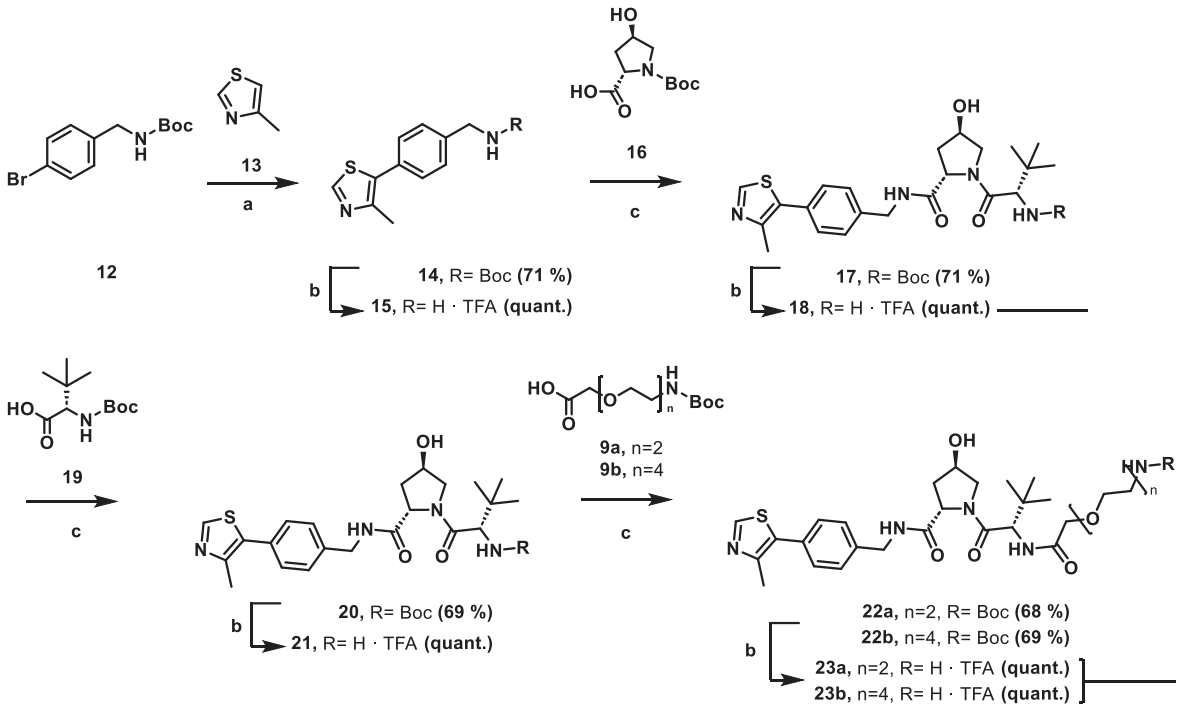

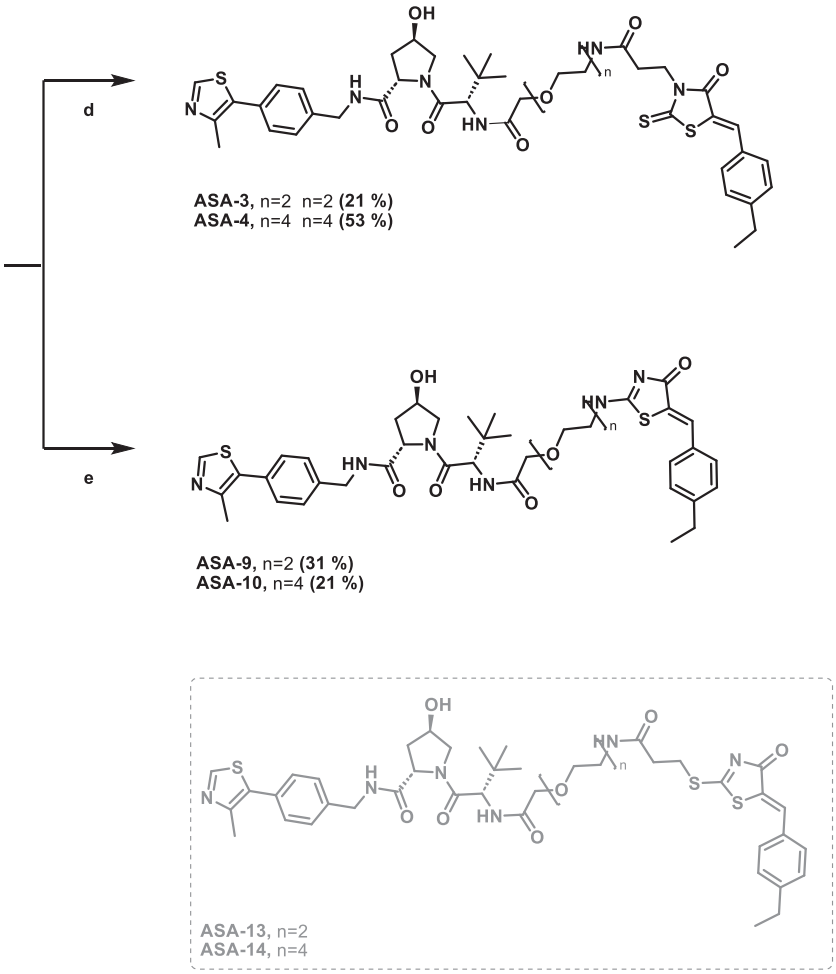

Scheme 5: Synthesis of VHL anchor ligands and **ASA-5** and **ASA-6** based PROTACs (**ASA-3, ASA-4, ASA-9, ASA-10**) and the expected **ASA-6** VHL based PROTACs (**ASA-13** and **ASA-14**, doted squared in grey)[a].

[a] *Reagents and conditions*: (a) $Pd(OAc)_2$, KOAc, DMAc, 130 ºC, 12 h; (b) TFA : DCM (1:1), r.t., 30 min; (c) HATU, DIPEA, DMF, r.t., overnight; (d) **ASA-5**, HATU, DIPEA, DMF, r.t., overnight; (e) **ASA-6**, HATU, DIPEA, DMF, r.t., overnight.

3.5 Degradation assays of 1st series of cMyc- based PROTACs

The proposed experiments consisted of the study of different time-treatment and dose-response assays to identify the best degrading conditions of the most potent degrader. To confirm that the degradation is Cullin RING ligase (CRL)- and proteasome-dependent, the cells are pre-treated with NEDD8-activating enzyme inhibitor **MLN-4924** and proteasome inhibitor **MG-132**, prior to the corresponding PROTACs treatment. Also, two different cell lines were used, kidney cells HEK293 and MYC-amplified colon cancer line HCT 116. To detect and analyze the protein degradation, Western-blot technique was employed. It should be noted that DMSO from 1 to 0.10 % was used as vehicle control, and independent biological and technical replicates (n= 2-3) were performed to ensure reproducibility.

3.5.1 Single-dose degradation assays

In a first screening, all the 1st series of PROTACs (**ASA-1, ASA-2, ASA-3, ASA-4, ASA-7, ASA-8, ASA-9, ASA-10**), were tested at one-single time point (t= 6 hours) in HEK 293 cells at a final concentration of 50 µM (three technical replicates per condition were performed). It should be noted that this high concentration was chosen initially due to the low-binding affinity of the cMyc ligand (K_d= 42 µM). [134]

As a result, **ASA-1** and **ASA-2** CRBN-based PROTACs, showed around 50 % degradation of cMyc while **ASA-7** and **ASA-8** showed around 60 % degradation. However, none of the VHL- based PROTACs (**ASA-3, ASA-4, ASA-9, ASA-10**) showed a good degradation profile. Unexpectedly, they showed an up-regulation of cMyc (**Figure 10**). Considering these results, CRBN-based PROTAC molecules ere chosen to perform further studies.

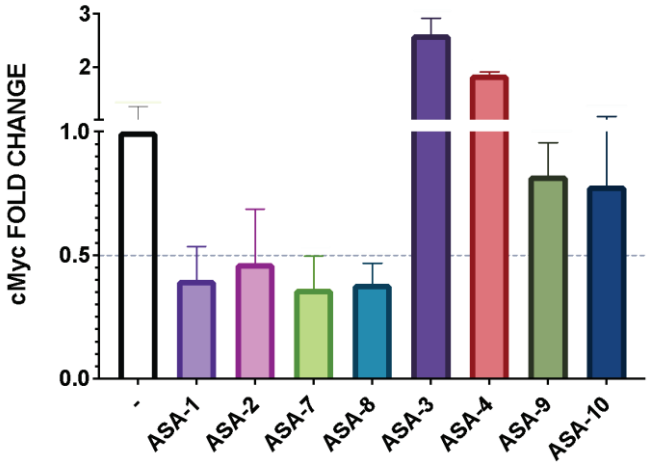

Figure 10: Quantification of three technical replicates corresponding to single dose screening of 1st series of cMyc- based PROTAC molecules treated for 6 h at a final concentration of 50 µM and DMSO as vehicle control. Doted lines mark 50% of cMyc fold change.

To further investigate the degradation profile of the four selected CRBN PROTACs and identify the most promising candidate, in the second screening, a dose-response assay setting a range of four different concentrations (100- 10- 1- 0.1 μM) at the same time point (t= 6 hours) in HEK 293 cells, was performed. Surprisingly, no significant degradation wass observed (data not showed).

Poor cellular permeability could be a major limiting factor, as the PROTACs may not efficiently cross the plasma membrane within 6 hours, leading to insufficient intracellular concentrations to trigger degradation. Additionally, inefficient ternary complex formation may also explain the lack of degradation. This could result from suboptimal binding of the PROTAC to either the target protein or CRBN within the cellular environment, impairing the assembly of a productive ternary complex, an essential step for effective ubiquitination and subsequent degradation.

It is also important to consider cMyc has a very fast turnover ($t_{1/2}$= 20- 30 minutes under normal conditions) due to its rapid regulation by the UPS mediated by the Fbxw7 protein and other E3 ligases, which help control cMyc short-lived nature and influence its role in cellular proliferation and tumorigenesis. [168] Consequently, the time exposure of the PROTAC in the cell is an important variable to consider and time-course screening experiments are necessary.

3.5.2 Degradation assays of CRBN-based PROTACs

In light of these last unexpected results, additional time-course (2, 6 and 24 hours at a final concentration of 50 μM) and dose-response assays were performed with the CRBN-based PROTACs (**ASA-1, ASA-2, ASA-7, ASA-8**) in HEK293 and HCT116 cell lines to further investigate their degradation profiles.

Notably, during the analysis of these assays, two additional lower molecular weight bands were consistently observed alongside the full-length MYC protein (apparent MW ~55 kDa). These bands correspond to two previously reported MYC proteoforms: MYC-nick (~42 kDa), a cytoplasm-localized, C-terminally truncated variant generated by calpain-mediated cleavage at residue K298, and MYC-S (~45 kDa), an N-terminally truncated variant arising from alternative translation initiation at Met100 or Met110. Both truncated forms have been described in the literature as biologically relevant MYC variants. [169] Given their reproducible detection across experiments and their potential contribution to the total cMYC protein pool, both MYC-nick and MYC-S were included in all quantification analyses, to ensure a comprehensive and accurate assessment of cMYC degradation by CRBN-based PROTACs, and preventing underestimation of compound efficacy.

Time- course degradation assays in HEK 293 cells

In this experiment, we observed between 20-25 % degradation of cMyc protein with **ASA-2** and **ASA-8** at 6 hours in a proteasome- dependent manner in HEK 293 cells (**Figure 11, A**). Also, 40- 50 % degradation was observed with **ASA-1** and **ASA-7**, respectively at 24 hours in a proteasome-dependent manner (**Figure 11, B**).

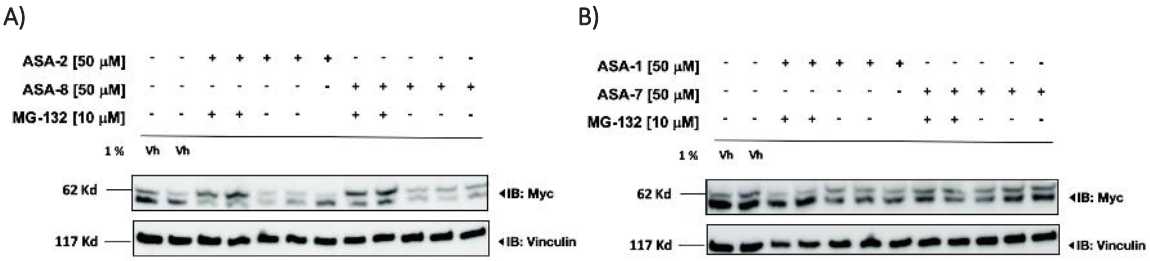

Figure 11: A) Western blot of **ASA-2** and **ASA-8** treated with the indicated single concentration (50 µM), pre-treated with **MG- 132** (10 µM) and DMSO as vehicle control for 6 h in HEK 293 cells. **B)** Western blot of **ASA-1** and **ASA-7** treated with the indicated single concentration (50 µM), pre-treated with **MG- 132** (10 µM) and DMSO as vehicle control for 6 h in HEK 293 cells. Vinculin: loading control. One-single biological replicate.

Overall, the degradation results obtained at this point with the 1st cMyc- based PROTACs in HEK293 cells did not show enough consistency to make a solid conclusion, as the previous degradation observed at 6 hours during the first screening was not reproduced again.

Time- course degradation assays in HCT 116 cells

Given the inconclusive previous results obtained in HEK293 cells, it was decided to evaluate the CRBN-based PROTACs in HCT116 cells for 6 and 24 hours at a concentration of 50 µM. At a time of 6 hours, no degradation was again observed (**Figure 12, A**). However, at 24 hours, 40 % degradation with **ASA-8** in a proteasome-dependent manner was observed in HCT116 cells but only in the first biological replicate (**Figure 12, B**).

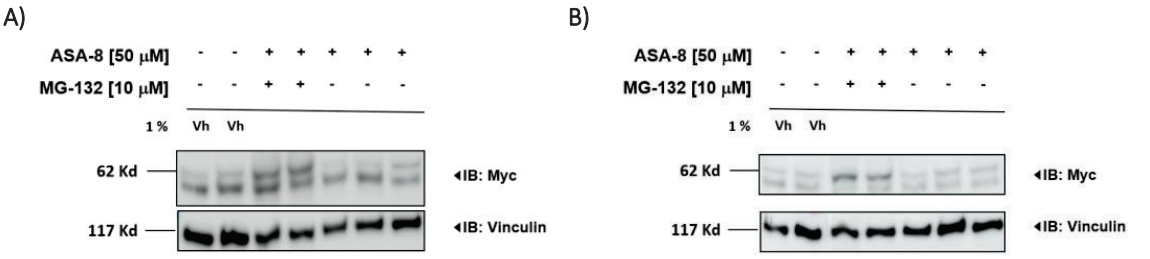

Figure 12: A) Western blot of **ASA-8** treated with the indicated single concentration (50 µM), pre-treated with **MG- 132** (10 µM) and DMSO as vehicle control for 6 h in HCT 116 cells. **B)** Western blot of **ASA-8** treated with the indicated single concentration (50 µM), pre-treated with **MG- 132** (10 µM) and DMSO as vehicle control for 24 h in HCT 116 cells. Vinculin: loading control. Three technical replicates.

Dose- response degradation assays in HCT 116 cells

Dose-response treatment was carried out with ASA-7 and ASA-8 at four different concentrations (100- 10- 1- 0.1 µM) for 24 hours in HCT 116 cells to investigate the impact of the two different PEG linker lentghts in the CRB-based PROTACs incorporating ASA-6 ligand. Unfortunately, again, no degradation was observed with the tested PROTACs (Figure 13 and Figure 14).

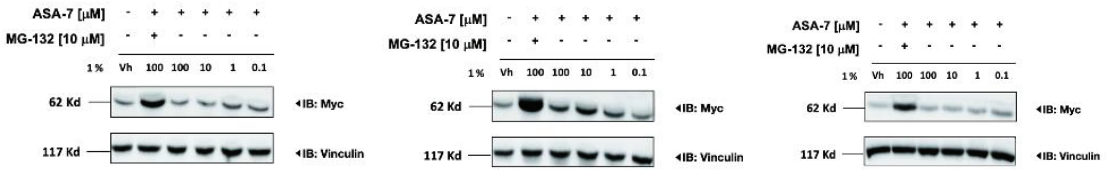

Figure 13: Western blot of ASA-7 treated with the indicated concentrations (100- 10- 1- 0.1 µM), pre-treated with MG- 132 (10 µM) and DMSO as vehicle control for 24 h in HCT 116 cells. Vinculin: loading control. Three independent biological replicates.

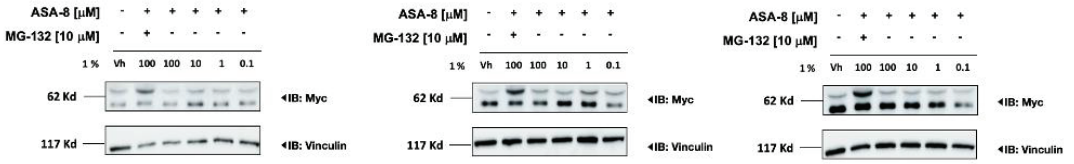

Figure 14: Western blot of ASA-8 treated with the indicated concentrations (100- 10- 1- 0.1 µM), pre-treated with MG- 132 (10 µM) and DMSO as vehicle control for 24 h in HCT 116 cells. Vinculin: loading control. Three independent biological replicates.

3.6 Design of 2nd series of cMyc - based PROTACs

Background: Publication of a novel cMyc-based PROTAC

During the development of this Thesis a single PROTAC, MDEG-541, was reported as a cMyc-degrading molecule by others. [170] MDEG-541 downregulates cMyc through a ubiquitin-, proteasome-, and CRBN-dependent manner. Additionally, this study demonstrated a dose-dependent decrease in cell viability, with efficacy in the single-digit micromolar range in both conventional and patient-derived organoid models. MDEG-541 was designed by combining an analog of the cMyc inhibitor 10058-F4 derivative, 28RH, which includes an isopropyl substituent instead of an ethyl one, linked to a CRBN-recruiting thalidomide derivative with an alkyl chain. [170]

When compared to the 1st series of cMyc-based PROTAC molecules, MDEG-541 demonstrates the importance of the linker components in enhancing degradation efficiency and physico-chemical properties. Considering its chemical structure, a series of modifications based on the 1st series of cMyc-based PROTACs. We aimed to understand if the differences seen in the degradation between MDEG-541 and our first series of PROTACs were due to (i) the substituents of the cMYC 10058-F4, (ii) the chemical nature of the linker (alkyl vs PEG) or the length of the linker.

As a result, a 2nd series of cMyc-based PROTACs were synthesized, which includes ASA_MDEG-542, featuring the 10058-F4 ligand instead of 28RH and an octyl linker (Scheme 6). Specifically, with the synthesis of ASA_MDEG-543, based on the 28RH ligand; and ASA_MDEG-544, based on the 10058-F4 ligand; we aimed to compare their degradation efficacy with MDEG-541 and ASA_MDEG-542, respectively, while maintaining the same E3 ligase and ligand for consistency (Scheme 6). This comparison could allow the assessment of the influence of different linker types on the overall performance in cMyc degradation.

For the PEG linker selection, a PEG chain consisting of three units (n = 3) is chosen to keep the carbon length of the original MDEG-541 degrader, which contains an aliphatic octyl chain (n = 8). This ensures that the PEG linker is comparable in size to the alkyl chain in the original compound, isolating the effect of the linker type on the degrader's activity.

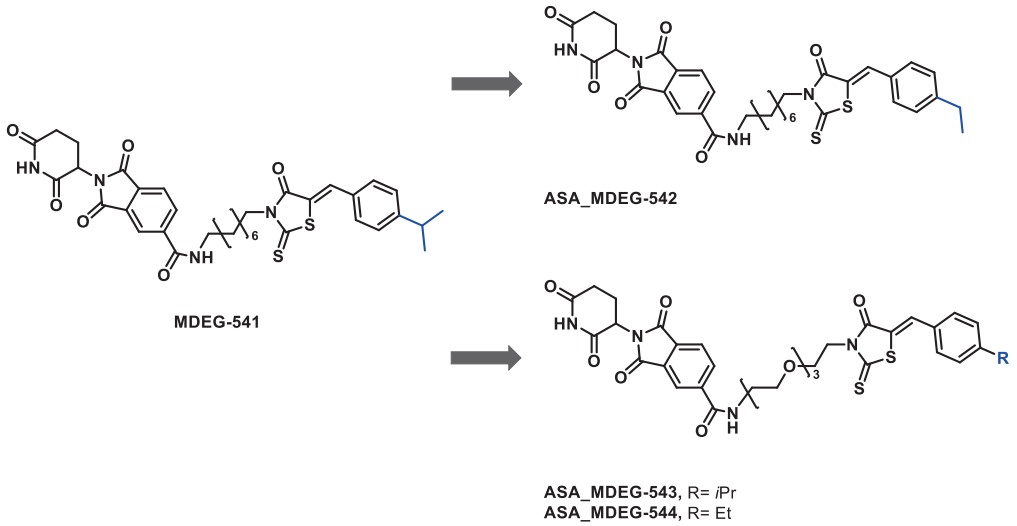

Scheme 6: Chemical structures of the 2nd series of cMyc- based PROTAC molecules: ASA_MDEG-542, ASA_MDEG-543 and ASA_MDEG-544.

3.7 Synthesis of 2nd series of cMyc PROTACs

Synthesis of MDEG-541

MDEG-541 was synthesized for use as a control in subsequent degradation studies. Following the reported synthesis, 24 reacted with bis(carboxymethyl)trithiocarbonate 25 and DIPEA, dissolved in DME, giving 26 with a 78 %. Next, a Knoevenagel-like *condensation* reaction between 26 and 27 (R^2 = *i*Pr) gave 28 with a 74 % yield. [148] The Boc group was deprotected under acidic conditions (TFA), giving 30, with a quantitative yield. Finally, 32, a thalidomide carboxylic acid derivative, was coupled with 30 under coupling conditions, achieving MDEG-541 with a yield of 74 %, which aligns with the reported spectral data (Scheme 7). [170, 171]

Synthesis of ASA_MDEG-542

To synthesize ASA_MDEG-542, the same synthetic approach was used that for MDEG-541. In this case, 26 reacted with 4-ethylbenzaldehyde 2 and DIPEA, dissolved in DME, to give 29 with a 76 %, which then the Boc group is deprotected under acidic conditions (TFA) to obtain 31 with quantitative yield. [170-172] Finally, ASA_MDEG-542 was obtained under coupling conditions between 31 and 32, with a yield of 45 % (Scheme 7). [52, 170]

Synthesis of ASA_MDEG-543 and ASA_MDEG-544

Following the same synthetic approach previously mentioned for MDEG-541 and ASA_MDEG-542, 33 was reacted bis(carboxymethyl)trithiocarbonate 25, and DIPEA, dissolved in DME, to give 34 with a high yield of 97 %. Then, a Knoevenagel-like condensation reaction between 34 and 27 gave 35 with a 76 % yield [148]; and with 2, gave a yield of 49 %. Both intermediates contain a Boc group which was deprotected in acid conditions (TFA) to give 37 and 38 with quantitative yields, respectively. [170-172] Finally, 32 was reacted with 37 and 38, under coupling conditions, giving ASA_MDEG-543 and ASA_MDEG-544, with a yield of 45 % and 29 %, respectively (Scheme 7). [52, 170]

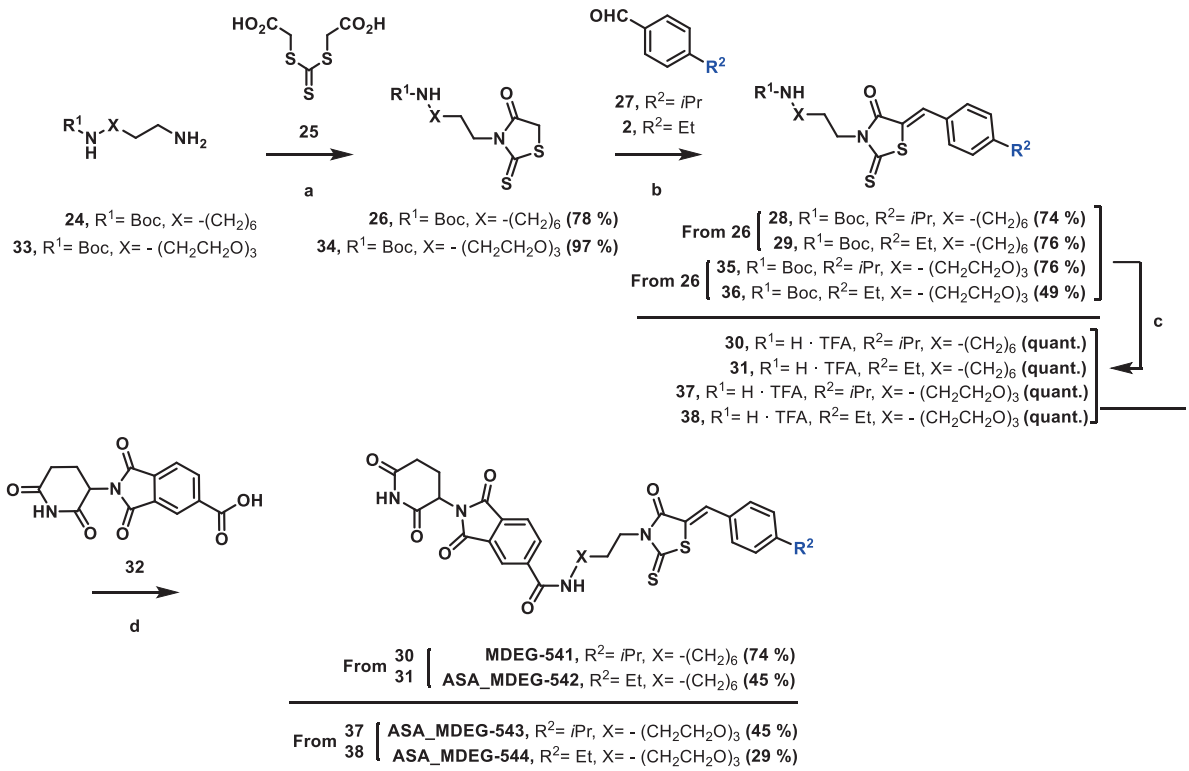

Scheme 7: Synthesis of MDEG-541, ASA_MDEG-542, ASA_MDEG-543 and ASA_MDEG-544 [a].
[a]*Reagents and conditions*: (a) DME, DIPEA, 90 ºC, 1h; (b) Solvent free, 140 ºC, overnight; (c) TFA: DCM (1:1), r.t., 30 min; (d) HATU, DIPEA, DMF, r.t., overnight.

3.8 Degradation studies of 2nd series of cMyc- based PROTACs

3.8.1 Study of the degradation profile of ASA_MDEG541 as a control

Dose-response degradation assays in HEK 293 cells

To confirm the cMyc described degradation of **MDEG-541** and taking into consideration the timing and dosage treatments that were reported in the original manuscript, **MDEG-541** was tested at a dose-response treatment of five different concentrations (250- 50- 10- 1- 0.1 µM) at 24 hours in HEK 293 cells. Also, a pre-treatment with the proteasome inhibitor **MG- 132** [10 µM] and the NEDD8-activating enzyme inhibitor **MLN- 4924** [1 µM] was conducted. In result, when the cells were treated with **MDEG-541**, 84 % of cMyc degradation at 50 µM and 77 % at 10 µM, was observed (**Figure 16**).

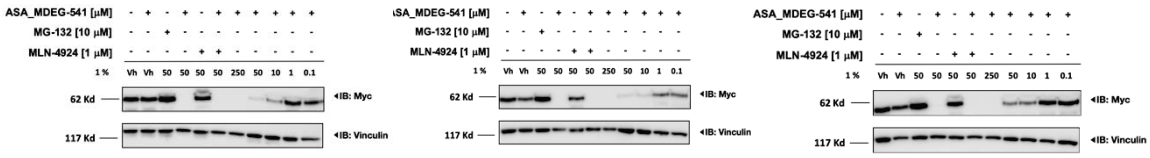

Figure 16: Western blot of **MDEG-541**(mentioned as ASA-MDEG-541 in the Western-blots) treated with the indicated concentrations (250- 50- 10- 1- 0.1 µM), pre-treated with **MG- 132** (10 µM) or **MLN- 4924** (1 µM), and DMSO as vehicle control for 24 h in HEK 293 cells. Vinculin: loading control. Three independent biological replicates.

Comparing these results with **MDEG-541** reported data, [170], we could corroborate that the reported PROTAC downregulates cMyc with a similar degradation profile than **MEG-541** (DC_{50}= 3.6 ± 1.7 µM) (**Figure 17**).

Regarding the MoA, cMyc levels were not rescued when treating the cells with the mentioned special treatments. This might be due to the high PROTAC dosage treatment at 50 µM which is too toxic and can mask the effect of the used inhibitors. Therefore, the MoA of **MDEG-541** with this assay cannot be disentangled. Hence, further assays to validate its MoA will be performed in HCT 116 cell lines. It should be noted that treating the cells at a final concentration of 250 µM is very toxic, however, it was chosen to see if Hook effect classical of PROTACs takes place with this molecule. As expected, cell-death was observed due to toxic dosage, and it will be discarded for future assays.

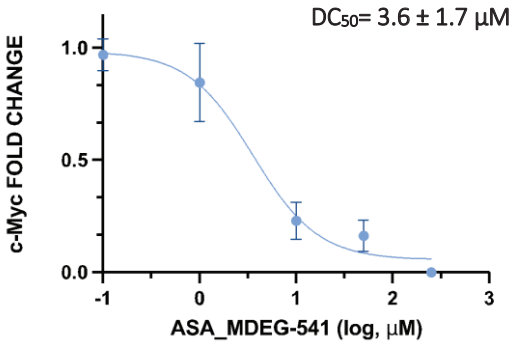

Figure 17: The DC_{50} of **MDEG-541** mentioned as ASA-MDEG-541 in the figure) was determined by a dose-response of five points (250- 50- 10- 1- 0.1 µM) in HEK293 cells treated for 24 h. Western-blot assays are used to determine the dose-response. Three technical replicates are analyzed. Shown is the mean ± SD.

Dose-response degradation assays in HCT 116 cells

MDEG-541 was also tested in HCT 116 cells, as it is the cell line reported in the original paper as well as used in our previous experiments. The degrader was tested at four different concentrations (50- 10- 1- 0.1 µM) for 24 hours and the cells are pre-treated with **MG- 132** [10 µM] (**Figure 18, A**). In parallel, another experiment was conducted by testing **MDEG-541** under the same dose with the pre-treatment of MLN- 4924 [1 µM] and using a concentration of 0.10 % of DMSO as vehicle control (**Figure 18, B**).

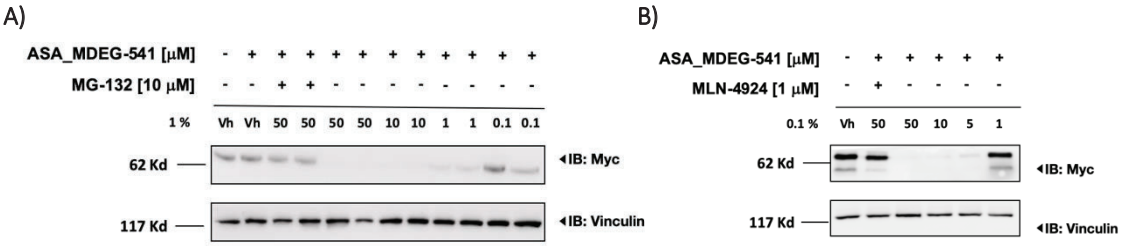

Figure 18: A) Western blot of **ASA_MDEG-541** (mentioned as ASA-MDEG-541 in the Western-blots) treated with the indicated concentrations (50- 10- 1- 0.1 µM), pre-treated with MG- 132 (10 µM) and DMSO as vehicle control for 24 h in HCT 116 cells. Two technical replicates. **B)** Western blot of **ASA_MDEG-541** treated with the indicated concentrations (50- 10- 5- 0.1 µM), pre-treated with **MLN- 4924** (1 µM) and DMSO as vehicle control for 24 h in HCT 116 cells. Vinculin: loading control. One-single biological replicate.

In this assay, striking cMyc degradation was observed: 90 % at both 50 and 10 µM concentrations, 60 % at 1 µM and 25 % at 0.1 µM. Also, pre-treatment with proteasome inhibitor **MG-132** and **MLN-4924** rescued the **MDEG-541** induced degradation, which proves that the degrader is CRL- and proteasome- dependent, as reported. Considering the degradation results, **MDEG-541** was used as a control for the future experiments Moreover, comparing to prior results in HEK293 cells, a more potent degradation of cMyc protein is observed in HCT 116 cells. Therefore, the next degradation assays where performed on this MYC- amplified colon cancer line.

3.8.2 Degradation assays of ASA_MDEG-542, ASA_MDEG-543 and ASA_MDEG544 in HCT 116 cells

Degradation Screening and MoA study of ASA_MDEG-542

In a first screening, ASA_MDEG-542 was tested at four different concentrations (50- 10- 5- 1 µM) at 24 hours. The following cMyc degradation was observed: 100 % degradation from 50 to 5 µM and 40 % degradation at 1 µM. Moreover, to study its MoA, the cells were pre-treated with MLN- 4924 (1 µM) for 1 hour and then treated with the PROTAC at a final concentration of 50 µM (Figure 19, A). cMyc levels were not rescued with this pre-treatment, so further experiments were conducted to elucidate another possible degradation pathway (*e.g.*, lysosomal) involved. Hence, the degrader was tested at 50 µM with a pre-treatment of MG- 132 [10 µM], MLN- 4924 [1 µM] and Bafilomycin-A1 (Baf-A1, 10 nm) (Figure 19, B). Baf-A1 is a vacuolar- type H^+- ATPase and autophagic degradation inhibitor. Unfortunately, cMyc levels were not rescued with any of these conditions in this preliminary assay with high concentrations (only a biological replicate).

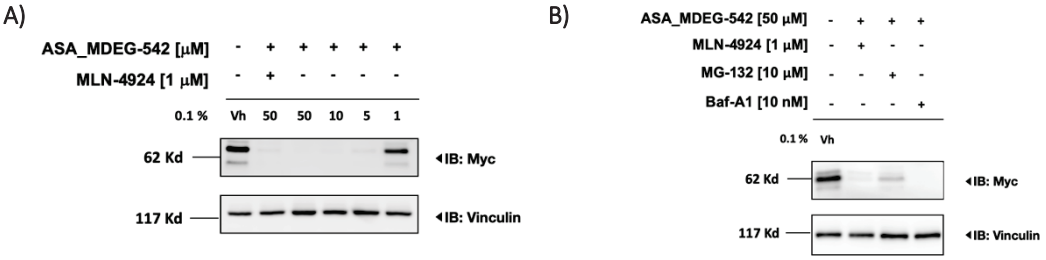

Figure 19: A) Western blot of ASA_MDEG-542 treated with the indicated concentrations (50- 10- 5- 1 µM), pre-treated with MLN- 4924 (1 µM) and DMSO as vehicle control for 24 h in HCT 116 cells. B) Western blot of MoA assay of ASA_MDEG-542 treated with the indicated concentration (50 µM), pre-treated with MG-132 (10 µM), MLN- 4924 (1 µM) or Baf- A1 (10 nM), and DMSO as vehicle control for 24 h in HCT 116 cells. Vinculin: loading control.

Taking into consideration these results, and the fact that 50 µM is a very high and toxic dosage for the cells, it was decided to perform two more experiments based on two independent biological replicates of the same pre-treatment conditions, but this time, testing ASA_MDEG-542 at a final concentration of 10 µM (Figure 20). In both assays, cMyc levels where rescued when pre-treating the cells with MG- 132 and MLN- 4924 but not with Baf- A1. Therefore, we could confirm that ASA_MDEG-542 reduces cMyc levels in a CRL- and proteasome-dependent manner and that 10 µM. This concentration concentration should be the maximum dosage used when co- treating the cells with MG-132 and MLN-4294 inhibitors.

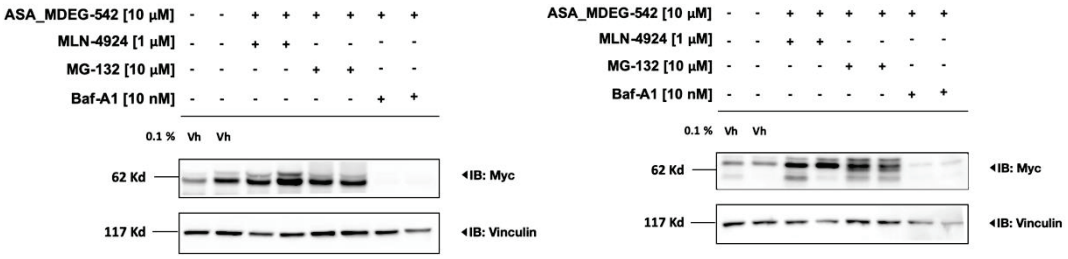

Figure 20: Western blot of MoA assay of ASA_MDEG-542 treated with the indicated concentration (10 µM), pre-treated with MG- 132 (10 µM), MLN- 4924 (1 µM) or Baf- A1 (10 nM), and DMSO as vehicle control for 24 h in HCT 116 cells. Vinculin: loading control. Two independent biological replicates.

However, a remaining 40 % of cMyc degradation was still observed at 1 µM of ASA-MDEG-542. Thus, another lower concentration was considered for the two following assays. HCT116 cells were treated with five different concentrations of ASA-MDEG-542 (50- 10- 5- 1- 0.5 µM) during 24 h (Figure 21). cMyc protein was 100 -72 % degraded at a dose-dependent manner, from 50 to 5 µM, and 10 % degradation was observed at 1 µM.

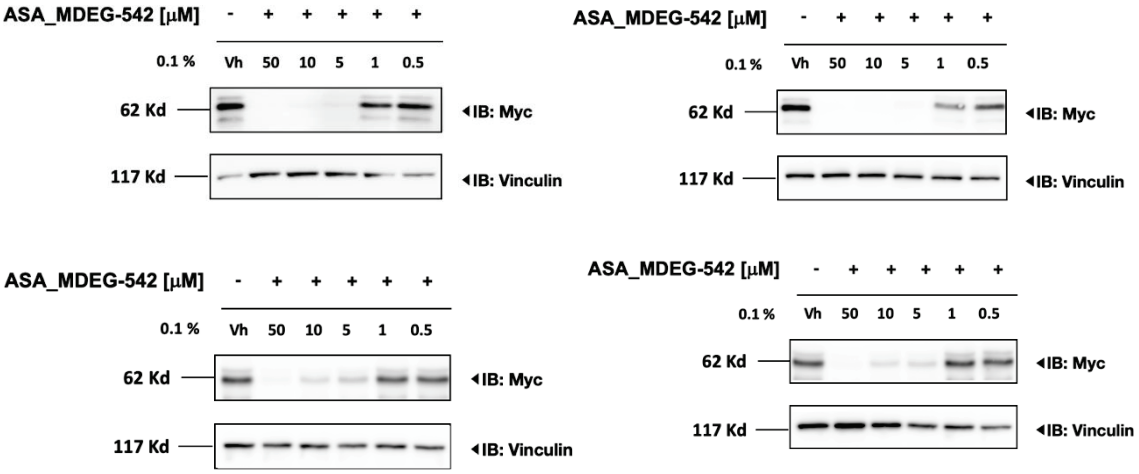

Figure 21: Western blot of ASA_MDEG-542 treated with the indicated concentrations (50- 10- 5- 1- 0.5 µM) and DMSO as vehicle control for 24 h in HCT 116 cells. Vinculin: loading control. Two independent biological replicates with two technical replicates, respectively.

Overall, ASA_MDEG-542 showed a dose-dependent reduction of cMyc in the single digit µM range (DC_{50}= 4.0 ± 1.5 µM) in HCT 116 cell lines and in a CRL- and proteasome-dependent manner (Figure 22).

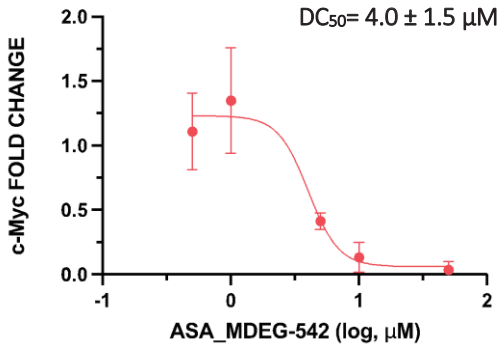

Figure 22: The DC_{50} of **ASA_MDEG-542** is determined by a dose- response of five points (50- 10- 5- 1- 0.5 µM) in HCT 116 cells treated for 24 h. Western blot assays are used to determine the dose-response. Three independent biological replicates are analyzed. Shown is the mean ± SD.

Degradation assays and MoA study of ASA_MDEG-543

ASA_MDEG-543 was initially tested at four different concentrations (50- 10- 5- 1 µM) for 24 hours. 100 % degradation of cMyc was observed at 50 µM and 40 % degradation from 10 to 5 µM. In this same assay, the cells were also pre-treated with **MLN- 4924** (1 µM) for 1 hour and then treated with the PROTAC at a final concentration of 50 µM. However, no rescue of cMyc levels were detected (**Figure 23**).

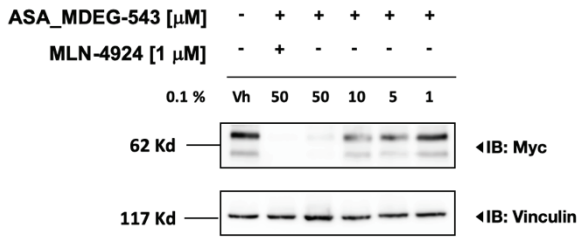

Figure 23: Western blot of **ASA_MDEG-543** treated with the indicated concentrations (50- 10- 5- 1 µM), pre-treated with **MLN- 4924** (1 µM) and DMSO as vehicle control for 24 h in HCT 116 cells. Vinculin: loading control. One- single biological replicate.

In accordance with the masking effect observed when studying the MoA of **MDEG541** and **ASA_MDEG542,** and performing a co-treatment of the cells at a final PROTAC concentration of 50 µM, **ASA_MDEG-543** was tested at a final concentration of 10 µM after the pre-treatment with **MG- 132** (10 µM), **MLN- 4924** (1 µM) and **Baf- A1** (10 nm). It was under these conditions when cMyc levels were restored and we could affirm that **ASA_MDEG-543** reduces cMyc in a CRL- and proteasome- manner (**Figure 24**).

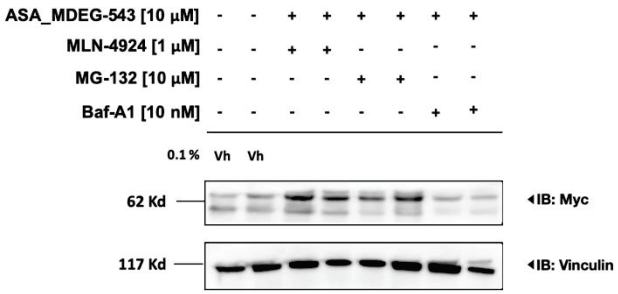

Figure 24: Western blot of MoA assay of ASA_MDEG-543 treated with the indicated concentration (10 µM), pre-treated with MG- 132 (10 µM), MLN- 4924 (1 µM) or Baf- A1 (10 nM), and DMSO as vehicle control for 24 h in HCT 116 cells. Vinculin: loading control. One- single biological replicate.

Moreover, following the same procedure as for ASA_MDEG-542, two more independent dose-response treatment assays were performed at five different concentrations (50- 10- 5- 1- 0.5 µM) with ASA_MDEG-543 (Figure 25). In this case, ASA_MDEG_543 did not degrade cMyc as efficiently as ASA_MDEG-542. Indeed, 23 % degradation was observed at 10 µM with no striking degradation at lowest concentrations. Up to this point, ASA_MDEG-543 did not show a good degradation profile of cMyc and the decrease in terms of degradation can be foreseen when using PEG as a linker.

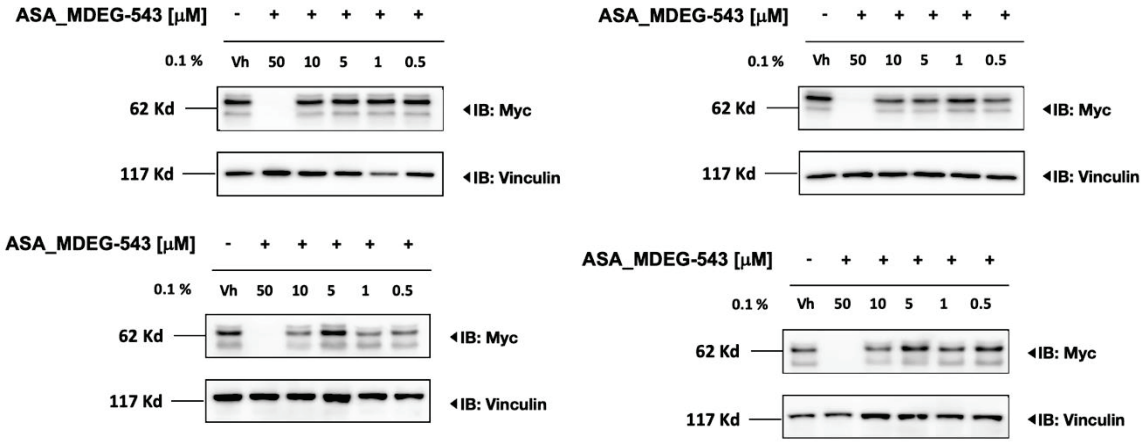

Figure 25: Western blot of ASA_MDEG-543 treated with the indicated concentrations (50- 10- 5- 1- 0.5 µM) and DMSO as vehicle control for 24 h in HCT 116 cells. Vinculin: loading control. Two independent biological replicates with two technical replicates, respectively.

Degradation assay and study of the MoA of ASA_MDEG-544

ASA_MDEG-544 was screened at five different concentrations (50- 10- 5- 1- 0.5 µM) during 24 hours in HCT 116 cells (Figure 26). The results showed a 100 % degradation at 50 µM and 5- 10 % degradation of cMyc at 5 and 10 µM respectively.

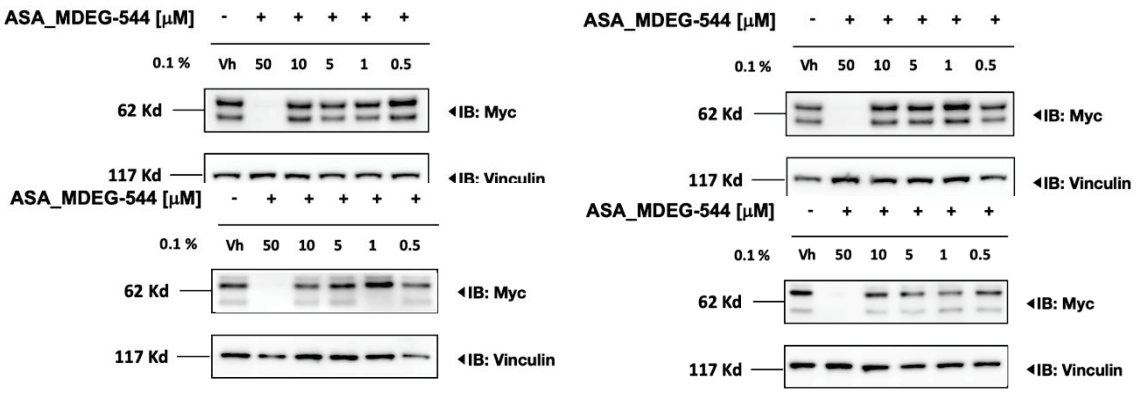

Figure 26: Western blot of ASA_MDEG-544 treated with the indicated concentrations (50- 10- 5- 1- 0.5 µM) and DMSO as vehicle control for 24 h in HCT 116 cells. Vinculin: loading control. Two independent biological replicates with two technical replicates, respectively.

Also, following the same procedure to disentangle the MoA of the PROTAC molecule the cells were pre-treated with MG- 132 (10 µM), MLN- 4924 (1 µM) and Baf- A1 (10 nm) at a final concentration of ASA_MDEG-544 of 10 µM (Figure 27). Restoral of the cMyc levels was observed with the mentioned treatments although ASA_MDEG-544 did not show significant nor good degradation profile of cMyc.

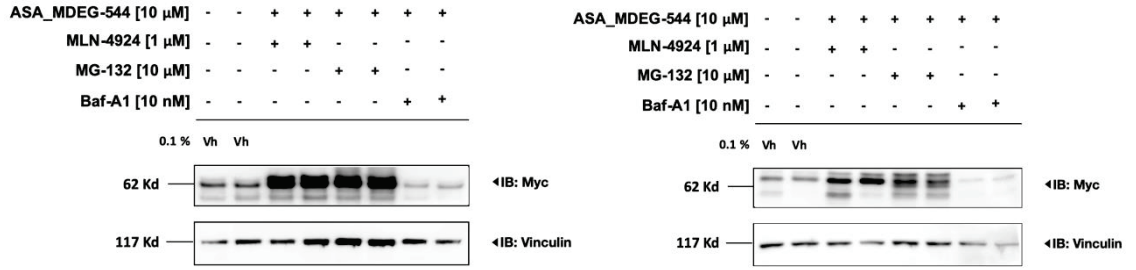

Figure 27: Western blot of MoA assay of ASA_MDEG-542 treated with the indicated concentration (10 µM), pre-treated with MG- 132 (10 µM), MLN- 4924 (1 µM) or Baf- A1 (10 nM), and DMSO as vehicle control for 24 h in HCT 116 cells. Vinculin: loading control. Two independent biological replicates.

3.9 Discussion

In this Chapter, the design and synthesis of cMyc PROTACs using different E3 ligase ligands, linker variations, and cMyc inhibitors have been explored, with a focus on overcoming challenges inherent to targeting cMyc and identifying the most effective degrader for cMyc degradation. Several significant findings emerge from the synthesis and structural characterization of these molecules.

The design of the 1st series of cMyc PROTACs leveraged well-established ligands, with VH032 chosen as the VHL ligand and lenalidomide as the CRBN ligand, based on prior publications that ensures a reliable foundation for their development. A critical element in the design of these PROTACs was the linker, which plays, among other functions, a key role in facilitating the formation of a ternary complex between the E3 ligase, the POI, and the PROTAC molecule and also, influences the physical properties, pharmacokinetics, and degradation activity of the PROTAC.

First, we explored PEG linkers of varying lengths (n=2 and n=4) as starting points, which can be fine-tuned to enhance PROTAC activity. Regarding the cMyc warhead, a derivative of 10058-F4 (3), a fragment-sized low- affinity cMyc inhibitor, was used. It was synthesized *in-house* with high yield, 98 %, via Knoevenagel-like reaction and structurally confirmed by X-Ray crystallographic studies. To synthesize the putative cMyc warhead ASA-5, alkylation of 3 was proposed. However, when 3 was reacted with alkylating agents such as 4, two alkylated products are obtained: ASA-5, resulting from *N-alkylation*, and ASA-6, from *S-alkylation*. The structures of these compounds were also elucidated thanks to X-ray crystallographic analysis, leading to big efforts to develop synthetic strategies to isolate them separately. The primary challenge during the synthesis of 6 and 5, laid in regioselectivity during the alkylation step, where these products were obtained in a 2:5 ratio, respectively. Additionally, purification was challenging due to the structural similarities between the two compounds, which required reverse-phase chromatographic techniques to separate them efficiently. Another significant hurdle is the low yield of ASA-5 from the alkylation reaction, which was achieved in only a 18 % yield, compared to ASA-6 with 46 % yield. To overcome these issues, a significantly improved synthesis of ASA-5 was developed using a one-pot microwave-assisted reaction with high yield (90 %). This new synthetic strategy significantly improves the synthesis of ASA-5, indicating that refining synthetic approaches could enhance overall yield and efficiency. Hence, by incorporating two distinct warhead ligands, the approach introduces structural diversity, enabling a more comprehensive evaluation of how variations in the cMyc warhead structure influence the efficiency of cMyc degradation and the selectivity of PROTAC action.

The final PROTAC molecules were synthesized by coupling the respective VHL and CRBN intermediates with the PEG linkers of two different lengths (n=2 and n=4), with the cMyc warheads, ASA-5 and ASA-6, achieving moderate to good yields. Although yields were initially lower due to purification complexity, the use of reverse-phase column chromatography improves isolation and ensures purity (>95%). As synthesis experience growed, reaction conditions were also optimized, leading to increasing yields and purity of the final products. An interesting and positive outcome occurred during the synthesis of ASA-6- based PROTACs. While amide bond formation was initially expected, a *N-C* nucleophilic substitution reaction took place instead, leading to the formation of ASA-7, ASA-8, ASA-9 and ASA-10. Although unexpected, this pathway leveraged an alternative reaction approach which expanded the scope of the cMyc- based PROTACs and introduced additional diversity into the design.

Degradation assays of 1st series of cMyc PROTACs

The first series of degradation assays with the CRBN PROTACs, ASA-1, ASA-2, ASA-7, and ASA-8, is set at a fixed time point of 6 hours, and at a single relatively high concentration of 50 μM due to the low binding affinity of the cMyc ligand (K_d = 42 μM). Initial results indicate that ASA-7 and ASA-8 are the most effective molecules, each showing approximately 60 % degradation of cMyc, as well as ASA-1 and ASA-2, which show around 50 % degradation. In fact, initial findings suggest promising potential degradation among the CRBN compounds. In contrast, VHL PROTACs (ASA-3, ASA-4, ASA-9, and ASA-10) fail to induce degradation, instead displaying an unexpected upregulation of cMyc. This lack of efficacy from the VHL PROTACs highlights possible issues with the binding affinity or cellular permeability of the VHL ligand.

To further study the degradation profiles of CRBN-based PROTACs, a dose-response analysis is conducted for ASA-1, ASA-2, ASA-7, and ASA-8, across a broader range of concentrations (100, 10, 1, and 0.1 μM) for a treatment time of 6 hours. However, contrary to initial expectations, this screening does not yield significant degradation, even for the previously successful compounds, ASA-7 and ASA-8. These inconsistent results suggest the need for further refinement of the experimental conditions.

Given the fast turnover nature of cMyc, with a half- life of 20- 30 minutes under normal conditions, additional time-treatment assays were studied with the CRBN- based PROTACs, at times of 2, 6, and 24 hours, at a final concentration of 50 μM. Proteasome inhibitor MG-132 pre- treatment is used to disentangle the degradation mechanism. At 6 hours, ASA-2 and ASA-8 show limited degradation of 20- 25 % for cMyc in a proteasome-dependent manner. ASA-1 and ASA-7 demonstrate slightly more efficacy, with 40- 50 % degradation at 24 hours. However, variability in degradation efficiency across different

time points arisen to inconsistencies in PROTAC-mediated targeting, likely related to the short half- life of cMyc and possible differential cellular uptake or retention of the PROTACs.

To further study the PROTAC molecules in a different cellular background, selected CRBN-based PROTACs (ASA-7 and ASA-8) were screened in cMyc-amplified HCT 116 cells at 6 and 24 hours with a pre-treatment using MG-132 to confirm proteasome-dependent degradation. As previously observed, no degradation is detected at 6 hours time point treatment. However, ASA-8 shows approximately 40 % degradation at 24 hours in the first biological replicate, suggesting that longer treatments are needed due to intracellular limitations (*e.g.*, intracellular accessibility), binding affinity or degradation kinetics, among others. These results highlight the potential role of cell line specificity in PROTAC efficacy, as degradation patterns differed from those observed in HEK 293 cells.

A final dose- response experiment with ASA-7 and ASA-8 at four concentrations (100, 10, 1, and 0.1 µM) is conducted in HCT 116 cells for 24 hours to investigate whether PEG linker length influences degradation. Unfortunately, no significant degradation is observed, underlining the inconsistency in the activity of these PROTACs across experimental conditions. This suggests that PEG linker length, while an important design factor, may not sufficiently enhance the degradation profile in the given cell lines and may require further optimizations.

At the same time as the degradation studies of the 1st series of cMyc-based PROTACs are undertaken, a novel cMyc degrader, MDEG-541, is published, which demonstrates dose-dependent cMyc reduction in a ubiquitin-, proteasome-, and CRBN-dependent manner, offering a promising approach to target cMyc degradation. Based on these results, MDEG-541 is synthesized *in-house* to serve as a control in subsequent degradation studies aiming to assess the effectiveness of the 1st and 2nd series of cMyc-based PROTACs.

Building upon the cMyc degradation success of MDEG-541, a 2nd series of cMyc-based PROTACs is synthesized to explore how variations in the E3 ligase-binding component, linker chemistry, and cMyc- based warheads influence PROTAC efficacy when degrading our POI. This series includes ASA_MDEG-542, whose synthesis follows similar steps to those used for MDEG-541, with the key difference being the substitution of the 28RH warhead with 10058-F4. It also includes ASA_MDEG-543 (28RH-based ligand) and ASA_MDEG-544 (10058-F4-based ligand), which are designed to explore the impact of linker type on degradation efficiency. In these compounds, a PEG linker consisting of 3 units is incorporated, enabling a direct comparison between the hydrophobic alkyl chain used in MDEG-541 and the more hydrophilic PEG linker. Moreover, the novel approach of using both the 28RH and 10058-F4 warheads allows for the exploration of how the

choice of ligand impacts the degradation process. This 2nd series is a significant step forward in terms of understanding how the cMyc warhead ligand as well as linker nature affect the activity of the PROTAC. Hence, different cellular degradation studies are carried out to identify the most potent degrader among the 2nd series of cMyc-based PROTAC molecules.

Degradation assays of 2nd series of cMyc PROTACs

In fact, while initial degradation studies on these 1st series of cMyc-based PROTACs yield inconsistent results, MDEG-541 demonstrated promising degradation of cMyc through a ubiquitin- and proteasome- dependent mechanism. Considering these results, MDEG-541 is used as a control after studying its degradation profile and MoA under different treatment conditions in HEK 293 and HCT 116 cells. Indeed, the degradation profile of MDEG-541, mentioned as ASA_MDEG-541 in the Western Blots, (DC_{50}= 3.6 ± 1.7 µM) aligns with the reported MDEG-541 data in HCT 116 cells.

Based on these findings, the focus shifts to evaluating the 2nd series of cMyc-based PROTACs, aiming to achieve more consistent and potent degradation outcomes. First, ASA_MDEG-542, is tested at concentrations of 1 to 50 µM in HCT 116 cells. This degrader displays 100 % degradation from 5 to 50 µM, with a DC_{50}= 4.0 ± 1.5 µM, indicating potent cMyc downregulation. Further experiments using MG-132, MLN-4924, and Baf-A1, reveal that ASA_MDEG-542 acts in a CRL- and proteasome- dependent manner, with proteasome inhibition fully rescuing cMyc levels at 10 µM concentration

Similarly, ASA_MDEG-543, tested in HCT 116 cells at concentrations of 1 to 50 µM, demonstrates moderate degradation activity with 23 % cMyc reduction at 10 µM but lacks efficiency at lower doses, reflecting lower potency than ASA_MDEG-542. Studies of its MoA indicate CRL- and proteasome- dependency at 10 µM, although the PEG linker seems to reduce cellular activity. Finally, ASA_MDEG-544 is evaluated in HCT 116 cells at a five different concentration range where 100 % degradation is observed at 50 µM, but potency decreases remarkably at lower doses, showing minimal degradation at 5 µM. Also, CRL- and proteasome- dependency is observed at a lower effective concentration of 10 µM.

Impact of the linker in cMyc degradation

To this point, we can highlight the importance on ligand and linker properties relative to PROTACs. Thus, chemical structure of the 2nd series of cMyc PROTACs is further discussed.

Regarding the ligand, the cMyc inhibitor 28RH used for the synthesis of ASA_MDEG-541 differs by a *methyl group* compared to 10058-F4 derivative warhead, used for the rational

design of the 1st cMyc- based PROTAC molecules. However, based on the degradation profiles of **MDEG-541** (DC_{50}= 3.6 ± 1.7 µM) and **ASA_MDEG-542** (DC_{50}= 4.0 ± 1.5 µM), where the only structural difference is the ligand, we cannot conclude that the methyl group difference significantly impacts cMyc degradation, given the close similarity of DC_{50} values in the single-digit micromolar range.

However, it is clearly observed that the linker nature significantly impacts on the degradation profile of the two series of PROTAC compounds, as no striking degradation of cMyc protein is observed along the 1st series of cMyc- based CRBN PROTACs as well as for **ASA_MDEG-543** and **ASA_MDEG544**, from the 2nd series of cMyc- based PROTACs, when using a PEG motif. In fact, for the 2nd series, a decrease of a 100 % degradation from 50 to 5 µM with **ASA_MDEG-542** to a 23 % with **ASA_MDEG-543** and 6 % with **ASA_MDEG-544** at 10 µM concentrations are detected. In consequence, the DC_{50} for **ASA_MDEG-543** and **ASA_MDEG-544** (**Figure 28**) cannot be calculated: 100% degradation is observed with both molecules at a final concentration of 50 µM, however the dose is too high and toxic to be considered to calculate the DC_{50} parameter.

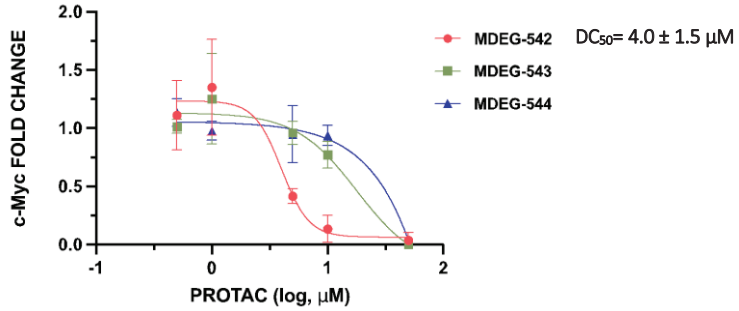

Figure 28: Representative **ASA-MDEG-542**, **ASA_MDEG-543** and **ASA_MDEG-544** dose- response curves at five points (50- 10- 5- 1- 0.5 µM) in HCT 116 cells for 24 h. Western blot assays are used to determine the dose-response. Three independent biological replicates are analyzed. Shown is the mean ± SD.

These results arise from the hypothesis that the use of a PEG moiety as a linker in the design of the two series of cMyc-based PROTAC molecules, decreases the potency of the degraders. In fact, it has become increasingly clear that the length and composition of the linker play crucial roles on the physicochemical properties and bioactivity of PROTACs.

A significant pharmacokinetic hurdle for large PROTACs tend to be permeability [173] and solubility [174] which has resulted in big efforts to develop strategies for improving bioactivity through increase membrane permeability during their design. These properties can be fine- tuned by modifying the linker nature and length, but also the number of HBDs and HBAs. In fact, structural modifications by reducing polarity and

modulating lipophilicity (within a range of 1-4 ΔlogP), combined with reduced HBA and solvent – exposed HBDs may result in an improvement of cell permeability [175, 176].

To gain a better understanding of the physicochemical properties and structure- property relationship of the 2nd series of cMyc- based PROTACs, SwissADME tool [177] is used (Table 2). Although PEG moieties offer higher flexibility chains (increase NRotB) facilitating PPI with the POI or / and E3 ligase, and better solubility, it significantly increases the number of HBA and TPSA, which leads to a decrease on permeability.

Notwithstanding, the use of alkyl linkers minimizes the TPSA and HBA (as observed with MDG-541 and ASA_MDEG-542) offering a better permeability and more rigid conformation, which in turn might result in a more stable structure that forms a productive ternary complex. [96]

PROTAC	MW (Da)	LogP	HBD	HBA	TPSA (Å^2)	NRotB
MDEG-541	674.83	4.96	2	6	190.35	14
ASA_MDEG-542	660.80	4.63	2	6	190.35	14
ASA_MDEG-543	722.83	3.28	2	9	218.04	17
ASA_MDEG-544	708.80	2.92	2	9	218.04	17

Table 2: Physicochemical properties of 2nd series of cMyc- based PROTACs predicted by SwissAdme software. Calculated MW, molecular weight; LogP, lipophilicity average of five predictions; hydrogen bond donor; HBA, hydrogen bond acceptor; TPSA, total polar surface area; NRotB, number of rotable bonds,

3.10 Conclusions

This chapter details the rational design, synthesis, and biological evaluation of two successive generations of PROTACs targeting the oncogenic transcription factor cMyc, with the overarching aim of addressing the long-standing challenge of targeting cMyc for degradation.

The **1st series of cMyc-based PROTACs**, a total of eight PROTAC molecules using both VHL and CRBN ligands, and PEG linkers of different lengths and derivatives of the **10058-F4** cMyc inhibitor, were successfully synthesized and structurally characterized.

- Successful synthesis and X-Ray structural characterization of two warhead derivatives, **ASA-5** and **ASA-6**, from the non-regioselective alkylation of **10058-F4**, demonstrated the feasibility of generating chemically tractable ligands for incorporation into PROTACs.
- Development of an optimized, high-yield synthetic route for **ASA-5** (90% yield via microwave-assisted synthesis) underscored the importance of refining synthetic methodologies to obtain suitable PROTAC building blocks efficiently and selectively.
- **ASA-6** enabled the formation of PROTACs (**ASA-7**, **ASA-8**, **ASA-9** and **ASA-10**), expanding chemical diversity within the series.
- Biological evaluation in HEK 293 and HCT 116 cells revealed limited and variable cMyc degradation activity, primarily among the CRBN-based PROTACs (**ASA-1**, **ASA-2**, **ASA-7**, and **ASA-8**), with some time- and dose-dependent degradation observed at high concentrations and extended treatment times.
- While some degradation was observed with **ASA-7** and **ASA-8**, under selected conditions, VHL-based molecules failed to induce cMyc degradation and in some cases upregulated its expression.
- These results suggest that CRBN may be a more effective E3 ligase for cMyc degradation in the tested models, although the overall limited efficacy highlights significant challenges, most notably poor cellular permeability and potentially suboptimal binding affinity, likely exacerbated by the hydrophilic nature of PEG-based linkers.

A **2nd series of PROTACs** were designed based on structural and mechanistic insights, incorporating the potent degrader **MDEG-541** as a benchmark.

- This series employed two key design refinements: (i) replacement of the 10058-F4 warhead with the higher-affinity 28RH ligand, and (ii) substitution of PEG linkers with more lipophilic and conformationally constrained alkyl chains to enhance membrane permeability.

- The 2nd series of PROTACs demonstrated markedly improved degradation efficacy. In particular, ASA_MDEG-542 induced potent, dose-dependent degradation of cMyc (DC_{50} = 4.0 ± 1.5 µM), closely matching the activity of MDEG-541. Mechanistic studies confirmed that cMyc degradation was both proteasome- and CRL-dependent.
- Comparison of MDEG-541 and ASA_MDEG-542 revealed that the cMyc warhead (28RH vs. 10058-F4) had a limited impact on degradation potency when the linker and E3 ligase ligand were optimized.
- ASA_MDEG-543 and ASA_MDEG-544, PEG-containing analogues, demonstrated substantially reduced activity, emphasizing the negative impact of PEG linkers on both cellular uptake and degradation potency.
- These findings established that linker design, specifically the use of alkyl-based linkers lead to superior degradation profiles, likely due to their more favorable physicochemical properties (lower polarity, higher lipophilicity, and rigidity) that support better cellular uptake.

Together, these results demonstrate the potential and the challenges of designing PROTACs for an "undruggable" target like cMyc. While the first-generation molecules provided essential insights, the second-generation PROTACs, particularly ASA_MDEG-542, represent significant progress toward achieving potent and consistent cMyc degradation. This result lays the groundwork for further rational design and optimization efforts aimed at developing therapeutically relevant cMyc degraders.

CHAPTER 4

Targeting Cyclin E/CDK2 with a novel dual PROTAC molecule

4. CHAPTER 4: Degrading Cyclin E/CDK2 with a novel dual PROTAC approach

In both unicellular and multicellular eukaryotes, cell division is regulated by a complex network of mechanisms, involving checkpoints and balances to ensure that no errors occur before a cell is permitted to enter and progress through the cell cycle for division. Progression through cell cycle phases is regulated by a family of Cyclin-Dependent Kinases (CDKs), which associate with their respective Cyclin regulatory subunits Specific accumulation in Cyclin levels determines fluctuations in CDK activity, which control the transition of the phases of the cell cycle. [178]

Cyclin E is a nuclear protein that mainly exerts its regulatory functions by interacting with and activating CDK2 during G_1/S interphase, leading to phosphorylation of target proteins and regulating the G1 phase progression of the cell cycle (Box 1). Hyperactivation of Cyclin E/CDK2 complex is the hallmark of DNA replication stress and genomic instability in human cancer. This oncogenic activation of Cyclin E/CDK2 complex can result from various genetic events, including amplification of Cyclin E genes (CCNE1 or CCNE2), disruption of the RB/E2F pathway (which increases Cyclin E transcription), and mutations in the Fbxw7 ubiquitin ligase (leading to the accumulation of Cyclin E protein). In addition, high levels of Cyclin E and CDK2 are both independently associated with poor prognosis, reduced survival, and therapy resistance in cancer patients. [179, 180]

Unfortunately, no small molecules directly targeting Cyclin E have been described. The modular nature of PROTACS allows the rapid conversion of ligands into full chemical protein degraders. As the ligand itself does not need to display any specific function, it can bind anywhere on the target protein, which increases the likelihood of finding suitable ligands when using appropriate binding site agnostic (biophysical) screening approaches. However, due to the lack of small- molecule binders, Cyclin E cannot be targeted by the conventional PROTAC strategy. In this scenario, the use of a “bridged PROTAC” [181] would target Cyclin E by using a small- molecule binder that recruits a bridge protein, CDK2, and its binding partner, Cyclin E, taking advantage of their complex formation during G_1 / S interphase. Following this strategy, we could: (i) degrade an undruggable protein and (ii) recruit and destabilize the Cyclin E / CDK2 complex which represents an attractive therapeutic strategy for specific cancer subtypes such as breast, uterine and ovarian cancers. [182]

Box 1: Cyclin E /CDK2 complex: master regulators of G_1 / S cell cycle interphase

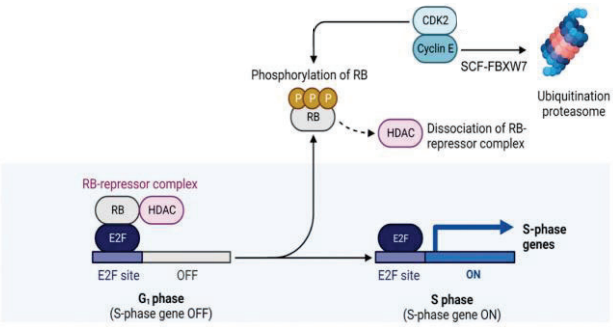

Molecular overview of the network involved on the G_1 /S transition phase. Adapted and created with BioRender.com [183]

The eukaryotic cell cycle is the process during which a cell duplicates its entire cellular content during interphase, and through division in M phase creates two genetically identical cells. The key regulator of cell cycle processes is CDK activity. Specific Cyclins accumulate during different stages of the cell cycle, driven by cell cycle- regulated transcription and the inhibition of protein degradation.

In normal conditions, Cyclin E1 and Cyclin E2 expression is activated by RB inactivation and E2F release, driven by Cyclin D / CDK4-6 during G_1. Then, Cyclin E accumulates, binds to CDK2 at the G1 / S transition phase, and promotes S phase entry and progression by phosphorylating key substrates. At the end of S phase, Cyclin E is phosphorylated (at the CDC phosphodegron represented by Serine and Threonine residues) and later recognized by the SCF- Fbxw7 complex, and directed to proteasomal degradation, halting its activity until next G_1 phase. [183, 184]

4.1 Previous results: Identification and characterization of Cyclin E ligands through a virtual- and biophysical- approach

A combined virtual- and biophysical- based workflow is employed in Galdeano's Lab by postdoc Dr. Alejandra Rodríguez-Gimeno to identify small molecules able to bind in the protein- protein interface of Cyclin E/CDK2 complex (Figure 29).

Using MDMix, a software that was developed in the group of Prof. Xavier Barril (University of Barcelona) which exploits the idea of promiscuity to identify high affinity interaction spots (*hot- spots*) over macromolecular systems by molecular dynamics simulations using small co-solvent molecules as solvation conditions, a druggable pocket in the Cyclin E/CDK2 protein-protein interface was identified, as well as the most important residues in the pocket, to generate possible polar and hydrophobic interactions with ligands. A pocket in the Cyclin E/CDK2 interface could be interesting for studying the possible PROTAC-mediated degradation of both proteins. In addition, as it was mentioned above, during the cellular cycle, Cyclin E from its synthesis to its degradation is complex with its CDK2 counterpart.

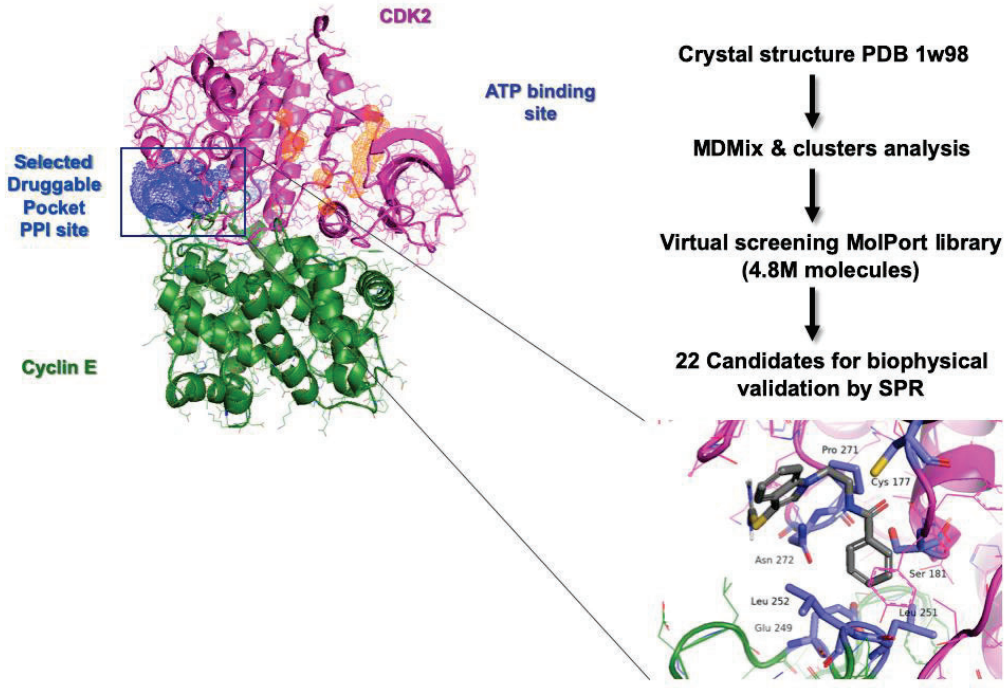

Figure 29: Workflow applied to identify ligands for Cyclin E/CDK2 complex.

Next, a virtual screening campaign was started using the open source rDock software where a library of 4.8 million compounds provided by MolPort were screened computationally for this specific site. In result, 22 molecules with maximal chemical and

structural diversity were identified which are tested experimentally by Dr. Alejandra Rodríguz- Gimeno using SPR, from which 2 compounds with nanomolar affinity were selected to further characterization: **ARG-15** (K_d = 0.2 ± 0.5 µM) and **ARG-9** (K_d = 4.0 ± 0.5 µM) (**Figure 30**). SAR by catalogue was also performed and 30 new additional analogues were purchased and tested in a dose-response manner presenting K_ds in the high nanomolar to three- digit micromolar range. Some substitutions were identified in the main scaffold that were accepted and used as points for the PROTAC design and synthesis to degrade Cyclin E/CDK2.

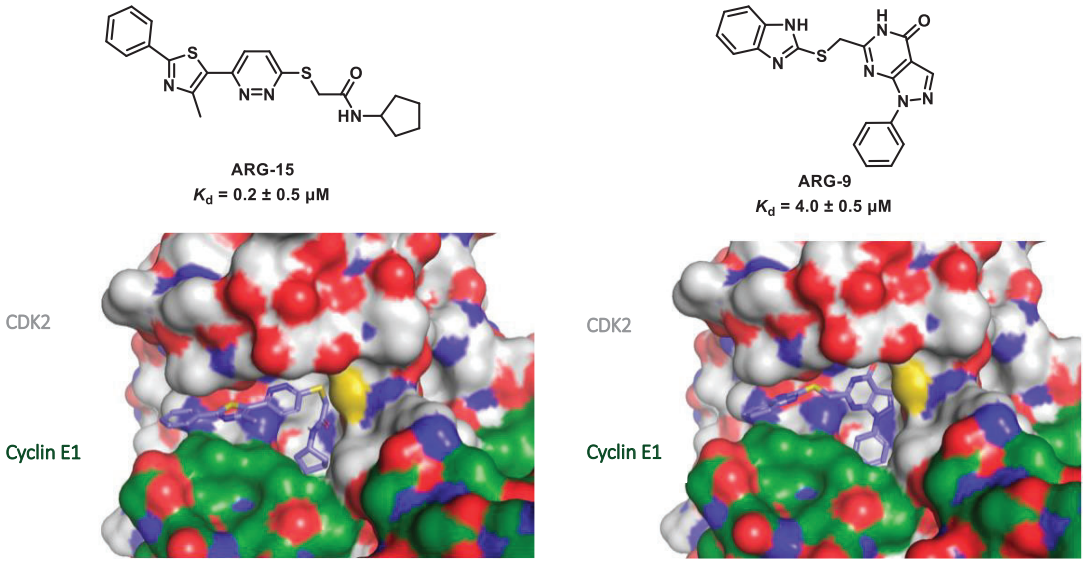

Figure 30: Docking of the selected compounds **ARG-9** and **ARG-15**, in the Cyclin E /CDK2 interface pocket. *Kd* values with SD mean which were obtained in SPR experiments are shown.

4.2 Specific objectives of Chapter 4

The following specific objectives were established:

i. First, the **design and synthesis of 1st series of bridged Cyclin E /CDK2- based PROTACs**, with the aim of identifying the most potent degrader from this initial generation. This series will incorporate:
   - **ARG-91** ligand derivative of **ARG-9**, validated by SPR and synthesized by Dr. Alejandra Rodríguez-Gimeno.
   - **VH032** and **lenalidomide** as E3 ligase- recruiting ligand, targeting VHL and CRBN, respectively.
   - PEG linkers of three different lengths (n=2, n=4, and n=6) to explore the impact on the linker when degrading Cyclin E and/ or CDK2 proteins.

ii. Second, the ***in vitro* evaluation of the degradation efficiency of this 1st series** using kidney cells HEK 293 and MYC- amplified colon cancer line HCT 116. These studies will include:
   - Single- dose, time- course, and dose- response assays.
   - MoA confirmation through pre-treatment with the proteasome inhibitor **MG-132** and NEDD8-activating enzyme inhibitor **MLN-4924**.
   - Degradation assays under synchronized cell cycle conditions, employing double- thymidine block to arrest the cells in the G1 / S phase, thereby increasing Cyclin E /CDK2 complex abundance and improving the likelihood of successful degradation.

   To assess intracellular target engagement, providing insight into PROTAC binding affinity, cellular permeability, and overall availability within the cellular environment, NanoBRET Target Engagement assays will be performed using permeabilized and live-cell models.

4.3 Design of 1st series of Cyclin E/CDK2- based PROTACs

The development of the 1st series of Cyclin E/ CDK2- based PROTACs follows a rational design similar to that employed for the 1st series of cMyc-targeting PROTACs. Given the established efficacy of the VHL and CRBN E3 ligases in PROTAC-mediated degradation, the most widely used E3 ligase ligands, VH032 for VHL and lenalidomide for CRBN, were selected as the anchor ligands for this series.

For the selection of a suitable Cyclin E/CDK2 ligand, the small- molecule compound ARG-9 was identified as a promising candidate for this 1st series, which was synthesized *in-house* by Dr. Alejandra Rodríguez-Gimeno at the Medicinal Chemistry Unit. Considering its chemical structure, ARG-91, derivative of ARG-9, featuring a carboxylic acid moiety at the *ortho* position of the aromatic ring was used to enable conjugation to the PROTAC linker. This derivative served as the Cyclin E/CDK2-targeting warhead in the 1st series of PROTACs (Scheme 8).

The choice of linker plays a crucial role in modulating the physicochemical properties, flexibility, and degradation efficiency of PROTAC molecules. In this series, PEG linkers of varying lengths (n=2, n=4, and n=6) were employed to explore the influence of linker length on the degradation activity and selectivity of the compounds. The incorporation of different linker lengths allowed for systematic assessment of linker-dependent effects on ternary complex formation and subsequent ubiquitination efficiency.

The final design of the 1st series of Cyclin E / CDK2-based PROTAC molecules consisted of the ARG-91 as the warhead, conjugated to either VH032 or lenalidomide *via* PEG linkers of three different lengths (n=2, n=4, and n=6). In total, six PROTAC molecules were synthesized, three VHL-based and three CRBN-based (Scheme 8).

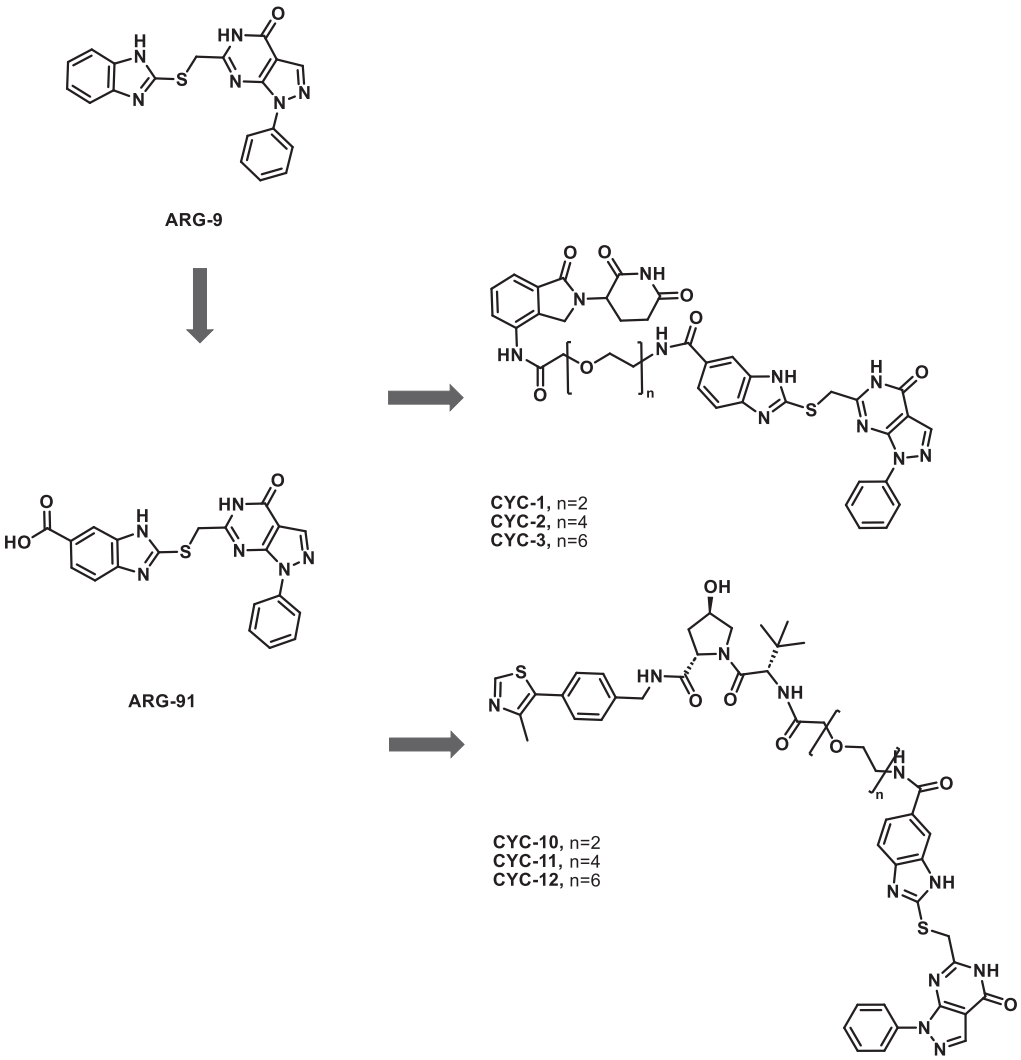

Scheme 8: Chemical structures of the 1st series of Cyclin E/CDK2- based PROTAC molecules: CRBN based (CYC-1, CYC-2, CYC-3) and VHL based (CYC-10, CYC-11, CYC-12).

4.4 Synthesis of 1st series of Cyclin E/CDK2- based PROTACs

Synthesis of CRBN- based PROTACs

Regarding the synthesis of the CRBN-based PROTACs, **8** was coupled to the respective PEG motifs of different lengths, **9a**, **9b** and **9c** to give **10a**, **10b** (n=4, R= Boc), and **10c**, with yields of 78 %, 82 %, and 75 %, respectively.

Subsequently, the Boc group was deprotected under acidic conditions (TFA) to afford **11a**, **11b**, and **11c** in quantitative yields, respectively (**Scheme 9**). [52, 157] Finally, those intermediates as TFA salts reacted with **ARG-91** under coupling conditions, giving **CYC-1**, **CYC-2**, and **CYC-3**, with yields of 33 %, 43 %, and 41 %, respectively (**Scheme 9**). [52]

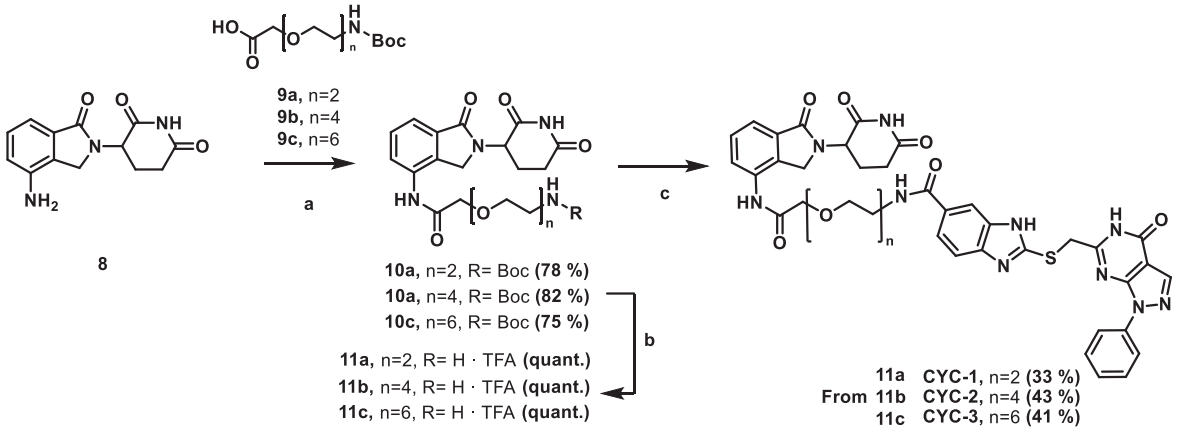

Scheme 9: Synthesis of CRBN- based PROTACs: **CYC-1, CYC-2** and **CYC-3**[a].
[a] *Reagents and conditions*: (a) HATU, DIPEA, DMF, r.t., overnight; (b) TFA: DCM (1:1), r.t., 30 min; (c) **ARG-91,** HATU, DIPEA, DMF, r.t., overnight.

Synthesis of VHL-based PROTACs

Regarding the synthesis of the VHL- based PROTACs, **39**, which is **VH032** ligand as HCl salt, was commercially available and purchased to facilitate the synthesis of the final PROTACs. Thus, **39** was coupled to the respective PEG motifs of different lengths, **9a**, **9b** and **9c** to give **22a**, and **22b**, with better yields than those previously obtained in the 1st series of cMyc-based PROTACs, of 70 % and 82 %; and **22c**, with a yield of 73 %, respectively. Subsequently, the Boc group was deprotected under acidic conditions (TFA) to afford **23a**, **23b** and **23c** in quantitative yields, respectively. [52, 166, 167, 185] Finally, those intermediates as TFA salts were coupled with **ARG-91** using HATU and DIPEA coupling reagents, yielding the final compounds **CYC-10, CYC-11,** and **CYC-12,** with a yield of 35 %, 6 %, and 15 %, respectively (**Scheme 10**). [52]

It should be mentioned that while the CRBN- based PROTACs displayed relatively moderate yields, the VHL-based PROTACs presented notably lower yields, particularly associated with purification and solubility challenges of such big polar compounds. Additionally, the low solubility of ARG-91 ligand in DMF contributed to incomplete consumption during the reaction, leaving significant traces of the starting material in the crude product which presented a similar polarity profile with the final compound (similar retention times with the final PROTAC molecules were observed at the HPLC / MS, when monitoring the reaction), resulting in trickier purification and, consequently, lower yields.

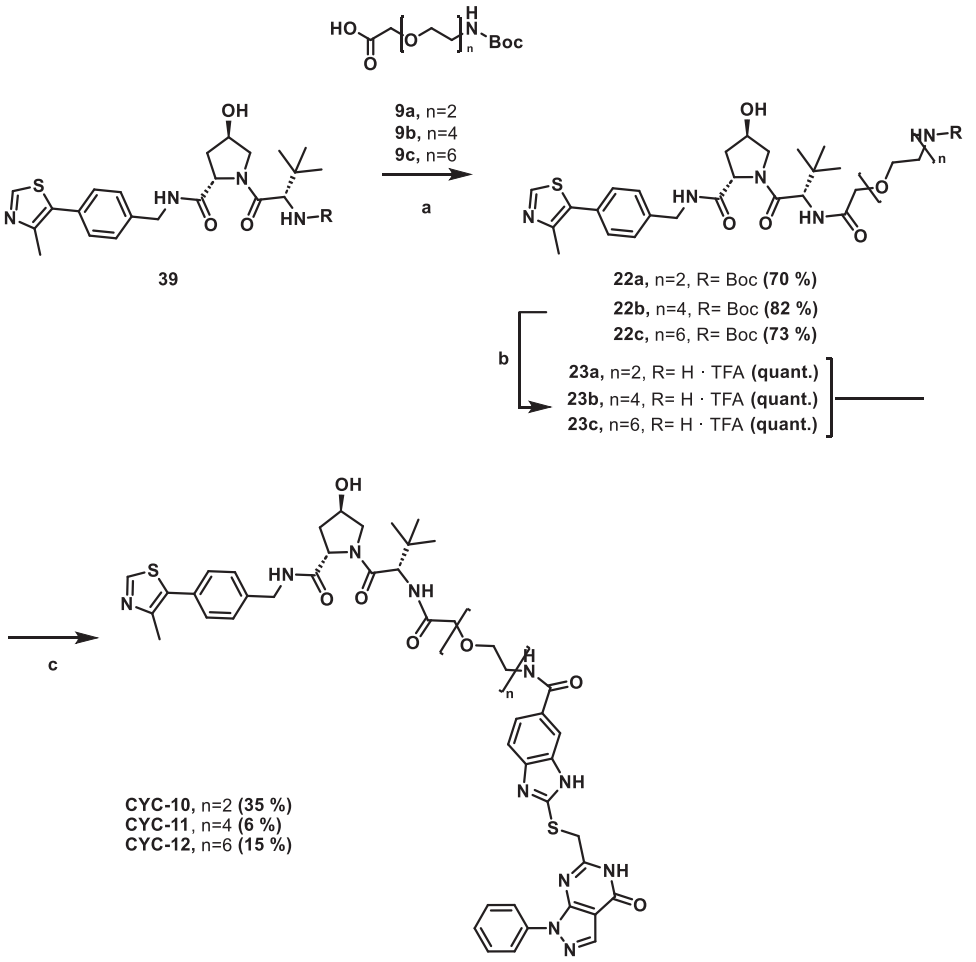

Scheme 10: Synthesis of VHL-based PROTACs: CYC-9, CYC-10 and CYC-11[a].

[a]*Reagents and conditions*: (a) HATU, DIPEA, DMF, r.t., overnight; (b) TFA: DCM (1:1), r.t., 30 min; (c) ARG-91, HATU, DIPEA, DMF, r.t., overnight.

4.5 Degradation studies of 1st series of Cyclin E/CDK2 - based PROTACs

Focusing on the second objective of this chapter, time and dose- treatment degradation assays are performed to find the most potent compound of the 1st series of Cyclin E / CDK2 - based PROTAC molecules. It is worth mentioning that all these studies were carried at the Centre for Targeted Protein Degradation (CeTPD), one of the world leading institutions in target protein degradation, led by Prof. Alessio Ciulli, as part of a Short-Term Scientific Mission Grant from Proteocure Cost Action program.

Therefore, the proposed workflow consists of a first screening at two different time points (t= 6 and 24 hours) at different dose-response treatments in HEK 293 cells. Also, to confirm that the degradation is Culling RING ligase (CRL)- and proteasome-dependent, in some assays the cells were pre-treated with the NEDD8-activating enzyme inhibitor MLN-4924 and the proteasome inhibitor MG- 132, prior to the corresponding PROTACs treatment. To detect and analyze the protein degradation, Western-blot technique was employed using Cyclin E and CDK2 antibodies, and tubulin as housekeeping control. DMSO at 0.10 % is used as a vehicle control and independent biological and technical replicates (n=2-3) are performed to ensure reproducibility. For more details see experimental chapter.

4.5.1 Degradation assays of CRBN- based PROTACs

Time- and dose-response degradation asays

In a first screening, the Cyclin E / CDK2 CRBN- based PROTACs (CYC-1, CYC-2, CYC-3), were tested at two different time points, 6 and 24 hours, at different concentrations in HEK 293 cells to choose the best time- treatment conditions. Again, highlight that the high concentration of 50 µM was chosen due to the low- binding affinity of ARG-9 with Cyclin E/CDK2 (K_d= 4.0 ± 0.5 µM), and to discard the presence of Hook- effect. For a better understanding of the MoA of the PROTACs, in some assays the cells were pre-treated with proteasome inhibitor MG- 132 [10 µM] or NEDD8- activating enzyme inhibitor MLN-4924 [1 µM].

When treating the cells for 6 hours at four different concentrations (10- 5- 1- 0.5 µM) with a pre-treatment of MG- 132 at a final PROTAC concentration of 50 µM, no striking degradation was observed with any of the compounds. However, testing them at a time treatment of 24 hours at different concentrations some degradation results were observed. The first biological replicate was performed at five different concentrations (50- 10- 5- 1- 0.5 µM) without any special pre-treatment. Regarding the second replicate, seven different concentrations (50- 10- 5- 1- 0.5- 0.1- 0.05 µM) were tested with a pre-

treatment of MLN-4924 [1 µM] at a final PROTAC concentration of 50 µM. The degradations observed with each PROTAC were elucidated:

- CYC-1. At the first biological replicate, 30- 40 % degradation of Cyclin E was observed from 10- 1 µM at both technical replicates (Figure 31, A). At the second biological replicate, no degradation of Cyclin E was observed, but 20- 30 % degradation of CDK2 at 0.1 and 0.05 µM was detected at the first technical replicate (Figure 31, B).

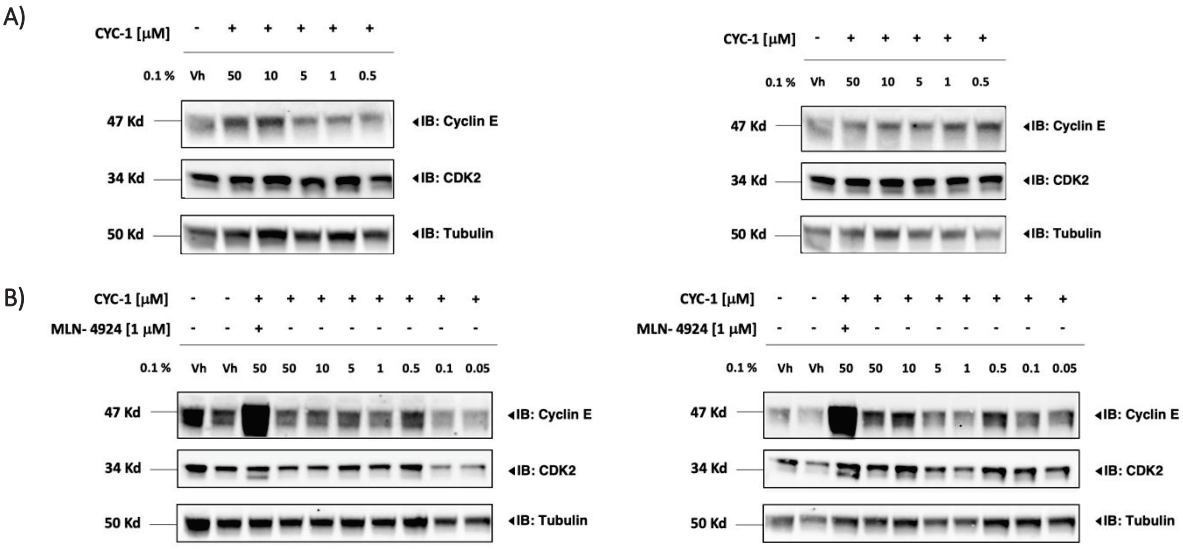

Figure 31: A) Western blot of CYC-1 treated with the indicated concentrations (50- 10- 1- 0.1 µM) at and DMSO as vehicle control for 24 h in HEK 293 cells. Two technical replicates. B) Western blot of CYC-1 treated with the indicated concentrations (50- 10- 5- 1- 0.5- 0.1- 0.05 µM), pre-treated with MLN- 4924 (1 µM), and DMSO as vehicle control for 24 h in HEK 293 cells. Tubulin: loading control. Two technical replicates.

- CYC-2. At the first biological replicate no degradation of Cyclin E and CDK2 was observed (Figure 32, A). Regarding the second biological replicate, 20 % degradation of Cyclin E was detected from 10- 5 µM but not at the third biological replicate as 20- 30 % degradation of CDK2 from 0.5 -0.05 µM was yet observed (Figure 32, B).

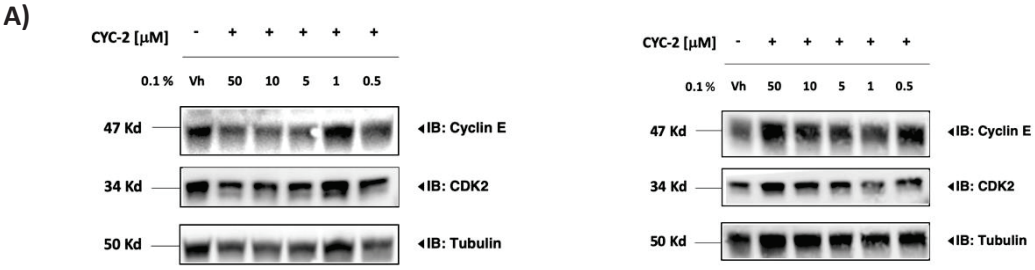

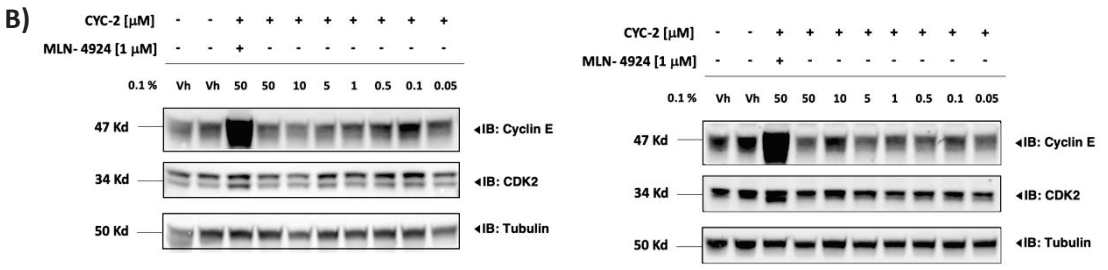

Figure 32: A) Western blot of CYC-2 treated with the indicated concentrations (50- 10- 1- 0.1 µM) at and DMSO as vehicle control for 24 h in HEK 293 cells. Two technical replicates. B) Western blot of CYC-2 treated with the indicated concentrations (50- 10- 5- 1- 0.5- 0.1- 0.05 µM), pre-treated with MLN- 4924 (1 µM), and DMSO as vehicle control for 24 h in HEK 293 cells. Tubulin: loading control. Two independent biological replicates.

- CYC-3. In this case, in two of the three independent biological replicates that were performed, CDK2 degradation was observed with 30 % from 5 -1 µM and 60 % at 0.5 µM, at the first one; and 30- 40 % from 10- 1 µM, at the third one (Figure 33, A). At the second biological replicate, no degradation was observed (Figure 33, B).

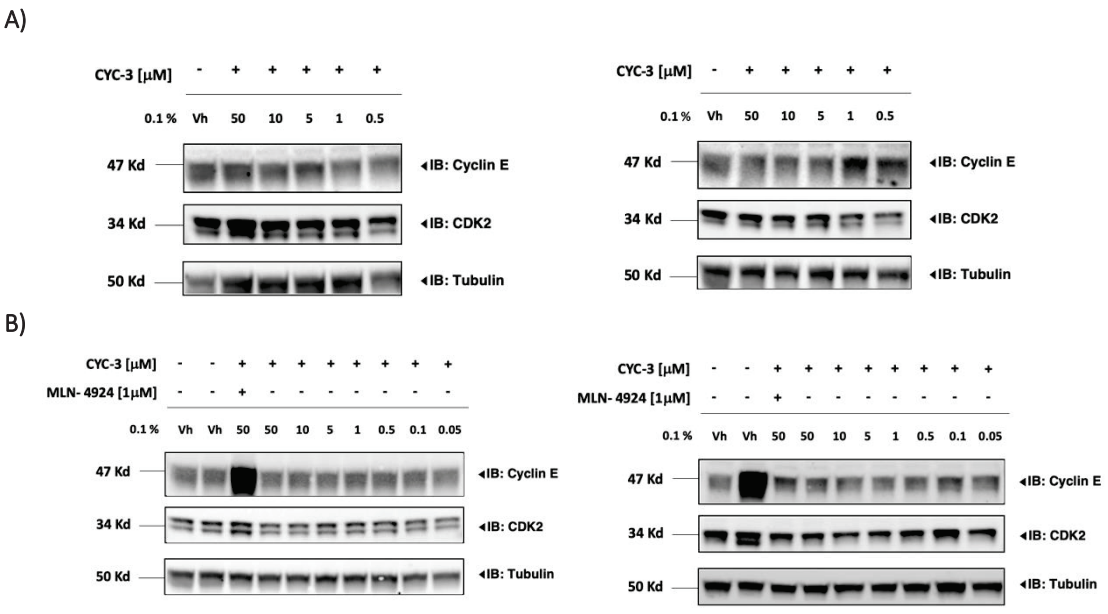

Figure 33: A) Western blot of CYC-3 treated with the indicated concentrations (50- 10- 1- 0.1 µM) at and DMSO as vehicle control for 24 h in HEK 293 cells. Two technical replicates. B) Western blot of CYC-3 treated with the indicated concentrations (50- 10- 5- 1- 0.5- 0.1- 0.05 µM), pre-treated with MLN- 4924 (1 µM), and DMSO as vehicle control for 24 h in HEK 293 cells. Tubulin: loading control. Two independent biological replicates.

Considering these results, none of the three CRBN-based PROTACs showed a striking degradation of Cyclin E. Notwithstanding the lack of degradation of Cyclin E with the three CRBN- based PROTACs, CDK2 downregulation was detected with **CYC-3**. However, DC_{50} values could not be calculated as no 50 % degradation of Cyclin E nor CDK2 was detected with the tested PROTACs in a reproducible manner.

4.5.2 Target engagement assay of CRBN-based PROTACs

To further characterize the CRBN-based PROTACs MoA and validate the findings, benefiting from the host institution knowledge in the PROTACs field and the accessibility to a vast of different biophysical techniques, NanoBRET® Target Engagement (TE) Intracellular E3 ligase assay (Promega CRBN kit) was performed. This is an energy transfer technique designed to measure molecular proximity in living cells, in this case, it allows live-cell measurement of the CRBN-based PROTAC molecules affinity for CRBN protein *via* displacement of a fluorescent CRBN probe (NanoBRET® Tracer). Additionally, as PROTACs often suffer from poor cell permeability, this assay can be used to measure intracellular availability of the degraders, providing a measure of compound permeability by applying a simple workflow that involves two modes a live- cell mode (t= 4 hours), where the intracellular affinity of the compound is measured and cellular factors can influence binding potency; and a permeabilized- cell mode, where the intrinsic affinity of the compound is measured in the absence of the cell membrane by the use of digitonin, mild nonionic detergent used for permeabilizing the cells (**Figure 34**). Comparing the affinity data, we can calculate the intracellular availability between compounds in both modes, relative to a compound control, providing meaningful information associated with permeability properties.

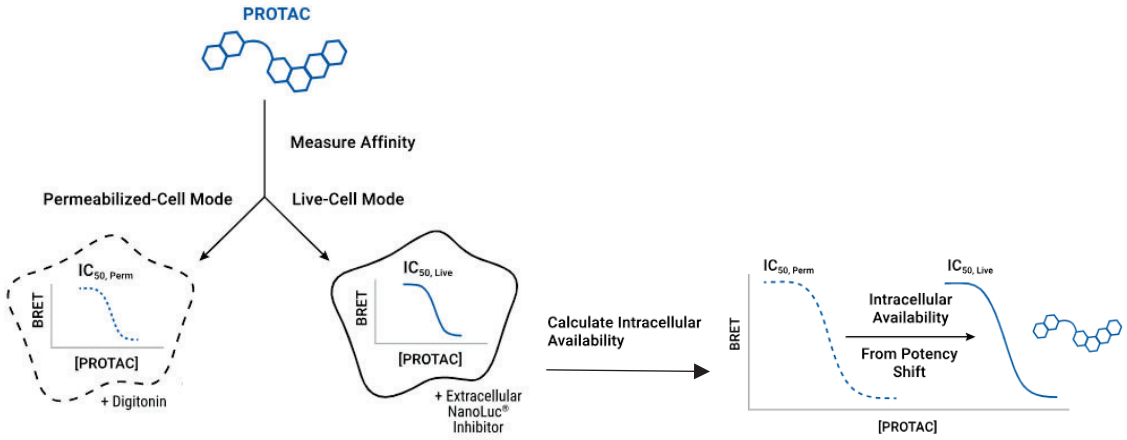

Figure 34: Workflow overview of TE and intracellular availability assay (from Promega).

Following the CeTPD optimized protocol recommendations, the CRBN-based PROTACs were screened at ten different concentrations (31600- 10000- 3160- 1000- 316- 100- 31.6- 10.0- 3.0- 1.0 nM) to obtain the corresponding IC_{50} values (three technical replicates per compound are performed). The close proximity of the tracer to NanoLuc® in the E3 ligase fusion resulted in a NanoBRET® signal, and, the addition of compounds to cells that bound to CRBN, resulted in a dose-dependent decrease in NanoBRET® signal. Thalidomide, small- molecule CRBN molecular glue; and dBET6, [186] high-cell permeable CRBN degrader, were used as permeable controls.

Following this orthogonal method, in the permeabilized-mode we could observe that the CRBN- based PROTACs showed a good engagement profile to CRBN, sharing a similar profile to thalidomide and better profile compared to dBET6, as positive controls (**Figure 35, A**). **CYC-2** (IC_{50} = 43.2 ± 5.7) showed the best engagement profile to CRBN, achieving a two-digit nanomolar IC_{50}, comparable to that of thalidomide (IC_{50} = 51.0 ± 4.4) and superior to the other screened PROTAC molecules (**Table 3**).

However, in live-mode, where the cellular factors, *e.g.*, cell membrane, can influence the binding potency to CRBN, the PROTAC compounds showed lower engagement with CRBN compared to the positive controls. In fact, 50 % of tracer displacement was not reached, and therefore, the IC_{50} could not be determined (**Figure 35, B**).

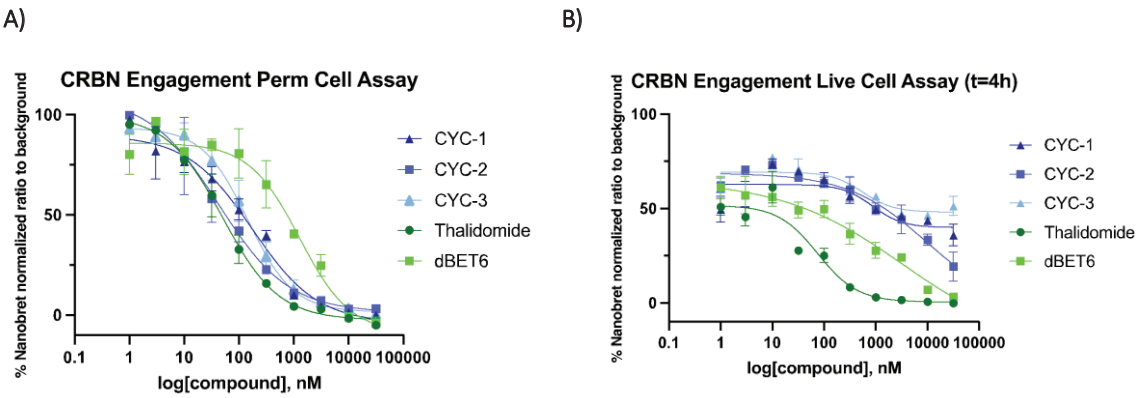

Figure 35: CRBN TE assay by NanoBRET in permeabilized mode (**A**) and live mode (t=4 h, **B**) in CRBN-NanoLuc® fusion protein expressed in HEK 293 cells for compounds **CYC-1**, **CYC-2** and **CYC-3.** dBET6 and Thalidomide were used as positive controls. Three technical replicates.

Compound	IC_{50} (nM, Lytic)
CYC-1	177.4 ± 5.9
CYC-2	43.2 ± 5.7
CYC-3	145.8 ± 5.6
Thalidomide	51.0 ± 4.4
dBET6	1287.0 ± 7.0

Table 3: IC_{50} values determined by plotting with GraphPad Prism software (v10.1.1) the competitive displacement data from NanoBRET® CRBN TE assay in permeabilized mode, using the [inhibitor] vs response – variable slope (four parameters). For this experiment, NanoBRET ratios are normalized to background correction and expressed in %.

High binding in permeabilized mode suggests that CRBN- based compounds have good affinity for CRBN under these conditions, whereas the low binding in live-mode may indicate that the compounds have poor permeability or that intracellular factors limit their availability in the cells. These results highlight a potential issue with cell permeability and the need for further optimization of the Cyclin E / CDK2 CRBN- based PROTACs. Additionally, these findings might explain the unconclusive degradation observed so far for both target proteins and suggest the necessity for extended treatment durations (*e.g.,* 24 hours).

4.5.3 Degradation assays of VHL- based PROTACs

In the initial screening of VHL- based PROTACs (**CYC-10, CYC-11, CYC-12**) the limited quantities obtained during chemical synthesis, along with the previous findings on treatment duration and dose responses observed with the CRBN-based PROTACs, resulted in testing them at seven different concentrations (50- 10- 5- 1- 0.5- 0.1- 0.05 µM) for 24 hours in HEK 293 cells. To gain a better understanding of the MoA, the cells are pre-treated with NEDD8- activating enzyme inhibitor **MLN- 4924** [1 µM] at a final PROTAC concentration of 50 µM.

CYC-10, showed a weak 10 % degradation of Cyclin E at 0.1 µM in both independent biological replicates (**Figure 36, A**). **CYC-11**, showed a 20 % degradation of CDK2 at concentrations ranging from 0.5-0.05 µM in the second biological replicate (**Figure 36, B**). In contract, **CYC-12,** demonstrated no degradation of either proteins in either assay (**Figure 36, C**).

VHL-based PROTACs did not show a good degradation profile for either Cyclin E or CDK2 proteins. In this case, TE Assays could not be performed due to the unavailability of PROTAC stock.

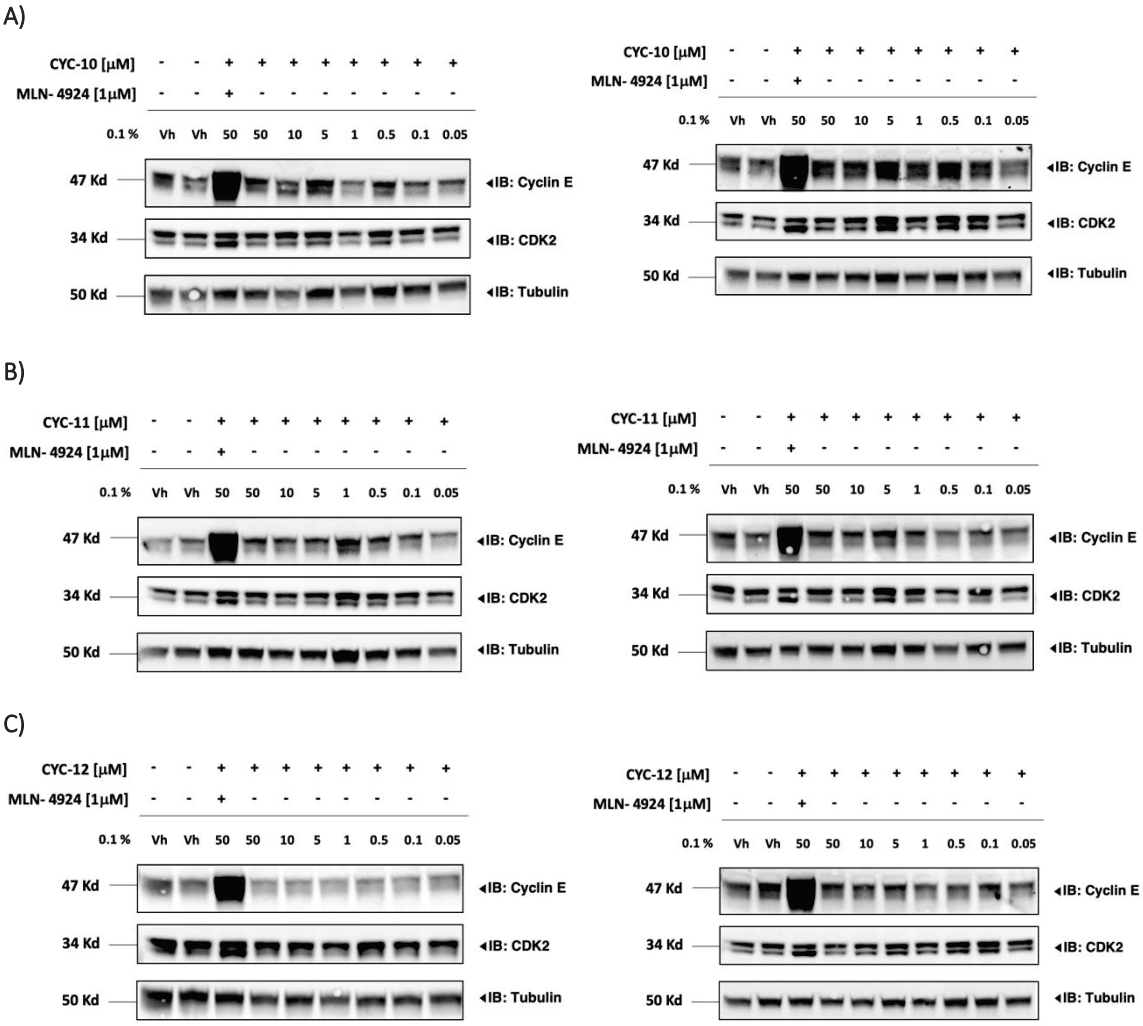

Figure 36: Western blot of CYC-10 (A), CYC-11 (B) and CYC-12 (C) treated with the indicated concentrations (50- 10- 5- 1- 0.5- 0.1- 0.05 µM), pre-treated with MLN- 4924 (1 µM), and DMSO as vehicle control for 24 h in HEK 293 cells. Tubulin: loading control. Two independent biological replicates.

4.5.4 Degradation assays under cell cycle arrest conditions

CDK2 and Cyclin E are proteins involved in the cell- cycle, specifically in the G_1/S transition phase. Thanks to Prof. Saurin's expertise in CDKs and the collaboration formed during the STSM stay in Dundee with his lab, along with Prof. Ciulli and Galdeano's lab, a cell cycle arrest assay was performed based on his suggestion to study the degradation profiles of Cyclin E and CDK2 during the G_1/S interphase when they are more abundant (Box 2).

Synchronization of the cells is particularly useful for investigating the effect of CDK / Cyclins complexes along the different cell phases, among others. Different techniques can be employed for synchronizing the cells, in this case, with the aim to study the impact on the cell cycle when degrading Cyclin E / CDK2 complex. In this case, the strategy used was based on a double- thymidine blockade which enriches the cells in G_1 / S phase, following the protocol in Chapter 6.2.2.6

It is essential to highlight that the cells underwent two treatments with the PROTAC compound at a final concentration of 5 µM. The first treatment occured during the second thymidine block, when the cells were incubated for 14 hours, and a significant portion was synchronized in G_1/S phase. The second treatment took place after the cells were released from the second thymidine block followed by a PBS wash, to restore the PROTAC levels in the cells and evaluate its effects on subsequent cell- cycle phases (e.g., G2 and M phases). Cells were released in a sequential manner at specific time points: 0 hours (G_1 / S phase), 4 hours (S phase), 6 hours (G2 phase), and 10 hours (M phase). It should also be noted that those assays lasted for one week, and due to time constraints, typically only one independent biological replicate wass performed.

Box 2: CDK-Cyclin complexes key to the control of the cell cycle progression

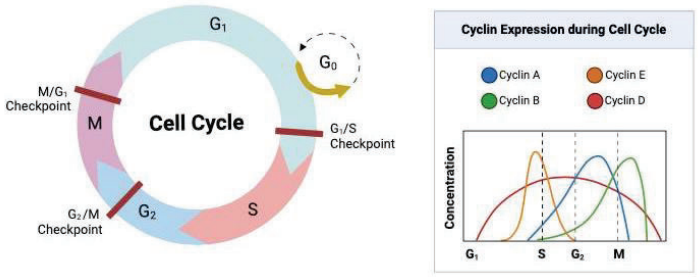

Phases of the cell cycle with the corresponding Cyclins expression (adapted with BioRender.com). [69]

Cell cycle progression is driven by the accumulation of CDKs activity during interphase and M phase. Entry into the cycle is initiated by Cyclin D – CDK4/6 accumulation, which prevents the cell from exiting the cycle. E2F- driven transcription promotes the accumulation of Cyclin E and A, which created a decision window to enter S phase. Cyclin E / CDK2 triggers a positive feedback loop that amplifies Cyclin E and Cyclin A/ CDK2 activity, leading into S phase entry. After S phase, Cyclin A- B/CDK1 then drives the cell into mitosis, where mitotic Cyclins are targeted for degradation to complete a cell- cycle. This interdependence establishes a regulatory network that ensures cell cycle progression occurs in a sequential and unidirectional manner.

Degradation of CRBN- based PROTACs in synchronic state

Degradation of Cyclin E and/or CDK should be first analyzed at 4 hours of thymidine release as the cell is in G_1/S or early S phase with maximum abundance of the POIs. In fact, CYC-1 showed 20- 30 % degradation of CDK2 after 4 hours as well as 6 and 10 hours compared to non-treated cells degradation that correlates with the degradation observed at the third biological replicate of the first screening (Figure 37, A). Regarding CYC-2, 40 % degradation of Cyclin E was observed after 6 hours, showing a higher degradation profile compared to the one detected at the second biological replicate of the first screening (Figure 37, B). However, more independent experiments should be conducted to have a better overview of the MoA of these two PROTAC molecules.

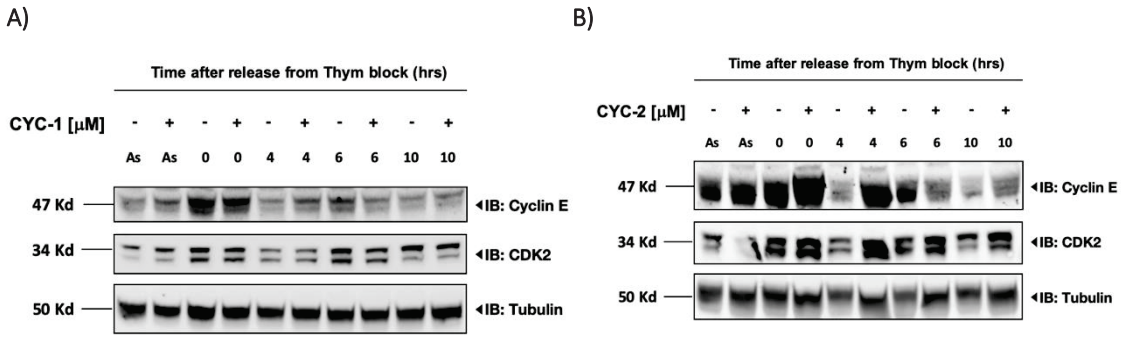

Figure 37: Western blots of CYC-1 (5 μM, A) and CYC-2 (5 μM, B) treatment in HEK 293 cells synchronized by double-thymidine blockade, harvested at the indicted time points after release from the block. ddH_2O as vehicle control. Tubulin: loading control. One-single biological replicate.

Comparing the results with the non- treated cells, 30 % degradation of CDK2 was observed when treating the cells with CYC-3 after 4, 6 and 10 hours, showing consistency with the previous results (Figure 38). Given these significant outcomes, a second biological replicate was performed to confirm the reproducibility of these results. Unfortunately, upregulation of CDK2 was observed, but 20- 40 % degradation of Cyclin E after 4, 6 and 10 hours in both technical replicates. These results did not align with previous findings, and issues related to antibody resolution emerged. It is for that reason that the second biological replicate was not considered, and further biological replicates will need to be performed.

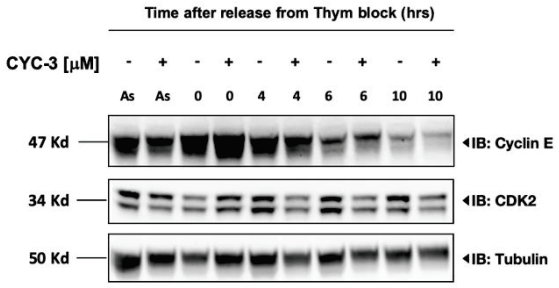

Figure 38: Western blot of CYC-3 (5 µM) treatment in HEK 293 cells synchronized by double- thymidine blockade, harvested at the indicted time points after release from the block. ddH_2O as vehicle control. Tubulin: loading control. One- single biological replicate.

Degradation of VHL- based PROTACs in synchronic state

Screening VHL- based PROTACs in cells with synchronized cell- cycle did not reveal better degradation profiles. CYC-10, showed again a weak 10 % degradation of Cyclin E in consistency with previous findings, while CYC-11 demonstrated a higher degradation level of 20- 40 % of Cyclin E, after 6 and 10 hours for both PROTAC compounds. In contrast, CYC-12 showed a 10- 20 % degradation of Cyclin E, which was not detected in the initial screening (Figure 39). Notwithstanding the observed Cyclin E degradations, the levels remain quite low, and issues with antibody resolution arisen which complicated data interpretation. Thus, further assays need to be performed.

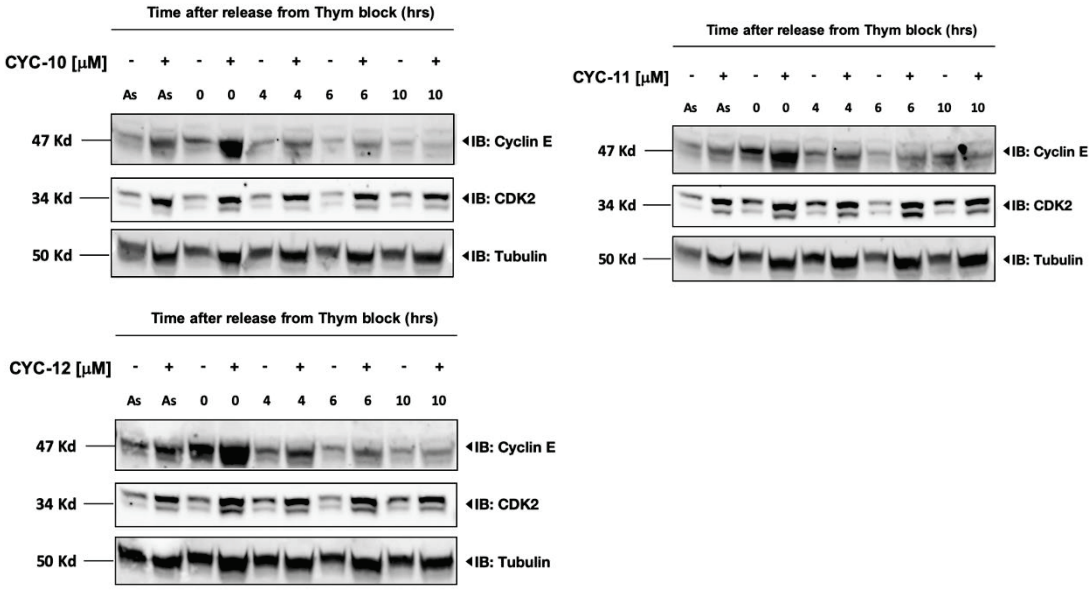

Figure 39: Western blots of CYC-10 (5 µM), CYC-11 (5 µM) and CYC-12 (5 µM) treatment in HEK 293 cells synchronized by double-thymidine bloc, harvested at the indicted time points after release from the block. ddH2O as vehicle control. Tubulin: loading control. One- single biological replicate.

4.6 Discussion

The synthesis of the first series of Cyclin E/CDK2-based PROTACs presented both challenges and successes, particularly regarding yield variations between CRBN- and VHL-based compounds. These molecules were designed using the **ARG-9** ligand for the Cyclin E/CDK2 complex, linked either to **VH032** (VHL) or **lenalidomide** (CRBN) via PEG chains of varying lengths (n = 2, 4, or 6). The CRBN-based PROTACs were obtained in moderate yields. In contrast, the synthesis of the VHL-based analogues proved more challenging, resulting in lower yields due to synthetic complexities related to polarity, solubility, and compound size. Additionally, significant traces of the starting material **ARG-91** remained in the crude products due to incomplete consumption, complicating the purification process. Despite these hurdles, the desired compounds were successfully synthesized.
The degradation profiles of the first series of Cyclin E/CDK2-targeting PROTACs were evaluated across multiple biological and technical replicates under varying cellular conditions (synchronous and asynchronous), complemented by biophysical analyses.

Focusing on the CRBN-based PROTACs (**CYC-1**, **CYC-2**, and **CYC-3**), degradation results for Cyclin E and CDK2 revealed variable efficacy across assays, indicating inconsistencies in degradation activity among these compounds.

CYC-1 induced Cyclin E degradation of approximately 30-40 % in the first biological replicate at concentrations between 10-1 µM. However, in the second replicate, Cyclin E levels remained unchanged, while CDK2 degradation of 20–30 % was observed at lower concentrations (0.1-0.05 µM). These results suggested that **CYC-1** might exhibit inconsistent target selectivity, favoring Cyclin E at higher concentrations in some contexts and CDK2 at lower concentrations in others.

CYC-2 did not show degradation activity in the first replicate but led to a 20 % reduction in Cyclin E levels in the second replicate at 10-5 µM. In the third replicate, 20–30 % CDK2 degradation occurred at concentrations of 0.5-0.05 µM, again highlighting concentration-dependent and replicate-specific effects, similar to **CYC-1**.
More consistent CDK2 degradation was observed with **CYC-3** in two out of three replicates. The first replicate showed CDK2 degradation of 30 % between 5-1 µM and up to 60 % at 0.5 µM. The third replicate also demonstrated 30-40 % degradation in the 10–1 µM range. No degradation was detected in the second replicate, highlighting variable behavior despite promising results in select conditions.

Target engagement (TE) assays supported these findings. High binding in the permeabilized mode reflected the expected strong affinity of CRBN-based PROTACs (**CYC-1, CYC-2, CYC-3**), driven by the **lenalidomide** warhead, for CRBN E3 in the absence of

cellular barriers. However, lower binding in the live-cell mode indicated poor membrane permeability or intracellular limitations. These permeability barriers may explain the inconsistent degradation outcomes, as insufficient intracellular concentrations likely hindered effective Cyclin E and CDK2 degradation. Extending treatment durations, such as to 24 hours, was considered a potential strategy to improve intracellular activity. In contrast, the VHL-based PROTACs (CYC-10, CYC-11, CYC-12) did not demonstrate effective degradation of either Cyclin E or CDK2. Due to limited compound availability, TE assays could not be performed, hindering further evaluation of their efficacy.

To better understand the degradation mechanisms, cell-cycle synchronization experiments were conducted, examining Cyclin E and/or CDK2 levels during the G1/S or early S phase (4 hours after thymidine release), when these proteins peak in abundance. Among the CRBN-based PROTACs, CYC-1 achieved consistent CDK2 degradation of 20-30 % at 4, 6, and 10 hours, aligning with prior observations in the third biological replicate. CYC-2 induced 40 % Cyclin E degradation at 6 hours, corresponding to G2/M phase, suggesting an improved activity profile. Similarly, CYC-3 consistently degraded CDK2 by ~30 % at 4, 6, and 10 hours, reinforcing its promising and more stable degradation capacity.

Regarding the VHL-based series, CYC-10 continued to show negligible degradation activity, consistent with earlier findings. In contrast, CYC-11 showed improved Cyclin E degradation of 20-40 % at 6 and 10 hours, indicating better interaction and suggesting the need for further evaluation across different concentrations. Interestingly, CYC-12 demonstrated 10-20 % degradation of Cyclin E, a result not previously detected in earlier assays, prompting interest in further exploration.

These findings indicate that while some progress has been made in achieving Cyclin E degradation, the overall potency of these VHL-based PROTACs requires further optimization. The low degradation levels and inconsistencies suggest that repeated assays are essential to confirm these results.

To fully understand the degradation mechanisms and improve consistency, additional studies with more biological replicates and refined concentrations are needed. Moreover, further structure optimization of these CRBN- based PROTACs (*e.g.,* SAR of the linker) to improve cell permeability, enhance selectivity and potency could be essential for achieving reliable and reproducible degradation profiles. Also, a 2nd series of Cyclin E/CDK2-based PROTACs utilizing the ARG-15 ligand (K_d = 0.2 ± 0.5 µM), which has a better *Kd* needs to be synthesized, as it is expected to exhibit improved degradation results on Cyclin E and/or CDK2.

4.7 Conclusions

This chapter describes the design, synthesis, and biological evaluation of the first-generation Cyclin E/ CDK2-based PROTACs, developed to address the challenge of targeting Cyclin E, an oncogenic driver traditionally considered undruggable due to its lack of small-molecule binders. By leveraging the natural interaction between Cyclin E and CDK2 during the G1 / S transition, a "bridged PROTAC" strategy is employed to hijack CDK2 for the indirect degradation of Cyclin E.

From the **1st series of Cyclin E/CDK2 PROTACs**, designed with PEG linkers of varying lengths and a derivative of **ARG-9**, **ARG-91**, a total of six PROTAC molecules were successfully synthesized and structurally characterized using both CRBN and VHL E3 ligase ligands

- CRBN-based compounds (**CYC-1**, **CYC-2**, and **CYC-3**) were obtained with moderate yields and VHL-based (**CYC-10**, **CYC-11**, and **CYC-12**) presented synthetic challenges, primarily due to solubility issues, polarity, and purification difficulties caused by incomplete consumption of **ARG-91**. Nevertheless, successful synthesis of all PROTAC compounds allowed their subsequent biological degradation studies.
- Biological evaluation in HEK 293 and HCT 116 cells revealed complex, concentration- and replicate-dependent outcomes, particularly for the CRBN-based PROTACs. **CYC-3** emerged as the most promising, demonstrating consistent **CDK2** degradation of up to 60 % in selected biological replicates. These findings highlight that while degradation of both Cyclin E and CDK2 is possible, reproducibility remains a key challenge, likely influenced by cellular permeability and potentially suboptimal binding affinity, exacerbated by the hydrophilic nature of PEG-based linkers
- NanoBRET® Target Engagement assays provided further insight into the intracellular behaviour of the compounds. Strong binding observed in permeabilized cells confirmed high affinity for CRBN, as expected due to the **lenalidomide** warhead ligand. However, significantly reduced binding observed in live cells suggests that poor permeability or limited intracellular stability may restrict their functional availability, contributing to the inconsistent degradation effects. These observations underscore the importance of optimizing physicochemical properties to enhance cellular uptake and intracellular efficacy.
- Cell cycle synchronization studies revealed that degradation activity was enhanced when the Cyclin E/CDK2 complex was more abundant (G1/S phase). **CYC-1** and **CYC-3** showed consistent CDK2 degradation under these conditions, while **CYC-2** exhibited Cyclin E degradation during later phases of the cycle. These

results suggest that synchronizing cells at defined cycle stages can facilitate more accurate evaluation of PROTAC activity for cell cycle–dependent targets.

- VHL-based PROTACs displayed overall weaker degradation profiles. CYC-10 remained largely inactive. CYC-11 and CYC-12 showed modest Cyclin E degradation under synchronized conditions, pointing to potential for further optimization. Unfortunately, due to limited compound availability, target engagement studies could not be conducted for this series, restricting mechanistic insights.

Together, these results provide a foundational proof of concept for targeting Cyclin E indirectly via Cyclin E / CDK2 complex. Despite synthetic and biological challenges, CYC-3 demonstrates encouraging CDK2 degradation activity. To enhance selectivity, potency, and cellular uptake, further structure- activity optimization is needed. In particular, the synthesis and evaluation of a second PROTAC series incorporating the higher- affinity ARG-15 ligand (*Kd* = 0.2 ± 0.5 μM) is anticipated to improve degradation efficiency and selectivity, especially for Cyclin E. These next steps are critical to advancing the development of effective PROTACs targeting Cyclin E undruggable oncogenic driver.

CHAPTER 5

Design and Synthesis of novel Brd4- targeting molecules with computer assisted FBDD

5. CHAPTER 5: Design and Synthesis of novel Brd4- targeting molecules with computer assisted FBDD

5.1 Development of an automated fragment evolution platform: Validating small-molecule binding to Brd4(BD1)

In this framework, two PhD students of the BarrilLab in collaboration with the GaldeanoLab, Dr. Moira Rachman and Dr. Serena Piticchio, worked in the development of a fragment evolution platform able to generate new chemical entities by exploring the chemical space, given the binding mode of a fragment. The platform is able to produce non- obvious fragments that maintain or improve affinity for the target, but raising the possibility to obtain new entities as starting point for lead optimization or with better physicochemical properties compared to the identified fragments.

The primary goal was to identify novel scaffolds for Brd4(BD1) and validate an automated protocol by using a well- characterized fragment known to bind Brd4(BD1) as a reference. Many studies in the literature report on Bromodomain inhibitors featuring diverse chemical scaffolds. Most of these inhibitors interfere with the critical interaction between acetylated lysine on histones and Asn140. One such example is fragment **1XA** (PDB 4RL6), which has an IC_{50}= 33 μM. [187] By applying the automated fragment evolution platform, beginning with fragment **1XA**, the protocol searched for a database for chemically related molecules of slightly larger size. These were then tethered and docked to the target protein to identify compatible candidates. The DUck tool was applied to filter out false positives, and the top candidates were selected. This process was repeated iteratively to yield drug-sized molecules (**Figure 40**). [188]

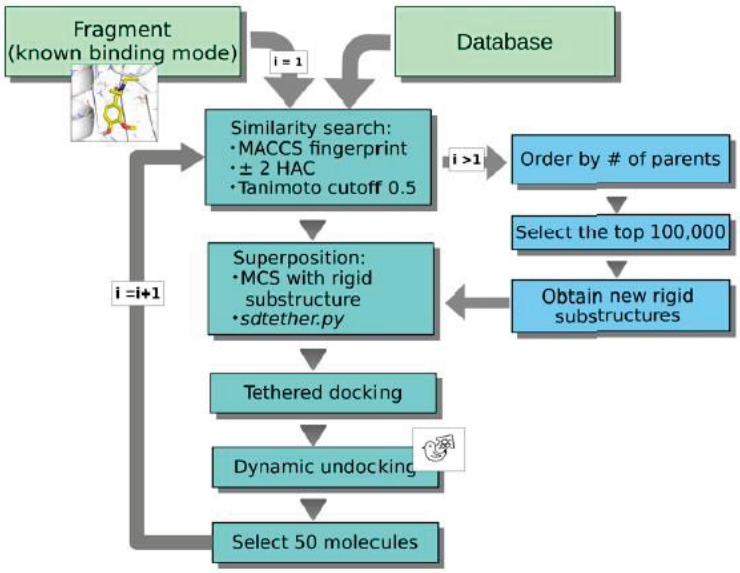

Figure 40: Flowchart of the fragment mining platform from [188]. In the first iteration (i = 1), five distinct computational steps (green-shaded boxes) sample the chemical space around the input fragment, identifying a set of 50 diverse analogues with maximal binding probability.

From the fragments identified by the automated platform with the different iterations, twenty- three out of these fragments were commercially available and six required *in-house* synthesis. At the end, four fragments with 5-phenylthiazolo[2,3-*c*][1,2,4]triazole scaffold with a substituent at the 3-position were synthesized [188] by Dr. Salvatore Scaffidi (who also led the biophysical assays along with Dr. Miriam Martinez) from the GaldeanoLab, and Dr. Sergio Rodríguez-Arévalo from Prof. Carmen Escolano's group (Scheme 11).

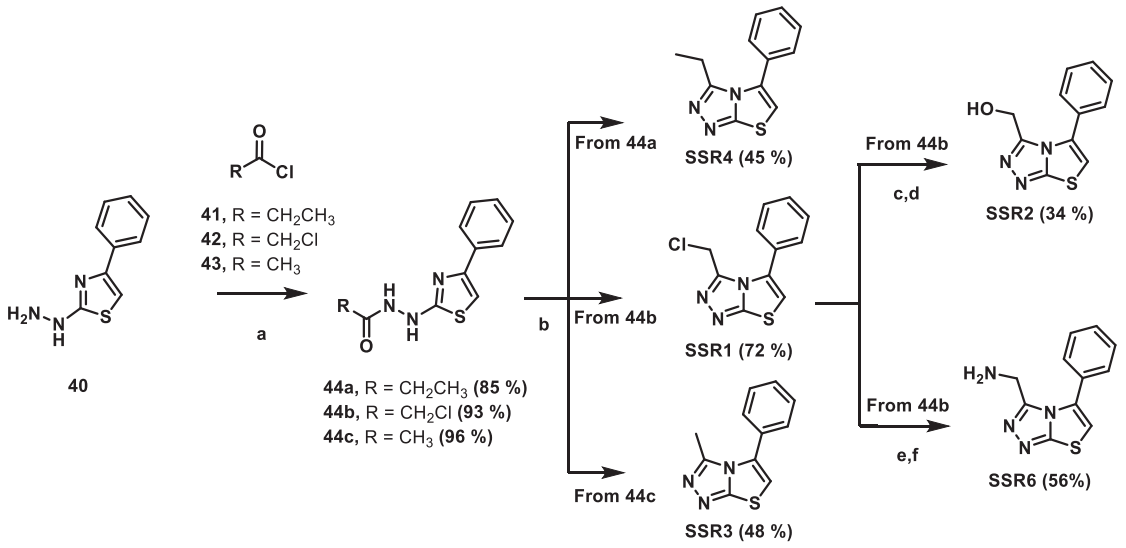

Scheme 11: Synthetic route of SSR1, SSR2, SSR3, SSR4 and SSR6[a].

[a] *Reagents and conditions:* (a) THF, 0º C, 30 min; (b) $POCl_3$, xylene, 110 ºC, 4 h; (c) AcONa, NaI, DMF, 100 ºC, 2 h; (d) NaOH 3N, MeOH, reflux, 15 min; (e) NaN_3, DMF, 50 ºC, 2 h; (f) PPh_3, THF / H_2O, 65 ºC, 2 h.

After performing Time- Resolved Förster's Resonance Energy Transfer (TR-FRET) experiments, three compounds showed better potency compared to the starting fragment, **1XA**, capable of displacing the peptide at a concentration < 50 µM. To know the binding mode of the new compounds, X- Ray structures were solved. **SSR4** (IC_{50} = 26 µM), resulted in the most active fragment when disrupting the interaction between Brd4(BD1) and the peptide (**Figure 41**).

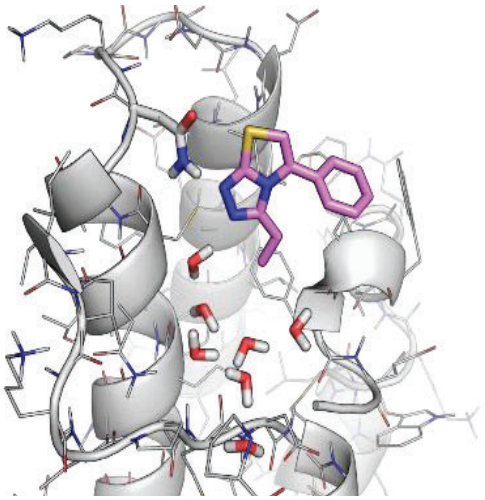

Figure 41: X- Ray structures of **SSR4** in complex with Brd4(BD1) (PDB 6ZF9). [188]

The platform allows for iterative use, enabling the gradual expansion of the initial fragment. It employs populations of compounds to focus the exploration on areas of chemical space where higher- scoring molecules are more likely. As demonstrated in the prospective example with Brd4(BD1), this approach achieves high hit rates and often converges on advantageous scaffolds. In particular, the bicyclic 5–5 fused ring system represented by **SSR4**, which is a completely novel scaffold for this target with excellent development potential to investigate in future works. Notwithstanding, it should be noted that, in its current implementation, the platform cannot be used for fragment growth.

5.2 Fragment-based Drug Discovery (FBDD) approach

Introduced in the pharmaceutical industry in the late 1990s, fragment-based screening has rapidly proven to be a robust and effective approach for identifying high- quality hits against protein targets. This method is now also widely recognized for evaluating target druggability both *in vitro* and in whole cells. [189,190]

Fragment-Based Drug Discovery (FBDD) is a leading approach for assessing protein-protein interactions, complex multi -targets, intrinsically disordered proteins, and other unconventional targets where traditional high- throughput screening (HTS) of larger libraries has been less successful. [191] A key advantage of FBDD is its ability to explore a significantly larger chemical space compared to HTS. The potential number of small, drug-like molecules is estimated at approximately 10^{63}, while current HTS libraries, containing around 10^6 small molecules, cover only a small fraction of this chemical space. [192, 193] Therefore, libraries containing billions of drug-sized molecules will need to be screened to improve the likelihood of discovering effective small molecules.

Instead, FBDD involves screening smaller libraries composed of smaller compounds (Figure 42, A). Fragments typically adhere to the 'Rule of Three,' meaning they have a molecular weight < 300 Da, fewer than three HBD and HBA, fewer than three rotatable bonds, and a cLogP of three or less. Compared to drug- like molecules, fragments are generally less complex but provide broader coverage of chemical space (Figure 42, B). This enables fragments to interact with a wider range of sites and proteins, which is especially advantageous for tackling challenging targets. However, fragments can also be less specific in their interactions. While fragment hits are weak binders, they need to form high- quality interactions with the target to achieve detectable binding affinity. Consequently, the ligand efficiency (LE) of fragments is often higher than that of initial drug- like hits. [190, 191]

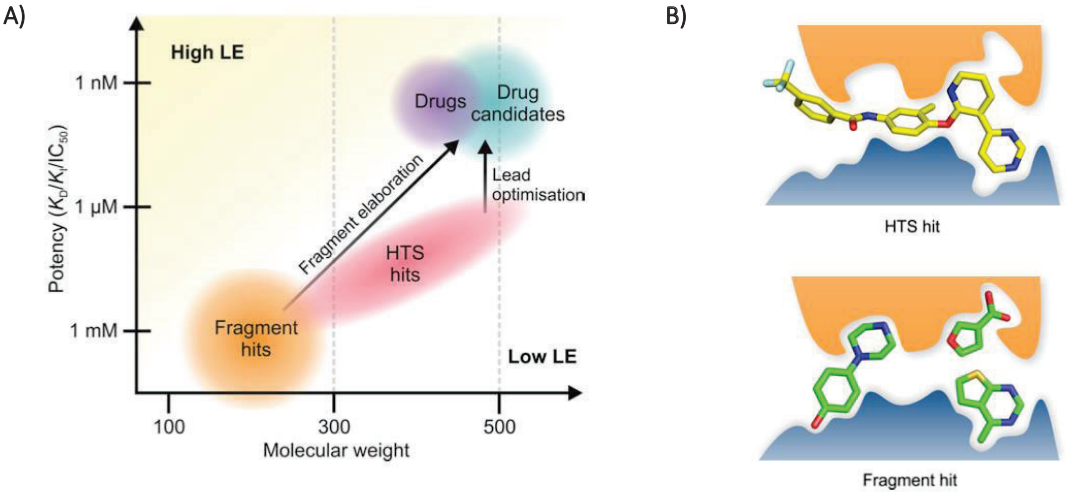

Figure 42: A) Representation of a comparison of molecular mass vs potency for leads developed using conventional HTS and FBDD approaches. The dashed lines represent the molecular weight cutoffs: 500 Da according to Lipinski's Rule of Five and 300 Da according to the Rule of Three. B) Illustration of HTS and fragments hit interactions. Data from [191].

The main challenge remains with the optimization process to achieve more potent compounds. Thus, three different strategies are used: fragment *merging* which combines distinct regions of overlapping molecules into a single compound; *linking*, where separate molecules that bind to non- overlapping sites in close proximity within the same protein are joined to form a larger compound; and *growing,* the most widely used method in FBDD which involved expanding molecules through chemical synthesis to add further binding contacts, enhancing their fit within the target cavity and improving drug- ike properties. [194]

5.2.1 Targeting bromodomains epigenetic proteins

Epigenetic proteins are intently pursued targets in drug discovery due to their role in regulating numerous cellular processes. [195] Epigenetic regulation is largely driven by chemical modifications on DNA and post-translational modifications (PTMs) on histones, such as acetylation, methylation, and phosphorylation. [196, 197] Consequently, targeting epigenetic proteins has become an expanding focus within medicinal chemistry and drug discovery. [198]

In eukaryotic cells, sequence-specific DNA-binding transcription factors activate target genes by recruiting multi- subunit coactivator complexes that utilize various biochemical mechanisms to activate RNA polymerase II. A key class of coactivators exhibits lysine acetyltransferase activity, transferring acetyl groups from acetyl- coenzyme A to the ε-amino group of lysine residues (KAc) on different substrate proteins. This acetylation of KAc is one of the most prevalent modifications on histone tails and is reversibly regulated by histone acetyltransferases and deacetylases, which respectively add and remove these PTMs. [199, 200] Dysregulation of these processes has been linked to diseases, including cancer, which has direct connections to epigenetic regulation, as well as inflammation.

The most well- established context- specific molecular readers of acetyl- lysines in histone tails are Bromodomains, present on 46 different proteins encoded in the human genome. [201, 202] Bromodomains, known as epigenetic readers, are a conserved family of 110 amino acid modules found in histone acetyl transferases and other chromatin- associated proteins and transcriptional regulators. Based on sequence similarity, the whole human family of Bromodomains can be divided into eight diverse subfamilies which contain at least three Bromodomains and comprising proteins of diverse functions. The Bromo and Extra- Terminal domain (BET) subfamily, which comprises four members in humans (Brd2,

Brd3, Brd4 and BrdT), take their name from the presence of two related tandem Bromodomains named BD1 and BD2, able to specifically recognize different acetylation patterns in H3 and H4 histone tails. [203]

Even though they show a low overall sequence identity (21 %), all Bromodomains are composed of a conserved left- handed bundle of four alpha helices (named αZ, αA, αB and αC) with other interhelical loops (**Figure 43**). Two of them (ZA and BC) belong to the KAc binding site, which contributes to substrate specificity. [204] This binding site has five waters structures at the bottom of it, which forms hydrogen bonds with protein residues.

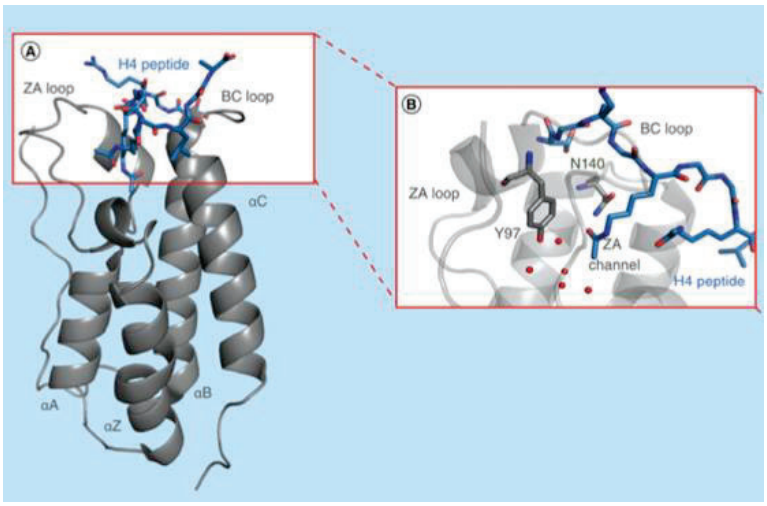

Figure 43: Structure and molecular recognition of BET bromodomains. **A)** X- Ray structure of the di-acetylated H4 peptide (double acetylation at H4K5acK8ac, in blue), bound to the BET bromodomain Brd4(BD1) in grey, PDB 3UVW). **B)** Highlighted the conserved Y97, N140 and the ZA channel of Brd4-BD1(PDB 3UVW). Adapted from [205].

Moreover, crystal structures with bound histone and substrate peptides reveal that KAc is recognized in a hydrophobic pocket, anchored by a conserved hydrogen bond between its amide side chain and the amide of a conserved Asn residue. Additionally, a water-mediated hydrogen bond is formed with the hydroxyl group of a conserved Tyr residue, both located at the base of the ZA loop in bromodomains. [206] In many Bromodomains, including the BET subfamily members and a few others, a conserved stretch of three amino acids known as the 'WPF shelf' is found. Its presence or absence can be explored to achieve selectivity between BET and non- BET- Bromodomains. [207]

The description of BET proteins suggests a role of these regulators in transcriptional control, particularly since acetylated TFs and histones are found at all active promoters and enhancers in the genome. Bromodomain- containing proteins (BCPs) are often deregulated in disease, and their Bromodomains appear to have crucial roles to disease

mechanism. [208] For this reason, the development of Bromodomain inhibitors for drug discovery purposes is spurred. [209,210]

The first class of highly potent and selective BET Bromodomain inhibitors were a series of thienotriazolodiazepines. (+)-JQ1 and iBET-762 demonstrated on- target activity *in vivo*, with effective in NUT midline carcinoma models and inflammation models, respectively. [211, 212] These discoveries demonstrated the high druggability of the Bromodomain-KAc interaction and motivated further drug development efforts in this area.

In the past five years, BET inhibitors have shown efficacy in numerous preclinical models of solid tumors. Noteworthy, deregulation of Brd4 has been strongly linked to acute myeloid leukemia, ovarian carcinoma, chronic obstructive pulmonary disease and other inflammatory processes. [213-216] However, despite demonstrating antitumor activity by blocking Brd4 binding to acetylated- lysines on histones, these inhibitors face challenges such as off- target effects and drug resistances. [217]

A more recent innovation in BET inhibitor design has been the use of PROTAC approach to conjugate (+)-JQ1 with chemical moieties that promote recruitment of E3 ubiquitin ligases. This catalytic mechanism allows PROTACs to induce more potent and sustained degradation of Brd4 compared to conventional inhibitors. Prime examples are MZ1 and ARV-825 degraders, which have shown significant efficacy in preclinical models, demonstrating potent anticancer effects by inducing selective degradation of Brd4. [205, 218]

Also, Brd4 has attracted enormous attention as a promising molecular target for cancer therapy in recent years because pharmacological inactivation of Brd4 was shown to remarkably suppress expression of the cMyc oncogene. [219-221] Thus, the pharmacological inhibition of Brd4 represents a promising indirect anticancer strategy to inhibit the hyperactive cMyc in tumors.

5.2.2 Exploring the chemical space of Brd4(BD1)

Computational methods can also help identify less obvious fragment candidates and guide their development into potential drug candidates. As previously stated, to increase potency in drug discovery, combining fragments that bind to the same cavity in different subpockets, or binding fragments in new ways, can be effective. [222] This strategy, known as *linking or merging*, combines parts of different molecules to amplify their binding affinity. However, a challenge lies in preserving the optimal orientation of each fragment when linking them together. Alternatively, *fragment growing* adds chemical groups sequentially to an initial fragment, capturing additional interactions within the

binding site. This approach, called "Fragment-to-Lead" (F2L), requires monitoring LE to ensure it does not decrease significantly during growth.

Without computational assistance, F2L can be a lengthy process for medicinal chemists. To address this, various computational tools have been developed in the past 15 years specifically to aid fragment growing and optimization, leading to an increase in F2L applications. [223]

On a prospective application, Bromodomains have proven to be highly ligandable targets and to be particularly suitable for biophysical fragment screening. For this reason, from a drug discovery perspective, epigenetic proteins are highly sought- after targets in medicinal chemistry and drug discovery. From the structural point of view of Bromodomains, crystallographic studies describe five water molecules as an integral part of the acetyl- lysine binding pocket, which are essential for its druggability and functional part of the protein. [205]

5.2.3 Fragment- to- Lead Approaches: *In silico* synthesis

Another option for F2L is to create new chemical space. De *novo* drug design methods are a useful computational tool in this endeavor. Developed around 30 years ago, these programs are designed to generate new molecules based on an initial ligand with a known binding mode. Typically, this binding mode is experimentally determined, but when it is not available, tools like docking programs or molecular dynamics simulations can position the fragment within the cavity. [223] The target structure acts as a template, enabling molecules to be constructed directly within the binding site and allowing affinity calculations to occur in real-time. Scoring functions used can be force field- based, [224] empirical, [225] or knowledge- based. [226] Additionally, ligand- based restraints are sometimes applied. When active ligands are known, they can be utilized to create 2D or 3D pharmacophores that guide the design of new molecules by retaining key structural features. [227, 228] De *novo* design programs grow molecules either atom- by- atom or through fragment-based methods. Modern programs favor fragments, derived from existing drugs or commercial sources, for manageable synthesis and efficient exploration of chemical space. [229, 230]

In silico synthesis is a computational approach that assembles functionalized building blocks using reaction rules modeled on real-world chemistry. This method not only ensures the generated molecules are synthetically feasible but also provides potential synthetic routes. [227, 231, 232] Given the immense chemical space, exhaustive searches are employed to find solutions efficiently. In an iterative process, candidate compounds are generated, evaluated, and the best-performing ones are selected as "parents" for the

next generation. Through mutations (small changes) and crossover (recombining parts), "children" compounds are created and similarly evaluated. This cycle repeats, refining molecules over time until reaching a desired endpoint. Stochastic methods may yield different solutions each run, so secondary constraints like Lipinski's rules, solubility, ADMET properties, and synthetic feasibility are often applied to narrow the search space. Multi- objective optimization tools are particularly valuable, as they balance primary objectives with these additional factors during the selection process. [233, 234]

Synthetic accessibility is crucial when designing novel molecules, as compounds that cannot be synthesized are practically unusable. Rather than assessing synthetic feasibility only at the end of a process using scoring methods, it is far more effective to incorporate synthetic accessibility considerations into the generation process itself. This approach actively guides the search towards molecules that are not only theoretically effective but also practically synthesizable, improving the likelihood of successful development. [235]

In silico synthesis with NAOMinext Software

Programs that perform virtual synthetic reactions as a growing strategy is NAOMinext, [236] a program developed in the group of Prof. Matthias Rarey (University of Hamburg, Germany) where Dr. Serena Piticchio from the BarrilLab did an internship stay.

NAOMInext enables "constrained synthetically feasible fragment growing" by virtually attaching building blocks to a fragment within its crystallized structure in the protein. Using 58 predefined virtual reactions, termed "Reaction SMARTS," the program identifies compatible reactions and matches building blocks from the library. After the virtual reaction, various conformations of the newly attached section are generated and scored, selecting the top-scoring conformation as the final pose. This process achieves three objectives: (1) fragment growth, (2) synthetic feasibility via rule-based reactions, and (3) optimal conformational fit within the protein cavity. The top-ranked compounds can then be prioritized for laboratory synthesis.

In this framework, NAOMINEXT program is used to do a fragment growing with a *de novo* approach on compound SSR4, using the crystal obtained in the previous study (PDB 6ZF9) for the correct pose of the ligand, to increase its affinity by adding more functional substituents.

5.3 Specific objectives of Chapter 5

The following specific objectives were established:

iii. First, the **design and synthesis of novel SSR4- derivatives** following a hit- to- lead approach, aiming to improve **SSR4** binding affinity and explore its chemical space, by incorporating available amine building blocks through proposed amine coupling reactions.
   - **Functionalization of SSR4:** synthesis of **AS-10** and **AS-11** as a result of **SSR4** compound functionalized with an additional bromine atom at the *meta* or *ortho* position of the phenyl ring.
   - **Synthesis of SSR4 derivates** as the potential lead compounds following the proposed amine cupling reactions by NAOMInext, including Cu- catalyzed Ullmann cross- coupling reaction and Pd-catalyzed Buchwald-Hartwig approach.
   - **Characterization and evaluation of SSR4- derivatives** binding to Brd4(BD1) through TR-FRET competition orthogonal assay.

iv. Second, the **optimization and synthesis of SSR12**, **SSR4-** derivative lead, aiming to further enhance ¡ binding affinity by incorporating two modifications proposed by NAOMInext software based on its predicted binding at the *meta* and *ortho* positions, respectively.
   - Synthesis of **AS-5**, featuring a methyl group in the *meta* position, and compound **AS-6**, incorporating a chlorine group in the *ortho* position
   - **Characterization and evaluation of SSR12- derivatives'** binding to Brd4(BD1) via TR-FRET competition orthogonal assay.

With these objectives, we aim to identify lead candidates with enhanced potency, expanding the chemical space of Bromodomains inhibitors scaffold. By applying a combination of computational design and synthetic chemistry, we aim to validate the NAOMInext software for fragment *growing* and to optimize the synthesis and binding affinity of novel **SSR4** derivatives targeting Brd4(BD1).

5.4 Design and synthesis of SSRN lead compounds

SSR4 fragment serves as the starting point for a fragment- growing strategy using an *in silico* synthesis to enhance its potency. To achieve this, the NAOMInext program is employed to computationally explore the addition of functional substituents and guide the synthetic expansion of SSR4.

Despite the advantages of NAOMInext in proposing synthetically feasible fragment-growing strategies, the program does not directly recognize SSR4 as a reactive fragment. To overcome this limitation, a bromine group is introduced at the *meta* and *ortho* positions of the SSR4 phenyl ring, synthesizing two key intermediates: AS-10 (*m*-bromo) and AS-11 (*o*-bromo). These brominated analogs serve as vectors for further structural elaboration, as the crystal structure (PDB 6ZF9) indicates that other positions are sterically hindered by a tryptophan residue or the cavity wall (Scheme 12).

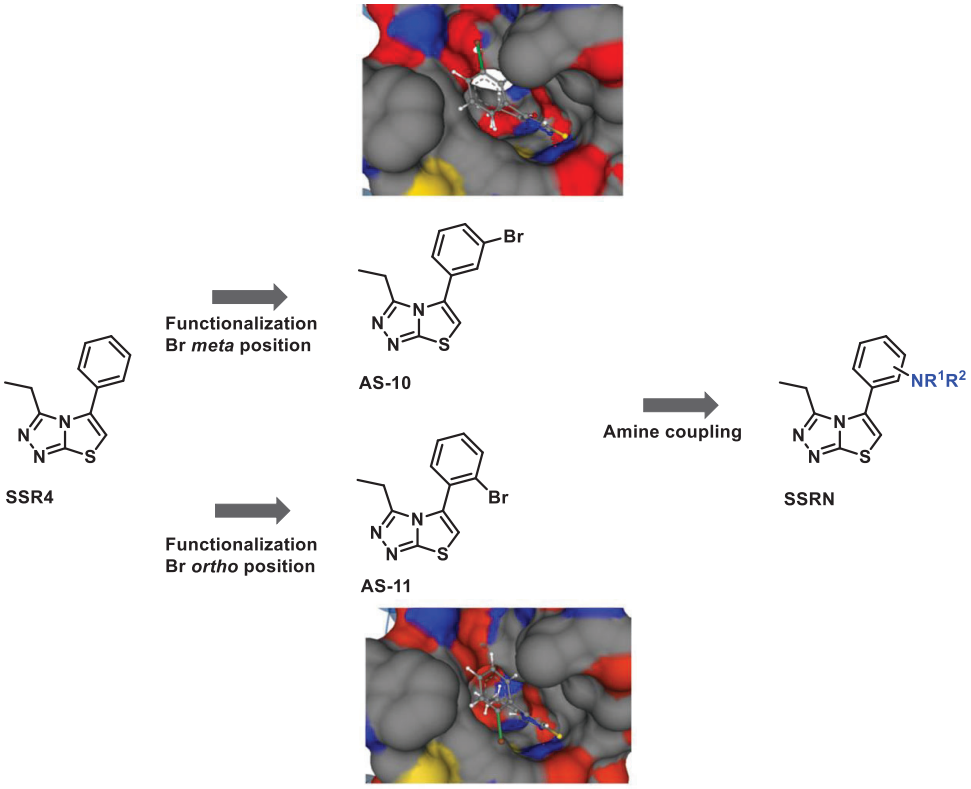

Scheme 12: Overview of SSR4 hit-to-lead optimization approach, with AS-10 (m-Br) and AS-11 (*o-Br*) as key intermediates with their predicted poses, followed by the synthesis of SSR4 derivatives through amine coupling to synthesize SSRN lead compounds.

Functionalization of SSR4: Synthesis of key intermediates AS-10 and AS-11

The synthesis of **AS-10** and **AS-11** intermediates follows the same methodology used to obtain **SSR4** [188], as the bromine group does not interfere in the previous reaction steps (**Scheme 11**). The initial step involved a Hantzsch- type cyclodehydration [175] between **45** and the corresponding bromoacetone derivative, 2-bromo-1-(3-bromophenyl)ethan-1-one **46** and 2-bromo-1-(2-bromophenyl)ethan-1-one **47** to give ***m*-1** and ***o*-1**, respectively, which were brought to the next step without further purification (**Scheme 13**). [237, 238]

This cyclodehydration of thiosemicarbazides with bromoacetophenones is a reaction used to synthesize heterocyclic compounds, particularly thiazole derivatives. Generally, it follows a mechanism where the thiosemicarbazide reacts with the bromoacetophenone to form a thiazole ring structure. The process typically involves the nucleophilic attack of the sulfur atom in the thiosemicarbazide on the carbonyl or electrophilic center of the bromoacetophenone, leading to the formation of a thiazole ring with the concomitant elimination of a proton (in an acidic medium) and bromoacetophenone derivatives. [175]

Following an acylation of the hydrazine with propionyl chloride **41**, intermediates ***m*-2** and ***o*-2,** were obtained, respectively, which were brought to the next step without further purification. [239] Finally, an intramolecular cyclization with $POCl_3$ at high temperatures gave **AS-10** and **AS-11** with an overall yield of 19 % and 16 %, respectively (**Scheme 13**). [240, 241] The main function of reagent $POCl_3$ is to give reactivity to the amide, which is very stable due to its resonance with the nitrogen. Thanks to this activation, the intermediate chloroimine is less stable than the previous amide, having the heterocyclic nitrogen enough capacity to react with the imine carbon and form a new cycle giving the desired heterocycle product.

For the synthesis of **AS-11**, the first and final steps were optimized and conducted under microwave conditions. The presence of a halogen at the *ortho* position introduces steric hindrance, which was effectively alleviated through microwave- assisted synthesis (**Scheme 13**). This strategy also shortened reaction time and enabled the use of greener solvents. [238, 241] Conversely, repeated attempts to apply the same conditions to the final step of **AS-10** synthesis prove unsuccessful, with no detectable product formation.

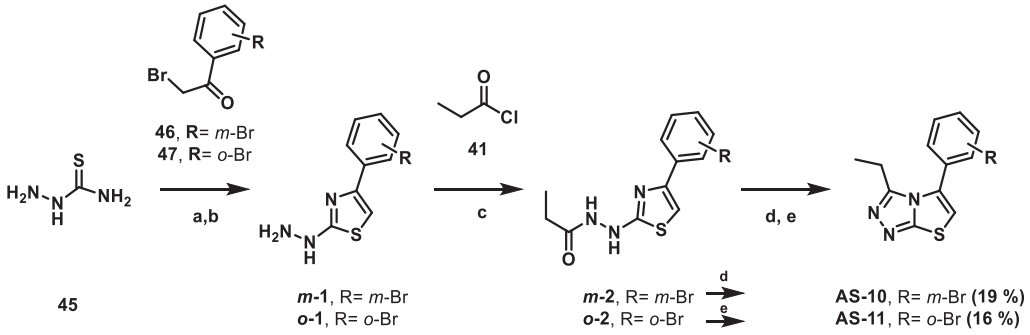

Scheme 13: Synthesis of AS-10 and AS-11. Microwave conditions (M/W)[a].
[a]*Reagents and conditions:* (a) Dioxane, r.t., overnight; (b) MeOH anh., 90 ºC, 20 min, M/W; (c) THF, 0º C, 30 min; (d) $POCl_3$, Xylene, 130 ºC, overnight; (e) $POCl_3$, solvent free, 150 ºC, 150 min, M/W.

Using AS-10 and AS-11 as starting points, NAOMInext proposed a set of feasible *C-C* and *C-N* bond- forming reactions, including Suzuki, Negishi, Heck, Stille, Grignard, Sonogashira, Buchwald- Hartwig, and decarboxylative couplings. Given that all these methodologies rely on halide- containing reactants, the bromine substituents enable efficient coupling with diverse functional groups. To streamline synthesis while maintaining structural diversity, only derivatives generated via Buchwald- Hartwig amine coupling reaction were selected for experimental validation. This decision was based on synthetic feasibility, the availability of intermediates and reagents, and the need for a single, scalable synthetic procedure. After computational re-scoring, 7508 potential derivatives were identified for AS-10 and 7346 for AS-11. Since the selected compounds were not commercially available, their synthesis was planned *in-house* as part of the hit-to-lead optimization strategy with the aim to enhance the binding affinity of SSR4 derivatives by introducing optimized functional groups while ensuring synthetic accessibility.

In this framework, the first batch of synthesized compounds incorporated amines with varying aromaticity, stability, reactivity, and electronic properties, coupled to AS-10 and AS-11, yielding the respective SSRNM and SSRNO potential lead compounds. Based on the binding poses of the lead compounds and their synthetic feasibility, a total of seven amine building blocks are selected for the *meta* position (Figure 44, A), while eight amines are chosen for the *ortho* position from the initially proposed set (Figure 44, B).

A)

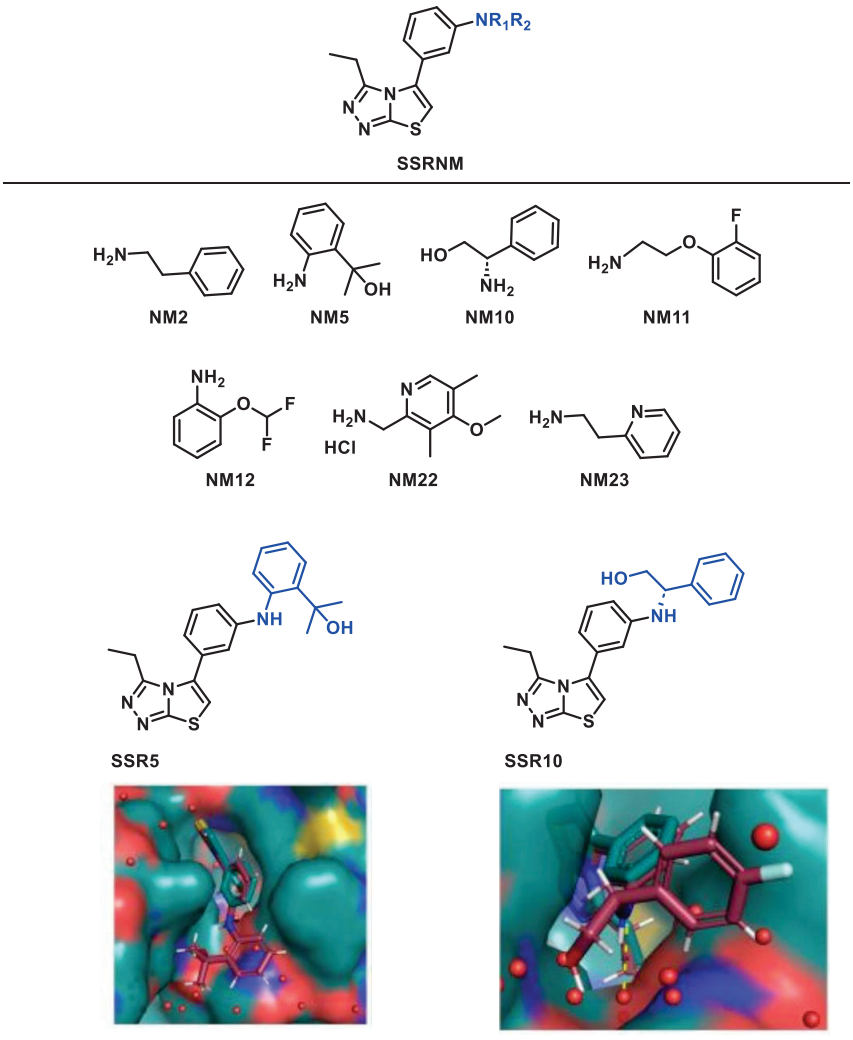
NR1R2
SSRNM
NM2
NM5
NM10
NM11
NM12
NM22
NM23
SSR5
SSR10

B)

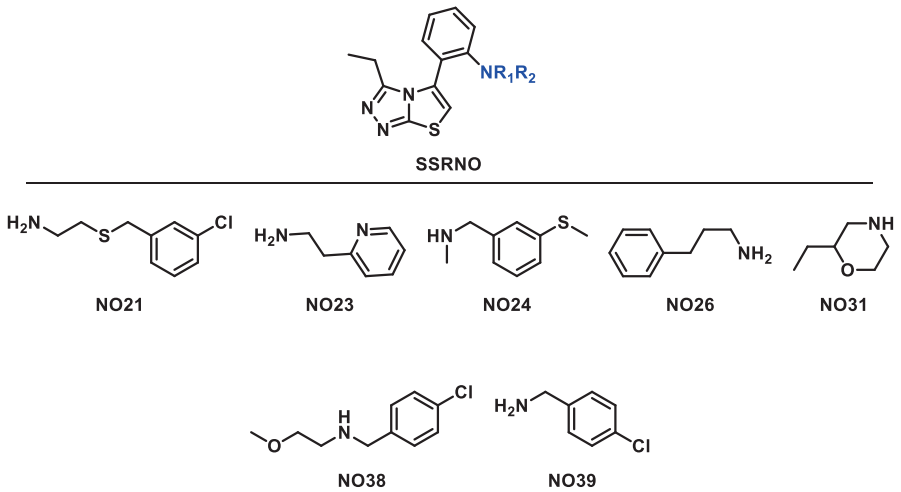
NR1R2
SSRNO
NO21
NO23
NO24
NO26
NO31
NO38
NO39

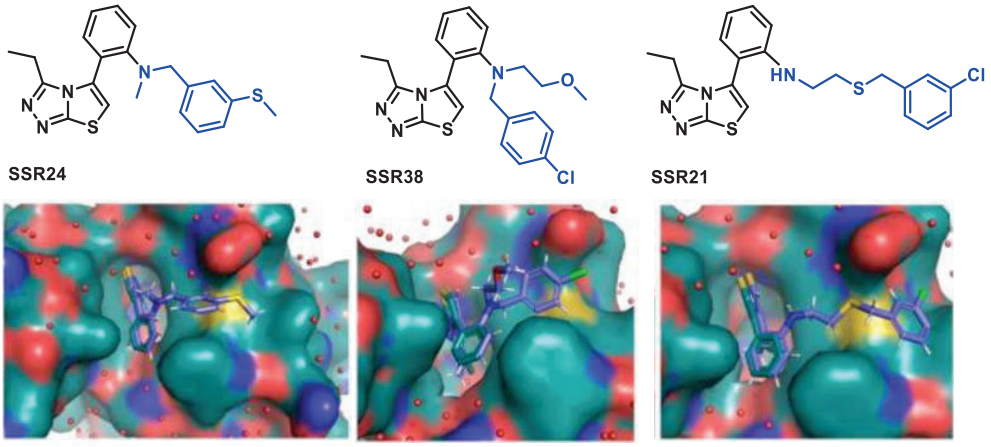

Figure 44: Selected amines and predicted binding poses of lead compounds: **A)** amino substituent in the *meta* position of the phenyl ring and **B)** amino substituent in the *ortho* position of the phenyl ring.

Previous results: Cu-catalyzed Ullmann cross-coupling approach

As previous results, Dr. Sergi Rodríguez-Arévalo, from Prof. Carmen Escolano's group, conducted several attempts to synthesize the proposed **SRNM** compounds through the Cu- catalyzed Ullmann cross- coupling reaction, which allowed efficient coupling of aryl halides with amines. [243] Also, the relatively low cost and low toxicity of Cu, the use of cheap and low molecular weight ligands, and good functional group tolerance made the reaction an attractive method to synthesize the proposed compounds.

Ultimately, he successfully synthesized compounds **SSR11** and **SSR12** [244, 245] by using CuI as catalyst and potassium carbonate (K_3PO_4) as base at 100 ºC, with low yields highlighting the synthetic challenges associated with **AS-10** amine-couplings (**Scheme 14**). The use of ligand-assisted methods, such as salicylic acid amides (*e.g.*, *N,N*-Diethylsalicylamide) in **SSR11** synthesis, further enhanced the catalytic system, improving reaction efficiency and minimizing excess amine under mild conditions.

Then, TR-FRET assays were performed by Dr. Andrea Bertran, from the GaldeanoLab, to test the inhibitory activity of both compounds. Surprisingly, both compounds showed an improvement in terms of potency: **SSR11**, IC_{50} = 10 µM; and **SSR12,** IC_{50} = 0.1 µM; compared to the initial hit **SSR4** (IC_{50} = 26 µM). Remarkably, **SSR12** showed a 650n-fold potency jump in affinity.

The binding modes of the two molecules differed significantly (**Scheme 14**). **SSR11** displaced two water molecules (W1 and W2) in the ZA channel, replacing one of W1's interactions with the protein by forming a bond between the oxygen of its methoxy group and the protein. Additionally, **SSR11** interacted with another water molecule (W3). In contrast, **SSR12** interacted with W1 and W2 while displacing W3. Although the two

molecules contain very similar chemical components, their differing distributions critically impact affinity, underscoring the importance of ligand architecture. The significance of water molecules in the ZA channel has been previously established, [205] and our findings further confirm that using these water molecules as bridges between the ligand and protein is preferable to displacing them. This highlights the necessity of considering not only "structural" water molecules during ligand design but also the first solvation layer of the protein. Even when solvent-exposed, such water molecules, particularly those interacting with protein hotspots, can significantly contribute to the free energy and enhance ligand-protein binding.

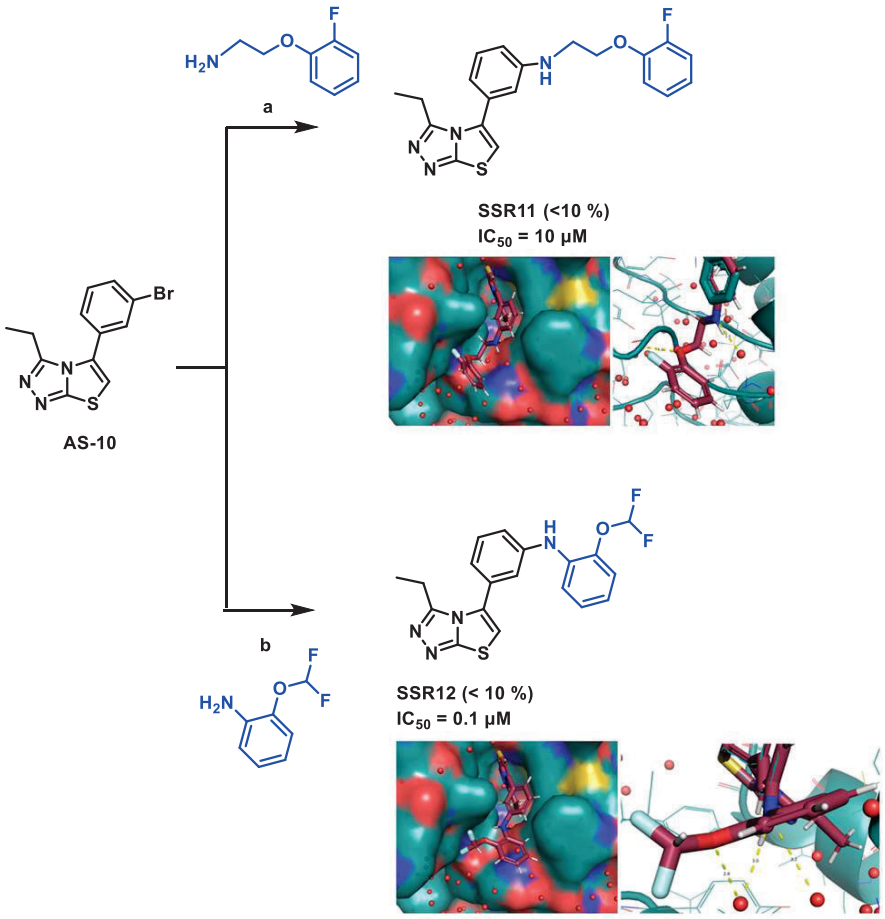

Scheme 14: Synthesis of **SSR11** and **SSR12** *via* Cu-catalyzed Ullmann cross-coupling with their predicted binding poses[a].

[a]*Reagents and conditions:* (a) CuI, *N,N*-Diethylsalicylamide, K_3PO_4, DMF anh., 100 ºC, overnight; (b) CuI, Pyrrole-2-carboxilic acid, K_3PO_4, DM anh., 100 ºC, overnight.

Pd-catalyzed Buchwald-Hartwig approach

Given those results and the structural complexity of the scaffold, the Pd-catalyzed Buchwald-Hartwig cross-coupling was proposed as an alternative strategy, which aligned with the NAOMInext software's preference for efficient *C-N* bond formation with the aim to address the challenges encountered in previous reactions, providing a more effective route to the desired SRNM compounds.

The Buchwald- Hartwig approach is widely recognized for facilitating aryl-amination reactions *via* Pd- catalyzed cross-coupling between an amine and an aryl halide, as supported by precedent literature (Scheme 15). [246] The catalytic cycle begins with the reduction of Pd(II) to Pd(0) by a ligand, followed by oxidative addition of the aryl halide to form a Pd(II) complex. Subsequently, the amine undergoes nucleophilic attack on the palladium center, leading to the formation of the desired product through reductive elimination, which regenerates the Pd(0) catalyst and completes the cycle. However, despite the advantages of this approach and the proposed synthetic strategy, several challenges arise in the synthesis of the new amine derivatives.

- Ligand: different ligands such as *rac*-BINAP and JohnPhos are tried but no product formation is observed. It is important to choose the right coordinating ligand according to the type of nucleophile you want to couple (primary, secondary, aliphatic, aniline derivatives) and Pd catalyst of use.
- Substrate: The scaffold of SSR4 contains a sulfur group, which, based on similar issues encountered by other members in the lab, is hypothesized to potentially poison the Pd catalyst. This interaction could prevent the oxidative addition step, hindering the reaction from proceeding as expected. This issue highlights the challenges in achieving efficient Pd-catalyzed reactions when functional groups may interfere with the catalytic cycle.
- Base: Several attempts varying the equivalents and bases (tBuONa, K_2CO_3, K_3PO_4) are performed, but no product formation is observed. It is crucial to identify an effective base to activate the proposed amine and facilitate the amination reaction.

Here, we outline the various unsuccessful reaction conditions tested for the coupling of AS-10 and AS-11, highlighting key challenges such as catalyst poisoning, ligand selection, and base choice (Table 4). [246-248]

From the table, it is evident that *Entries 1–11* focused on coupling AS-10 to different nucleophiles (*e.g.,* aniline, NM1, NM11, NM12) across a range of Pd catalysts and ligands. The consistent failure of these reactions suggested that the electronic and steric properties of AS-10 significantly hinder its reactivity under Buchwald–Hartwig conditions.

Similarly, *Entries 12–14* explored modifications of AS-11 using nucleophiles such as NO21 and NO24, but those also failed, further supporting the notion that the *ortho*-bromo substitution introduces steric hindrance and reactivity limitations (Table 4).

These failed attempts underscore the complexities in optimizing reaction parameters and the difficulties in achieving efficient product formation. Despite systematically varying key components, including the Pd source, ligand, base, and amine nucleophiles, no successful coupling was observed.

The choice of ligand had a particularly significant impact on reactivity. Despite screening several commonly used ligands—*rac*-BINAP, JohnPhos, PPh_3, and DPPF, none facilitated productive coupling, suggesting that the coordination environment was suboptimal for efficient oxidative addition or reductive elimination. Moreover, catalyst poisoning or deactivation observed in several entries underscores the importance of selecting a compatible combination of Pd catalyst, ligand, and base to promote effective amine coupling. The base also played a critical role. Although both *t*-BuONa and Cs_2CO_3 were tested, neither consistently enabled successful coupling. In particular, *entries 3 and 4*, which used Cs_2CO_3, showed no product formation, potentially due to the base's inefficiency in deprotonating the amines under the given conditions. To overcome these challenges, microwave heating was employed in select entries (*4, 6, 8, and 11*) to enhance reactivity. However, this approach also failed to yield the desired products, indicating that the underlying issues likely stem from more fundamental steric or electronic constraints within the scaffold rather than from insufficient thermal activation (Table 4).

Overall, these results highlight the synthetic challenges associated with this scaffold. Both AS-10 and AS-11 present significant obstacles, stemming from either steric hindrance or incompatibility with the selected nucleophiles, that must be addressed in future optimization efforts.

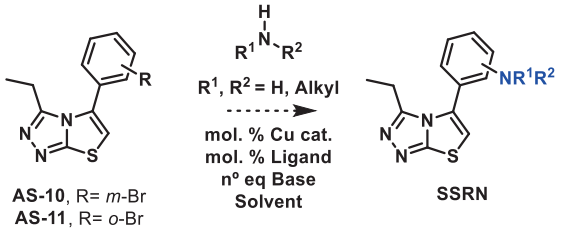

Entry	Substrate	HNR^1R^2 nº eq	Pd cat. mol. %	Ligand mol. %	Base nº eq
1^	AS-10	**NM1** 1,2 eq	$Pd(OAC)_2$ 2 %	JohnPhos 6 %	*t*-BuONa, 1.4 eq
2		**NM1**, 1.2 eq	Pd_2dba_3, 5 %	*rac*-BINAP 5 %	*t*-BuONa, 2.0 eq
3		**NM1**, 1.6 eq	$Pd(OAC)_2$ 5 %	*rac*-BINAP 7.5 %	Cs_2CO_3, 1.4 eq
4*		**NM1**, 1.2 eq	$Pd(OAC)_2$ 5 %	*rac*-BINAP 7.5 %	Cs_2CO_3, 1.4 eq
5		**NM11,** 1.5 eq	Pd_2dba_3, 3 %	*rac*-BINAP 9 %	*t*-BuONa, 3.0 eq
6*		**NM11**, 1.2 eq	Pd_2dba_3 5 %	*rac*-BINAP 7.5 %	*t*-BuONa, 1.4 eq
7^		**NM12,** 1.2 eq	Pd_2dba_3 10 %	PPh_3 1.6 %	*t*-BuONa, 1.4 eq
8*^		**NM1**, 1.2 eq	Pd_2dba_3 5 %	*rac*-BINAP 7.5 %	*t*-BuOK, 1.4 eq
9		**NM12**, 2.4 eq	$Pd(OAC)_2$ 6 %	*rac*-BINAP 10 %	*t*-BuONa, 3.0 eq
10		**NM12,** 1.2 eq	$Pd(OAC)_2$ 10 %	DPPF 10 %	*t*-BuONa, 2.0 eq
11*		**NM12**, 1 eq	$Pd[P(o\text{-tolyl})_3]_2Cl$ 2 %	*rac*-BINAP 5 %	Cs_2CO_3, 1.2 eq
12	AS-11	**NO21,** 2.0 eq	$Pd(OAC)_2$ 5 %	*rac*-BINAP 6 %	*t*-BuOK, 1.4 eq
13		**NO24,** 1.2 eq	$Pd(OAC)_2$ 2 %	JohnPhos 4 %	*t*-BuONa, 2.2 eq
14		**NO21,** 2.0 eq	$Pd(OAC)_2$ 2 %	JohnPhos 4 %	*t*-BuONa, 2.2 eq

Table 4: Reaction conditions explored using a Pd-catalyzed approach. All reactions were performed on a 1 mmol scale at 100 °C under microwave irradiation (if indicated with*) in toluene, unless otherwise noted (dioxane indicated with ^). Inspired by [246-248].

After all those multiple unsuccessful attempts, the following optimized conditions were proposed: $Pd_2(dba)_3$ as the catalyst, serving as a precatalyst that provides a stable and soluble source of Pd(0); XantPhos as the ligand, which coordinates to the palladium center, stabilizing the active catalytic species while its bulky nature minimizes side reactions and enhances selectivity; Cs_2CO_3 as the base, offering excellent functional group tolerance and solubility; and DMF as the solvent, with the reaction conducted under microwave irradiation for 150 minutes. [249] Under those conditions, SSR12 and AS-1 were successfully synthesized *via* the Pd-catalyzed Buchwald-Hartwig cross-coupling, albeit with low yields of 9 % and 8 %, respectively (Scheme 15). To note, despite extensive efforts, SSR11, which was previously synthesized *via* the Cu-catalyzed Ullmann approach, could not be successfully resynthesized.

While effective in certain cases, the reaction exhibited limitations in reproducibility across all proposed amines and scaffolds, as evidenced by unsuccessful amination attempts on AS-10 and AS-11. Although yields remained low, the primary objective was to obtain sufficient material for potency testing relative to SSR4.

Future optimization of reaction conditions will be explored based on the biological activity of the synthesized compounds. These challenges highlight the complexity of achieving efficient coupling reactions, particularly with this scaffold.

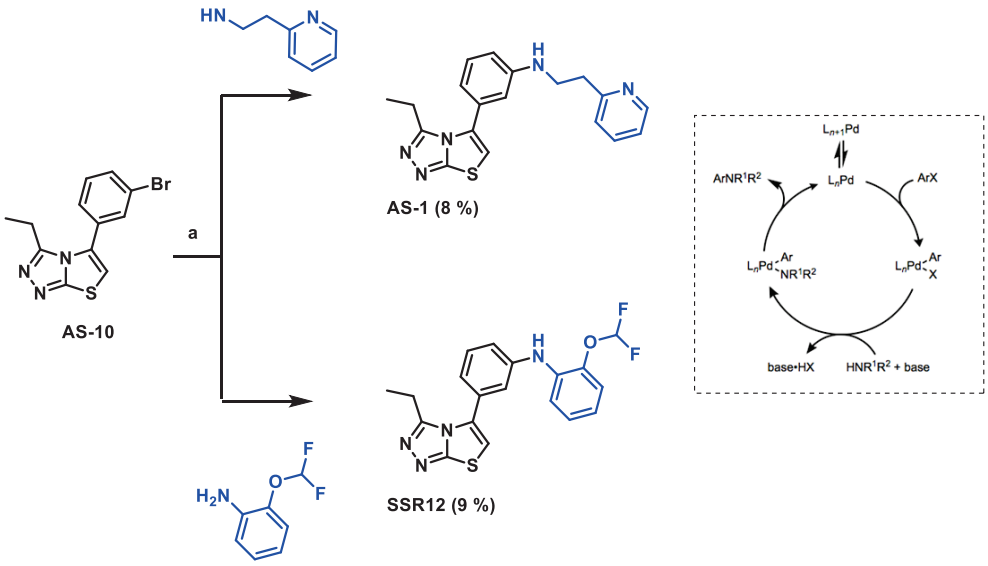

Scheme 15: Synthesis of AS-1 and SSR12 *via* Pd-catalyzed Buchwald-Hartwig reaction followed by the overview of the reaction meachanism[a].

[a]*Reagents and conditions:* (a) Pd_2dba_3, Cs_aCO_3, XantPhos, DMF anh., 153 ºC, 150 min, M/W.

5.5 Optimization of SSR12 lead compound

In parallel, given the significant potency increase of **SSR12** (IC_{50} = 0.1 µM), with a 650- fold improvement over **SSR4**, and its predicted binding mode (**Scheme 15**), NAOMInext software proposed two modifications to its phenyl ring-methyl and chlorine groups in the *meta* and *ortho* positions, respectively. Those modifications aim to further enhance potency by establishing additional interactions within the binding pocket.

Synthesis of AS-5

The synthesis of these new compounds, **AS-5** and **AS-6**, followed the same methodology used for **SSR12,** as the methyl and chlorine groups are introduced *via* the bromoacetophenone derivative in the first reaction step. Specifically, bromo derivatives **AS-12** and **AS-13** were synthesized through a Hantzsch-type cyclodehydration reaction between compound **45** and the corresponding bromoacetone derivatives, 2-bromo-1-(3-bromo-5-methylphenyl)ethan-1-one **48** and 2-bromo-1-(5-bromo-2-chlorophenyl)ethan-1-one **49**. These reactions gave intermediates ***m*-3** and ***o*-3**, respectively. Subsequent acylation of he hydrazine group with propionyl chloride **41** gave intermediates ***m*-4** and ***o*-4**. Both steps were carried out without further purification. [237, 249]] Finally, intramolecular cyclization using $POCl_3$ at high temperatures, as previously described, yielded **AS-12** and **AS-13** with low overall yields of 10 % and 4 %, respectively. [240, 241]

Notably, **AS-13** was synthesized under microwave conditions to overcome the steric hindrance caused by the additional halogen at the *ortho* position. Following the same Buchwald- Hartwig amination conditions, **AS-5** was successfully synthesized, albeit with a low yield of 9 %. [248] Unfortunately, despite significant efforts, **AS-6** (derived from **AS-13**) could not be successfully synthesized (**Scheme 16**).

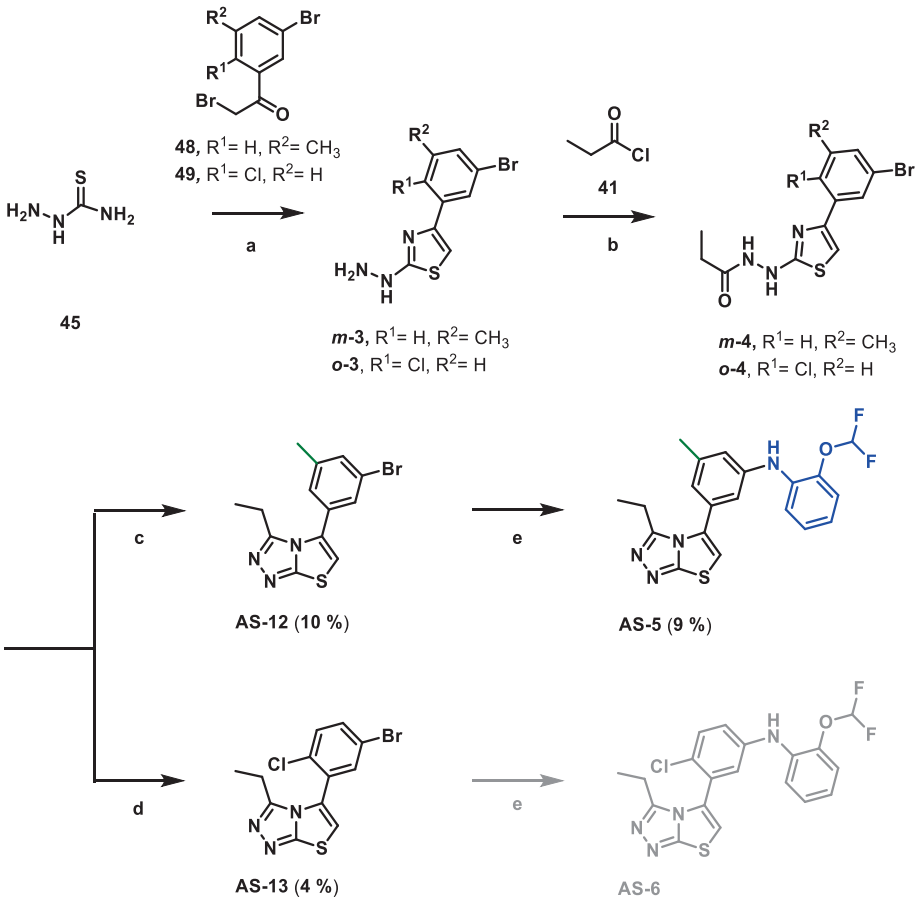

Scheme 16: Synthesis of AS-12, AS-13 and AS-5. AS-6, which could not be synthesized, is shown in grey[a]. [a]*Reagents and conditions*: (a) Dioxane, r.t., overnight; (b) THF, 0 ºC, 30 min; (c) $POCl_3$, Xylene, 130 ºC, overnight; (d) $POCl_3$, solvent free, 150 ºC, 150 min, M/W; (e) Pd_2dba_3, Cs_2CO_3, XantPhos, DMF anh., 150 ºC, 150 min, M/W.

5.6 TR-FRET assays of SSR4 and SSR12- derivative compounds

TR-FRET technique was used to properly characterize the binding event between Brd4(BD1) and the synthesized compounds (**AS-10, AS-11, AS-12, AS-13, SSR12, AS-1** and **AS-5**). The experiment was set up following an optimized protocol developed by Dr. Andrea Bertran from the Galdeano Lab, as described in the literature, [250] alongside the production and purification of recombinant His- tagged Brd4(BD1) protein. The TR-FRET competition assay provides an orthogonal and distinct method to characterize the binding of all identified compounds. This assay was based on the ability of the compounds to displace the interaction between the Brd4(BD1) protein and an acetylated peptide, Lys(Ac)5/8/12/16]- Histone H4 (1-21)-GGK(Biotin), thereby demonstrating the compounds' binding affinity to the Brd4(BD1) protein in IC_{50} values.

As an initial screening, the seven compounds and **(+)-JQ1**, as positive binder control, [211] was tested by duplicate as described in Chapter 6.3.2.1. A 16-point concentration curve was titrated against the acetylated peptide- Brd4(BD1) complex and incubated for 90 minutes to allow the displacement of the interaction and to determine more accurately the inhibitory capacity of the compounds screened. The data was normalized for each compound and fitted using a non-linear regression standard sigmoidal curve (GraphPad software). The analysis of both replicates for each compound enabled a determination of a likelihood profile of an IC_{50} within a 95% of confidence intervals (CI_{95}) (**Figure 45**). Each IC_{50} value with its own CI_{95} of all the screened compounds (**Table 5**).

Compound	*IC_{50} (µM) t=90 min*	*CI_{95} (µM)*	*R^2*
(+)- JQ1 (control)	23.3 ± 7.9	16.7 – 32.4	0.92
AS-10	5.8 ± 3.8	3.1 – 10.7	0.74
AS-11	25.3 ± 60.6	5.9 – 127.1	0.12
AS-12	11.3 ± 9.6	5.2 – 24.5	0.62
AS-13	10.4 ± 13.4	3.8 – 30.6	0.51
SSR12	1.1 ± 0.7	0.6 – 2.0	0.78
AS-1	9.6 ± 39.8	1.6 – 81.1	-0.33
AS-5	30.4 ± 24.3	15.2 to 63.9	0.64

Table 5: TR-FRET results. IC_{50} is determined within a 95% confidence Interval calculated from two replicates (CI_{95}). Shown is the mean ± SD. R^2 value indicates the quality of the fitting.

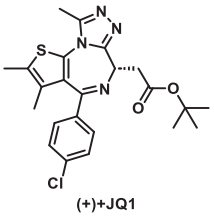

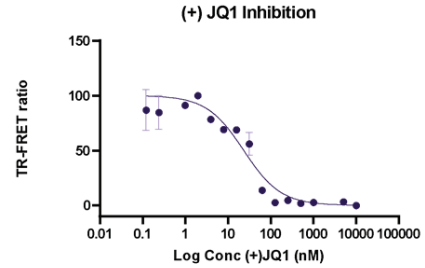

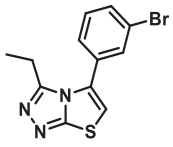

AS-10

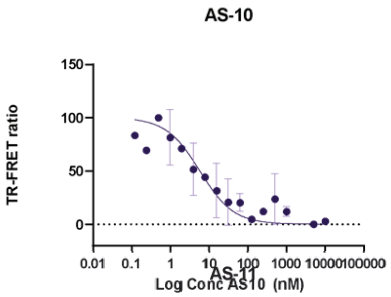

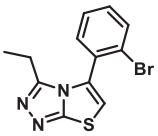

AS-11

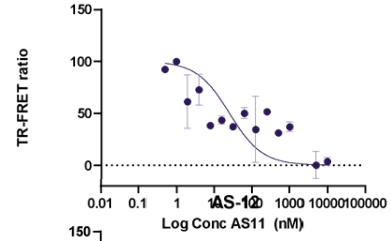

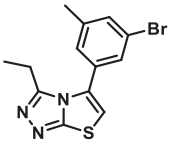

AS-12

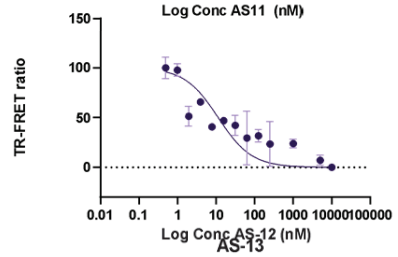

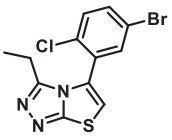

AS-13

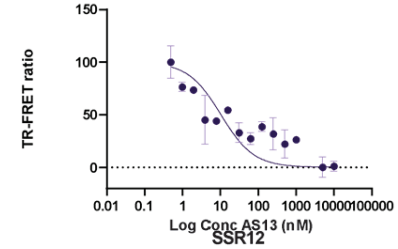

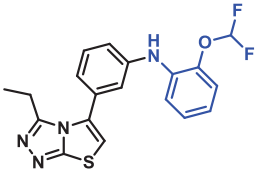

SSR12

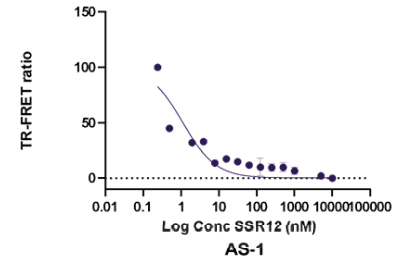

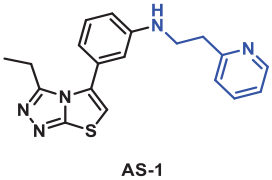

AS-1

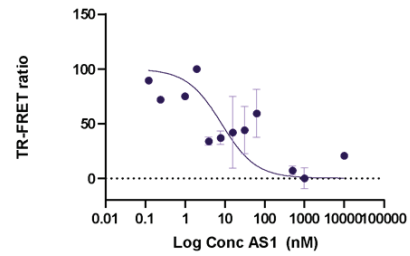

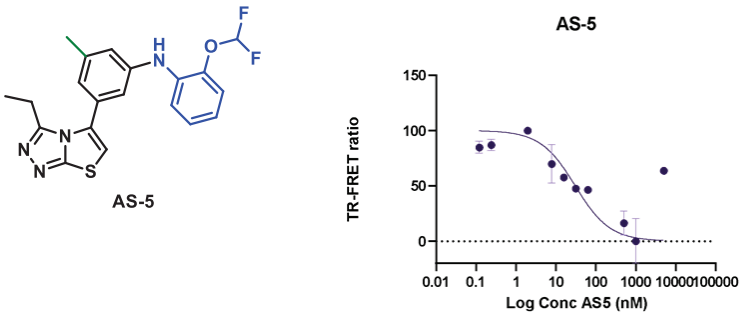

Figure 45: Normalized TR-FRET assay showing dose-dependently displacement of a tetra-acetylated H4 peptide from Brd4(BD1) in the presence of each compound after equilibration of 90 min.

5.7 Discussion

After confirming that the virtual platform successfully identified novel scaffolds—as demonstrated in the prospective example with Brd4(BD1), where the SSR4 fragment emerged as the most active compound in the reported series, we aimed to enhance its affinity by growing this optimized fragment into a lead-sized ligand.

Since no commercial derivatives were available, we synthesized them. To facilitate this, the NAOMInext software was used, a program for virtual synthesis that generates molecules *de novo*. The software enabled the growth of SSR4 from two different vectors on the phenyl ring (*meta* and *ortho*) by incorporating commercial building blocks through a set of known reactions, ensuring synthetic accessibility. Simultaneously, NAOMInext predicted the binding poses and evaluated binding scores of the newly generated molecules. At this stage, medicinal chemistry expertise played a critical role, as the phenyl ring required previous functionalization to introduce new building blocks. A bromine group was proposed for this purpose, leading to the design of AS-10 and AS-11, for growth at the *meta* and *ortho* positions of the SSR4 phenyl ring, respectively.

In previous experiments, from the selected building blocks, two molecules, SSR11 and SSR12, were successfully synthesized using a Cu-Ullmann cross coupling reaction and further evaluated in competitive TR-FRET assays. As a result, SSR12 demonstrated a remarkable 650-fold increase in potency compared to SSR4, placing it in a potency range comparable to the standard BET inhibitor (+)-JQ1.

Building on these results, and with the dual aim of further enhancing the affinity of SSR4 fragment hit and validating the NAOMInext software, extensive efforts were dedicated to synthesizing additional compounds using the newly identified building blocks *via* the proposed Buchwald- Hartwig amination synthetic approach. Ultimately, SSR12 was successfully resynthesized following the mentioned approach, along with the new compound AS-1.

Additionally, based on the predicted binding pose of SSR12, two different growth vectors on the phenyl ring were proposed: compound AS-5, featuring a methyl group in the *meta* position, and compound AS-6, incorporating a chlorine group in the *ortho* position. However, only AS-5 was successfully synthesized and with a very low yield, while AS-6 remains challenging to synthesize. Further efforts and optimization of synthetic strategies will be necessary to achieve the synthesis of AS-6 and explore its potential as a derivative. These efforts underscore the challenges associated with efficient coupling reactions, particularly with this specific scaffold. The low yields observed highlight the inherent complexity of the process and the necessity for further optimization of reaction

conditions. This is crucial not only to ensure the successful synthesis of SSR4 and SSR12 derivatives but also to realize the full potential of the proposed compounds with the new building blocks. Such optimization will improve the synthetic accessibility of these molecules and enable a broader exploration of the chemical space surrounding this promising scaffold.

Finally, TR-FRET assays were conducted to evaluate the binding capacity of the synthesized compounds by measuring their ability to disrupt the interaction between Brd4(BD1) and an acetylated peptide, determining their inhibitory capacity (IC_{50}). In the initial screening, all synthesized final compounds (SSR12, AS-1 and AS-5) as well as intermediate compounds (AS-10, AS-11, AS-12 and AS-13) were tested. A 16-point concentration titration was performed to cover a broad range of concentrations, allowing for the determination of accurate IC_{50} values.

During the assay, discrepancies in fluorescence signals were observed across compounds, potentially due to microscopic aggregation or intrinsic fluorescence of certain molecules, which could have affected the raw fluorescence data. To address this issue, the data was normalized before analysis. For each compound, the minimal signal was set to 0 % (representing maximal inhibition), while the maximal signal was set to 100 % (representing minimal inhibition). To further ensure the validity of the results and exclude potential false positives, a negative control was included. This control consisted of compound titration without the presence of Brd4(BD1) in the samples. This additional step allowed for the discrimination of true inhibitory effects from artifacts caused by compound aggregation or intrinsic fluorescence. This normalization and control approach ensured a more reliable interpretation of the TR-FRET assay results, accounting for compound-specific anomalies and enabling a clearer evaluation of their inhibitory capacities.

In a first screening, the control compound (+)-JQ1 demonstrated consistent and reliable binding, with a well- defined IC_{50} value and high R^2, indicating a robust fit to the dose-response curve and validating the assay's accuracy for benchmarking the novel compounds.

Among the SSR4-derivatives, AS-10 showed a promising IC_{50} indicative of moderate to strong inhibition. Although the data exhibited some variability, the compound remained a viable candidate for further development. In contrast, AS-11 and AS-1 exhibited extremely wide confidence intervals and significant variability, leading to poor curve fitting and unreliable data, which diminished their reliability as inhibitors in their current form. However, SSR12 emerged as the most potent compound, with the strongest binding affinity and a substantially lower IC_{50} compared to the control (+)-JQ1. This

highlights its potential as a highly potent inhibitor. Despite its moderate R^2 value and standard deviation indicating some variability, SSR12 remains a top candidate for validation in future experiments.

Among the SSR12- derivatives, AS-12 and AS-13 displayed moderate activity. However, their wider confidence intervals and lower R^2 values suggested variability and room for improvement. Meanwhile, AS-5 showed weaker inhibitory activity compared to SSR12, demonstrating a decrease in potency when a methyl group is incorporated in the *meta* position.

Overall, SSR12 remains the top candidate of the synthesized series, demonstrating significantly higher potency and a 650-fold improvement over SSR4. Nonetheless, the wide confidence intervals and low R^2 values observed in several compounds underscore the need for improved experimental consistency and assay optimization. Refining these conditions will be crucial to accurately assess the potential of these compounds and guide future developments.

5.8 Conclusions

This chapter explores the potential of FBDD to design and synthesize novel inhibitors targeting Brd4(BD1) an important epigenetic regulator. Using an *in-house* automated fragment evolution platform, SSR4 fragment, a novel 5–5 fused bicyclic scaffold, is identified as the most active fragment, demonstrating the platform's ability to efficiently evolve fragments into potent lead candidates. Through a computationally in silico approach, the NAOMInext tool proposes a series of SSR4 derivatives by incorporating amine building blocks via amine coupling reactions.

- The functionalization of SSR4 with two bromine derivatives at the *meta* and *ortho* positions of the phenyl ring was successfully achieved, resulting in the synthesis of AS-10 and AS-11, respectively. However, low yields underscore the challenges associated with functionalizing the SSR4 scaffold and highlight the need for further optimization of reaction conditions.
- SSR12 and AS-1 were successfully synthesized using a Buchwald-Hartwig amination coupling. Despite the successful synthesis, challenges remain in achieving higher yields and more efficient coupling reactions, emphasizing the complexity of the fragment-growing process and the need for continued optimization of synthetic strategies.
- TR-FRET assays confirm SSR12 as the most potent compound, showing a 650-fold increase in affinity compared to SSR4, placing it in a potency range similar to the well-known BET inhibitor (+)-JQ1.
- Optimization of SSR12, including modifications at the *meta* and *ortho* positions of the phenyl ring, led to the successful synthesis of AS-5. However, synthesizing AS-6 proved challenging, underscoring the need for new synthetic strategies.

In this chapter, we successfully validate and demonstrate the utility of computational tools like NAOMInext in fragment growing for FBDD. The identification and optimization of SSR4 derivatives advance the field of Bromodomain inhibitors, with SSR12 showing the most promise. The challenges encountered in synthesizing certain derivatives highlight the complexities of fragment growing and the need for further optimization in synthetic methods. These findings contribute valuable insights into developing potent epigenetic inhibitors, which could ultimately pave the way for discovering novel therapeutic agents targeting epigenetic regulation in drug discovery.

CHAPTER 6

Experimental Section

6. CHAPTER 6: EXPERIMENTAL SECTION

6.1 Chapter 3: Degrading cMyc with low-affinity small molecule-based PROTACs

6.1.1 Chemistry Section

General Information

Reagents, solvents and starting products were acquired from commercial sources. The term "concentration" refers to the vacuum evaporation using a Büchi rotavapor. The progress of the reactions was monitored by thin-layer chromatography (TLC) with aluminium- backed sheets with silica gel 60 F254 (Merck, ref 1.05554), and spots were visualized with UV light. When indicated, column chromatography was performed on silica gel 60 Å (Sigma Aldrich, 40 - 63 µm, 230-400 mesh) or with a PuriFlash 5.052 Interchim provided with multi wavelength UV detection using pre- packed RediSep Rf silica gel cartridges normal phase (silica gel, 35–70 µm) and reversed phase (C18) columns with the indicated solvent system.

Data Analysis

The ^{1}H NMR spectra were recorded on a 400 MHz or 500 MHz NMR spectrometer, ^{13}C NMR spectra at 101 MHz or 126 MHz, and chemical shifts are reported in δ values downfield from TMS or relative to residual chloroform (7.26 ppm, 77.0 ppm) as an internal standard. Data are reported in the following manner: chemical shift, multiplicity, coupling constant (J) in hertz (Hz), integrated intensity and assignment (when possible). Multiplicities are reported using the following abbreviations: s, singlet; d, doublet; dd, doublet of doublets; ddd, double double of doublets; dq, doble quadruplet; t, triplet; quin, quintet; m, multiplet; brs, broad signal, app, apparent. Assignments and stereochemical determinations are given only when they are derived from definitive two-dimensional NMR experiments (^{1}H-^{1}H COSY, ^{1}H-^{13}C HSQC, and ^{1}H-^{13}C HMBC spectra). Mass Spectrometry was performed using LC/MSD TOF Agilent Technologies G1969A spectrometer by the Mass Spectrometry for Molecular Characterization Unit (Biomolecular Analysis Unit), from Scientific and Technological Centers (CCiTUB), University of Barcelona. The analytical samples of all the new compounds, which were subjected to pharmacological evaluation, possessed purity ≥95 % as evidenced by their HPLC- UV. HPLC- UV were determined with a HPLC Agilent 1260 Infinity II LC / MSD coupled to a photodiode array and mass spectrometer. Samples (5 µL, 0.5 mg/mL) in a 1:1 mixture of water with 0.05 % HCO_2H (A) and CH_3CN with 0.05 % HCO_2H (B) were injected using an Agilent Poroshell 120 EC-C18 (2.7 µm, 50 mm × 4.6 mm) column at 40 °C. The mobile phase was a mixture of A and B, with a flow 0.6 mL/min, using the following gradients: from 95 % A–5 % B to 100 % B in 3 min; 100 % B for 3 min; from 100 % B to 95 % A–5 % B in 1 min; and 95 % A–5 % B for 3 min. Purity is given as % of absorbance at 254 nm, or in some cases at 220 nm.

6.1.1.1 Synthetic Procedures and Characterization Data

Synthesis of 1st Series of cMyc- based PROTACs

(*Z*)-5-(4-Ethylbenzylidene)-2-thioxothiazolidin-4-one (3)

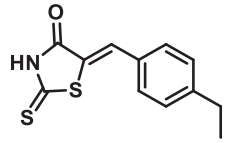

3

To a solution of rhodanine (**1**; 800 mg, 6.01 mmol, 1 eq) and ammonium acetate (1784 mg, 6.61 mmol, 3 eq) in glacial acetic acid (9 mL) were slowly added *p*-ethylbenzaldehyde (**2**; 1 mL, 6.61 mmol, 1.1 eq). The resulting mixture was heated to 117 ºC and stirred for 3 h. Reaction progression and completion was monitored by TLC. After cooling to room temperature, the product was collected *via* filtration and washed with water to give **3**, also known as inhibitor **10058-F4,** as a yellow solid (1470 mg, **98 %**). [149] The reaction is stereoselective and only *Z* product was detectable by NMR. **^{1}H NMR** (400 MHz, DMSO) δ 1.19 (t, *J* = 7.6 Hz, 3H, $CH_2C\underline{H}_3$), 2.66 (q, *J* = 7.6 Hz, 2H, $C\underline{H}_2CH_3$), 7.39 (d, *J* = 8.2 Hz, 2H, C<u>H</u>Ar), 7.53 (d, *J* = 8.2 Hz, 2H, C<u>H</u>Ar), 7.62 (s, 1H, C<u>H</u>), 13.81 (s, 1H, N<u>H</u>). **^{13}C NMR** (101 MHz, DMSO) δ 15.2 ($CH_2\underline{C}H_3$), 28.1 ($\underline{C}H_2CH_3$), 128.9 (<u>C</u>S), 130.5 (<u>C</u>Ar), 130.7 (<u>C</u>Ar), 131.7 (<u>C</u>Ar), 147.2 (<u>C</u>H), 169.7 (<u>C</u>=O), 196.0 (<u>C</u>=S). **HRMS** *m/z* calc. for $C_{12}H_{12}NOS_2$ $[M+H]^+$ 250.0280, found 250.0359.

(*Z*)-3-(5-(4-Ethylbenzylidene)-4-oxo-2-thioxothiazolidin-3-yl)propanoic acid (ASA-5)

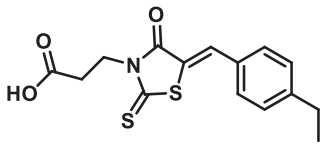

ASA-5

A mixture of *p*-ethylbenzaldehyde (**2**; 0.3 mL, 2.44 mmol, 1 eq) and 3-(4-oxo-2-thioxothiazolidin-3-yl)propanoic acid (**7**; 501 mg, 2.44 mmol, 1 eq) was placed in a microwave vial equipped with a magnetic stir bar. The reaction vessel was sealed and irradiated under solvent-free conditions in a microwave reactor at 90 ºC for 10 min. After the crude reaction mixture was cooled down to room temperature, 5 mL of Ethanol / Hexane (1:1 *v / v*) were added directly to the glass vial. The resulting precipitate was filtered on a Büchner funnel, and the insoluble residue was washed two times with the same mixture (2 x 5 mL). The crude was concentrated and purified with column chromatography (100 % AcOEt) to give **ASA-5** as a yellow solid (704 mg, **90 %**). [154] **^{1}H NMR** (400 MHz, DMSO, COSY, HETCOR) δ 1.20 (t, *J* = 7.6 Hz, 3H, $CH_2C\underline{H}_3$), 2.58 – 2.72 (m, 4H, $C\underline{H}_2$COOH, $C\underline{H}_2CH_3$), 4.23 (t, *J* = 7.6 Hz, 2H, $C\underline{H}_2$N), 7.41 (d, *J* = 8.3 Hz, 2H, C<u>H</u>Ar), 7.57

(d, *J* = 8.3 Hz, 2H, CHAr), 7.80 (s, 1H, CH), 12.51 (s, 1H, OH). **^{13}C NMR** (101 MHz, DMSO, HETCOR) δ 15.2 (CH_2CH_3), 28.2 (CH_2CH_3), 30.8 (CH_2CH_2COOH), 40.0 (CH_2N), 121.2 (CS), 129.0 (2CAr), 130.5 (CAr CH_2CH_3), 130.9 (CAr), 133.1 (CH), 147.6 (CAr), 166.8 (C=O), 171.8 (COOH), 193.3 (C=S). **HRMS** *m/z* calc. for $C_{15}H_{15}NO_3S_2$ $[M+H]^+$ 322.0490, found 322.0571.

tert-Butyl (*Z*)-3-((5-(4-ethylbenzylidene)-4-oxo-4,5-dihydrothiazol-2-yl)thio)propanoate (6)

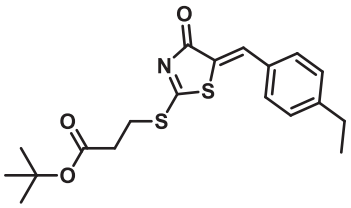

6

A mixture of (*Z*)-5-(4-ethylbenzylidene)-2-thioxothiazolidin-4-one (**3**; 200 mg, 0.80 mmol, 1 eq) was dissolved in acetone (10 mL) in the presence of K_2CO_3 (116 mg, 0.84 mmol, 1.05 eq) and heated at 56 ºC. After reflux was observed, *tert*-butyl-3-bromopropionate (**4**; 0.1 mL, 0.84 mmol, 1.05 eq) was added and the reaction was left stirring fro 30 min until completion of the starting material was observed by TLC. The reaction mixture was cooled to room temperature, the precipitate salts were removed by filtration and the solvent was evaporated under reduced pressure. Then, the organic layer was washed with AcOEt and saturated aqueous NaCl, dried over Na_2SO_4, filtered, and concentrated. The crude was purified with reverse-phase column chromatography (91 % CH_3CN in 0.1 % aq. HCO_2H) to give **6** as a yellow solid (138, **46 %**). [153] **^{1}H NMR** (500 MHz, DMSO) δ 1.19 (t, J = 7.6 Hz, 3H, CH_2CH_3), 1.42 (s, 9H, $3CH_3$-*t*Bu), 2.66 (q, J = 7.6 Hz, 2H, CH_2CH_3), 2.80 (t, J = 6.8 Hz, 2H, CH_2COOH), 3.55 (t, J = 6.8 Hz, 2H, CH_2S), 7.39 (d, J = 8.2 Hz, 2H, Ar-H), 7.58 (d, J = 8.2 Hz, 2H, Ar-H), 7.84 (s, 1H, CH). **HRMS** *m/z* calc. for $C_{15}H_{16}NO_3S_2$ $[M+H]^+$ 378.1120, found 378.1187.

(*Z*)-3-((5-(4-Ethylbenzylidene)-4-oxo-4,5-dihydrothiazol-2-yl)thio)propanoic acid (ASA-6)

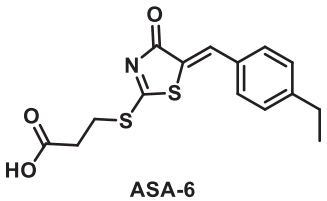

ASA-6

tert-Butyl (*Z*)-3-((5-(4-ethylbenzylidene)-4-oxo-4,5-dihydrothiazol-2-yl)thio)propanoate (**6**; 165 mg, 0.44 mmol, 1 eq) was dissolved in dry DCM (0.6 mL, 0.73 M) and TFA (0.6 mL) was slowly added. The mixture was stirred for 30 min upon completion as observed by TLC. After a basic extraction and removal of the volatiles, the residue was concentrated to give **ASA-6**, without further purification in quantitative yield. [52] **^{1}H NMR** (400 MHz, DMSO, HETCOR) δ 1.19 (t, *J* = 7.6 Hz, 3H, CH_2CH_3), 2.66 (q, *J* = 7.5 Hz, 2H, CH_2CH_3), 2.82 (t, *J* = 6.8 Hz, 2H, CH_2COOH), 3.55 (t, *J* = 6.8 Hz, 2H, CH_2S), 7.40 (d, *J* = 8.1 Hz, 2H, CHAr), 7.58 (d, *J* = 8.2 Hz, 2H, CHAr), 7.83 (s, 1H, CH), 12.58 (s, 1H, OH). **^{13}C NMR** (101 MHz,

DMSO, HETCOR) δ 15.2 (CH$_3$), 28.2 (CH$_2$S), 28.5 (CH$_2$CH$_3$), 33.2 (CH$_2$,COOH), 124.8 (CS), 129.0 (CAr), 130.7 (CAr), 130.7 (CAr), 135.4 (CAr), 147.6 (CAr), 172.5 (C=O), 179.0 (COOH), 191.7 (C=S). **HRMS** *m/z* calc. for $C_{15}H_{15}NO_3S_2$ $[M+H]^+$ 322.0490, found: 322.0565.

2-(2-(2-Aminoethoxy)ethoxy)-*N*-(2-(2,6-dioxopiperidin-3-yl)-1-oxoisoindolin-4-yl)acetamide 2,2,2-trifluoroacetate (11a)

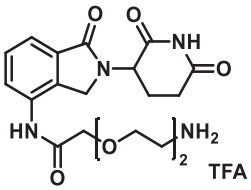

11a

2,2-Dimethyl-4-oxo-3,8,11-trioxa-5-azatridecan-13-oic acid (**9a**; 244 mg, 0.93 mmol, 1.2 eq) was added to a stirring solution of **lenalidomide** (**8**, 200 mg, 0.77 mmol, 1 eq) and DIPEA (0.4 mL, 2.30 mmol, 3 eq) in dry DMF (3.5 mL, 0.17 M). After 15 min, HATU (352 mg, 0.93 mmol, 1.2 eq) was added and the reaction mixture was allowed to stir at room temperature for 12 h. Upon completion of the reaction as determined by HPLC / MS, the organic layer was washed with AcOEt and water, dried over Na_2SO_4, filtered, and concentrated. The crude was purified with reverse-phase column chromatography (38 % CH_3CN in 0.1 % aq. HCO_2H) to give **10a** as a white solid (304 mg, **78 %**). [52] **^{1}H NMR** (400 MHz, $CDCl_3$) δ 1.38 (s, 9H), 2.11 – 2.19 (m, 1H), 2.24 – 2.40 (m, 1H), 2.75 – 2.82 (m, 2H), 3.22 – 3.31 (m, 2H), 3.55 (t, *J* = 5.5 Hz, 2H), 3.65 – 3.70 (m, 2H), 3.74 – 3.78 (m, 2H), 4.14 (d, *J* = 1.7 Hz, 2H), 4.41 (d, *J* = 3.9 Hz, 2H), 4.95 (s, 1H), 5.18 (dd, *J* = 5.2, 13.2 Hz, 1H), 7.46 (t, *J* = 7.7 Hz, 1H), 7.69 (d, *J* = 3.8 Hz, 1H), 7.71 (d, *J* = 3.3 Hz, 1H), 8.73 (s, 1H), 8.88 (s, 1H). **HRMS** *m/z* calc. for $C_{24}H_{32}N_4O_8$ $[M+H]^+$ 505.2220, found 505.2297. Then, *tert*-butyl (2-(2-(2-((2-(2,6-dioxopiperidin-3-yl)-1-oxoisoindolin-4-yl)amino)-2-oxoethoxy)ethoxy)ethyl) carbamate (**10a**; 100 mg, 0.20 mmol, 1 eq) was dissolved in dry DCM (0.8 mL, 0.25 M), and TFA (0.8 mL) was slowly added. The mixture was stirred for 30 min upon completion as determined by TLC. After removal of the volatiles, the oily residue was dried further under high vacuum to give **11a** as TFA salt, [52] without further purification in quantitative yield that matched the reported spectral data. [157].

2-(2-(2-Aminoethoxy)ethoxy)-*N*-(2-(2,6-dioxopiperidin-3-yl)-1-oxoisoindolin-4-yl)acetamide 2,2,2-trifluoroacetate (11b)

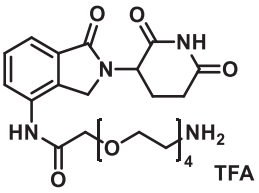

11b

2,2-Dimethyl-4-oxo-3,8,11,14,17-pentaoxa-5-azanonadecan-19-oic acid (**9b**; 163 mg, 0.46 mmol, 1.2 eq) was added to a stirring solution of **lenalidomide** (**8**; 100 mg, 0.39 mmol, 1 eq) and DIPEA (0.2 mL, 1.16 mmol, 3 eq) in dry DMF (3.5 mL, 0.17 M). After 15 min, HATU (176 mg, 0.46 mmol, 1.2 eq) was added and the reaction mixture was allowed to stir at room temperature for 12 h. Upon completion of the reaction as determined by HPLC / MS, the organic layer was washed with AcOEt and water, dried over Na_2SO_4, filtered, and concentrated. The crude was purified with reverse-phase column chromatography (65 % CH_3CN in 0.1 % aq. HCO_2H) to give **10b** as a white solid (97 mg, **53 %**). [52] **^{1}H NMR** (400 MHz, $CDCl_3$) δ 1.43 (s, 9H), 2.15 – 2.26 (m, 1H), 2.37 (dd, *J* = 5.3, 13.1 Hz, 1H), 2.73 – 2.94 (m, 2H), 3.25 (d, *J* = 5.6 Hz, 2H), 3.43 – 3.50 (m, 6H), 3.58 (s, 2H), 3.66 – 3.70 (m, 2H), 3.71 – 3.74 (m, 2H), 3.77 – 3.81 (m, 2H), 4.14 (dd, *J* = 4.7, 16.2 Hz, 2H), 4.44 (s, 2H), 5.11 (s, 1H), 5.22 (dd, *J* = 5.2, 13.3 Hz, 1H), 7.48 (t, *J* = 7.7 Hz, 1H), 7.69 – 7.78 (m, 2H), 8.52 (s, 1H), 9.01 (s, 1H). **HRMS** *m/z* calc. for $C_{28}H_{40}N_4O_{10}$ $[M+H]^+$ 593.2740, found 593.2816. Then, *tert*-butyl (14-((2-(2,6-dioxopiperidin-3-yl)-1-oxoisoindolin-4-yl)amino)-14-oxo-3,6,9,12-tetraoxatetradecyl)carbamate (**10b**; 90 mg, 0.15 mmol, 1 eq) was dissolved in dry DCM (0.6 mL, 0.25 M), and TFA (0.6 mL) was slowly added. The mixture was stirred for 30 min upon completion as determined by TLC. After removal of the volatiles, the oily residue was dried further under high vacuum to give **11b** as TFA salt, [52] without further purification in quantitative yield that matched the reported spectral data. [157]

(4-(4-Methylthiazol-5-yl)phenyl)methanamine 2,2,2-trifluoroacetate (15)

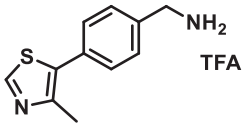

15

tert-Butyl (4-bromobenzyl)carbamate (**12**; 700 mg, 2.45 mmol, 1 eq), $Pd(OAc)_2$ (5.5 mg, 0.02 mmol, 0.01 eq) and KOAc (480 mg, 4.89 mmol, 2 eq) were dissolved in *N*,*N*-dimethylacetamide (8 mL). Then, 4-methylthiazole (**13**; 0.5 mL, 4.89 mmol, 2 eq) was added, and the solution was heated to 130 ºC under argon atmosphere for 12 h. Subsequently, the mixture was cooled to room temperature and the organic layer was washed with DCM and water, dried over Na_2SO_4, filtered, and concentrated. The crude

was purified with column chromatography (80 % Hexane / 20 % AcOEt) to give **14** as a brownish solid (527 mg, **71 %**) that matched the reported spectral data. [159] Then, *tert*-butyl *N*-{[4-(4-methyl-1,3-thiazol-5-yl)phenyl]methyl}carbamate (**14**; 225 mg, 0.74 mmol, 1 eq) was dissolved in dry DCM (3 mL, 0.25 M), and TFA (3 mL) was slowly added. The mixture was stirred for 30 min upon completion as determined by TLC. After removal of the volatiles, the oily residue was dried further under high vacuum to give **15** as TFA salt, without further purification in quantitative yield. [52]

(2*S*,4*R*)-4-Hydroxy-*N*-(4-(4-methylthiazol-5-yl)benzyl)pyrrolidine-2-carboxamide 2,2,2-trifluoroacetate (18)

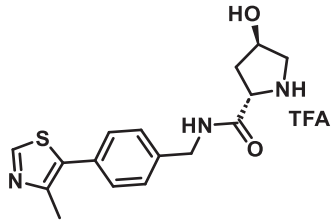

18

(4-(4-Methylthiazol-5-yl)phenyl)methanamine 2,2,2-trifluoroacetate (**15**; 330 mg, 1.04 mmol, 1 eq) was added to a stirring solution of (2*S*,4*R*)-1-(tert-butoxycarbonyl)-4-hydroxypyrrolidine-2-carboxylic acid (**16**; 288 mg, 1.25 mmol, 1.2 eq) and DIPEA (1 mL, 6.23 mmol, 6 eq) in anhydrous DMF (2.8 mL, 0.37 M). After 15 min, HATU (474 mg, 1.25 mmol, 1.2 eq) was added and the reaction mixture was allowed to stir at room temperature for 12 h. Upon completion of the reaction as determined by HPLC / MS, the organic layer was washed with AcOEt and water, dried over Na_2SO_4, filtered, and concentrated. The crude was purified with reverse-phase column chromatography (57 % CH_3CN in 0.1 % aq. HCO_2H) to give **17** as a white solid (257 mg, **71 %**) [159] that matched the reported spectral data. [164] Then, *tert*-butyl (2*S*,4*R*)-4-hydroxy-2-((4-(4-methylthiazol-5-yl)benzyl)carbamoyl)pyrrolidine-1-carboxylate (**17**; 257 mg, 0.61 mmol) was dissolved in dry DCM (2.5 mL, 0.25 M), and TFA (2.5 mL) was slowly added. The mixture was stirred for 30 min upon completion as determined by TLC. After removal of the volatiles, the oily residue was dried further under high vacuum to give **18** as TFA salt, without further purification in quantitative yield that matched the reported spectral data. [159]

(2*S*,4*R*)-1-((*S*)-2-Amino-3,3-dimethylbutanoyl)-4-hydroxy-N-(4-(4-methylthiazol-5-yl)benzyl)pyrrolidine-2-carboxamide 2,2,2-trifluoroacetate (21)

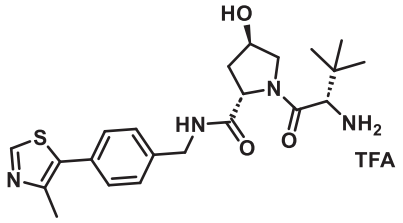

21

(2*S*,4*R*)-4-Hydroxy-*N*-(4-(4-methylthiazol-5-yl)benzyl)pyrrolidine-2-carboxamide-2,2,2-trifluoroacetate (18; 230 mg, 0.53 mmol, 1 eq) was added to a stirring solution of and (*S*)-2-((tert-butoxycarbonyl)amino)-3,3-dimethylbutanoic acid (19; 148 mg, 0.64 mmol, 1.2 eq) and DIPEA (0.56 mL, 3.20 mmol, 6.00 eq) in anhydrous DMF (3.10 mL, 0.17M). After 15 min, HATU (243 mg, 0.64 mmol, 1.2 eq) was added and the reaction mixture was allowed to stir at room temperature for 12 hours. Upon completion of the reaction as determined by HPLC / MS, the organic layer was washed with AcOEt and water, dried over Na_2SO_4, filtered, and concentrated. The crude was purified with reverse-phase column chromatography (50 % CH_3CN in 0.1 % aq. HCO_2H) to give 20 as a white solid (195 mg, 69 %) [52] that matched the reported spectral data. [165] Then, *tert*-butyl ((*S*)-1-((2*S*,4*R*)-4-hydroxy-2-((4-(4-methylthiazol-5-yl)benzyl)carbamoyl) pyrrolidine-1-yl)-3,3-dimethyl-1-oxobutan-2-yl)carbamate (20; 140 mg, 0.26 mmol, 1 eq) was dissolved in dry DCM (1 mL, 0.25 M), and TFA (1 mL) was slowly added. The mixture was stirred for 30 min upon completion as determined by TLC. After removal of the volatiles, the oily residue was dried further under high vacuum to give 21 as TFA salt, without further purification in quantitative yield, without further purification in quantitative yield that matched the reported spectral data. [52]

(2*S*,4*R*)-1-((*S*)-2-(2-(2-Aminoethoxy)acetamido)-3,3-dimethylbutanoyl)-4-hydroxy-*N*-(4-(4-methylthiazol-5-yl)benzyl)pyrrolidine-2-carboxamide 2,2,2-trifluoroacetate (23a)

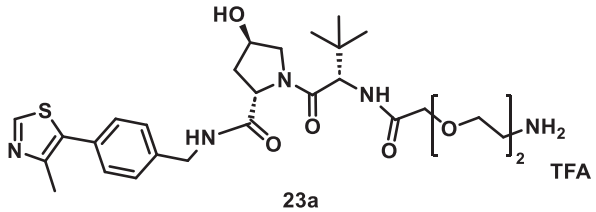

23a

2,2-Dimethyl-4-oxo-3,8,11-trioxa-5-azatridecan-13-oic acid (9a; 116 mg, 0.44 mmol, 1.2 eq) was added to a stirring solution of 21 as TFA salt (200 mg, 0.37 mmol, 1 eq) and DIPEA (0.4 mL, 2.20 mmol, 6 eq) in dry DMF (2.2 mL, 0.17 M). After 15 min, HATU (168 mg, 0.44 mmol, 1.2 eq) was added and the reaction mixture was allowed to stir at room temperature for 12 h. Upon completion of the reaction as determined by HPLC / MS, the organic layer was washed with AcOEt and water, dried over Na_2SO_4, filtered, and concentrated. The crude was purified with reverse-phase column chromatography (43 %

CH_3CN in 0.1 % aq. HCO_2H) to give **22a** as a white solid (170 mg, **68 %**) [52] that matched the reported spectral data. [166] **HRMS** *m/z* calc. for $C_{33}H_{49}N_5O_8S$ $[M+H]^+$ 676.3375, found 676.3370.Then, *tert*-butyl (2-(2-(((*S*)-1-((2*S*,4*R*)-4-hydroxy-2-((4-(4-methylthiazol-5-yl)benzyl)carbamoyl)pyrrolidin-1-yl)-3,3-dimethyl-1-oxobutan-2-yl)amino)-2 oxoethoxy)ethyl)carbamate (**22a**; 100 mg, 0.15 mmol, 1 eq) was dissolved in dry DCM (0.6 mL, 0.25 M) and, TFA (0.6 mL) was slowly added. The mixture was stirred for 30 min upon completion as determined by TLC. After removal of the volatiles, the oily residue was dried further under high vacuum to give **23a** as TFA salt, without further purification in quantitative yield. [52]

(2*S*,4*R*)-1-((*S*)-2-(2-(2-Aminoethoxy)acetamido)-3,3-dimethylbutanoyl)-4-hydroxy-*N*-(4-(4-methylthiazol-5-yl)benzyl)pyrrolidine-2-carboxamide 2,2,2-trifluoroacetate (23b)

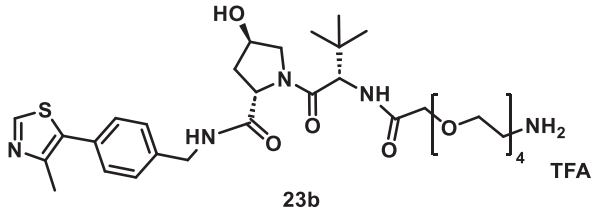

23b

2,2-Dimethyl-4-oxo-3,8,11,14,17-pentaoxa-5-azanonadecan-19-oic acid (**9b**; 155.00 mg, 0.44 mmol, 1.20 eq) was added to a stirring solution of **21** as TFA salt (200.00 mg, 0.37 mmol, 1.00 eq) and DIPEA (0.38 mL, 2.20 mmol, 6.00 eq) in dry DMF (2.20 mL, 0.17 M). After 15min, HATU (168.00 mg, 0.44 mmol, 1.20 eq) was added and the reaction mixture was allowed to stir at room temperature for 12 h. Upon completion of the reaction as determined by HPLC / MS, the organic layer was washed with AcOEt (x3) and water, dried over Na_2SO_4, filtered, and concentrated. The crude was purified with reverse-phase column chromatography (49 % CH_3CN in 0.1 % aq. HCO_2H) to give **22b** as a white solid (193.60 mg, **69 %**). [52] **HRMS** *m/z* calc. for $C_{37}H_{57}N_5O_{10}S$ $[M+H]^+$ 764.3830, found 764.3893. Then, *tert*-butyl (2-(2-(((*S*)-1-((2*S*,4*R*)-4-hydroxy-2-((4-(4-methylthiazol-5-yl)benzyl)carbamoyl)pyrrolidin-1-yl)-3,3-dimethyl-1-oxobutan-2-yl)amino)-2-oxoethoxy)ethyl)carbamate (**22b**; 90.00 mg, 0.12 mmol, 1.00 eq) was dissolved in dry DCM (0.47 mL, 0.25 M) and TFA (0.47 mL) was slowly added. The mixture was stirred for 30 min upon completion as determined by TLC. After removal of the volatiles, the oily residue was dried further under high vacuum to give **23b** as TFA salt, [52] without further purification in quantitative yield that matched the reported spectral data. [167]

(Z)-N-(2-(2-(2-((2-(2,6-Dioxopiperidin-3-yl)-1-oxoisoindolin-4-yl)amino)-2-oxoethoxy) ethoxy)ethyl)-3-(5-(4-ethylbenzylidene)-4-oxo-2-thioxothiazolidin-3-yl)propanamide (ASA-1)

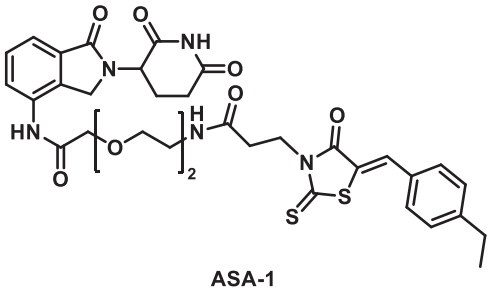

ASA-1

2-(2-(2-Aminoethoxy)ethoxy)-*N*-(2-(2,6-dioxopiperidin-3-yl)-1-oxoisoindolin-4-yl)acetamide 2,2,2-trifluoroacetate (**11a**; 100 mg, 0.19 mmol, 1 eq) was added to a stirring solution of **ASA-5** (74 mg, 0.23 mmol, 1.2 eq) and DIPEA (0.2 mL, 1.16 mmol, 6 eq) in dry DMF (1 mL, 0.19 M). After 15 min, HATU (88 mg, 0.23 mmol, 1.2 eq) and the reaction mixture was allowed to stir at room temperature for 12 h. Upon completion of the reaction as determined by HPLC / MS, the organic layer was washed with AcOEt and water, dried over Na_2SO_4, filtered, and concentrated. The crude was purified with reverse-phase column chromatography (47 % CH_3CN in 0.1 % aq. HCO_2H) to give **ASA-1** as a yellow solid (67 mg, **49 %**). [52] **^{1}H NMR** (400 MHz, $CDCl_3$) δ 1.26 (t, *J* = 7.8 Hz, 3H), 2.16 – 2.23 (m, 1H), 2.32 – 2.42 (m, 1H), 2.52 – 2.60 (m, 2H), 2.70 (q, *J* = 7.5 Hz, 2H), 2.75 – 2.84 (m, 1H), 2.85 – 2.93 (m, 1H), 3.23 – 3.33 (m, 1H), 3.36 – 3.48 (m, 1H), 3.54 – 3.58 (m, 2H), 3.66 – 3.72 (m, 2H), 3.76 – 3.80 (m, 2H), 4.15 (d, *J* = 6.1 Hz, 2H), 4.34 – 4.39 (m, 2H), 4.42 (s, 1H), 4.46 (s, 1H), 5.22 (dd, *J* = 5.2, 13.3 Hz, 1H), 6.29 (t, *J* = 5.7 Hz, 1H), 7.31 (d, *J* = 8.3 Hz, 2H), 7.41 (d, *J* = 8.3 Hz, 2H), 7.48 (t, *J* = 7.8 Hz, 1H), 7.71 (d, *J* = 1.0 Hz, 1H), 7.73 (s, 1H), 7.80 (d, *J* = 1.0 Hz, 1H), 8.69 (s, 1H), 8.74 (s, 1H).**^{13}C NMR** (101 MHz, $CDCl_3$) δ 15.3, 23.6, 29.1, 31.7, 33.4, 39.2, 40.9, 46.3, 52.0, 70.0, 70.1, 70.7, 71.4, 121.5, 121.6, 126.0, 129.2, 129.2, 129.5, 130.8, 131.1, 131.1, 132.0, 132.9, 134.0, 134.2, 148.3, 168.0, 168.5, 168.9, 169.9, 170.2, 171.5, 193.4. **HRMS** *m/z* calc. for $C_{34}H_{37}N_5O_8S_2$ $[M+H]^+$ 708.2080, found 708.2149.

(Z)-N-(2-(2,6-Dioxopiperidin-3-yl)-1-oxoisoindolin-4-yl)-14-(3-(5-(4-ethylbenzylidene)-4-oxo-2-thioxothiazolidin-3-yl)propanamido)-3,6,9,12-tetraoxatetradecanamide (ASA-2)

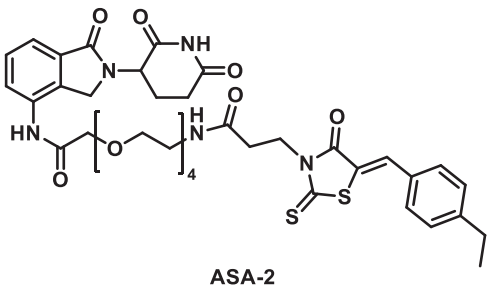

ASA-2

2-(2-(2-Aminoethoxy)ethoxy)-*N*-(2-(2,6-dioxopiperidin-3-yl)-1-oxoisoindolin-4-yl)acetamide 2,2,2-trifluoroacetate (**11b**; as TFA salt (90 mg, 0.15 mmol, 1 eq) was added to a stirring solution of **ASA-5** (57 mg, 0.18 mmol, 1.2 eq) and DIPEA (0.2 mL, 0.89 mmol, 6 eq) in dry DMF (0.9 mL, 0.16 M). After 15 min, HATU (68 mg, 0.18 mmol, 1.2 eq) and the reaction mixture was allowed to stir at room temperature for 12 h. Upon completion of the reaction as determined by HPLC / MS, the organic layer was washed with AcOEt and water, dried over Na_2SO_4, filtered, and concentrated. The crude was purified with reverse-phase column chromatography (49 % CH_3CN in 0.1 % aq. HCO_2H) to give **ASA-2** as a yellow solid (42 mg, **36 %**). [52] **^{1}H NMR** (400 MHz, $CDCl_3$) δ 1.25 (t, *J* = 3.8 Hz, 3H), 2.19 – 2.25 (m, 1H), 2.33 – 2.42 (m, 1H), 2.61 (t, *J* = 7.9 Hz, 2H), 2.70 (q, *J* = 7.6 Hz, 2H), 2.77 – 2.90 (m, 2H), 3.28 – 3.40 (m, 2H), 3.42 – 3.48 (m, 6H), 3.55 – 3.59 (m, 2H), 3.66 – 3.69 (m, 2H), 3.70 – 3.73 (m, 2H), 3.76 – 3.80 (m, 2H), 4.15 (d, *J* = 4.6 Hz, 2H), 4.39 – 4.44 (m, 2H), 4.44 (s, 2H), 5.25 (dd, *J* = 5.2, 13.3 Hz, 1H), 6.58 (t, *J* = 5.5 Hz, 1H), 7.31 (d, *J* = 8.2 Hz, 2H), 7.42 (d, *J* = 8.2 Hz, 2H), 7.48 (t, *J* = 7.7 Hz, 1H), 7.72 – 7.74 (m, 2H), 7.82 (d, *J* = 7.9 Hz, 1H), 8.69 (s, 1H), 9.00 (s, 1H). **^{13}C NMR** (101 MHz, CDCl3) δ 15.3, 23.6, 29.1, 29.8, 31.7, 33.2, 39.2, 41.1, 46.3, 51.9, 69.9, 70.0, 70.0, 70.2, 70.4, 70.6, 70.7, 71.4, 121.5, 121.7, 126.3, 129.1, 129.3, 130.9, 131.1, 131.1, 132.3, 132.8, 134.0, 134.3, 148.2, 167.9, 168.6, 169.0, 169.7, 170.0, 171.6, 193.4. **HRMS** *m/z* calc. for $C_{38}H_{45}N_5O_8S_2$ $[M+H]^+$ 796.2600, found 796.2700.

(Z)-N-(2-(2,6-Dioxopiperidin-3-yl)-1-oxoisoindolin-4-yl)-2-(2-(2-((5-(4-ethylbenzylidene)-4-oxo-4,5-dihydrothiazol-2-yl)amino)ethoxy)ethoxy)acetamide (ASA-7)

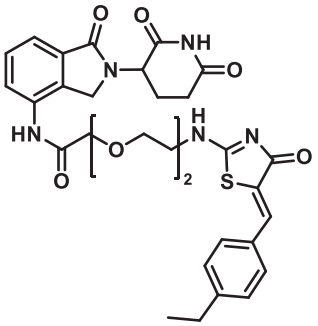

ASA-7

2-(2-(2-Aminoethoxy)ethoxy)-*N*-(2-(2,6-dioxopiperidin-3-yl)-1-oxoisoindolin-4-yl)acetamide 2,2,2-trifluoroacetate (**11a**; 122 mg, 0.24 mmol, 1 eq) was added to a stirring solution of **ASA-6** (91 mg, 0.28 mmol, 1.2 eq) and DIPEA (0.3 mL, 1.14 mmol, 6 eq) in dry DMF (1 mL, 0.20 M). After 15 min, HATU (107 mg, 0.28 mmol, 1.2 eq) and the reaction mixture was allowed to stir at room temperature for 12 h. Upon completion of the reaction as determined by HPLC / MS, the organic layer was washed with AcOEt and water, dried over Na_2SO_4, filtered, and concentrated. The crude was purified with reverse-phase column chromatography (47 % CH_3CN in 0.1 % aq. HCO_2H) to give **ASA-7** as a white solid (75.60 mg, **45 %**). [52] **^{1}H NMR** (400 MHz, $CDCl_3$) δ 1.26 (t, *J* = 7.0 Hz, 3H), 2.12 – 2.22 (m, 1H), 2.26 – 2.42 (m, 1H), 2.63 – 2.73 (m, 2H), 2.75 – 2.91 (m, 2H), 3.56 (t, *J* = 5.3 Hz, 1H), 3.76 (dd, *J* = 5.9, 18.6 Hz, 6H), 3.84 – 3.96 (m, 1H), 4.14 – 4.20 (m, 2H), 4.35 – 4.55 (m, 2H), 5.15 – 5.26 (m, 1H), 7.23 (d, *J* = 8.2 Hz, 1H), 7.28 (d, *J* = 8.2 Hz, 1H), 7.34 (d, *J* = 8.2 Hz, 1H), 7.42 (s, 1H), 7.42 – 7.45 (m, 1H), 7.66 (d, *J* = 7.5 Hz, 1H), 7.72 (d, *J* = 7.1 Hz, 1H), 7.79 (dd, *J* = 8.0, 8.0 Hz, 1H), 8.67 – 8.82 (m, 2H), 9.28 (s, 1H). **^{13}C NMR** (126 MHz, CDCl3) δ 15.4, 23.4, 29.0, 29.8, 31.6, 52.0, 70.3, 70.4, 70.7, 71.3, 121.4, 126.2, 128.7, 128.9, 129.4, 130.1, 130.1, 131.6, 132.0, 132.1, 132.7, 132.8, 134.3, 147.2, 168.5, 168.9, 169.0, 170.8, 171.8, 175.6, 181.5. **HRMS** *m/z* calc. for $C_{31}H_{33}N_5O_7S$ $[M+H]^+$ 620.2100, found 620.2169.

(Z)-N-(2-(2,6-Dioxopiperidin-3-yl)-1-oxoisoindolin-4-yl)-14-((5-(4-ethylbenzylidene)-4-oxo-4,5-dihydrothiazol-2-yl)amino)-3,6,9,12-tetraoxatetradecanamide (ASA-8)

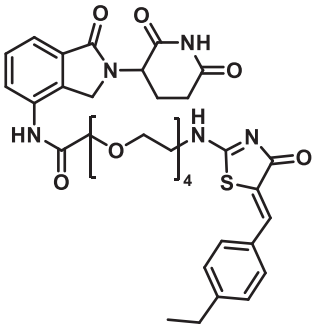

ASA-8

2-(2-(2-Aminoethoxy)ethoxy)-*N*-(2-(2,6-dioxopiperidin-3-yl)-1-oxoisoindolin-4-yl)acetamide 2,2,2-trifluoroacetate (**11b**; 100 mg, 0.17 mmol, 1 eq) was added to a stirring solution of **ASA-6** (64 mg, 0.20 mmol, 1.2 eq) and DIPEA (0.2 mL, 0.99 mmol, 6 eq) in dry DMF (1 mL, 0.17 M). After 15 min, HATU (75 mg, 0.20 mmol, 1.2 eq) and the reaction mixture was allowed to stir at room temperature for 12 h. Upon completion of the reaction as determined by HPLC / MS, the organic layer was washed with AcOEt and water, dried over Na_2SO_4, filtered, and concentrated. The crude was purified with reverse-phase column chromatography (47 % CH_3CN in 0.1 % aq. HCO_2H) to give **ASA-8** as a white solid, (25 mg, **19 %**). [52] **^{1}H NMR** (400 MHz, $CDCl_3$) δ 1.26 (t, *J* = 3.5 Hz, 3H), 2.16 – 2.26 (m, 1H), 2.30 – 2.43 (m, 1H), 2.68 (q, *J* = 5.3 Hz, 2H), 2.76 – 2.94 (m, 4H), 3.43 – 3.48 (m, 2H), 3.49 – 3.52 (m, 2H), 3.53 – 3.61 (m, 2H), 3.62 – 3.74 (m, 6H), 3.76 – 3.87 (m, 2H), 4.19 (d, *J* = 6.0 Hz, 2H), 4.43 – 4.48 (m, 2H), 5.21 – 5.28 (m, 1H), 7.25 (s, 1H), 7.29 (s, 1H), 7.41 (d, *J* = 8.2 Hz, 1H), 7.45 (d, *J* = 8.2 Hz, 1H), 7.51 (t, *J* = 7.4 Hz, 1H), 7.73 – 7.77 (m, 2H), 7.77 (s, 1H), 8.51 (s, 1H), 8.93 (s, 1H), 9.28 (s, 1H). **^{13}C NMR** (126 MHz, $CDCl_3$) δ 15.4, 23.6, 29.0, 29.9, 31.7, 52.0, 68.8, 69.2, 70.0, 70.2, 70.3, 70.6, 71.4, 71.5, 121.6, 126.1, 127.0, 127.8, 128.7, 129.2, 129.4, 130.0, 131.7, 131.8, 132.3, 132.4, 134.1, 146.6, 168.6, 169.1, 169.9, 171.1, 171.5, 175.1, 181.4. **HRMS** *m/z* calc. for $C_{35}H_{41}N_5O_9S$ $[M+H]^+$ 708.2620, found 708.2693.

(2*S*,4*R*)-1-((*S*)-2-(*tert*-Butyl)-15-(5-((*Z*)-4-ethylbenzylidene)-4-oxo-2-thioxothiazolidin-3-yl)-4,13-dioxo-6,9-dioxa-3,12-diazapentadecanoyl)-4-hydroxy-*N*-(4-(4-methylthiazol-5-yl)benzyl)pyrrolidine-2-carboxamide (ASA-3)

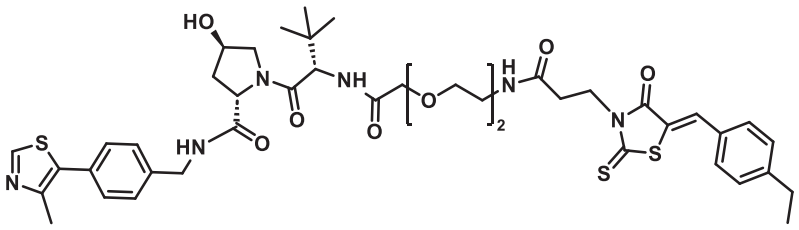

ASA-3

(2*S*,4*R*)-1-((*S*)-2-(2-(2-Aminoethoxy)acetamido)-3,3-dimethylbutanoyl)-4-hydroxy-*N*-(4-(4-methylthiazol-5-yl)benzyl)pyrrolidine-2-carboxamide 2,2,2-trifluoroacetate (**23a**; 100 mg, 0.15 mmol, 1 eq) was added to a stirring solution of **ASA-5** (56 mg, 0.17 mmol, 1.2 eq) and DIPEA (0.2 mL, 0.87 mmol, 6 eq) in dry DMF (1 mL, 0.18 M). After 15 min, HATU (66 mg, 0.17 mmol, 1.2 eq) and the reaction mixture was allowed to stir at room temperature for 12 h. Upon completion of the reaction as determined by HPLC / MS, the organic layer was washed with AcOEt and water, dried over Na_2SO_4, filtered, and concentrated. The crude was purified with reverse-phase column chromatography (25 % CH_3CN in 0.1 % aq. HCO_2H) to give **ASA-3** as a yellow solid (27 mg, **21 %**). [52] **^{1}H NMR** (400 MHz, $CDCl_3$) δ 0.99 (s, 9H), 1.24 – 1.26 (m, 3H), 2.19 – 2.28 (m, 1H), 2.38 – 2.47 (m, 1H), 2.51 (d, *J* = 2.4 Hz, 1H), 2.51 (s, 3H), 2.67 – 2.71 (m, 2H), 2.72 – 2.83 (m, 1H), 3.05 (s, 1H), 3.22 – 3.31 (m, 1H), 3.40 – 3.57 (m, 3H), 3.58 – 3.64 (m, 2H), 3.67 – 3.77 (m, 2H), 3.82 – 3.89 (m, 1H), 3.90 – 3.94 (m, 2H), 3.96 – 3.99 (m, 1H), 4.15 – 4.25 (m, 1H), 4.36 – 4.44 (m, 1H), 4.46 – 4.63 (m, 4H), 4.69 (t, *J* = 8.3 Hz, 2H), 7.23 (d, *J* = 5.2 Hz, 1H), 7.30 (d, *J* = 8.2 Hz, 2H), 7.35 (s, 4H), 7.40 (d, *J* = 8.2 Hz, 2H), 7.53 (d, *J* = 9.6 Hz, 1H), 7.67 (s, 1H), 8.67 (s, 1H). **^{13}C NMR** (101 MHz, $CDCl_3$) δ 15.3, 16.3, 22.8, 26.6, 29.1, 29.8, 31.7, 33.0, 36.5, 36.9, 39.4, 40.9, 43.5, 56.8, 57.5, 59.1, 70.3, 70.4, 70.6, 70.7, 71.7, 121.8, 128.2, 128.2, 129.2, 129.7, 129.7, 130.8, 131.1, 131.1, 131.2, 133.9, 138.1, 148.3, 148.7, 150.5, 168.2, 170.2, 170.8, 171.1, 171.2, 193.2. **HRMS** *m/z* calc. for $C_{43}H_{54}N_6O_8S_3$ $[M+H]^+$ 879.3170, found 879.33.

(2*S*,4*R*)-1-((S)-2-(*tert*-Butyl)-21-(5-((*Z*)-4-ethylbenzylidene)-4-oxo-2-thioxothiazolidin-3-yl)-4,19-dioxo-6,9,12,15-tetraoxa-3,18-diazahenicosanoyl)-4-hydroxy-*N*-(4-(4-methylthiazol-5-yl)benzyl)pyrrolidine-2-carboxamide (ASA-4)

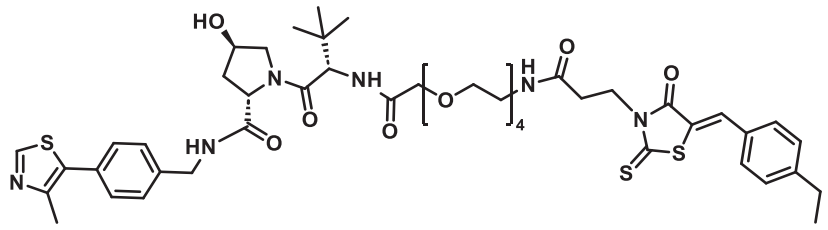

ASA-4

(2*S*,4*R*)-1-((*S*)-2-(2-(2-Aminoethoxy)acetamido)-3,3-dimethylbutanoyl)-4-hydroxy-*N*-(4-(4-methylthiazol-5-yl)benzyl)pyrrolidine-2-carboxamide 2,2,2-trifluoroacetate (**23b**; 90 mg, 0.12 mmol, 1 eq) was added to a stirring solution of **ASA-5** (45 mg, 0.14 mmol, 1.2 eq) and DIPEA (0.1 mL, 0.69 mmol, 6 eq) in dry DMF (0.7 mL, 0.18 M). After 15 min, HATU (53 mg, 0.14 mmol, 1.2 eq) and the reaction mixture was allowed to stir at room temperature for 12 h. Upon completion of the reaction as determined by HPLC / MS, the organic layer was washed with AcOEt and water, dried over Na_2SO_4, filtered, and concentrated. The crude was purified with reverse-phase column chromatography (59 % CH_3CN in 0.1 % aq. HCO_2H) to give **ASA-4** as a yellow solid (60 mg, **53 %**). [52] **^{1}H NMR** (400 MHz, $CDCl_3$) δ 0.95 (s, 9H), 1.24 (t, *J* = 3.2 Hz, 3H), 2.19 – 2.23 (m, 1H), 2.50 (s, 3H), 2.51 (s, 1H), 2.63 (d, *J* = 7.6 Hz, 1H), 2.66 – 2.71 (m, 2H), 3.34 – 3.40 (m, 2H), 3.52 (t, *J* = 5.0 Hz, 2H), 3.59 (s, 4H), 3.61 – 3.67 (m, 10H), 4.00 (d, *J* = 1.7 Hz, 2H), 4.04 – 4.08 (m, 1H), 4.40 – 4.45 (m, 2H), 4.48 – 4.53 (m, 2H), 4.54 – 4.61 (m, 2H), 4.80 (t, *J* = 8.2 Hz, 1H), 6.72 – 6.79 (m, 1H), 7.24 (d, *J* = 8.4 Hz, 1H), 7.29 (d, *J* = 8.2 Hz, 2H), 7.34 (d, *J* = 5.0 Hz, 1H), 7.36 (s, 3H), 7.38 (d, *J* = 8.2 Hz, 2H), 7.46 (t, *J* = 6.0 Hz, 1H), 7.65 (s, 1H), 7.94 (d, *J* = 8.2 Hz, 1H), 8.66 (s, 1H). **^{13}C NMR** (101 MHz, $CDCl_3$) δ 15.3, 16.2, 22.8, 26.6, 29.1, 29.8, 31.7, 33.1, 35.6, 36.6, 39.5, 41.1, 43.4, 57.1, 57.2, 58.8, 69.7, 70.3, 70.5, 70.5, 70.6, 70.7, 70.7, 70.8, 71.0, 121.7, 128.2, 128.2, 129.1, 129.6, 129.6, 130.9, 131.0, 131.1, 131.1, 131.8, 134.0, 138.4, 148.2, 148.6, 150.4, 167.9, 170.0, 170.2, 171.3, 171.3, 193.5. **HRMS** *m/*z calc. for $C_{47}H_{62}N_6O_{10}S_3$ $[M+H]^+$ 967.3690, found 967.3765.

(2*S*,4*R*)-1-((*S*)-2-(2-(2-(2-((5-((*Z*)-4-Ethylbenzylidene)-4-oxo-4,5-dihydrothiazol-2-yl)amino)ethoxy)ethoxy)acetamido)-3,3-dimethylbutanoyl)-4-hydroxy-*N*-(4-(4-methylthiazol-5-yl)benzyl)pyrrolidine-2-carboxamide (ASA-9)

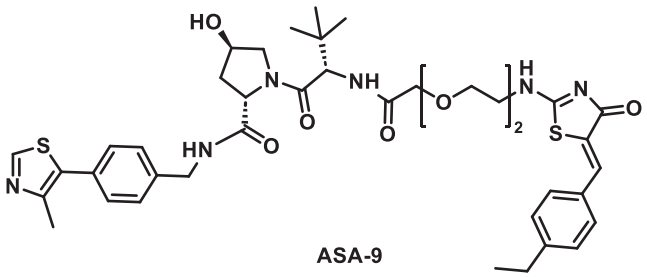

ASA-9

(2*S*,4*R*)-1-((*S*)-2-(2-(2-Aminoethoxy)acetamido)-3,3-dimethylbutanoyl)-4-hydroxy-*N*-(4-(4-methylthiazol-5-yl)benzyl)pyrrolidine-2-carboxamide 2,2,2-trifluoroacetate (**23a**; 100 mg, 0.15 mmol, 1 eq) was added to a stirring solution of **ASA-6** (56 mg, 0.17 mmol, 1.2 eq) and DIPEA (0.2 mL, 0.87 mmol, 6 eq) in dry DMF (1 mL, 0.18 M). After 15 min, HATU (66 mg, 0.17 mmol, 1.2 eq) and the reaction mixture was allowed to stir at room temperature for 12 h. Upon completion of the reaction as determined by HPLC / MS, the organic layer was washed with AcOEt and water, dried over Na_2SO_4, filtered, and concentrated. The crude was purified with reverse-phase column chromatography (45 % CH_3CN in 0.1 % aq. HCO_2H) to give **ASA-9** as a white solid (35 mg, **31 %**). [52] **^{1}H NMR** (400 MHz, $CDCl_3$) δ 1.06 (s, 9H), 1.25 (d, *J* = 3.7 Hz, 3H), 2.29 – 2.38 (m, 1H), 2.46 (s, 3H), 2.69 (q, *J* = 7.5 Hz, 2H), 3.22 – 3.32 (m, 1H), 3.35 – 3.46 (m, 1H), 3.50 – 3.60 (m, 2H), 3.61 – 3.64 (m, 2H), 3.66 – 3.72 (m, 2H), 3.84 – 3.92 (m, 2H), 3.92 – 3.97 (m, 2H), 3.98 – 4.04 (m, 2H), 4.08 (s, 1H), 4.65 – 4.80 (m, 2H), 4.81 – 4.87 (m, 2H), 7.20 – 7.23 (m, 2H), 7.25 (s, 2H), 7.26 – 7.29 (m, 2H), 7.41 (d, *J* = 8.2 Hz, 2H), 7.61 (d, *J* = 9.7 Hz, 1H), 7.73 (s, 1H), 8.64 (s, 1H), 8.89 (dd, *J* = 4.2, 7.8 Hz, 1H), 4.64 – 4.69 (m, 1H). **^{13}C NMR** (101 MHz, $CDCl_3$) δ 15.3, 16.2, 26.4, 26.5, 28.9, 29.7, 31.6, 36.8, 37.9, 43.0, 44.8, 56.3, 57.3, 59.8, 69.7, 69.9, 70.4, 71.3, 77.2, 125.4, 128.2, 128.5, 128.6, 128.7, 128.9, 129.5, 129.8, 130.3, 131.4, 131.8, 132.2, 139.1, 146.8, 148.3, 150.1, 150.4, 169.9, 170.1, 171.8, 180.2. **HRMS** *m/z* calc. for $C_{40}H_{50}0N_6O_7S_2$ $[M+H]^+$ 791.3180, found 791.3239.

(2*S*,4*R*)-1-((S)-2-(*tert*-Butyl)-17-((5-((*Z*)-4-ethylbenzylidene)-4-oxo-4,5-dihydrothiazol-2-yl)amino)-4-oxo-6,9,12,15-tetraoxa-3-azaheptadecanoyl)-4-hydroxy-*N*-(4-(4-methylthiazol-5-yl)benzyl)pyrrolidine-2-carboxamide (ASA-10)

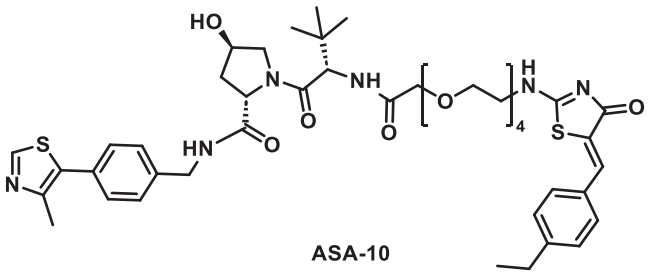

ASA-10

(2*S*,4*R*)-1-((*S*)-2-(2-(2-Aminoethoxy)acetamido)-3,3-dimethylbutanoyl)-4-hydroxy-*N*-(4-(4-methylthiazol-5-yl)benzyl)pyrrolidine-2-carboxamide 2,2,2-trifluoroacetate (**23b**; 90 mg, 0.12 mmol, 1 eq) was added to a stirring solution of **ASA-6** (45 mg, 0.14 mmol, 1.2 eq) and DIPEA (0.1 mL, 0.69 mmol, 6 eq) in dry DMF (0.8 mL, 0.15 M). After 15 min, HATU (53 mg, 0.14 mmol, 1.2 eq) and the reaction mixture was allowed to stir at room temperature for 12 h. Upon completion of the reaction as determined by HPLC / MS, the organic layer was washed with AcOEt and water, dried over Na_2SO_4, filtered, and concentrated. The crude was purified with reverse-phase column chromatography (59 % CH_3CN in 0.1 % aq. HCO_2H) to give **ASA-10** as a yellow solid (29 mg, **21 %**). [52] **^{1}H NMR** (400 MHz, $CDCl_3$) δ 0.94 – 1.00 (m, 9H), 1.21 – 1.24 (m, 3H), 2.11 – 2.23 (m, 1H), 2.49 (s, 1H), 2.50 – 2.52 (m, 3H), 2.65 – 2.69 (m, 2H), 2.85 (q, *J* = 7.0 Hz, 1H), 3.61 – 3.65 (m, 8H), 3.68 – 3.72 (m, 6H), 3.79 – 3.85 (m, 1H), 4.02 – 4.08 (m, 2H), 4.11 (d, *J* = 1.4 Hz, 1H), 4.13 – 4.19 (m, 1H), 4.33 – 4.39 (m, 1H), 4.51 – 4.65 (m, 4H), 4.73 (t, *J* = 8.0 Hz, 1H), 7.24 (s, 1H), 7.27 – 7.28 (m, 1H), 7.30 – 7.33 (m, 1H), 7.34 – 7.36 (m, 4H), 7.40 (d, *J* = 8.1 Hz, 1H), 7.42 – 7.47 (m, 1H), 7.75 (s, 1H), 7.90 (t, *J* = 6.0 Hz, 1H), 8.36 (s, 1H), 8.64 – 8.70 (m, 1H). **^{13}C NMR** (101 MHz, $CDCl_3$) δ 15.3, 16.1, 26.4, 26.5, 28.8, 29.7, 35.3, 35.5, 43.2, 45.0, 56.8, 57.1, 57.4, 58.6, 59.1, 69.2, 70.2, 70.3, 70.5, 70.6, 70.7, 70.9, 77.2, 126.9, 128.1, 128.1, 128.6, 128.6, 129.3, 129.4, 129.5, 129.9, 129.9, 131.3, 132.1, 138.1, 146.3, 146.7, 148.4, 150.4, 170.4, 170.8, 171.2, 174.9. **HRMS** *m/z* calc. for $C_{44}H_{58}N_6O_9S_2$ $[M+H]^+$ 879.3710, found 879.3763.

Synthesis of 2nd series of cMyc- based PROTACs

tert-Butyl (8-(4-oxo-2-thioxothiazolidin-3-yl)octyl)carbamate (26)

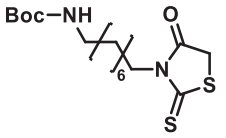

26

In a 10 mL Pyrex glass tube were placed bis(carboxymethyl)trithiocarbonate (**25**; 278 mg, 1.23 mmol, 1 eq), DME (1.4 mL, 0.88 M), DIPEA (0.2 mL, 1 eq) and *tert*-butyl (8-aminooctyl)carbamate (**24**; 300 mg, 1.23 mmol, 1 eq). The reaction mixture was heated at 90 ºC for 1 h. After completion of the reaction followed by TLC, the organic layer was washed with AcOEt and water, dried over Na_2SO_4, filtered, and concentrated. The crude was purified with column chromatography (100 % DCM) to give **26** as a yellow oil (331 mg, **78 %**) that matched the reported spectral data. [170, 171] **^{1}H NMR** (400 MHz, $CDCl_3$) δ 1.30 (s, 8H, C$\underline{H_2}$ octyl chain), 1.44 (s, 11H, 3C$\underline{H_3}$Boc + C$\underline{H_2}$ octyl chain), 1.62 (t, *J* = 7.3 Hz, 2H, C$\underline{H_2}$ octyl chain), 3.10 (q, *J* = 6.7 Hz, 2H, $CH_2C\underline{H_2}NH$), 3.96 (t, *J* = 8.3 Hz, 4H, N-C$\underline{H_2}C\underline{H_2}$), 4.49 (bs, 1H, N$\underline{H}$). **^{13}C NMR** (101 MHz, $CDCl_3$) δ 26.8 (C$\underline{H_2}$ octyl chain), 26.8 (C$\underline{H_2}$ octyl chain), 28.6 (3C$\underline{H_3}$-Boc), 29.1, 29.2 (2C, C$\underline{H_2}$ octyl chain), 30.2 (C$\underline{H}$), 35.5 (N-$CH_2C\underline{H_2}$), 40.7 ($CH_2C\underline{H_2}NH$), 44.9 (N-C$\underline{H_2}CH_2$), 79.2 (C-Boc), 156.1 (NH-C=O), 174.0 (C=O), 201.4 (C=S). **HRMS** *m/z* calc. for $C_{16}H_{28}N_2O_3S_2$ $[M+H]^+$ 361.1540, found 361.1621.

tert-Butyl (2-(2-(2-(2-(4-oxo-2-thioxothiazolidin-3-yl)ethoxy)ethoxy)ethoxy)ethyl) carbamate (34)

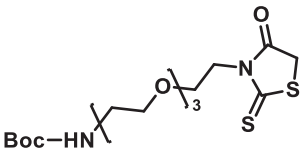

34

In a 10 mL Pyrex glass tube were placed bis(carboxymethyl)trithiocarbonate (**25**; 97 mg, 0.43 mmol, 1 eq), DME (0.5 mL, 0.88 M), DIPEA (0.1 mL, 1 eq) and *tert*-butyl (2-(2-(2-(2-aminoethoxy)ethoxy)ethoxy)ethyl)carbamate (**33**; 125 mg, 0.43 mmol, 1 eq). The reaction mixture was heated at 90 ºC for 1 h. After 30 min and completion of the reaction followed by TLC, the organic layer was washed with AcOEt and water, dried over Na_2SO_4, filtered, and concentrated. The crude was purified with column chromatography (100 % DCM) to give **34** as a yellow oil (170 mg, **97 %**). [170, 171] **^{1}H NMR** (400 MHz, $CDCl_3$, HETCOR) δ 1.44 (s, 9H, 3C$\underline{H_3}$Boc), 3.28 – 3.34 (m, 2H, $CH_2C\underline{H_2}NH$), 3.53 (t, *J* = 5.1 Hz, 2H, C$\underline{H_2}CH_2NH$), 3.58 – 3.60 (m, 2H, C$\underline{H_2}$ octyl chain), 3.61 (s, 4H, C$\underline{H_2}$ octyl chain), 3.62 – 3.65 (m, 2H, C$\underline{H_2}$ octyl chain), 3.75 (t, *J* = 5.8 Hz, 2H, N-$CH_2C\underline{H_2}O$), 3.99 (s, 2H, C$\underline{H_2}$), 4.22 (t, *J* = 5.8 Hz, 2H, N-C$\underline{H_2}CH_2O$), 5.06 (s, 1H, N$\underline{H}$). **^{13}C NMR** (101 MHz, $CDCl_3$, HETCOR) δ 28.4 (3C$\underline{H_3}$ Boc), 35.3 (C$\underline{H_2}$), 40.4 ($CH_2C\underline{H_2}NH$), 43.5 (N-C$\underline{H_2}CH_2O$), 66.5 (N-$CH_2C\underline{H_2}O$), 70.2 (C$\underline{H_2}$ octyl

chain), 70.3 (<u>C</u>$H_2$$CH_2$NH), 70.6 (<u>C</u>$H_2$ octyl chain), 70.6 (<u>C</u>H_2 octyl chain), 79.3 (<u>C</u>-Boc), 156.1 (<u>C</u>=O Boc), 173.9 (<u>C</u>=O), 201.4 (<u>C</u>=S). **HRMS** *m/z* calc. for $C_{16}H_{28}N_2O_6S_2$ $[M+H]^+$ 409.1390, found 409.1460.

(*Z*)-3-(8-Aminooctyl)-5-(4-isopropylbenzylidene)-2-thioxothiazolidin-4-one 2,2,2-trifluoroacetate (30)

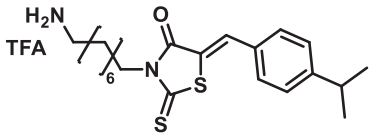

30

4-Isopropylbenzaldehyde (**27**; 0.1 mL, 0.43 mmol, 1 eq) and **26** (307 mg, 0.85 mmol, 2 eq) were placed in a 10 mL Pyrex glass tube and stirred overnight at 140 ºC. After completion followed by HPLC / MS, the organic layer was washed with AcOEt and water, dried over Na_2SO_4, filtered, and concentrated. The crude was purified with column chromatography (95 % Hex / 5 % AcOEt) to give **28** as a yellow solid (154 mg, **74 %**) [172] that matched the reported spectral data. [170] Then, *tert*-butyl (*Z*)-(8-(5-(4-isopropylbenzylidene)-4-oxo-2-thioxothiazolidin-3-yl)octyl)carbamate (**28**; 247 mg, 0.51 mmol) was dissolved in dry DCM (2 mL, 0.25 M), and TFA (2 mL) was slowly added. The mixture was stirred for 30 min upon completion as determined by TLC. After removal of the volatiles, the oily residue was dried further under high vacuum to give **30** as TFA salt, [52] without further purification in quantitative yield that matched the reported spectral data. [170] **^{1}H NMR** (400 MHz, $CDCl_3$) δ 1.27 (s, 3H), 1.28 (s, 3H), 1.29 – 1.32 (m, 4H), 1.32 – 1.36 (m, 4H), 1.44 (s, 11H), 1.66 – 1.75 (m, 2H), 2.92 – 3.00 (m, 1H), 3.06 – 3.13 (m, 2H), 4.11 (t, *J* = 7.4 Hz, 2H), 4.49 (bs, 1H), 7.34 (d, *J* = 8.4 Hz, 2H), 7.44 (d, *J* = 8.3 Hz, 2H), 7.71 (s, 1H). **HRMS** *m/z* calc. for $C_{26}H_{38}N_2O_3S_2$ $[M+H]^+$ 491.2320, found 491.2399.

(*Z*)-3-(8-Aminooctyl)-5-(4-ethylbenzylidene)-2-thioxothiazolidin-4-one 2,2,2-trifluoroacetate (31)

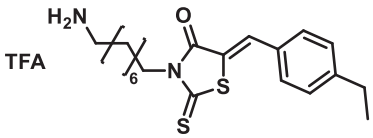

31

4-Ethylbenzaldehyde (**2**; 59 mg, 0.44 mmol, 1 eq) and **26** (319 mg, 0.88 mmol, 2 eq) were placed in a 10 mL Pyrex glass tube and stirred overnight at 140 ºC. After completion followed by HPLC / MS, the organic layer was washed with AcOEt and water, dried over Na_2SO_4, filtered, and concentrated. The crude was purified with column chromatography (96 % Hex / 4 % AcOEt) to give **29** as a yellow solid (161 mg, **76 %**). [171, 172]
Then, *tert*-butyl (*Z*)-(8-(5-(4-Ethylbenzylidene)-4-oxo-2-thioxothiazolidin-3-yl)octyl)carbamate (**29**; 161 mg, 0.34 mmol, 1 eq) was dissolved in dry DCM (1.4 mL, 0.25

M), and TFA (1.4 mL) was slowly added. The mixture was stirred for 30 min upon completion as determined by TLC. After removal of the volatiles, the oily residue was dried further under high vacuum to give **31** as TFA salt, [52] without further purification in quantitative yield. **^{1}H NMR** (400 MHz, $CDCl_3$, HETCOR) δ 1.26 (t, *J* = 7.6 Hz, 3H, CH_2CH_3), 1.29 – 1.32 (m, 4H, CH_2 octyl chain), 1.33 – 1.37 (m, 4H, CH_2 octyl chain), 1.44 (s, 11H, CH_2 octyl chain + $3CH_3$ Boc), 1.71 (d, *J* = 7.8 Hz, 2H, CH_2 octyl chain), 2.70 (q, *J* = 7.6 Hz, 2H, CH_2CH_3), 3.10 (q, *J* = 6.7 Hz, 2H, (CH_2CH_2NH), 4.11 (t, *J* = 8.8 Hz, 2H, N-CH_2CH_2-O), 4.49 (bs, 1H, CH_2CH_3), 7.31 (d, *J* = 8.2 Hz, 2H, CHAr), 7.43 (d, *J* = 8.2 Hz, 2H, CHAr), 7.71 (s, 1H, CH). **^{13}C NMR** (101 MHz, $CDCl_3$,HETCOR) δ 15.2 (CH_2CH_3), 26.7 (CH_2 octyl chain), 26.7 (CH_2 octyl chain), 26.9 (CH_2 octyl chain), 28.4 ($3CH_3$ Boc), 28.9 (CH_2CH_3), 29.1 (CH_2 octyl chain), 29.1 (CH_2 octyl chain), 30.0 (CH_2 octyl chain), 40.6 (CH_2CH_2NH), 44.6 (N-CH_2CH_2-O), 79.0 (CCH_3 Boc, 121.9 (CS), 129.0 (2C, CH_2CH_3- CAr), 130.8 (2C, CAr), 130.9 (C-Aryl), 133.2 (CH), 147.8 (C=O Boc), 167.9 (C=O), 193.5 (C=S). **HRMS** *m/z* calc. for $C_{25}H_{36}N_2O_3S_2$ $[M+H]^+$ 477.217, found 477.2240.

(*Z*)-3-(2-(2-(2-(2-Aminoethoxy)ethoxy)ethoxy)ethyl)-5-(4-isopropylbenzylidene)-2-thioxothiazolidin-4-one 2,2,2-trifluoroacetate (37)

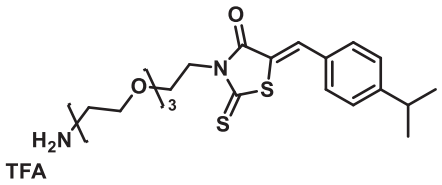

37

4-Isopropylbenzaldehyde (**27**; 50 mg, 0.34 mmol, 1 eq) and **34** (138 mg, 0.34 mmol, 1 eq) were placed in a 10 mL Pyrex glass tube and stirred overnight at 140 ºC. After completion followed by HPLC / MS, the organic layer was washed with AcOEt and water, dried over Na_2SO_4, filtered, and concentrated. The crude was purified with column chromatography (96 % Hex / 4 % AcOEt) to give **35** as a yellow solid (137 mg, **76 %**). [170, 171] Then, *tert*-butyl (*Z*)-(2-(2-(2-(2-(5-(4-isopropylbenzylidene)-4-oxo-2-thioxothiazolidin-3yl)ethoxy)ethoxy)ethoxy)ethyl) carbamate (**35**; 122 mg, 0.23 mmol, 1 eq) was dissolved in dry DCM (1 mL, 0.25 M), and TFA (1 mL) was slowly added. The mixture was stirred for 30 min upon completion as determined by TLC. After removal of the volatiles, the oily residue was dried further under high vacuum to give **37** as TFA salt, [52] without further purification in quantitative yield. **^{1}H NMR** (400 MHz, $CDCl_3$, HETCOR) δ 1.26 (s, 3H, CH_3), 1.28 (s, 3H, CH_3), 1.43 (s, 9H, $3CH_3$ Boc), 2.91 – 2.99 (m, 1H, $CHCH_3$), 3.29 (q, *J* = 5.4 Hz, 2H, CH_2CH_2NH), 3.50 (t, *J* = 5.1 Hz, 2H, CH_2CH_2NH), 3.57 – 3.63 (m, 6H, CH_2 PEG chain), 3.65 – 3.68 (m, 2H, CH_2 PEG chain), 3.81 (t, *J* = 6.0 Hz, 2H, N-CH_2CH_2O), 4.36 (t, *J* = 6.0 Hz, 2H, N-CH_2CH_2O), 5.03 (bs, 1H, NH-Boc), 7.34 (d, *J* = 8.3 Hz, 2H, CHAr), 7.44 (d, *J* = 8.3 Hz, 2H, CHAr), 7.71 (s, 1H, CH). **^{13}C NMR** (101 MHz, $CDCl_3$, HETCOR) δ 23.6 ($2CH_3$), 28.4 ($3CH_3$ Boc), 34.2 (C-*i*Pr), 40.4 (CH_2CH_2NH), 43.4 (N-CH_2CH_2-O), 66.7 (N-CH_2CH_2-O), 70.2 (CH_2 PEG

chain), 70.3 (CH$_2$ PEG chain), 70.4 (N-CH$_2$CH$_2$-OCH$_2$), 70.5 (CH$_2$ PEG chain), 70.6 (CH$_2$ PEG chain), 79.2 (C- Boc), 121.7 (CS), 127.6 (CAr), 130.9 (CAr), 131.0, 133.4 (CH), 152.5 (C=O Boc), 156.0, 167.9 (C=O), 193.7 (C=S). **HRMS** *m/z* calc. for $C_{26}H_{38}N_2O_6S_2$ $[M+H]^+$ 539.2170, found 539.2240.

(*Z*)-3-(2-(2-(2-(2-Aminoethoxy)ethoxy)ethoxy)ethyl)-5-(4-ethylbenzylidene)-2-thioxothiazolidin-4-one 2,2,2-trifluoroacetate (38)

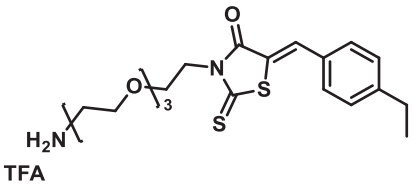

38

4-Ethylbenzaldehyde(**2**; 93 mg, 0.69 mmol, 1 eq) and **34** (283 mg, 0.69 mmol, 1 eq) were placed in a 10 mL Pyrex glass tube and stirred overnight at 140 ºC. After completion followed by HPLC / MS, the organic layer was washed with AcOEt and water, dried over Na_2SO_4, filtered, and concentrated. The crude was purified with reverse-phase column chromatography (85 % CH_3CN in 0.1 % aq. HCO_2H) to give **36** as a yellow solid (179 mg, **49 %**). [170, 171] Then, *tert*-butyl (*Z*)-(2-(2-(2-(2-(5-(4-ethylbenzylidene)-4-oxo-2-thioxothiazolidin-3yl)ethoxy)ethoxy)ethoxy)ethyl) carbamate (**36**; 167 mg, 0.32 mmol, 1 eq) was dissolved in dry DCM (1.3 mL, 0.25 M), and TFA (1.3 mL) was slowly added. The mixture was stirred for 30 min upon completion as determined by TLC. After removal of the volatiles, the oily residue was dried further under high vacuum to give **38** as TFA salt, [52] without further purification in quantitative yield. **^{1}H NMR** (400 MHz, $CDCl_3$) δ 1.26 (t, *J* = 7.6 Hz, 3H, CH_2CH_3), 1.44 (s, 9H, 3 CH_3 Boc), 2.70 (q, *J* = 7.6 Hz, 2H, CH_2CH_3), 3.29 (q, *J* = 5.1 Hz, 2H, CH_2CH_2NH), 3.51 (t, *J* = 5.1 Hz, 2H, CH_2CH_2NH), 3.57 – 3.64 (m, 6H, CH$_2$ PEG chain), 3.65 – 3.69 (m, 2H, CH$_2$ PEG chain), 3.81 (t, *J* = 5.9 Hz, 2H, N-CH_2CH_2O), 4.36 (t, *J* = 5.9 Hz, 2H, N-CH_2CH_2O), 5.02 (bs, 1H, NH-Boc), 7.31 (d, *J* = 8.1 Hz, 2H, CHAr), 7.43 (d, *J* = 8.1 Hz, 2H, CHAr), 7.71 (s, 1H, CH). **^{13}C NMR** (101 MHz, $CDCl_3$,) δ 15.2 (CH_2CH_3), 28.5 (3CH_3 Boc), 28.9 (CH_2CH_3), 40.4 (CH_2CH_2NH), 43.4 (N-CH_2CH_2-O), 66.7 (N-CH_2CH_2-O), 70.2 (CH$_2$ PEG chain), 70.3 (CH$_2$ PEG chain), 70.4 (N-CH_2CH_2-OCH$_2$), 70.5 (CH$_2$ PEG chain), 70.6 (CH$_2$ PEG chain), 79.2 (C-Boc), 121.7 (CS), 128.1 (CAr), 129.0 (2C, CH_2CH_3- CAr), 130.8 (2C, C-Aryl), 131.9 (CAr), 133.4 (CH), 147.9 (C=O Boc), 167.9 (C=O), 193.7 (C=S). **HRMS** *m/z* calc. for $C_{25}H_{36}N_2O_6S_2$ $[M+H]^+$ 525.2010, found 525.2069.

(*Z*)-2-(2,6-Dioxopiperidin-3-yl)-N-(8-(5-(4-isopropylbenzylidene)-4-oxo-2-thioxothiazolidin-3-yl)octyl)-1,3-dioxoisoindoline-5-carboxamide (ASA_MDEG-541)

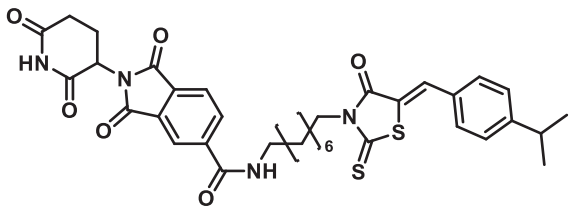

ASA_MDEG-541

(*Z*)-3-(8-Aminooctyl)-5-(4-isopropylbenzylidene)-2-thioxothiazolidin-4-one 2,2,2-trifluoroacetate (**30**; 247 mg, 0.49 mmol, 1 eq) was added to a stirring solution of 2-(2,6-dioxopiperidin-3-yl)-1,3-dioxoisoindoline-5-carboxylic acid (**32**; 178 mg, 0.59 mmol, 1.2 eq) and DIPEA (0.5 mL, 2.94 mmol, 6 eq) in dry DMF (3 mL, 0.17 M). After 15 min, HATU (223 mg, 0.59 mmol, 1.2 eq) and the reaction mixture was allowed to stir at room temperature for 12 h. Upon completion of the reaction as determined by HPLC / MS, the organic layer was washed with AcOEt and water, dried over Na_2SO_4, filtered, and concentrated. The crude was purified with reverse-phase column chromatography (86 % CH_3CN in 0.1 % aq. HCO_2H) to give **ASA_MDEG-541** (245 mg, **74 %**), [52] that matched the reported spectral data. [170] **^{1}H NMR** (500 MHz, $CDCl_3$) δ 1.26 (s, 3H), 1.28 (s, 3H), 1.37 (s, 8H), 1.64 (t, *J* = 7.2 Hz, 2H), 1.72 (t, *J* = 7.5 Hz, 2H), 2.13 – 2.20 (m, 1H), 2.71 – 2.87 (m, 2H), 2.88 – 2.97 (m, 2H), 3.48 (q, *J* = 5.8 Hz, 2H), 4.11 (t, *J* = 7.6 Hz, 2H), 5.00 (dd, *J* = 5.4, 12.5 Hz, 1H), 6.31 (t, *J* = 5.5 Hz, 1H), 7.34 (d, *J* = 8.3 Hz, 2H), 7.43 (d, *J* = 8.3 Hz, 2H), 7.70 (s, 1H), 7.93 – 7.97 (m, 1H), 8.10 (s, 1H), 8.19 (s, 1H), 8.23 (dd, *J* = 1.5, 7.7 Hz, 1H). **^{13}C NMR** (101 MHz, $CDCl_3$) δ 22.7, 23.8, 26.7, 27.0, 29.1, 29.1, 29.6, 31.5, 34.4, 40.6, 44.7, 49.7, 121.9, 122.0, 124.4, 127.7, 131.1, 131.1, 132.0, 132.2, 133.4, 133.9, 141.0, 152.6, 165.3, 166.6, 166.6, 167.8, 168.1, 170.8, 193.7. **HRMS** *m/z* calc. for $C_{35}H_{38}N_4O_6S_2$ $[M+H]^+$ 675.2230, found 675.2318.

(*Z*)-2-(2,6-Dioxopiperidin-3-yl)-*N*-(8-(5-(4-ethylbenzylidene)-4-oxo-2-thioxothiazolidin-3-yl)octyl)-1,3-dioxoisoindoline-5-carboxamide (ASA_MDEG-542)

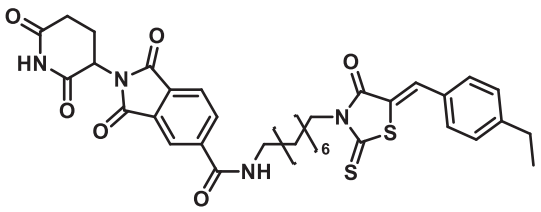

ASA_MDEG-542

(*Z*)-3-(8-Aminooctyl)-5-(4-ethylbenzylidene)-2-thioxothiazolidin-4-one 2,2,2-trifluoroacetate (**31**; 165 mg, 0.34 mmol, 1 eq) was added to a stirring solution of 2-(2,6-dioxopiperidin-3-yl)-1,3-dioxoisoindoline-5-carboxylic acid (**32**; 122 mg, 0.40 mmol, 1.2 eq) and DIPEA (0.4 mL, 2.02 mmol, 6 eq) in dry DMF (2 mL, 0.17 M). After 15 min, HATU (154 mg, 0.40 mmol, 1.2 eq) and the reaction mixture was allowed to stir at room temperature for 12 h. Upon completion of the reaction as determined by HPLC / MS, the organic layer was washed with AcOEt and water, dried over Na_2SO_4, filtered, and concentrated. The crude was purified with reverse-phase column chromatography (21 % CH_3CN in 0.1 % aq. HCO_2H) to give **ASA_MDEG-542** as a yellow solid (100.90 mg, **45 %**). [52, 170] **^{1}H NMR** (400 MHz, $CDCl_3$, COSY, HETCOR) δ 1.26 (t, *J* = 7.6 Hz, 3H, $CH_2C\underline{H}_3$), 1.39 (s, 8H, $C\underline{H}_2$ octyl chain), 1.64 (t, *J* = 6.9 Hz, 2H, $C\underline{H}_2$ octyl chain), 1.71 (t, *J* = 7.5 Hz, 2H, $C\underline{H}_2$ octyl chain), 2.11 – 2.21 (m, 1H, glut$C\underline{H}_2$CHN), 2.70 (q, *J* = 7.5 Hz, 2H, $C\underline{H}_2CH_3$), 2.74 – 2.97 (m, 3H, glut$C\underline{H}_2$CHN, glut$C\underline{H}_2$C=O), 3.47 (q, *J* = 6.7 Hz, 2H, $CH_2C\underline{H}_2$NH), 4.11 (d, *J* = 7.5 Hz, 2H, N-$C\underline{H}_2CH_2$), 5.00 (dd, *J* = 5.2, 12.2 Hz, 1H, C<u>H</u>-N), 6.43 (s, 1H, N<u>H</u>C=O), 7.31 (d, *J* = 8.0 Hz, 2H, C<u>H</u>Ar), 7.42 (d, *J* = 8.2 Hz, 2H, C<u>H</u>Ar), 7.70 (s, 1H, C<u>H</u>), 7.94 (d, *J* = 7.7 Hz, 1H, C<u>H</u>Ar), 8.18 (s, 1H, N<u>H</u>glut), 8.23 (d, *J* = 7.1 Hz, 2H, C<u>H</u>Ar). **^{13}C NMR** (101 MHz, $CDCl_3$, HETCOR) δ 15.2 ($CH_2\underline{C}H_3$), 22.6 (glut$\underline{C}H_2$CHN), 26.6 (N-$\underline{C}H_2CH_2$), 26.9, 28.9, 29.0, 29.4 ($\underline{C}H_2CH_3$), 31.4 glut$\underline{C}H_2$C=O), 40.5 ($\underline{C}H_2$NHC=O), 44.6, 49.6 (<u>C</u>H-N), 121.8, 121.9, 124.2, 128.0, 129.0 (<u>C</u>Ar), 130.9, 130.9 (<u>C</u>Ar), 131.8, 132.0, 133.3, 133.6 (<u>C</u>H), 133.8 (<u>C</u>Ar), 140.9, 147.9, 165.2 (glutNH<u>C</u>=O), 166.4 (<u>C</u>=O), 166.5 (<u>C</u>=O), 167.8 (glutCH-<u>C</u>=O), 168.0 (<u>C</u>=O), 170.7, 193.6 (<u>C</u>=S). **HRMS** *m/z* calc. for $C_{34}H_{36}N_4O_6S_2$ $[M+H]^+$ 661.2080, found 661.2153.

(*Z*)-2-(2,6-Dioxopiperidin-3-yl)-N-(2-(2-(2-(2-(5-(4-isopropylbenzylidene)-4-oxo-2-thioxothiazolidin-3-yl)ethoxy)ethoxy)ethoxy)ethyl)-1,3-dioxoisoindoline-5-carboxamide (ASA_MDEG-543)

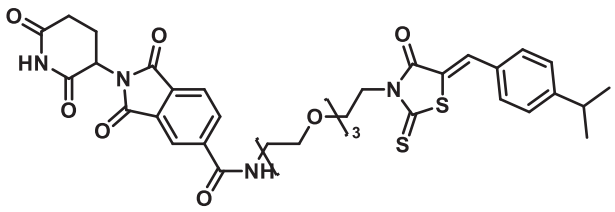

ASA_MDEG-543

(*Z*)-3-(2-(2-(2-(2-Aminoethoxy)ethoxy)ethoxy)ethyl)-5-(4-isopropylbenzylidene)-2-thioxothiazolidin-4-one 2,2,2-trifluoroacetate (**37**; 125 mg, 0.23 mmol, 1 eq) was added to a stirring solution of 2-(2,6-dioxopiperidin-3-yl)-1,3-dioxoisoindoline-5-carboxylic acid (**32**; 82 mg, 0.27 mmol, 1.2 eq) and DIPEA (0.2 mL, 1.36 mmol, 6 eq) in dry DMF (1.3 mL, 0.17 M). After 15 min, HATU (103 mg, 0.27 mmol, 1.2 eq) and the reaction mixture was allowed to stir at room temperature for 12 h. Upon completion of the reaction as determined by HPLC / MS, the organic layer was washed with AcOEt and water, dried over Na_2SO_4, filtered, and concentrated. The crude was purified with reverse-phase column chromatography (74 % CH_3CN in 0.1 % aq. HCO_2H) to give **ASA_MDEG-543** as a yellow solid (74 mg, **45 %**). [52, 170] **^{1}H NMR** (400 MHz, $CDCl_3$, HETCOR) δ 1.27 (s, 3H, C$\underline{H}_3$), 1.28 (s, 3H, C$\underline{H}_3$), 2.13 – 2.21 (m, 1H, glutC$\underline{H}_2$CHN), 2.72 – 2.79 (m, 1H, glut$\underline{CH}_2$C=O), 2.83 (dd, *J* = 4.0, 12.6 Hz, 1H, glutC$\underline{H}_2$CHN), 2.88 – 2.94 (m, 1H, glutC$\underline{H}_2$C=O), 2.95 – 3.00 (m, 1H, C$\underline{H}$-isopropyl), 3.66 (s, 8H, C$\underline{H}_2$ PEG chain), 3.68 – 3.70 (m, 4H, C$\underline{H}_2$NHC=O, C$\underline{H}_2$ PEG chain), 3.77 (t, *J* = 5.9 Hz, 2H, N-CH$_2$C$\underline{H}_2$-O), 4.32 (t, *J* = 5.9 Hz, 2H, , N-C$\underline{H}_2$CH$_2$O), 4.99 (dd, *J* = 5.3, 12.4 Hz, 1H, C$\underline{H}$-N), 7.34 (d, *J* = 8.3 Hz, 2H, C$\underline{H}$Ar), 7.39 (s, 1H, N$\underline{H}$C=O), 7.42 (d, *J* = 8.3 Hz, 2H, C$\underline{H}$Ar), 7.66 (s, 1H, C$\underline{H}$), 7.92 (dd, *J* = 0.9, 7.6 Hz, 1H, C$\underline{H}$Ar), 8.14 (s, 1H, N$\underline{H}$-glut), 8.26 – 8.31 (m, 2H, C$\underline{H}$Ar). **^{13}C NMR** (101 MHz, $CDCl_3$, HETCOR) δ 22.6 (glut$\underline{C}$H$_2$CHN), 23.7 (2CH$_3$), 31.4 (glut$\underline{C}$H$_2$C=O), 34.3 ($\underline{C}$-2CH$_3$), 40.3 ($\underline{C}$H$_2$NHC=O), 43.5 (N-$\underline{C}$H$_2$CH$_2$O), 49.5 ($\underline{C}$H-N), 66.7 (N-CH$_2$$\underline{C}H_2$-O), 69.6 ($\underline{C}H_2CH_2$NHC=O), 70.27, 70.41(O-$\underline{C}H_2CH_2$), 70.64, 121.53, 122.3 ($\underline{C}$Ar), 124.0 ($\underline{C}$Ar), 127.6 ($\underline{C}$Ar), 130.9, 131.0 ($\underline{C}$Ar), 131.9, 132.0, 133.6 ($\underline{C}$H), 134.1 ($\underline{C}$Ar), 140.7, 152.6, 165.2 (glutNH$\underline{C}$=O), 166.5 ($\underline{C}$=O), 167.7 (glutCH-$\underline{C}$=O), 168.0 ($\underline{C}$=O), 170.6, 193.7 ($\underline{C}$=S). **HRMS** *m/z* calc. for $C_{35}H_{38}N_4O_9S_2$ $[M+H]^+$ 723.2080, found 723.2150.

(*Z*)-2-(2,6-Dioxopiperidin-3-yl)-*N*-(2-(2-(2-(2-(5-(4-ethylbenzylidene)-4-oxo-2-thioxothiazolidin-3-yl)ethoxy)ethoxy)ethoxy)ethyl)-1,3-dioxoisoindoline-5-carboxamide (ASA_MDEG-544)

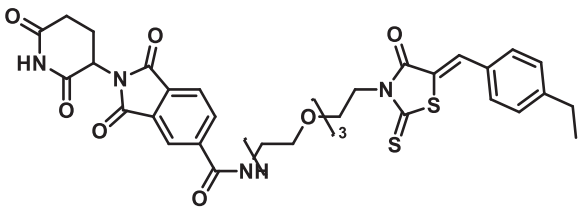

ASA_MDEG-544

(*Z*)-3-(2-(2-(2-(2-Aminoethoxy)ethoxy)ethoxy)ethyl)-5-(4-ethylbenzylidene)-2-thioxothiazolidin-4-one 2,2,2-trifluoroacetate (**38**; 186 mg, 0.44 mmol, 1 eq) was added to a stirring solution of 2-(2,6-dioxopiperidin-3-yl)-1,3-dioxoisoindoline-5-carboxylic acid (**32**; 159 mg, 0.53 mmol, 1.2 eq) and DIPEA (0.2 mL, 1.31 mmol, 3 eq) in dry DMF (2.5 mL, 0.17 M). After 15 min, HATU (200 mg, 0.53 mmol, 1.2 eq) and the reaction mixture was allowed to stir at room temperature for 12 h. Upon completion of the reaction as determined by HPLC / MS, the organic layer was washed with AcOEt and water, dried over Na_2SO_4, filtered, and concentrated. The crude was purified with reverse-phase column chromatography (66 % CH_3CN in 0.1 % aq. HCO_2H) to give **ASA_MDEG-544** as a yellow solid (91 mg, **29 %**). [52, 170] **^{1}H NMR** (400 MHz, $CDCl_3$, COSY, HETCOR) δ 1.26 (t, *J* = 7.6 Hz, 3H, CH_2CH_3), 2.13 – 2.19 (m, 1H, glutCH_2CHN), 2.70 (q, *J* = 7.6 Hz, 2H, CH_2CH_3), 2.74 – 2.79 (m, 1H, glutCH_2C=O), 2.83 (dd, *J* = 4.3, 12.7 Hz, 1H, glutCH_2CHN), 2.87 – 2.94 (m, 1H, glutCH_2C=O), 3.65 (s, 8H, CH_2 octyl chain), 3.68 – 3.70 (m, 4H, CH_2NHC=O, CH_2 octyl chain), 3.76 (t, *J* = 5.9 Hz, 2H, N-CH_2CH_2-O), 4.31 (t, *J* = 5.9 Hz, 2H, N-CH_2CH_2O), 4.99 (dd, *J* = 5.3, 12.4 Hz, 1H, CH-N), 7.31 (d, *J* = 8.3 Hz, 2H, CHAr), 7.36 (s, 1H, NHC=O), 7.40 (d, *J* = 8.3 Hz, 2H, CHAr), 7.66 (s, 1H, CH), 7.92 (dd, *J* = 1.0, 7.5 Hz, 1H, CHAr), 8.12 (s, 1H, NHglut), 8.26 – 8.30 (m, 2H, CHAr). **^{13}C NMR** (101 MHz, $CDCl_3$, HETCOR) δ 15.15 (CH_2CH_3), 22.60 (glutCH_2CHN), 28.94 (CH_2CH_3), 31.40 (glutCH_2C=O), 40.25 (CH_2NHC=O), 43.49 (N-CH_2CH_2O), 49.52 (CH-N), 66.74 (N-CH_2CH_2-O), 69.55 (CH_2CH_2NHC=O), 70.27, 70.41 (O-CH_2CH_2), 70.63, 121.52, 122.33 (CAr), 124.01 (CAr), 129.02 (CAr), 130.73, 130.91 (CAr), 131.90, 133.59, 133.63 (CH), 134.06 (CAr), 140.72, 148.07, 165.20 (glutNHC=O), 166.54 (C=O), 167.71 (glutCH-C=O), 167.94 (C=O), 170.68, 193.66 (C=S). **HRMS** *m/z* calc. for $C_{34}H_{36}N_4O_9S_2$ $[M+H]^+$ 709.1920, found 709.2017.

6.1.1.2 NMR Spectra and HPLC / MS Report of Selected Compounds

(5*Z*)-5-[(4-Ethylphenyl)methylidene]-2-sulfanylidene-1,3-thiazolidin-4-one (3)

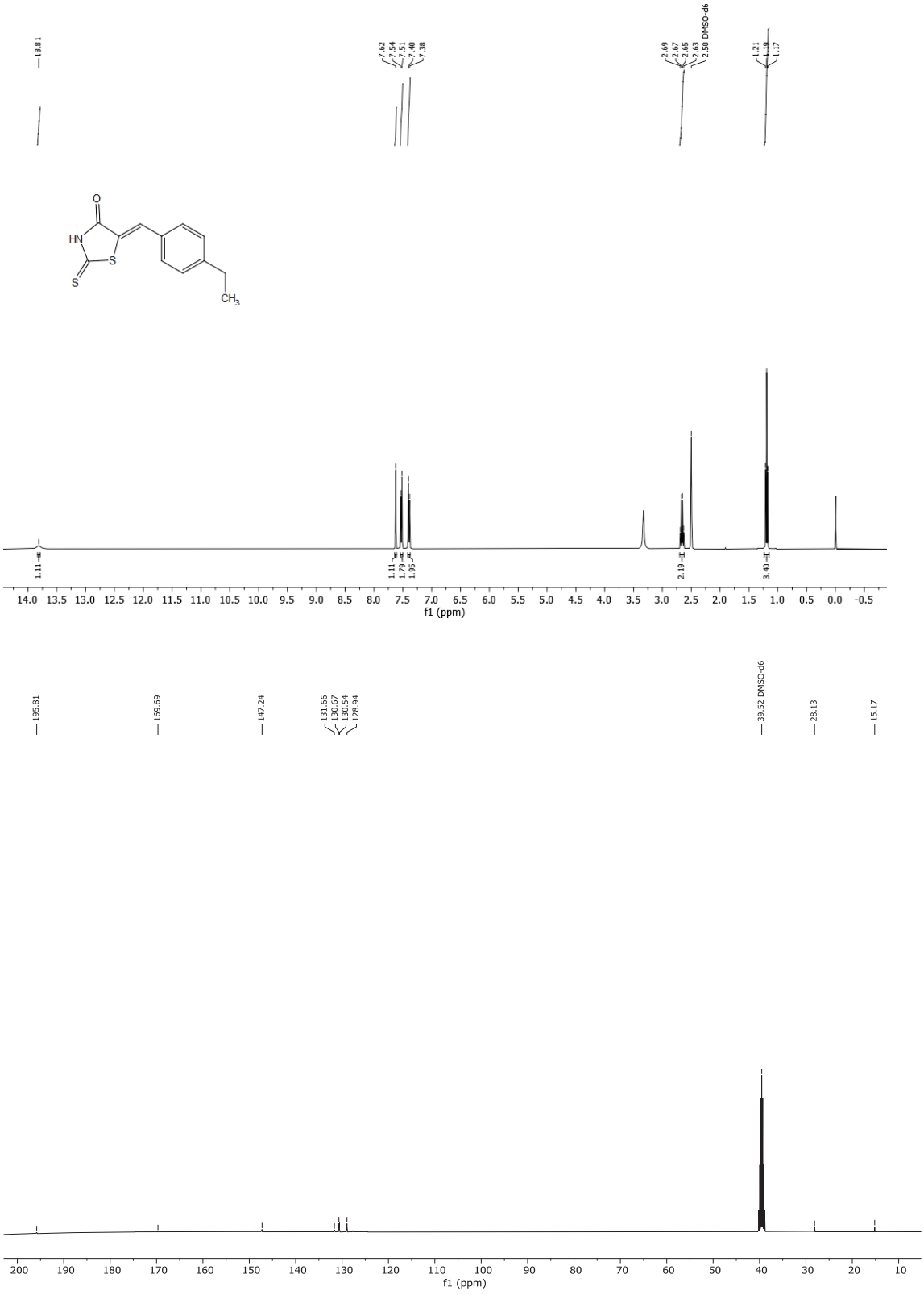

(*Z*)-3-(5-(4-Ethylbenzylidene)-4-oxo-2-thioxothiazolidin-3-yl)propanoic acid (ASA-5)

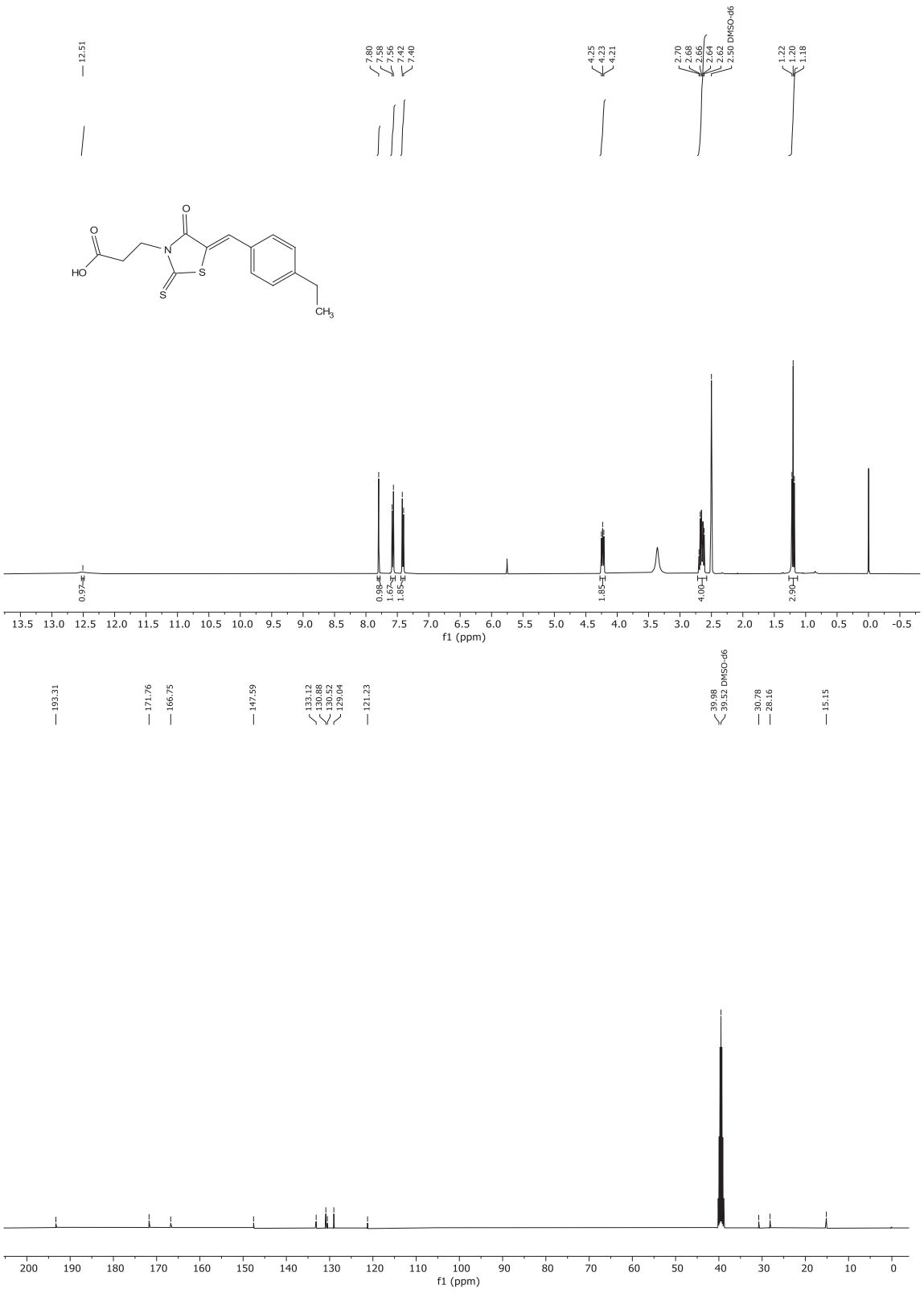

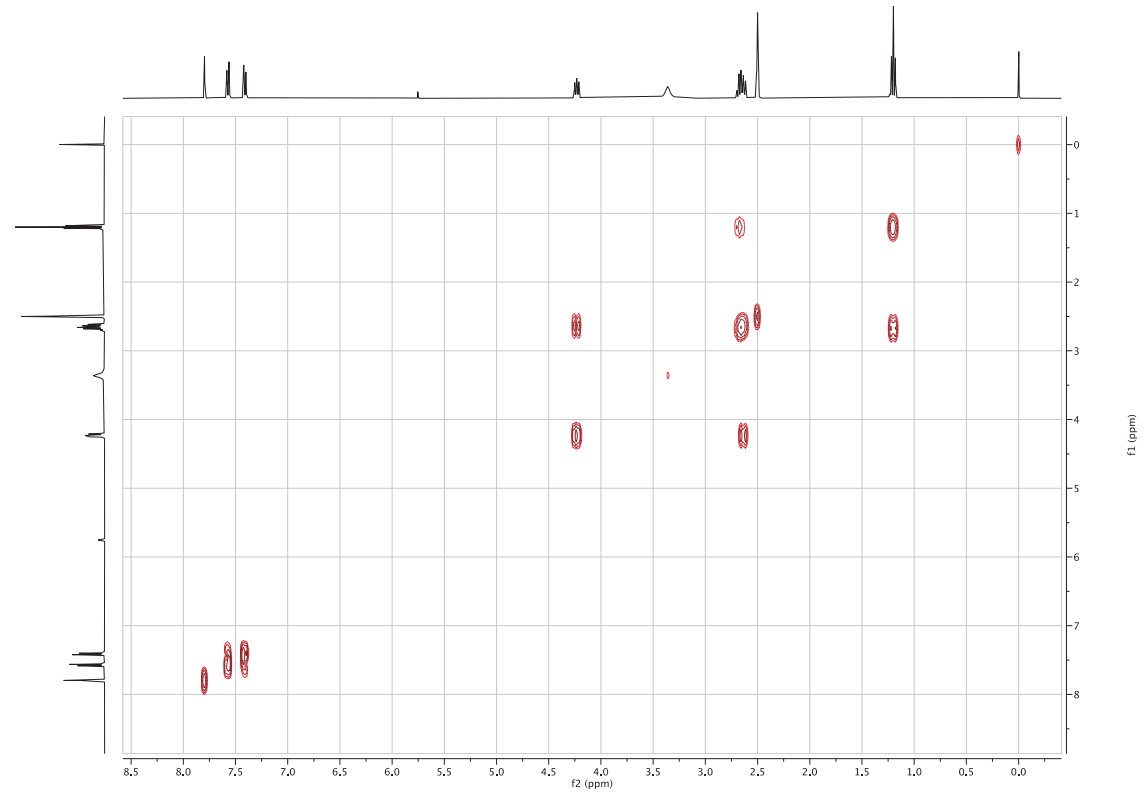
f2 (ppm)
f1 (ppm)

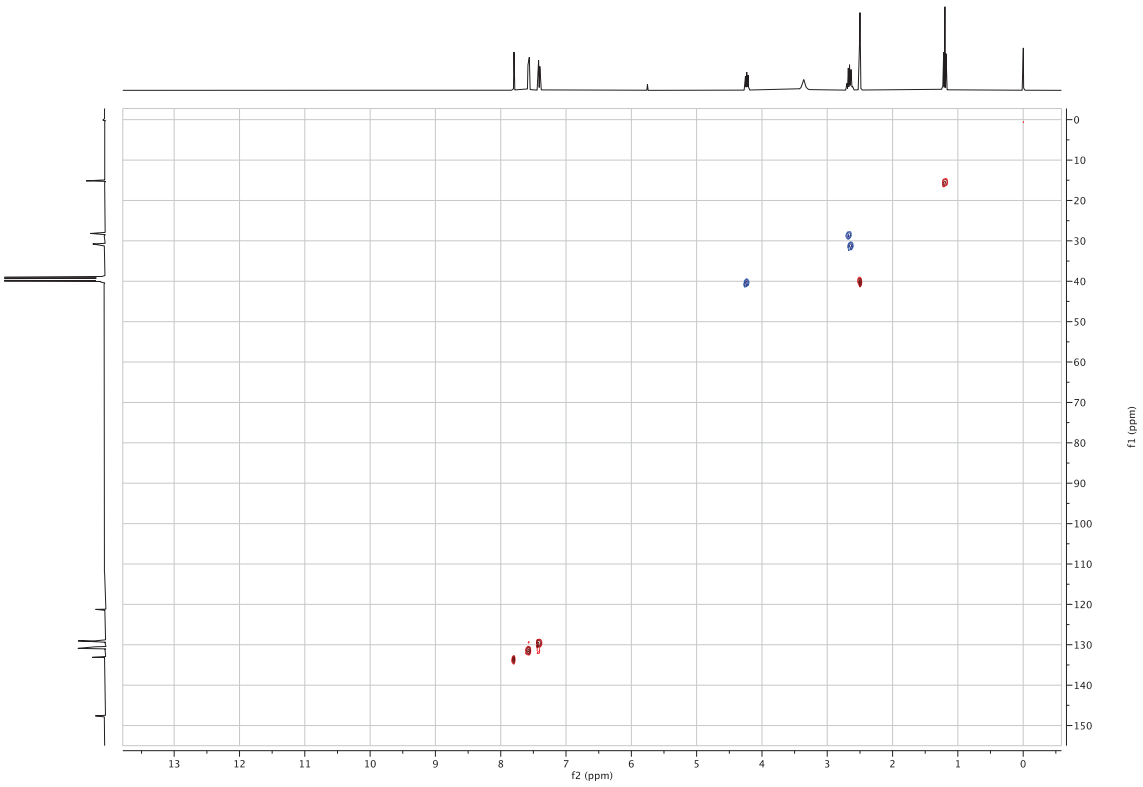
f2 (ppm)
f1 (ppm)

tert-Butyl (*Z*)-3-(5-(4-ethylbenzylidene)-4-oxo-2-thioxothiazolidin-3-yl)propanoate (5)

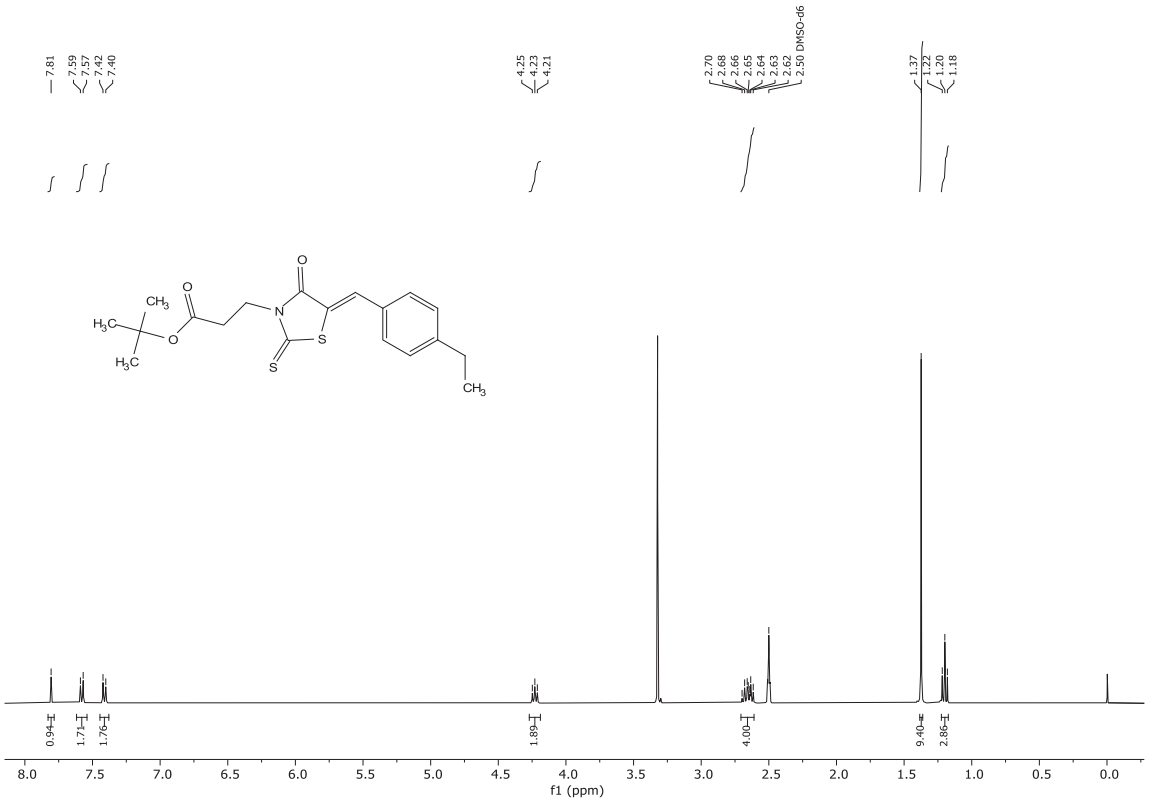

tert-Butyl (*Z*)-3-((5-(4-ethylbenzylidene)-4-oxo-4,5-dihydrothiazol-2-yl)thio)propanoate (6)

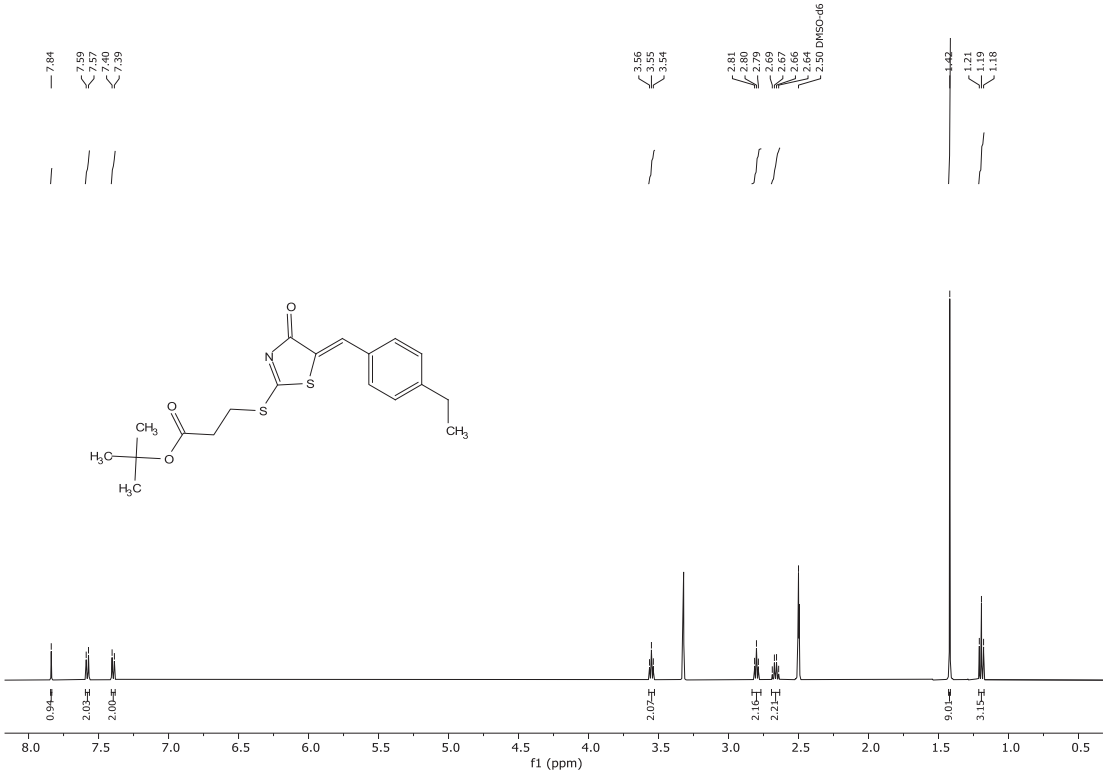

(*Z*)-3-((5-(4-Ethylbenzylidene)-4-oxo-4,5-dihydrothiazol-2-yl)thio)propanoic acid (ASA-6)

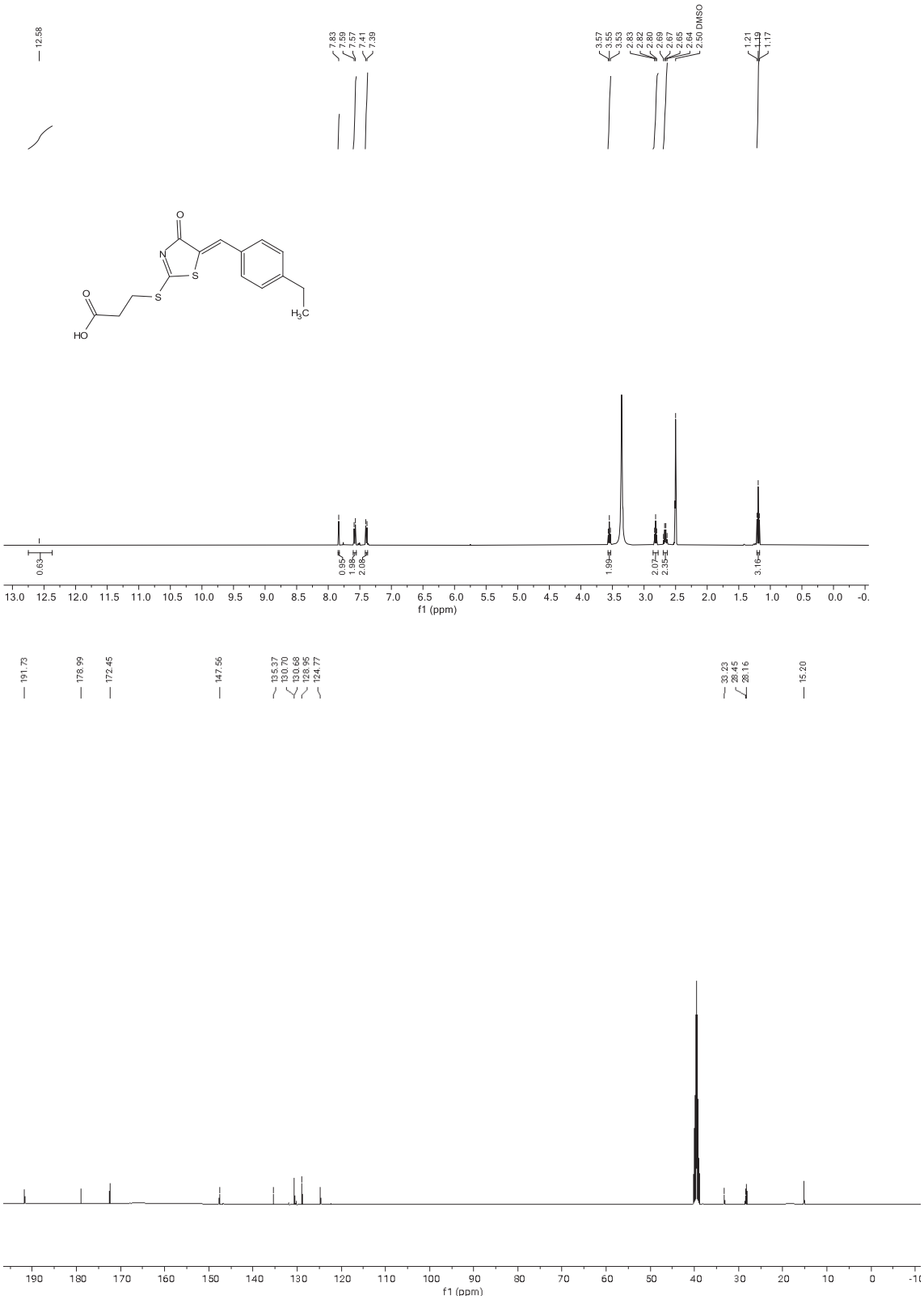

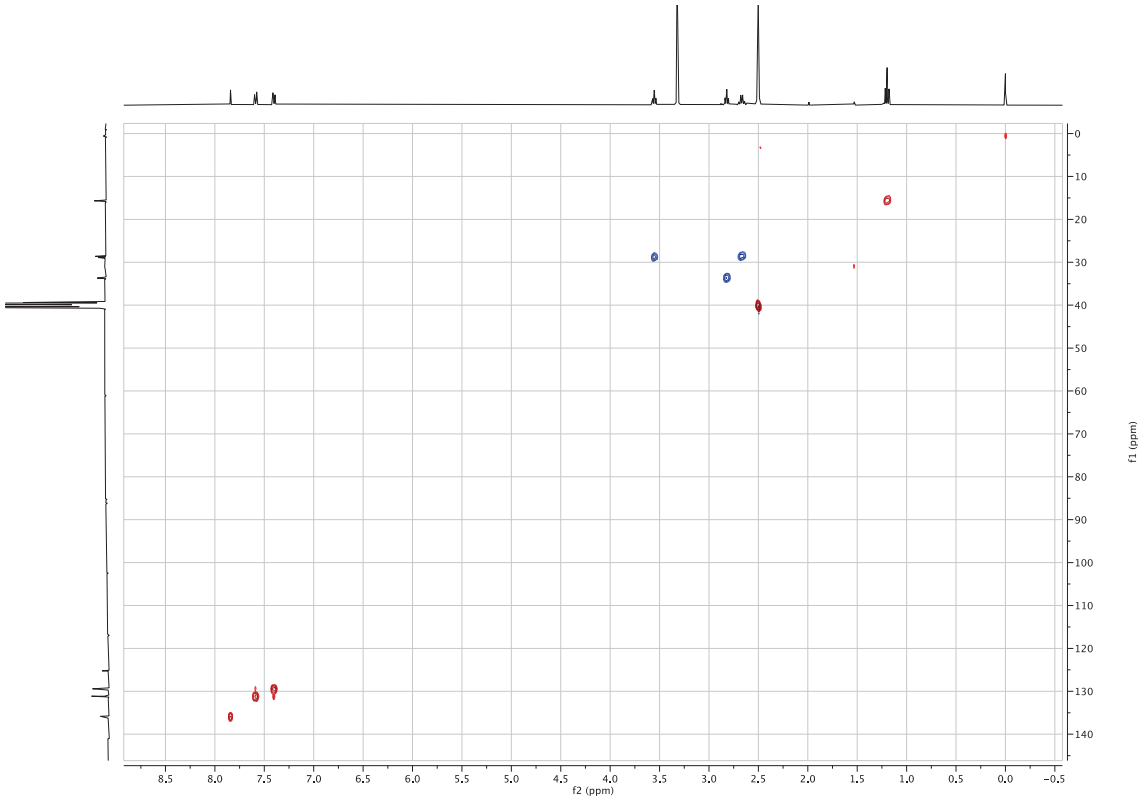

tert-Butyl *N*-{2-[2-({[2-(2,6-dioxopiperidin-3-yl)-1-oxo-2,3-dihydro-1H-isoindol-4-yl]carbamoyl}methoxy)ethoxy]ethyl}carbamate (9a)

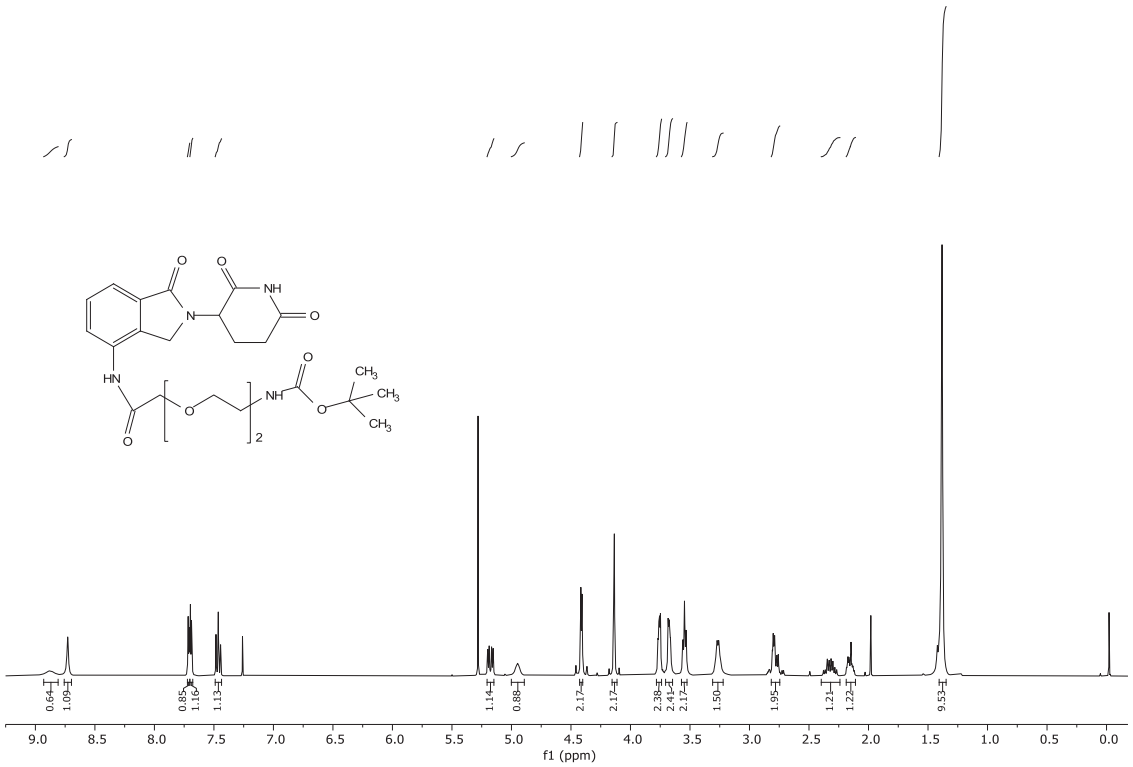

tert-Butyl *N*-(1-{[2-(2,6-dioxopiperidin-3-yl)-1-oxo-2,3-dihydro-1H-isoindol-4-yl]carbamoyl}-2,5,8,11-tetraoxatridecan-13-yl)carbamate (9b)

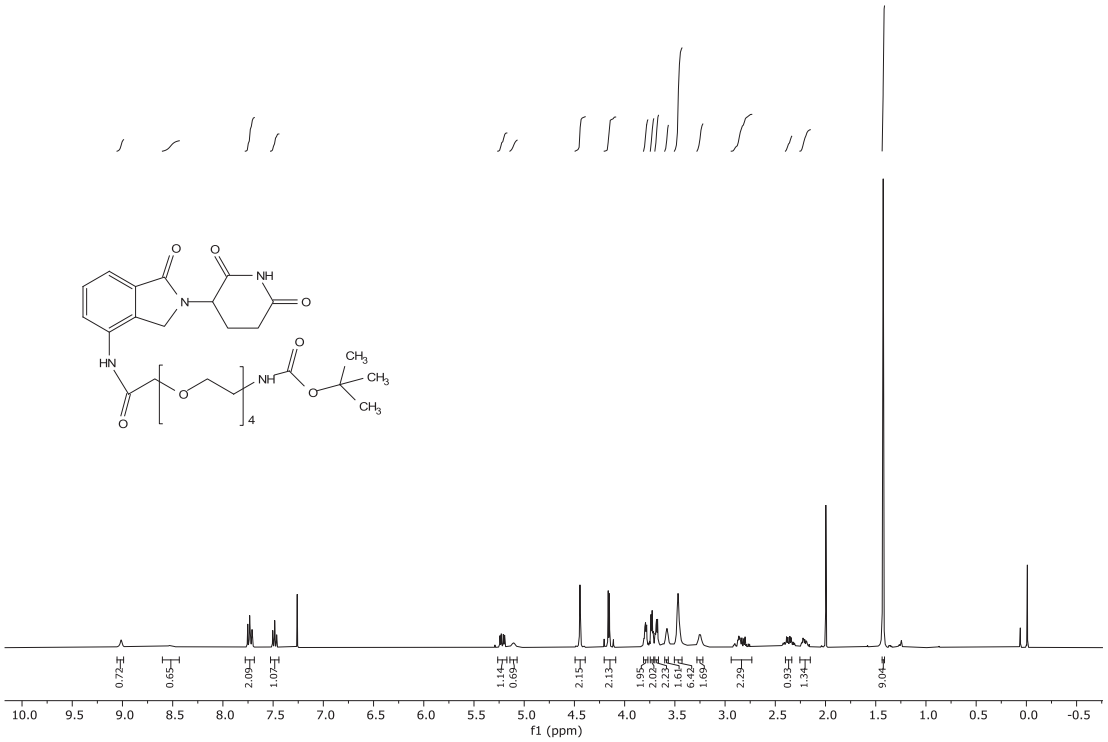

(Z)-*N*-(2-(2-(2-((2-(2,6-Dioxopiperidin-3-yl)-1-oxoisoindolin-4-yl)amino)-2-oxoethoxy)ethoxy)ethyl)-3-(5-(4-ethylbenzylidene)-4-oxo-2-thioxothiazolidin-3-yl)propanamide (ASA-1)

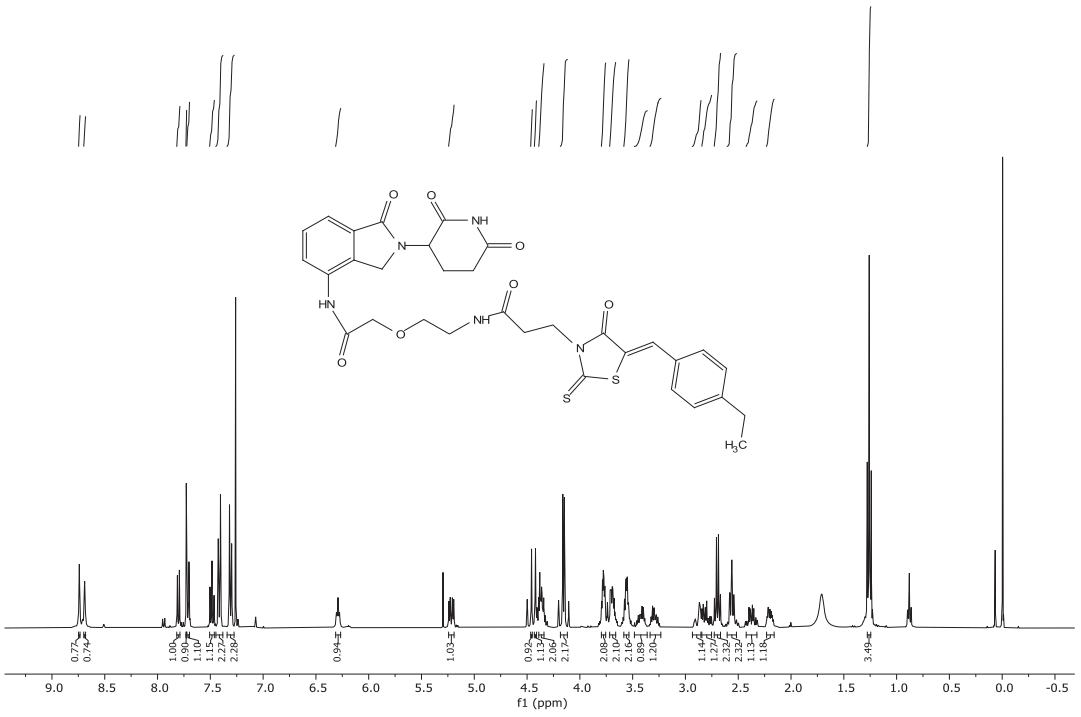

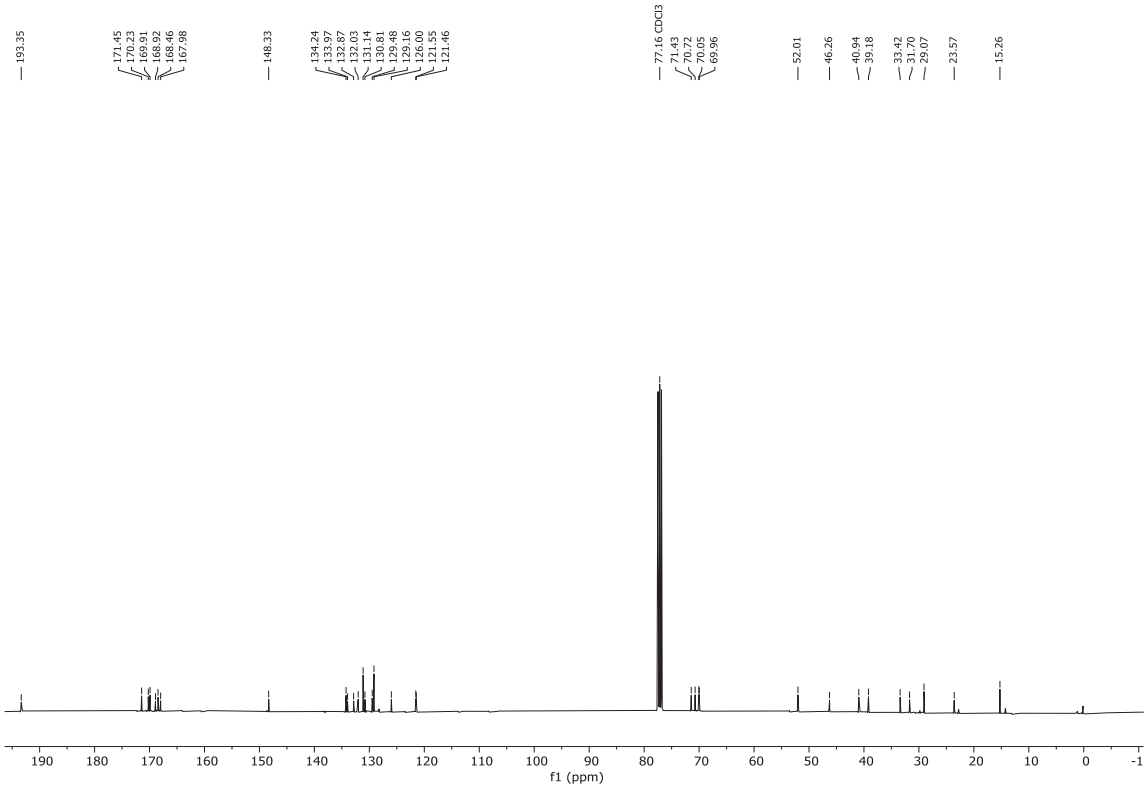
193.35
171.45
170.23
169.91
168.92
168.46
167.98
148.33
134.24
133.97
132.87
132.03
131.14
130.61
129.48
129.16
126.00
121.55
121.46
77.16 CDCl3
71.43
70.72
70.05
69.96
52.01
46.26
40.94
39.18
33.42
33.20
29.07
23.57
15.26
f1 (ppm)

HPLC / MS ASA-1

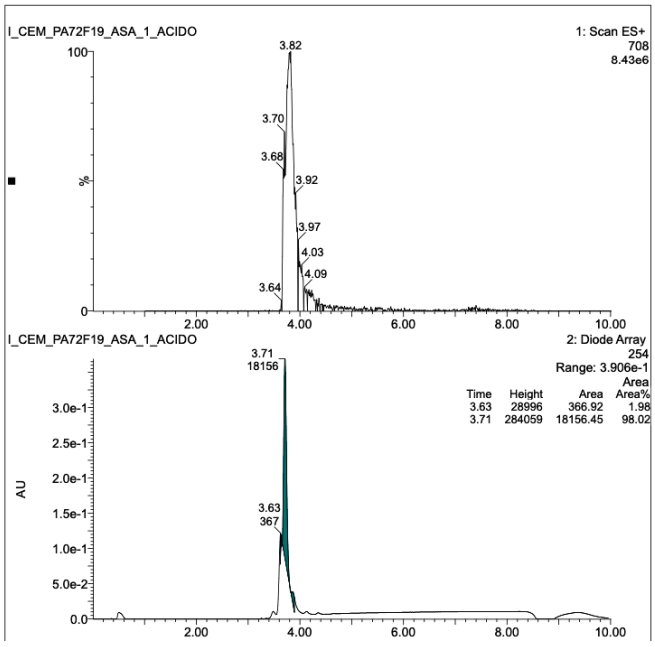
I_CEM_PA72F19_ASA_1_ACIDO
1: Scan ES+
708
8.43e6
3.82
3.70
3.68
3.92
3.97
4.03
4.09
3.64
%
I_CEM_PA72F19_ASA_1_ACIDO
2: Diode Array
254
Range: 3.906e-1
Area
Time Height Area Area%
3.63 28996 366.92 1.98
3.71 284059 18156.45 98.02
3.71
18156
3.63
367
AU

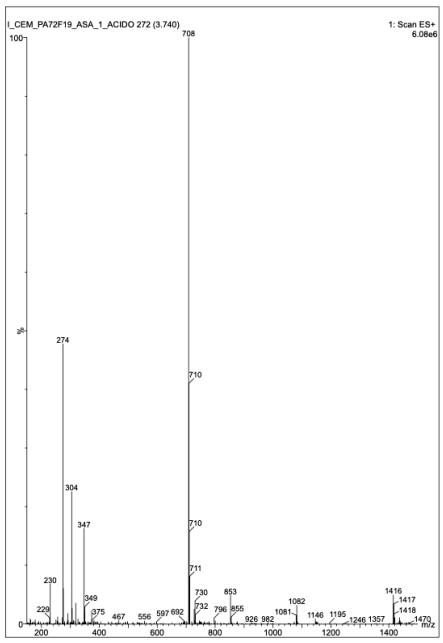
I_CEM_PA72F19_ASA_1_ACIDO 272 (3.740)
1: Scan ES+
6.08e6
708
710
274
304
347
230
349
711
730
853
1082
1416
1417
1418
1470
m/z

(Z)-N-(2-(2,6-Dioxopiperidin-3-yl)-1-oxoisoindolin-4-yl)-14-(3-(5-(4-ethylbenzylidene)-4-oxo-2-thioxothiazolidin-3-yl)propanamido)-3,6,9,12-tetraoxatetradecanamide (ASA-2)

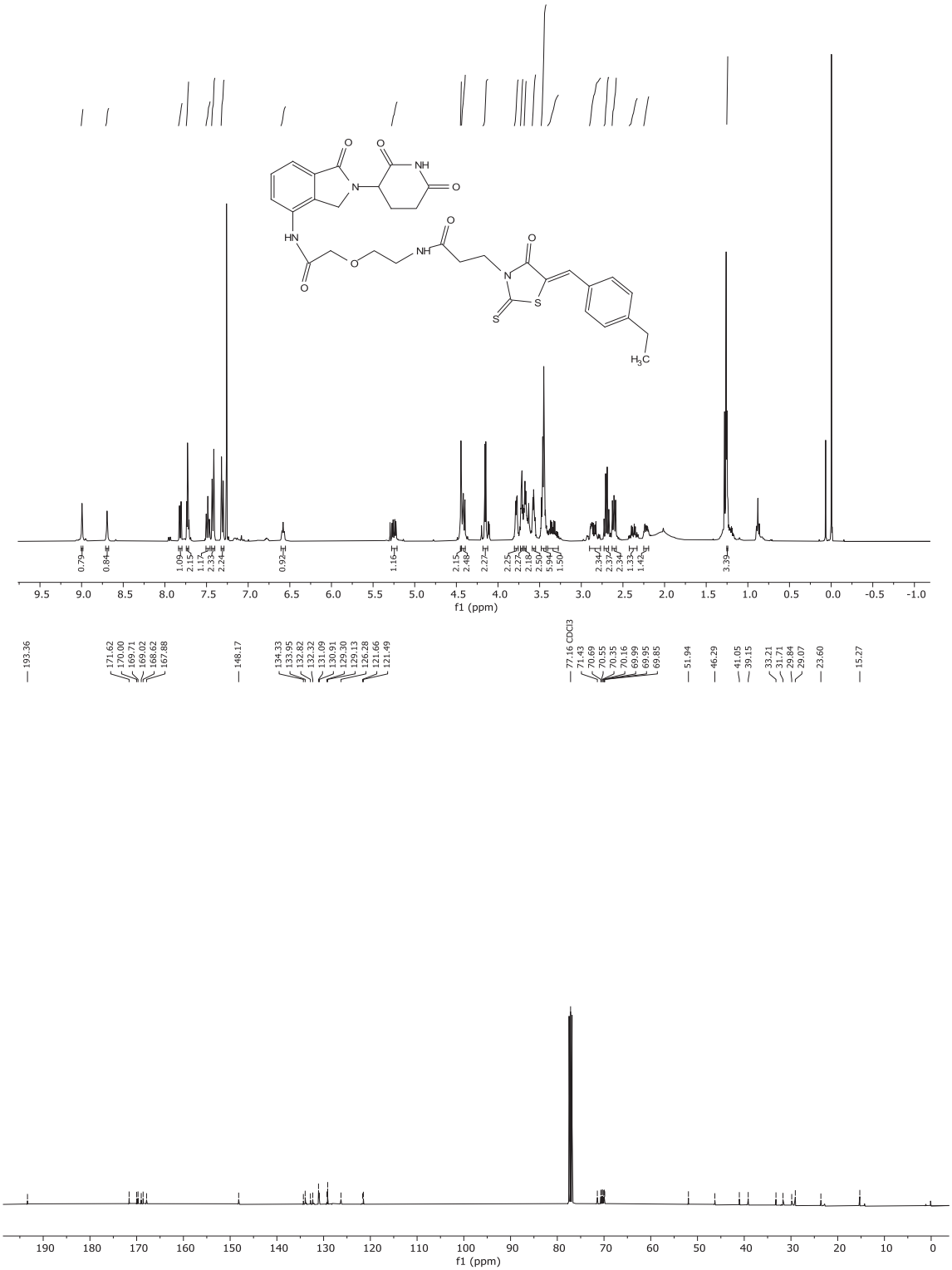

HPLC / MS ASA-2

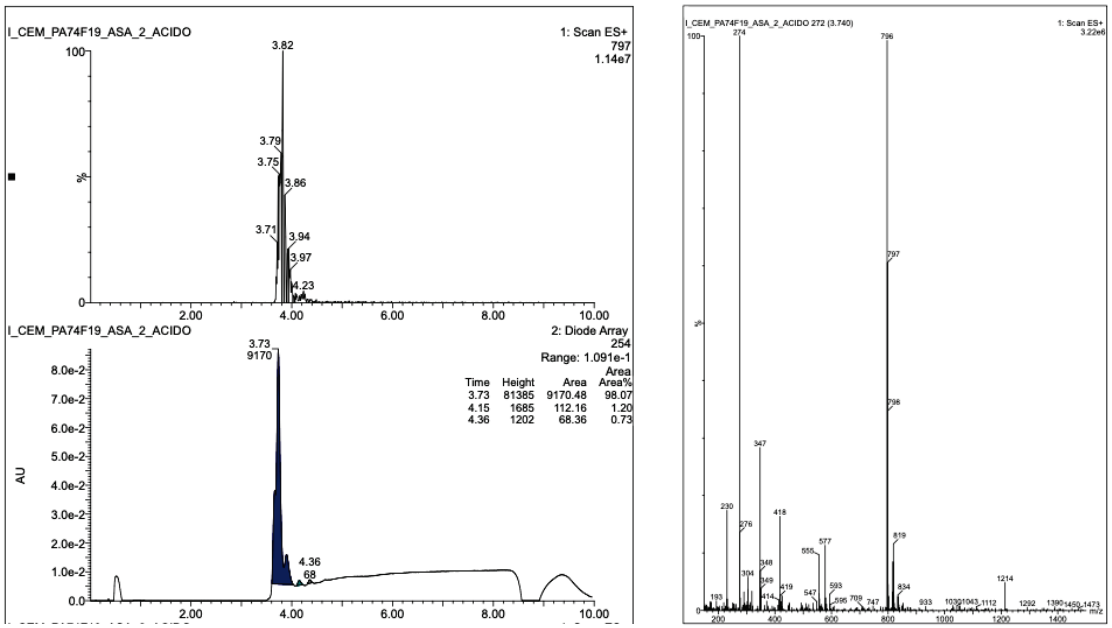

(2*S*,4*R*)-1-((*S*)-2-(*tert*-Butyl)-15-(5-((*Z*)-4-ethylbenzylidene)-4-oxo-2-thioxothiazolidin-3-yl)-4,13-dioxo-6,9-dioxa-3,12-diazapentadecanoyl)-4-hydroxy-*N*-(4-(4-methylthiazol-5-yl)benzyl)pyrrolidine-2-carboxamide (ASA-3)

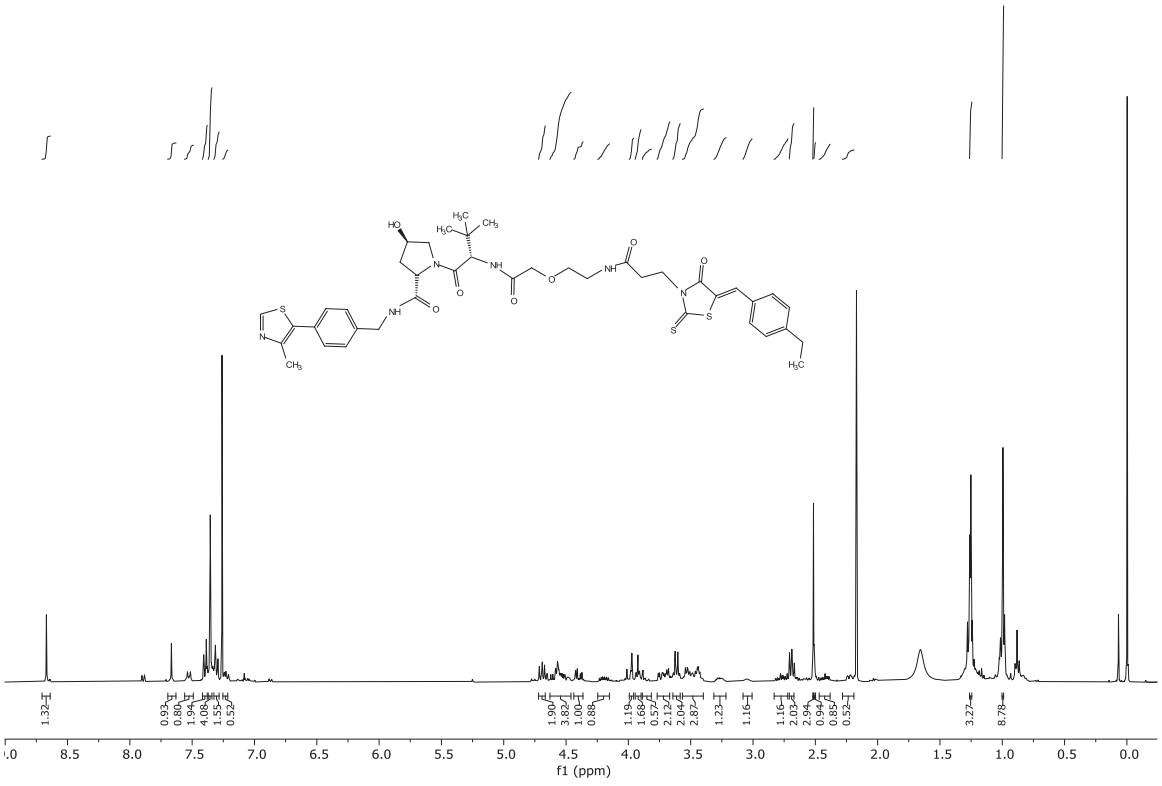

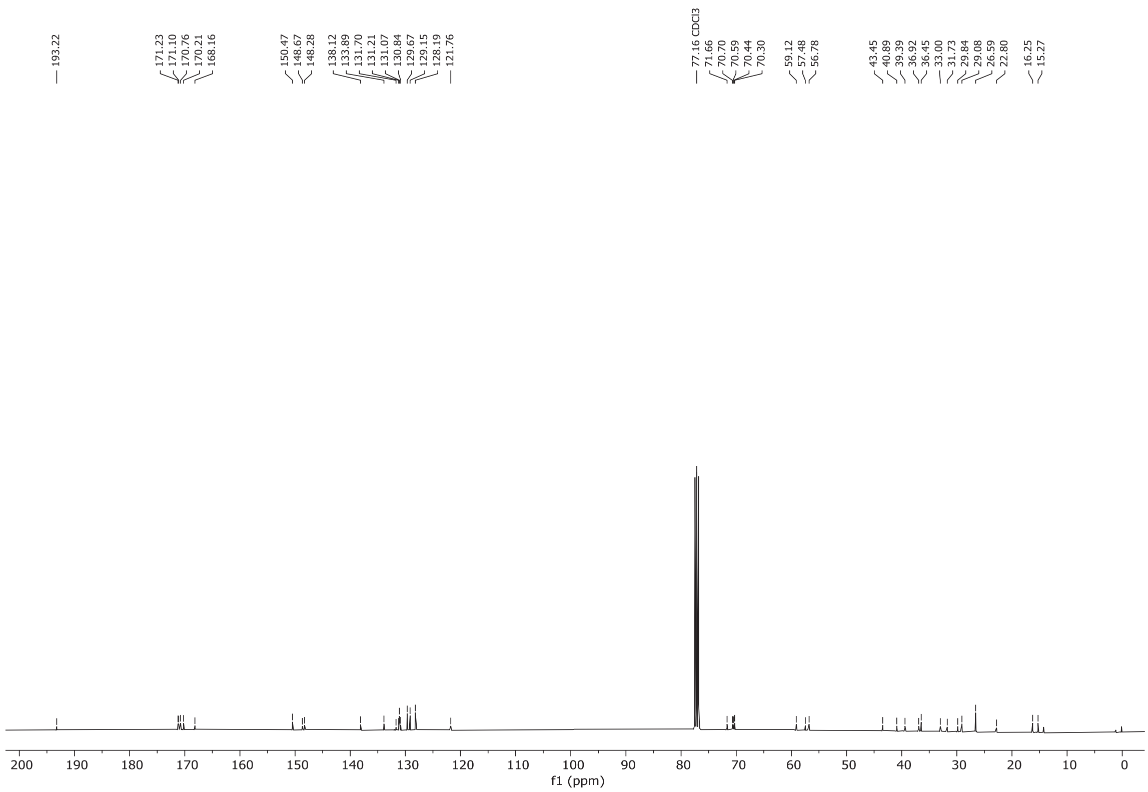
193.22
171.23
171.10
170.76
170.21
168.16
150.47
148.67
148.28
138.12
133.89
131.70
131.21
131.07
130.84
129.67
129.15
128.19
121.76
77.16 CDCl3
71.66
70.70
70.59
70.44
70.30
59.12
57.48
56.78
43.45
40.89
39.39
36.92
36.45
33.00
31.73
29.84
29.08
26.59
22.80
16.25
15.27
f1 (ppm)

HPLC / MS ASA-3

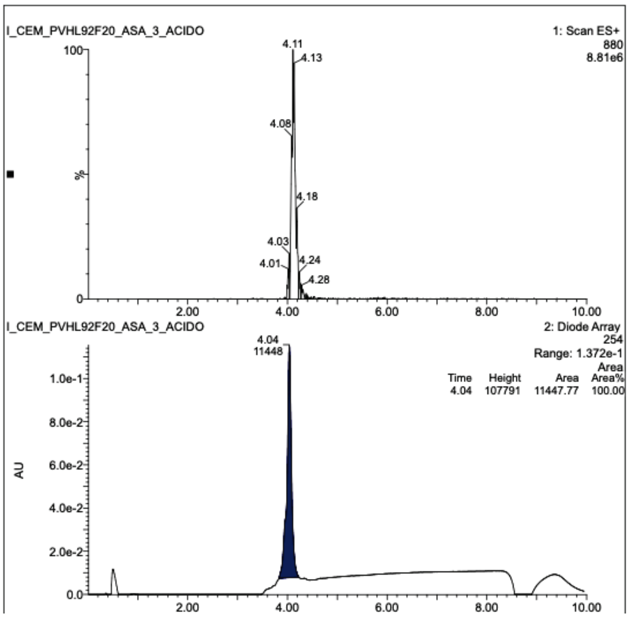
I_CEM_PVHL92F20_ASA_3_ACIDO
1: Scan ES+
880
8.81e6
I_CEM_PVHL92F20_ASA_3_ACIDO
2: Diode Array
254
Range: 1.372e-1
Time Height Area Area%
4.04 107791 11447.77 100.00
AU

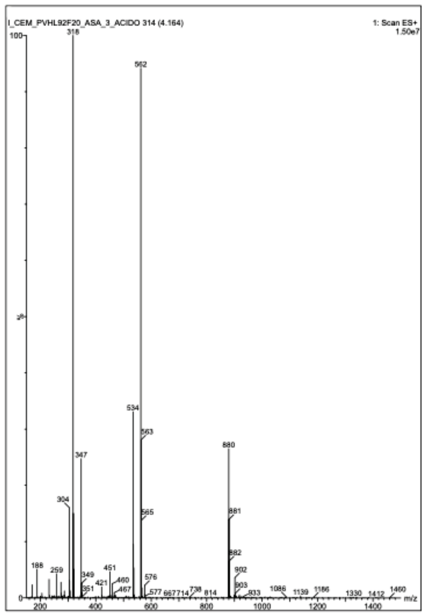
I_CEM_PVHL92F20_ASA_3_ACIDO 314 (4.164)
1: Scan ES+
1.50e7
m/z

(2*S*,4*R*)-1-((S)-2-(*tert*-Butyl)-21-(5-((*Z*)-4-ethylbenzylidene)-4-oxo-2-thioxothiazolidin-3-yl)-4,19-dioxo-6,9,12,15-tetraoxa-3,18-diazahenicosanoyl)-4-hydroxy-*N*-(4-(4-methylthiazol-5-yl)benzyl)pyrrolidine-2-carboxamide (ASA-4)

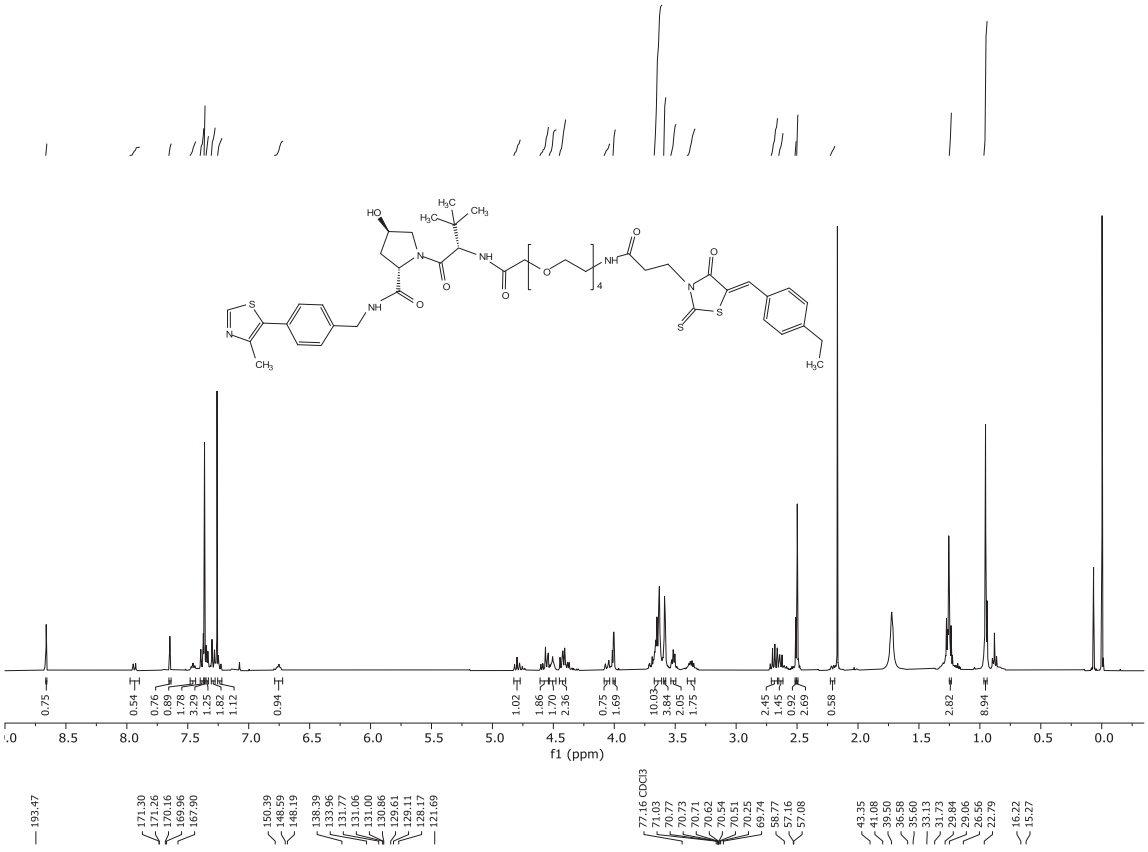

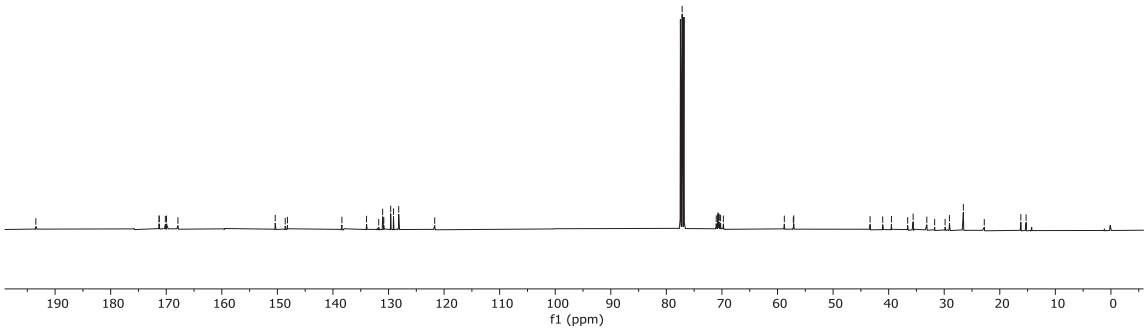

HPLC / MS ASA-4

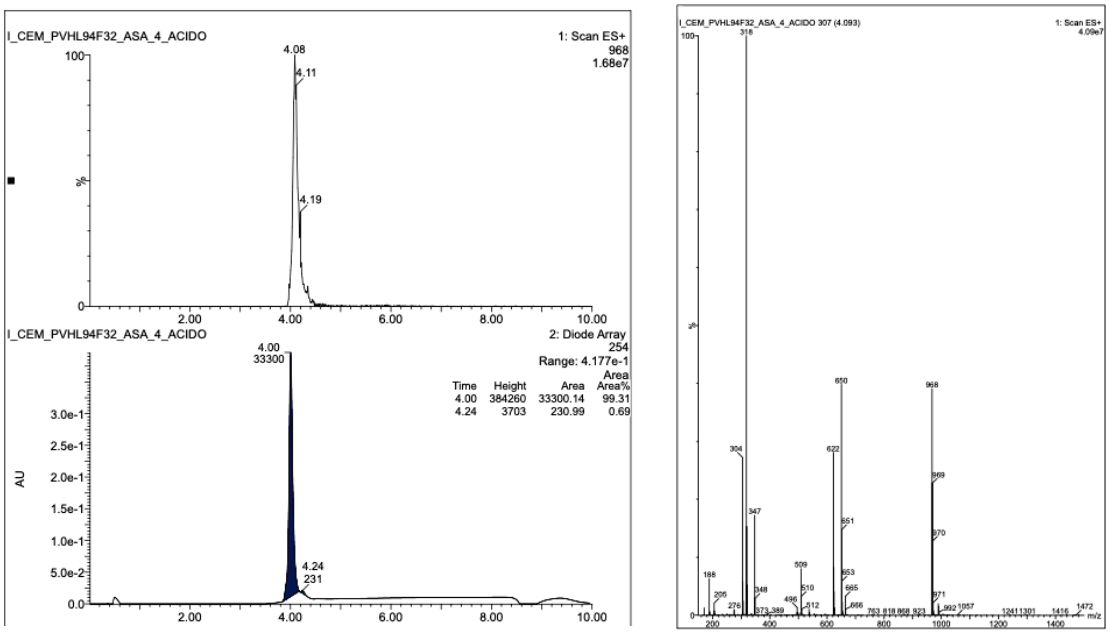

(Z)-N-(2-(2,6-Dioxopiperidin-3-yl)-1-oxoisoindolin-4-yl)-2-(2-(2-((5-(4-ethylbenzylidene)-4-oxo-4,5-dihydrothiazol-2-yl)amino)ethoxy)ethoxy)acetamide (ASA-7)

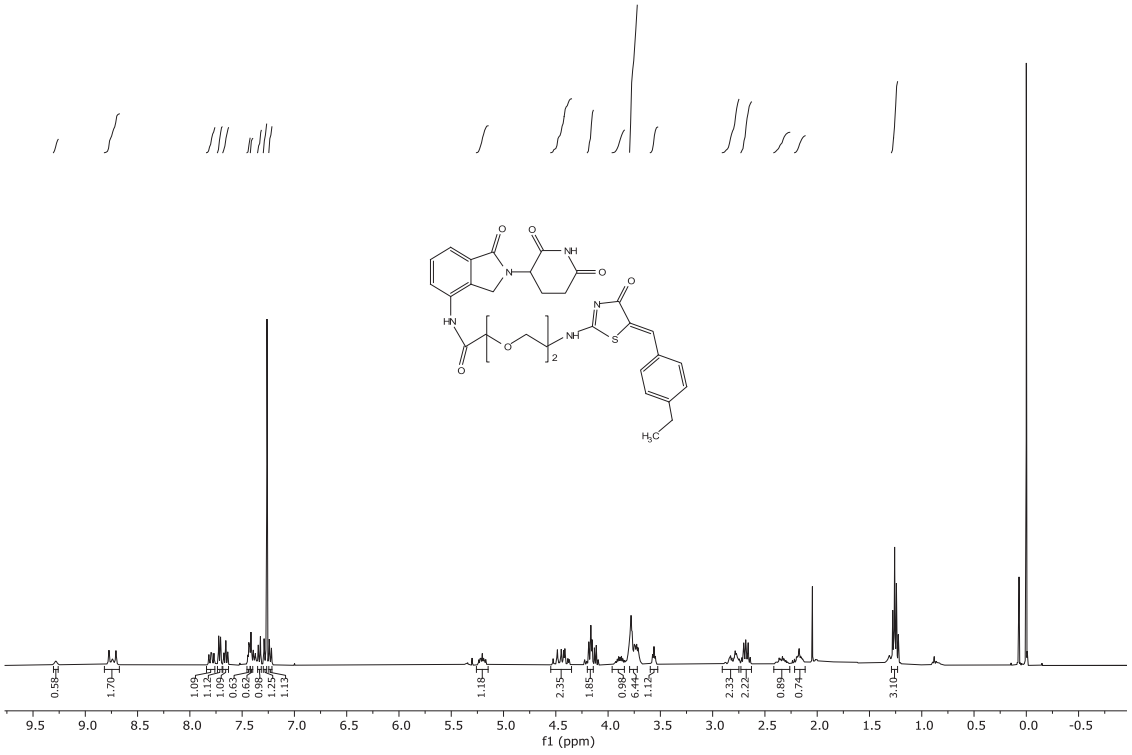

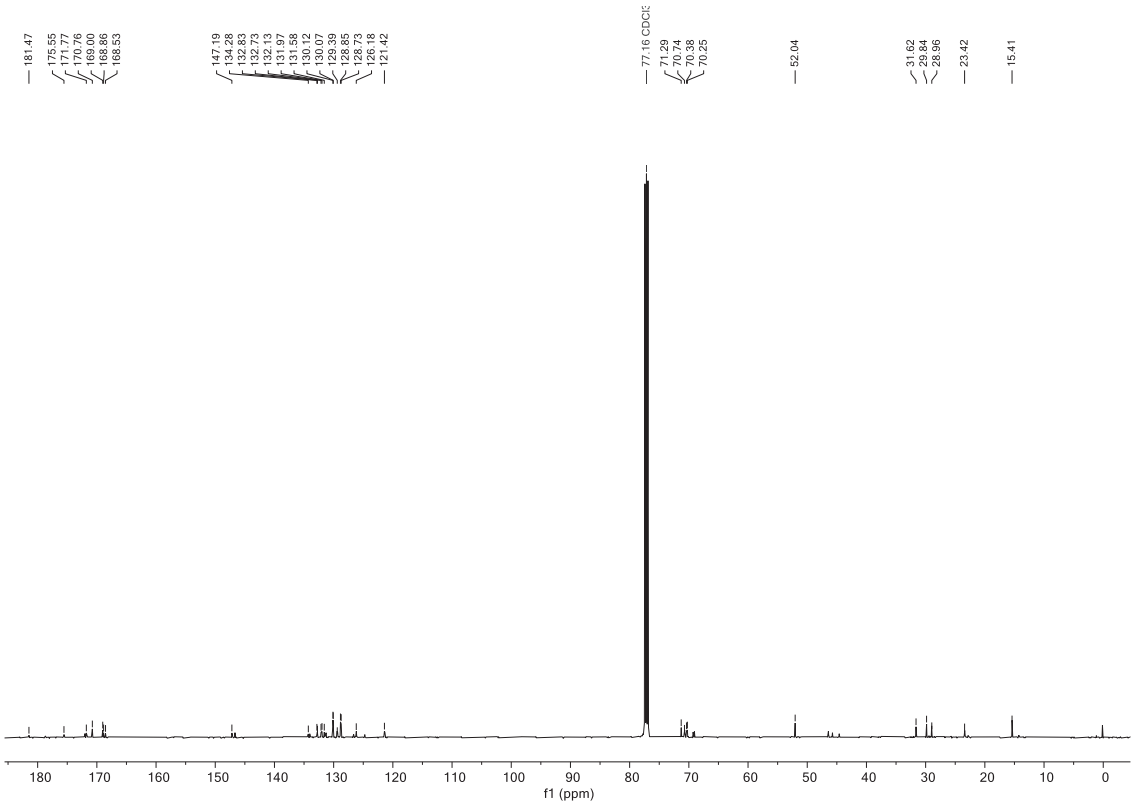
181.47
175.55
171.77
170.76
169.00
168.86
168.53
147.19
134.28
132.83
132.73
132.13
131.97
131.58
130.12
130.07
129.39
128.85
128.73
126.18
121.42
77.16 CDCl3
71.29
70.74
70.38
70.25
52.04
31.62
29.84
28.96
23.42
15.41
180 170 160 150 140 130 120 110 100 90 80 70 60 50 40 30 20 10 0
f1 (ppm)

HPLC / MS ASA-7

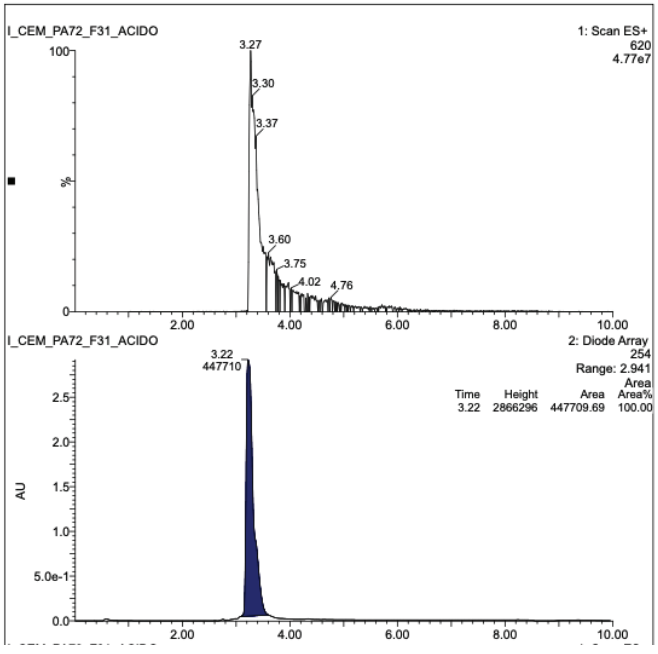
I_CEM_PA72_F31_ACIDO
1: Scan ES+
620
4.77e7
3.27
3.30
3.37
3.60
3.75
4.02
4.76
%
2.00 4.00 6.00 8.00 10.00
I_CEM_PA72_F31_ACIDO
2: Diode Array
254
Range: 2.941
Area
Time Height Area Area%
3.22 2866296 447709.69 100.00
3.22
447710
AU
2.5
2.0
1.5
1.0
5.0e-1
0.0
2.00 4.00 6.00 8.00 10.00

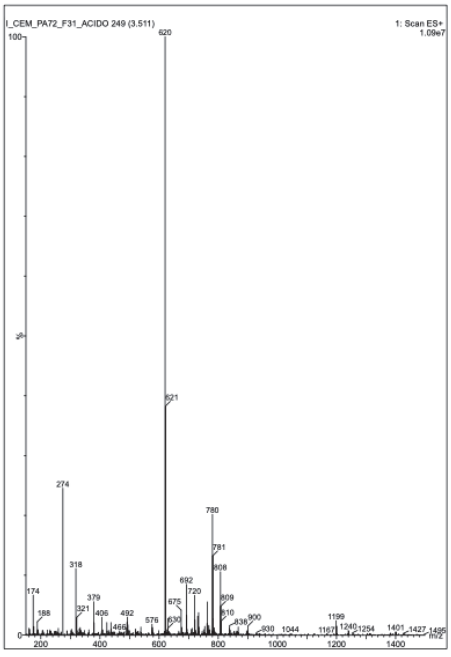
I_CEM_PA72_F31_ACIDO 249 (3.511)
1: Scan ES+
1.09e7
100
%
620
621
274
318
174
188
321
379
406
492
576
675
692
720
780
781
808
809
810
838
900
930
1044
1199
1240
1254
1401
1427
1495
200 400 600 800 1000 1200 1400
m/z

(Z)-N-(2-(2,6-Dioxopiperidin-3-yl)-1-oxoisoindolin-4-yl)-14-((5-(4-ethylbenzylidene)-4-oxo-4,5-dihydrothiazol-2-yl)amino)-3,6,9,12-tetraoxatetradecanamide (ASA-8)

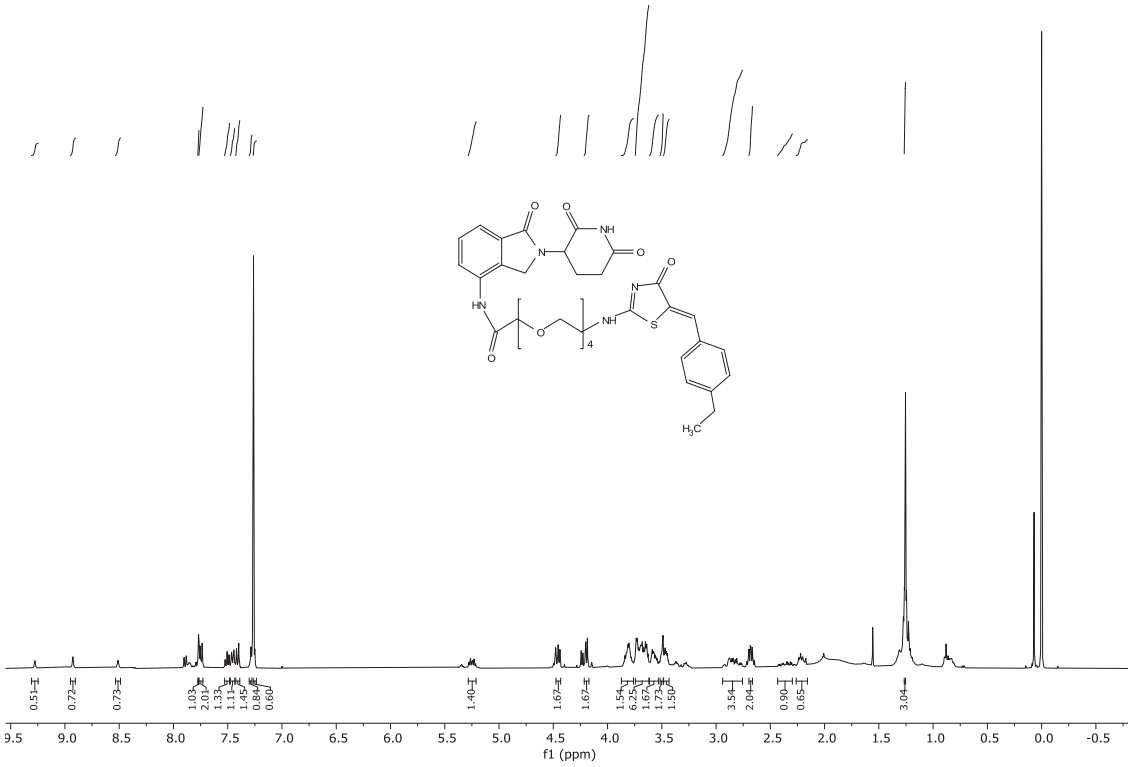

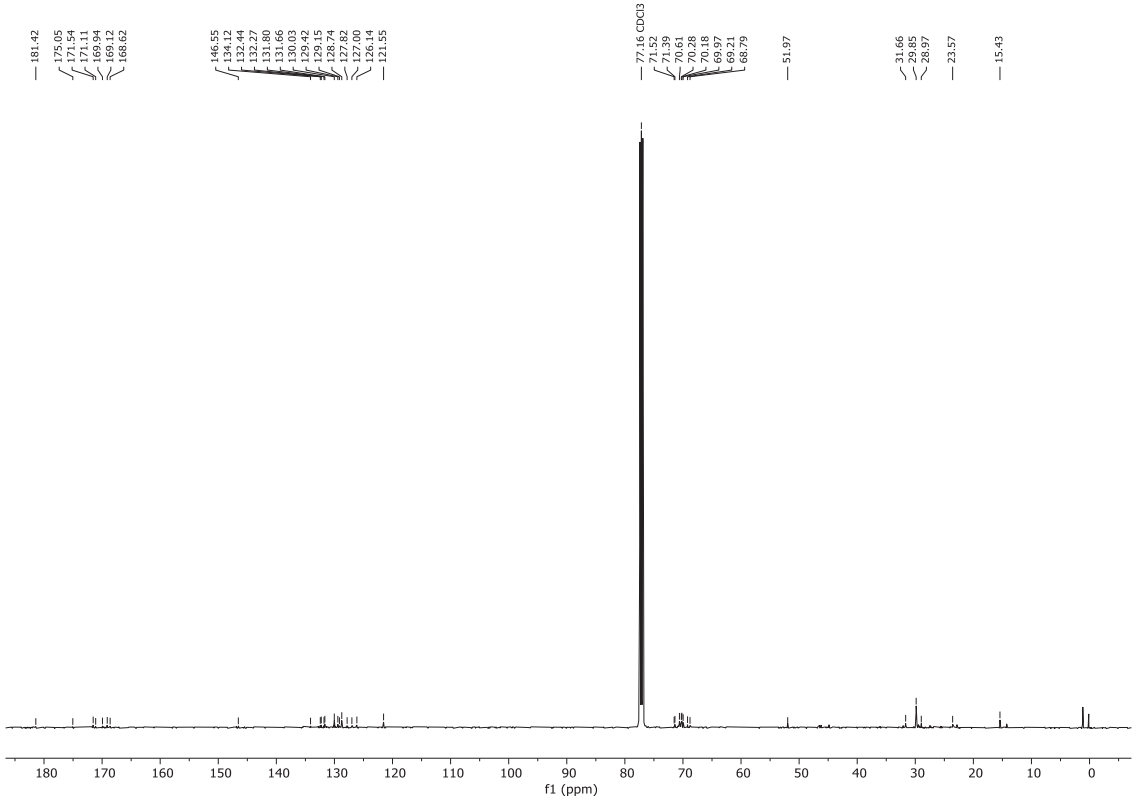

HPLC / MS ASA-8

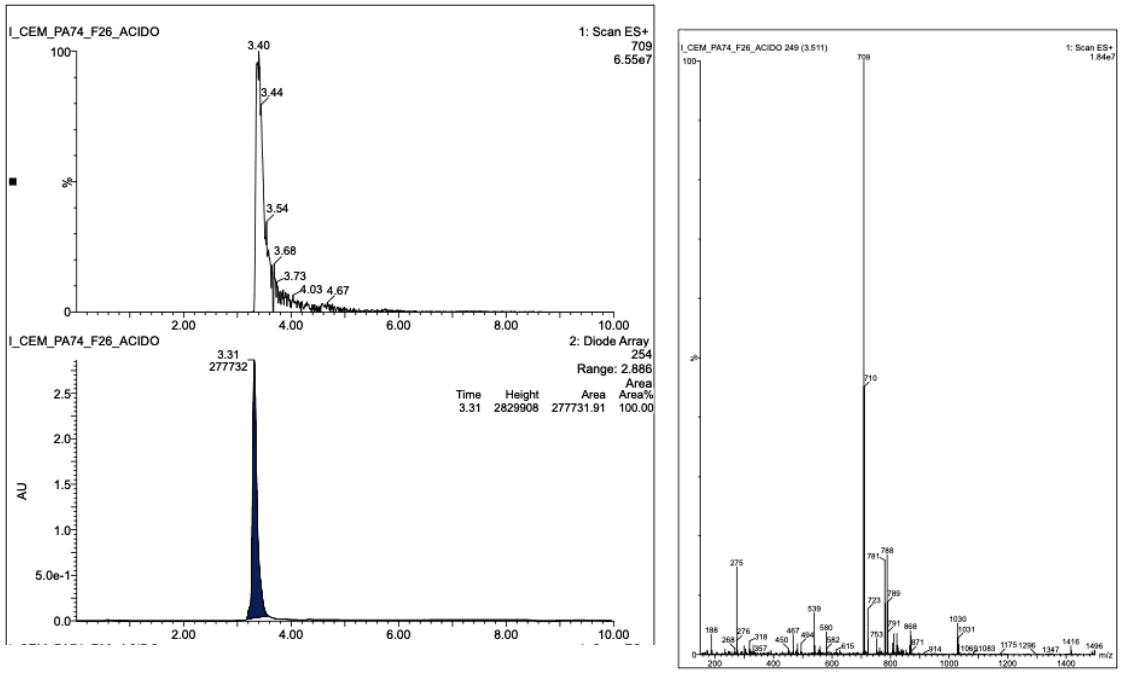

(2*S*,4*R*)-1-((*S*)-2-(2-(2-(2-((5-((*Z*)-4-Ethylbenzylidene)-4-oxo-4,5-dihydrothiazol-2-yl)amino)ethoxy)ethoxy)acetamido)-3,3-dimethylbutanoyl)-4-hydroxy-*N*-(4-(4-methylthiazol-5-yl)benzyl)pyrrolidine-2-carboxamide (ASA-9)

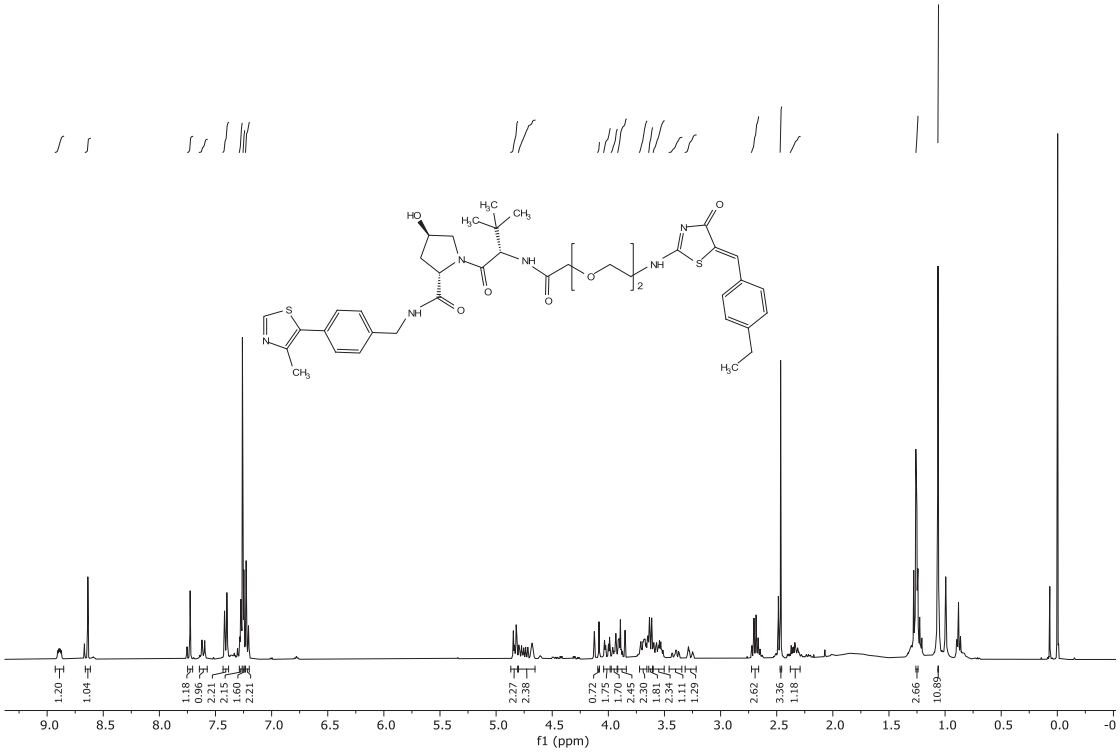

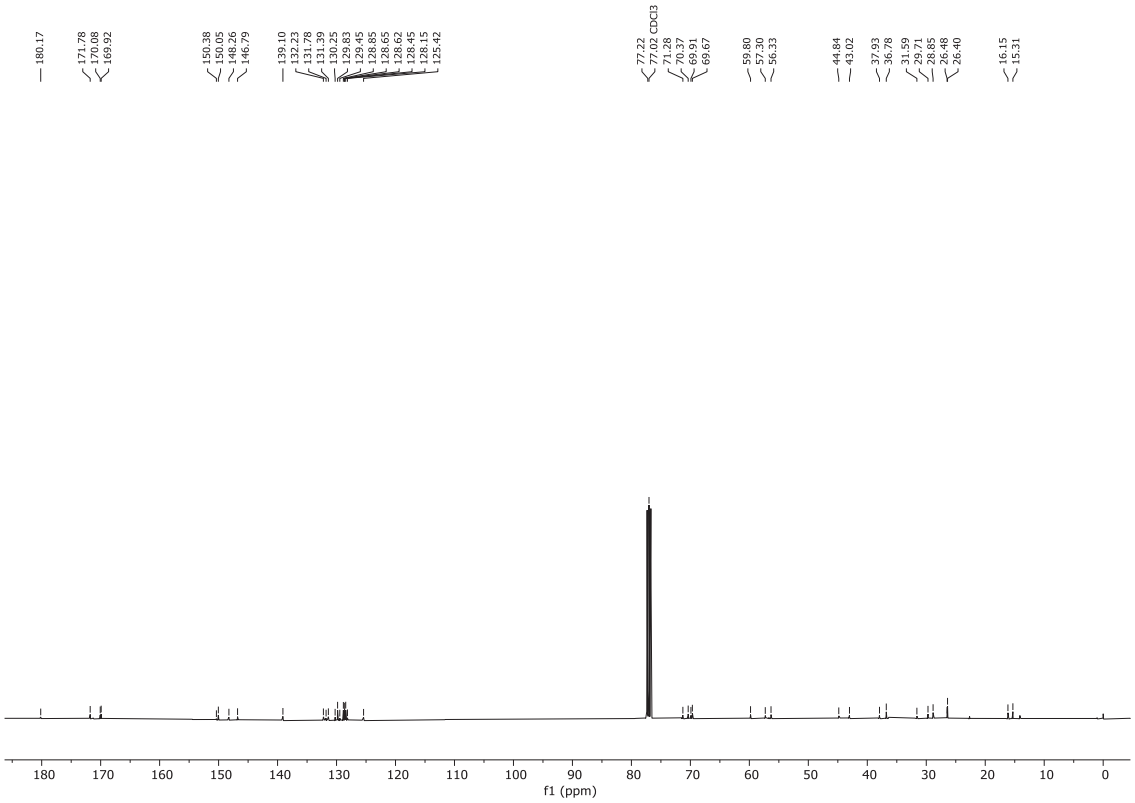

HPLC / MS ASA-9

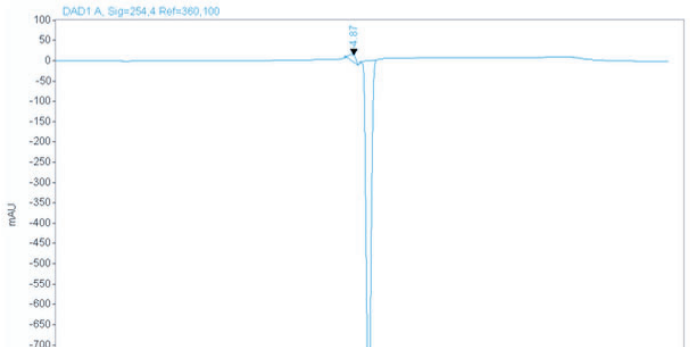

Signal: DAD1 A, Sig=254,4 Ref=360,100

RT [min]	Type	Width [min]	Area	Height	Area%	Name
4.870	MM	0.1215	125.4999	17.2179	2.6677	
5.116	MM N	0.0906	4578.8667	842.1780	97.3323	
		Sum	4704.3666			

(2*S*,4*R*)-1-((S)-2-(*tert*-Butyl)-17-((5-((*Z*)-4-ethylbenzylidene)-4-oxo-4,5-dihydrothiazol-2-yl)amino)-4-oxo-6,9,12,15-tetraoxa-3-azaheptadecanoyl)-4-hydroxy-*N*-(4-(4-methylthiazol-5-yl)benzyl)pyrrolidine-2-carboxamide (ASA-10)

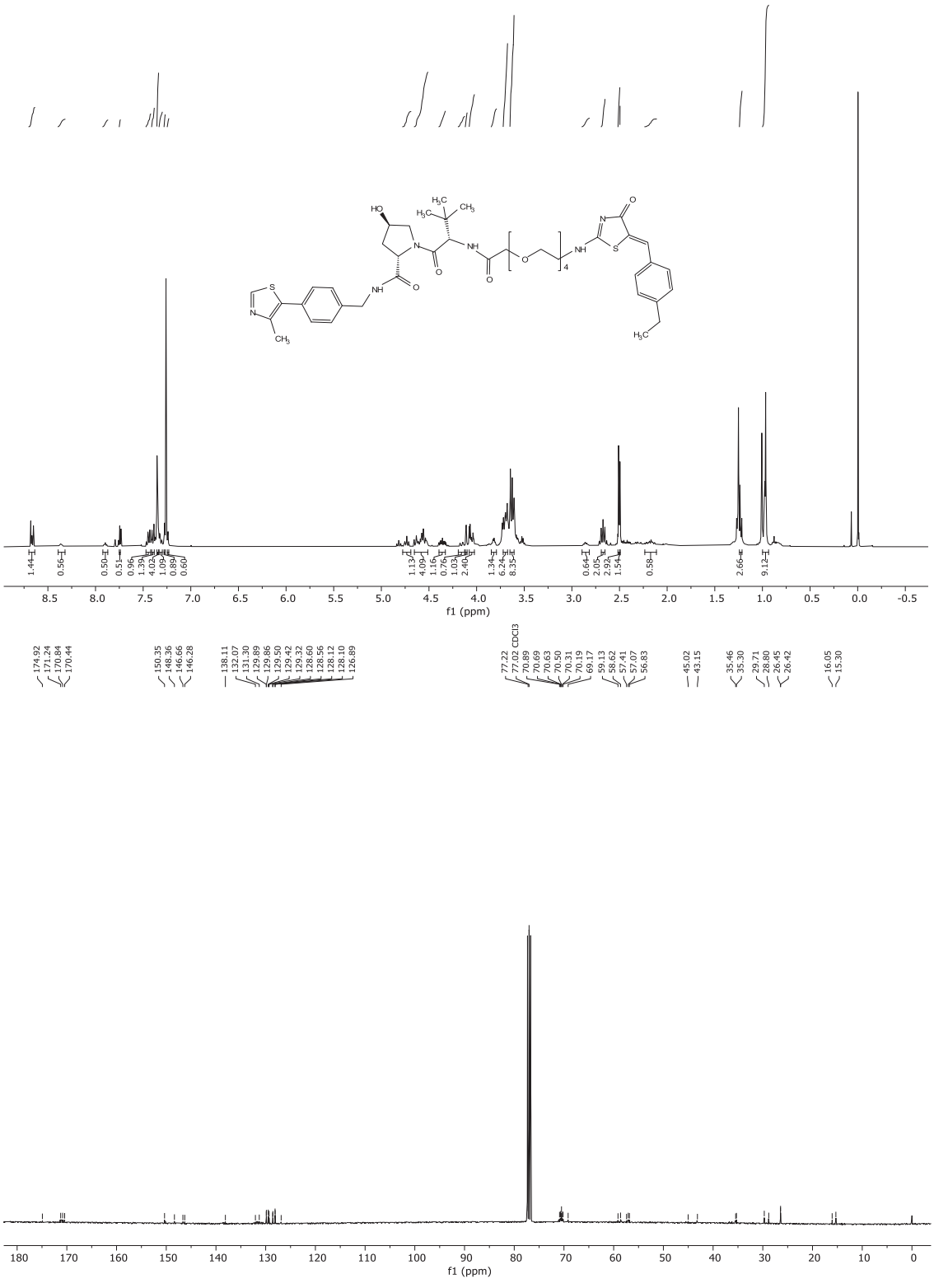

HPLC / MS ASA-10

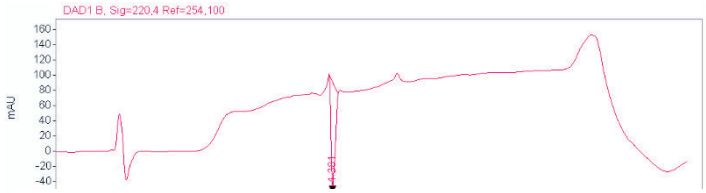

Signal: DAD1 B, Sig=220,4 Ref=254,100

RT [min]	Type	Width [min]	Area	Height	Area%	Name
4.381	MM N	0.0691	610.8548	147.2304	100.0000	
		Sum	610.8548			

tert-Butyl (8-(4-oxo-2-thioxothiazolidin-3-yl)octyl)carbamate (26)

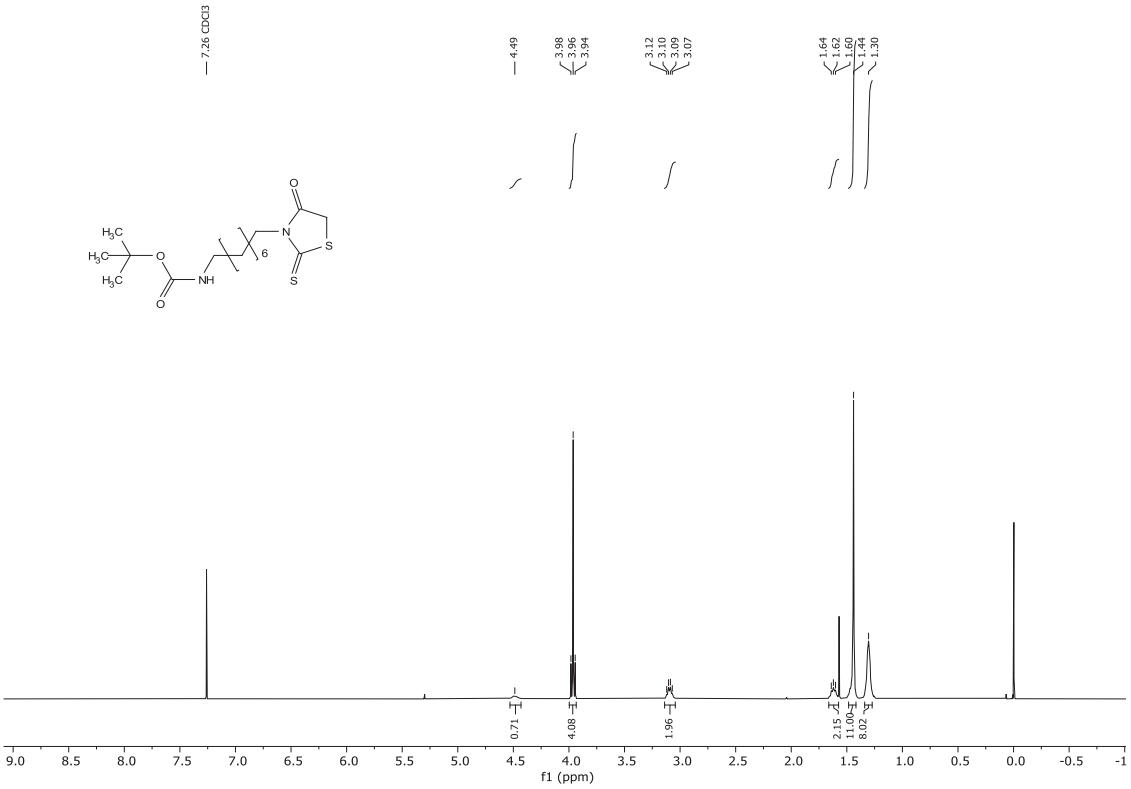

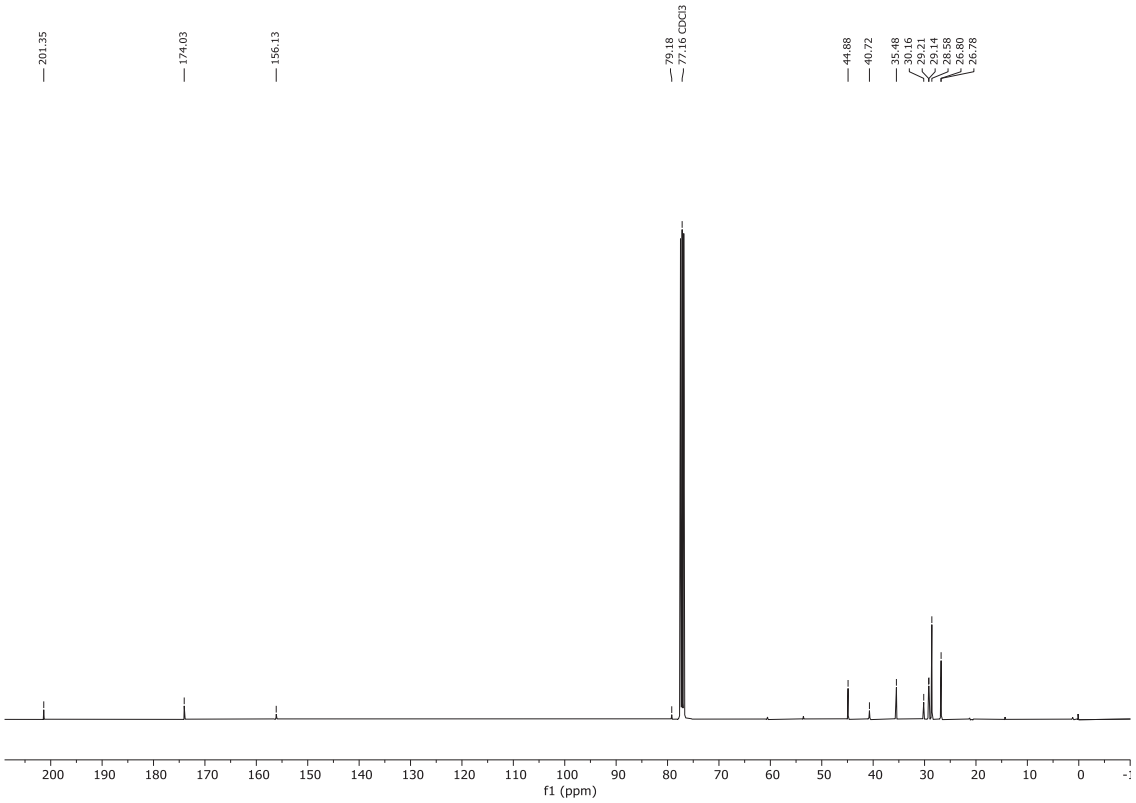

tert-Butyl (2-(2-(2-(2-(4-oxo-2-thioxothiazolidin-3-yl)ethoxy)ethoxy)ethoxy)ethyl) carbamate (34)

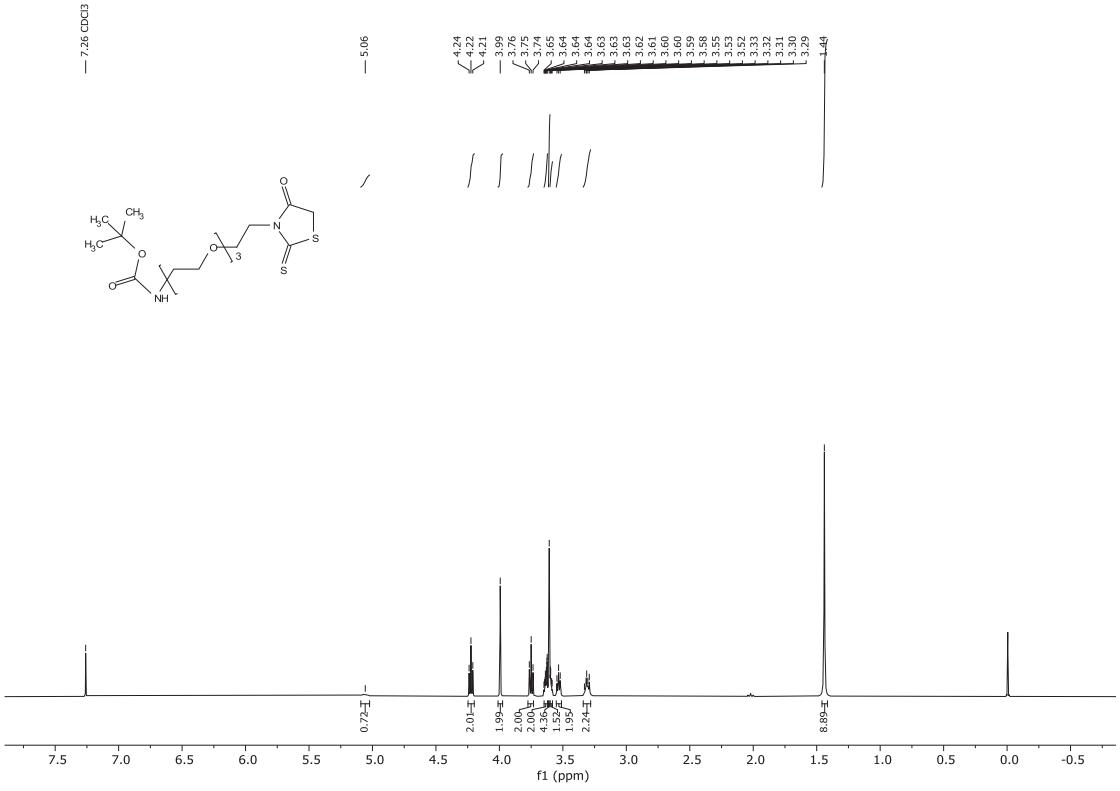

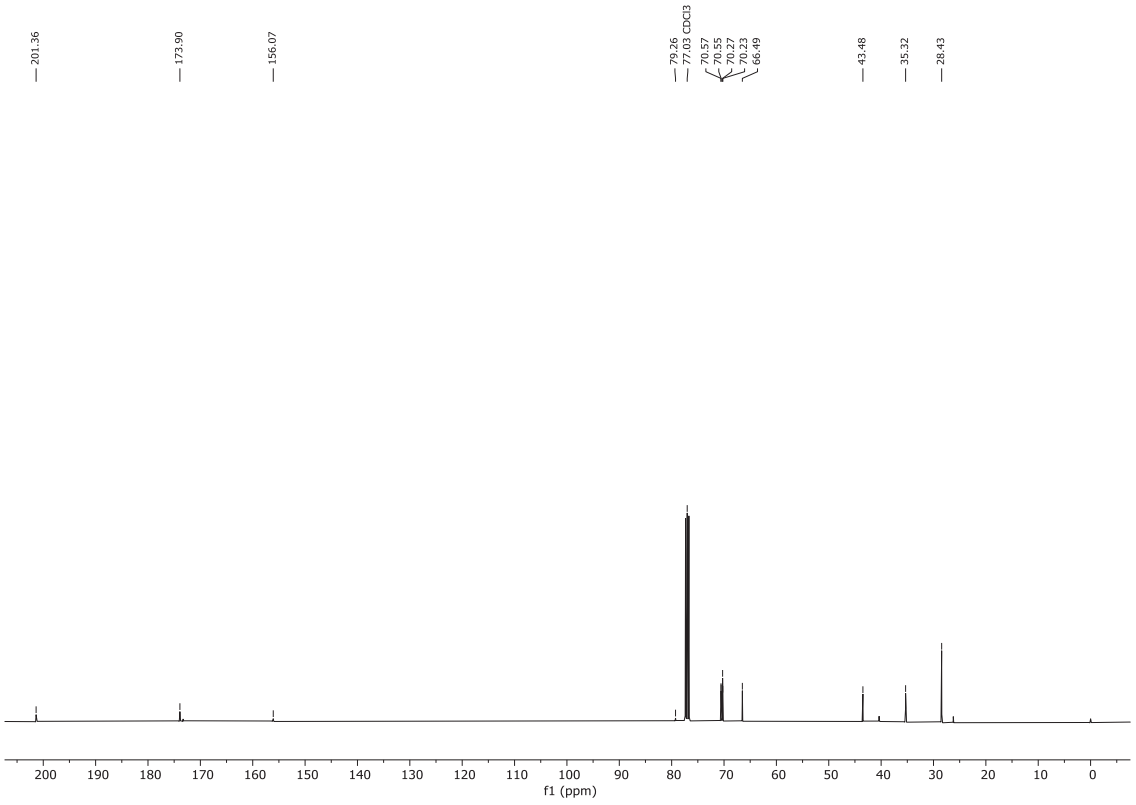
201.36
173.90
156.07
79.26
77.03 CDCl3
70.57
70.55
70.27
70.23
66.49
43.48
35.32
28.43
f1 (ppm)

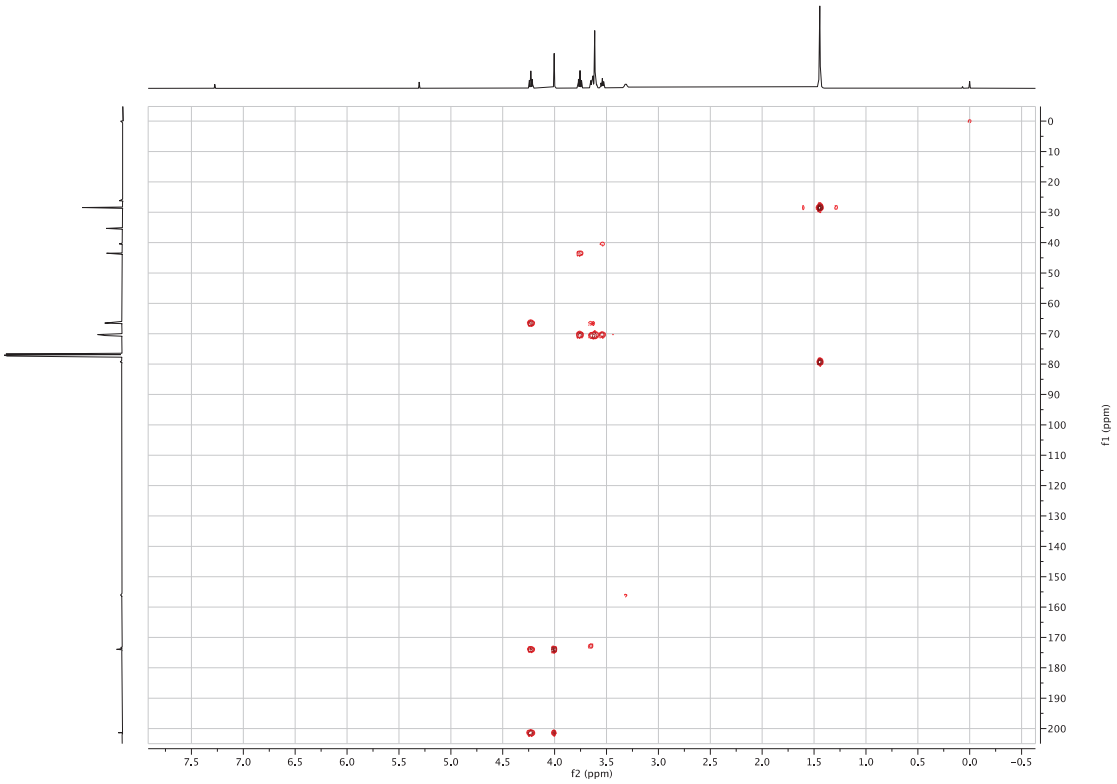
f2 (ppm)
f1 (ppm)

tert-Butyl (*Z*)-(8-(5-(4-isopropylbenzylidene)-4-oxo-2-thioxothiazolidin-3-yl)octyl) carbamate (28)

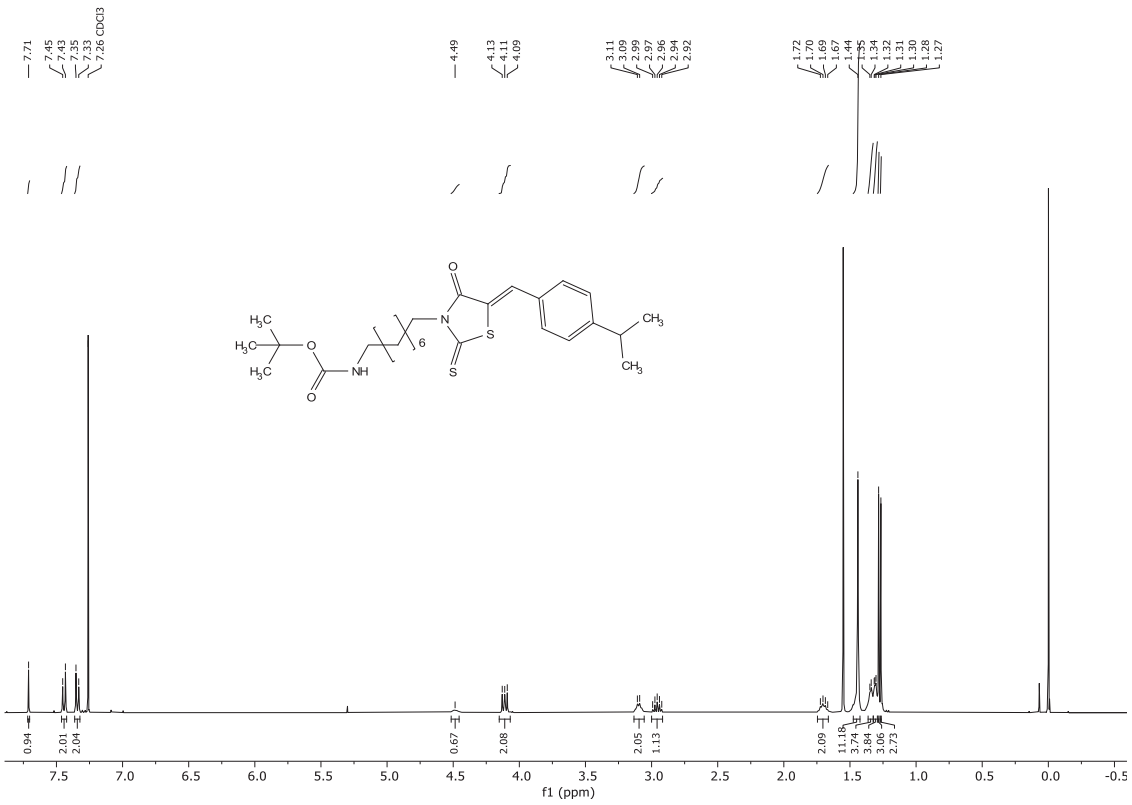

tert-butyl (*Z*)-(8-(5-(4-Ethylbenzylidene)-4-oxo-2-thioxothiazolidin-3-yl)octyl)carbamate (29)

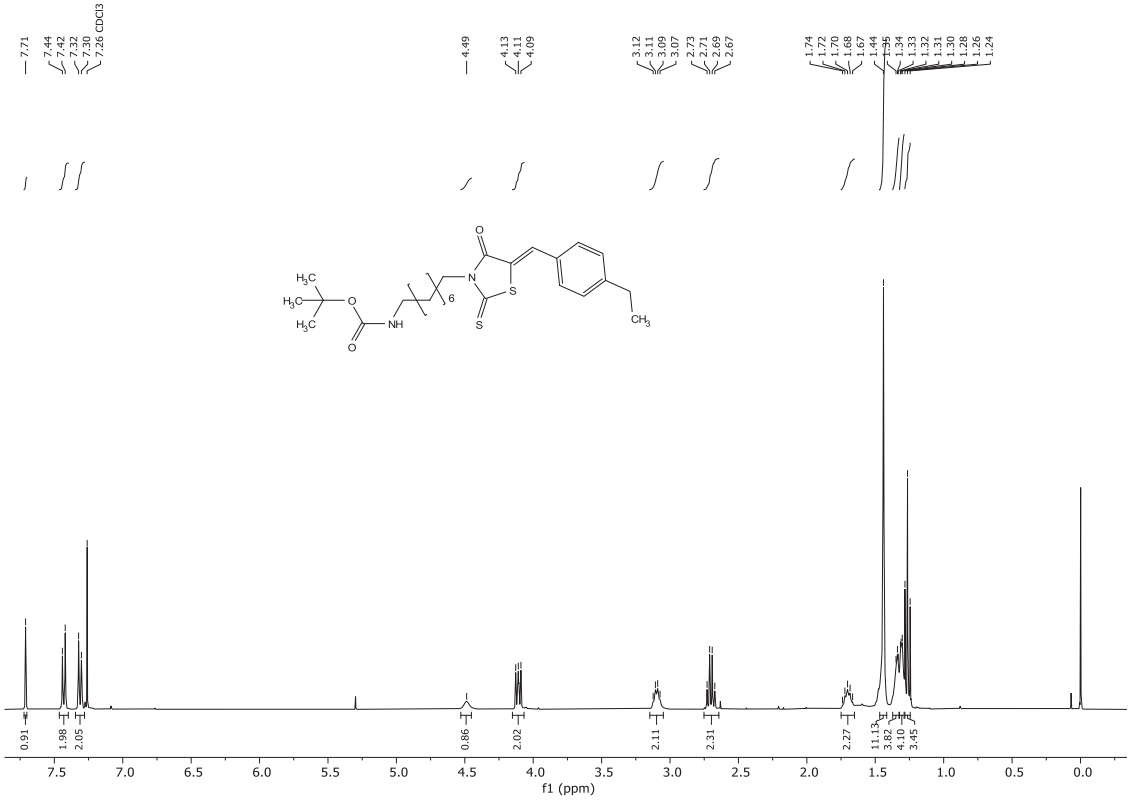

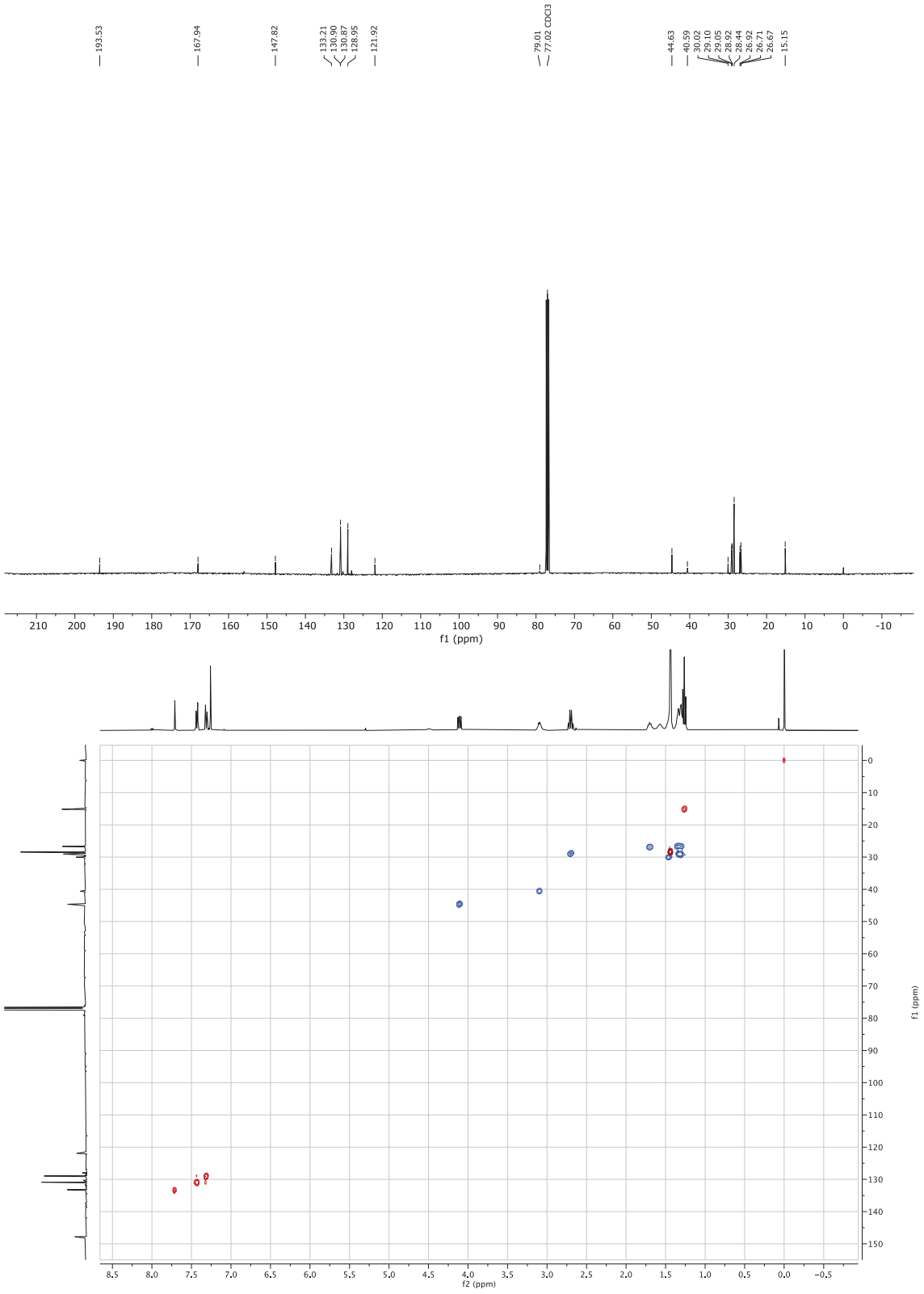
193.53
167.94
147.82
133.21
130.90
130.87
128.95
121.92
79.01
77.02 CDCl3
44.63
40.59
30.02
29.10
29.05
28.92
28.44
26.92
26.71
26.67
15.15
f1 (ppm)
f2 (ppm)
f1 (ppm)

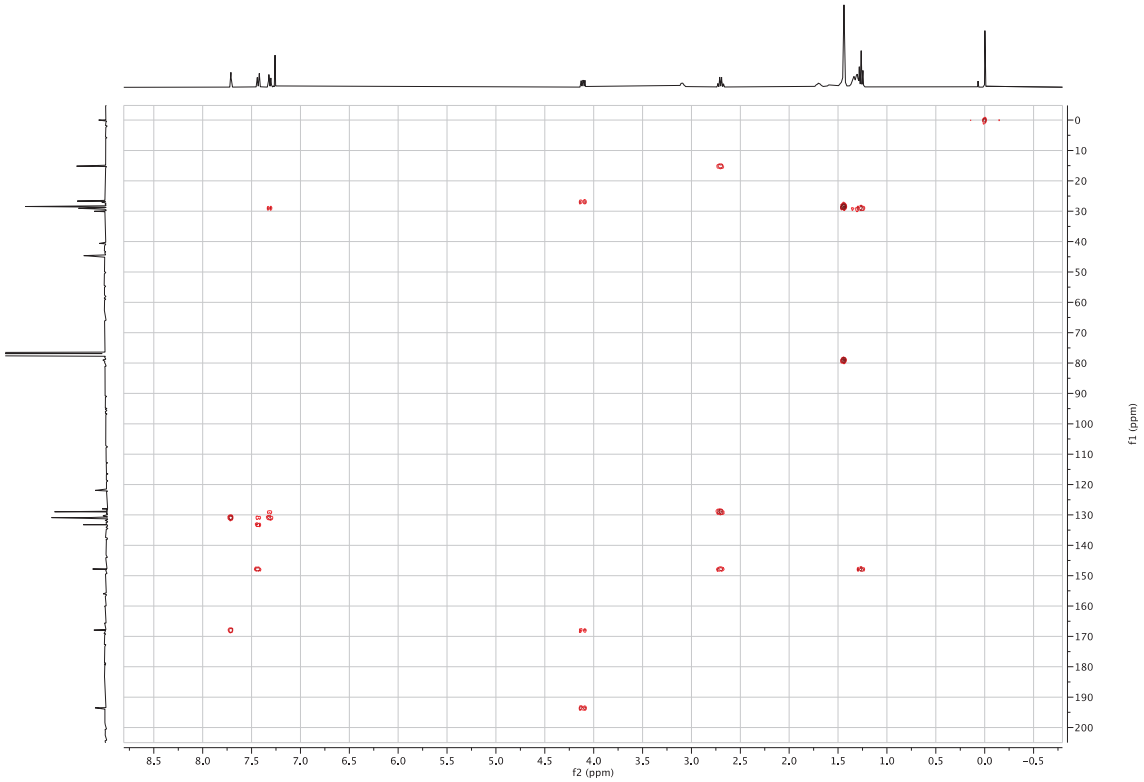

tert-Butyl (*Z*)-(2-(2-(2-(2-(5-(4-isopropylbenzylidene)-4-oxo-2-thioxothiazolidin-3-yl)ethoxy)ethoxy)ethoxy)ethyl)carbamate (35)

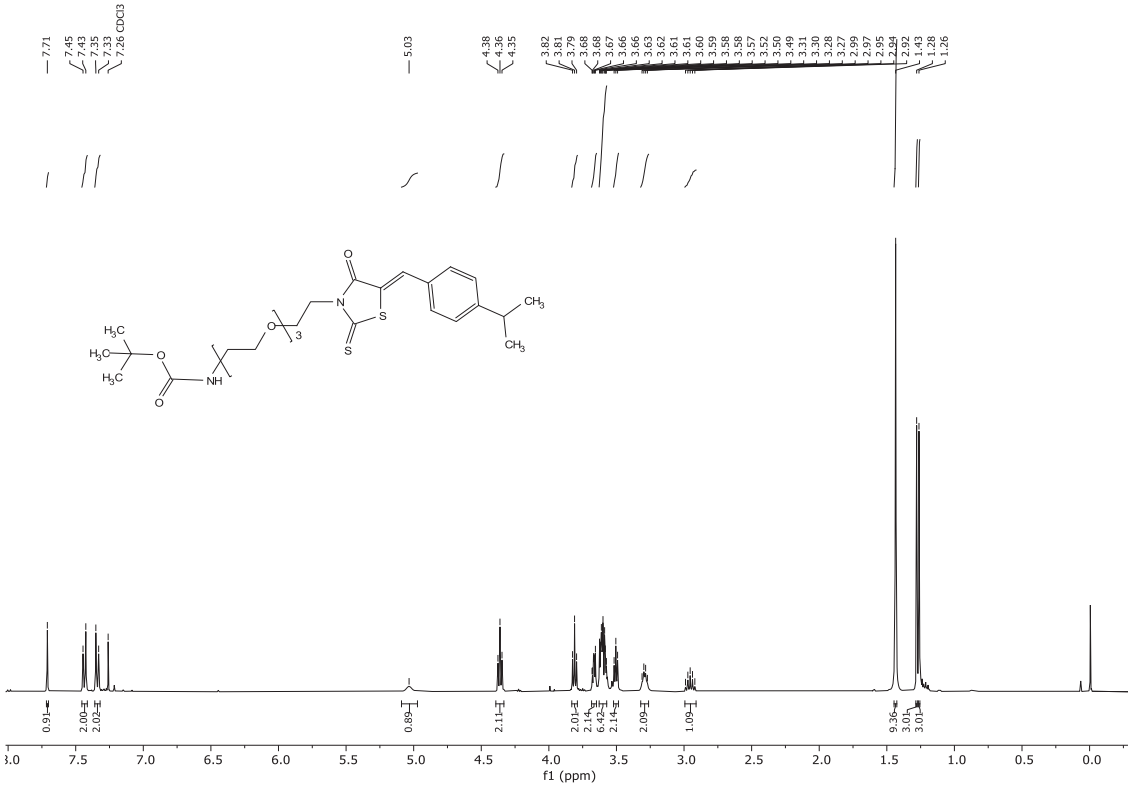

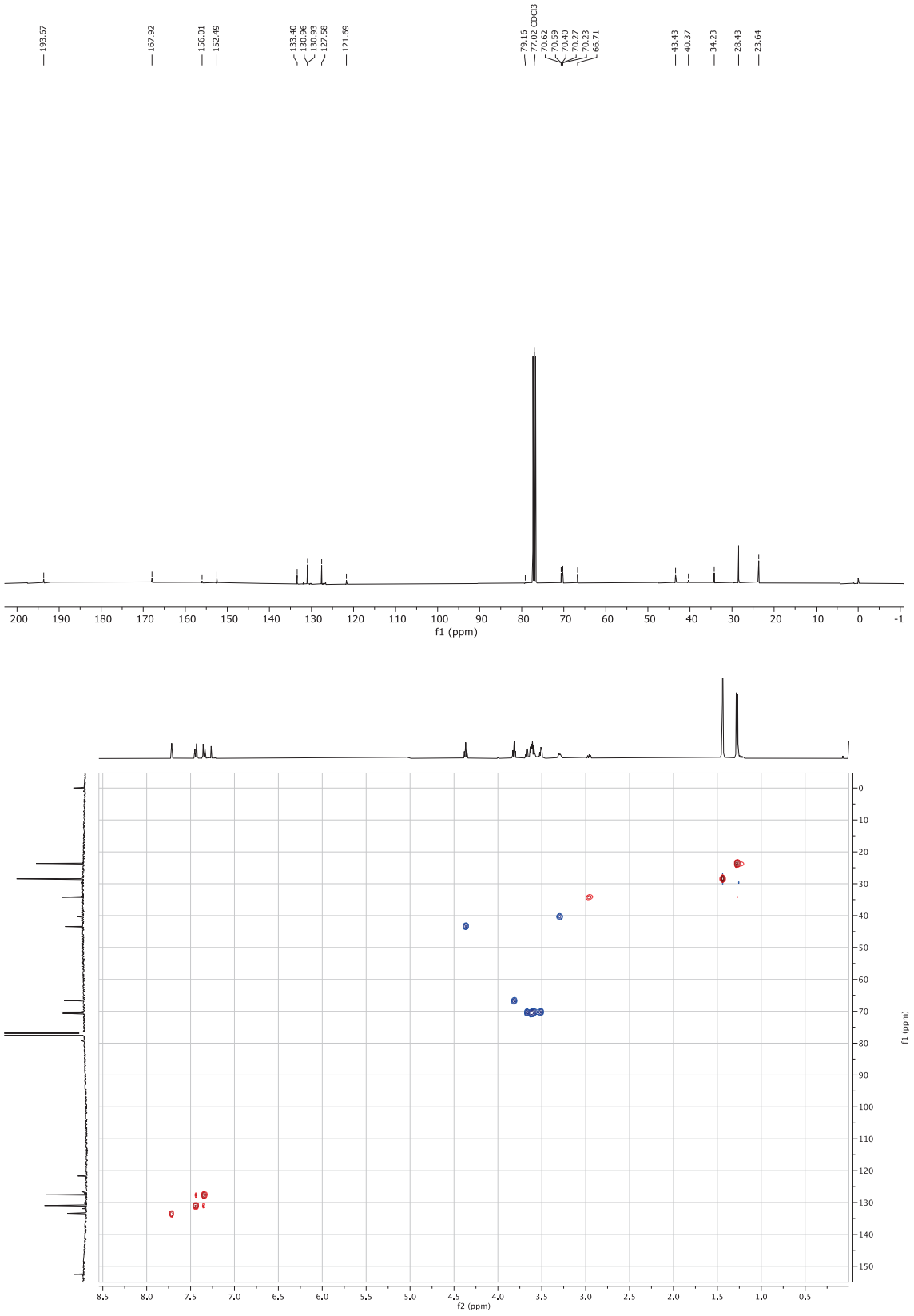
193.67
167.92
156.01
152.49
133.40
130.96
130.93
127.58
121.69
79.16
77.02 CDCl3
70.62
70.59
70.40
70.27
70.23
66.71
43.43
40.37
34.23
28.43
23.64
f1 (ppm)
f2 (ppm)
f1 (ppm)

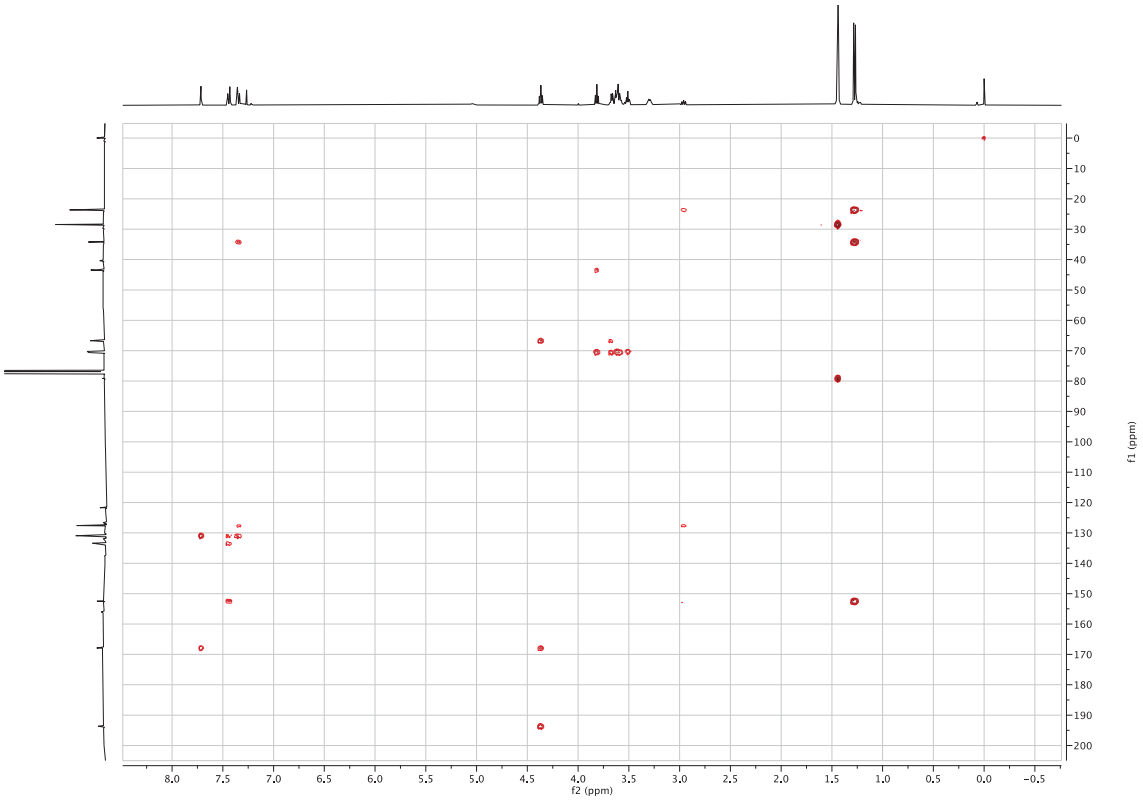

tert-Butyl (*Z*)-(2-(2-(2-(2-(5-(4-ethylbenzylidene)-4-oxo-2-thioxothiazolidin-3-yl)ethoxy)ethoxy)ethoxy)ethyl)carbamate (36)

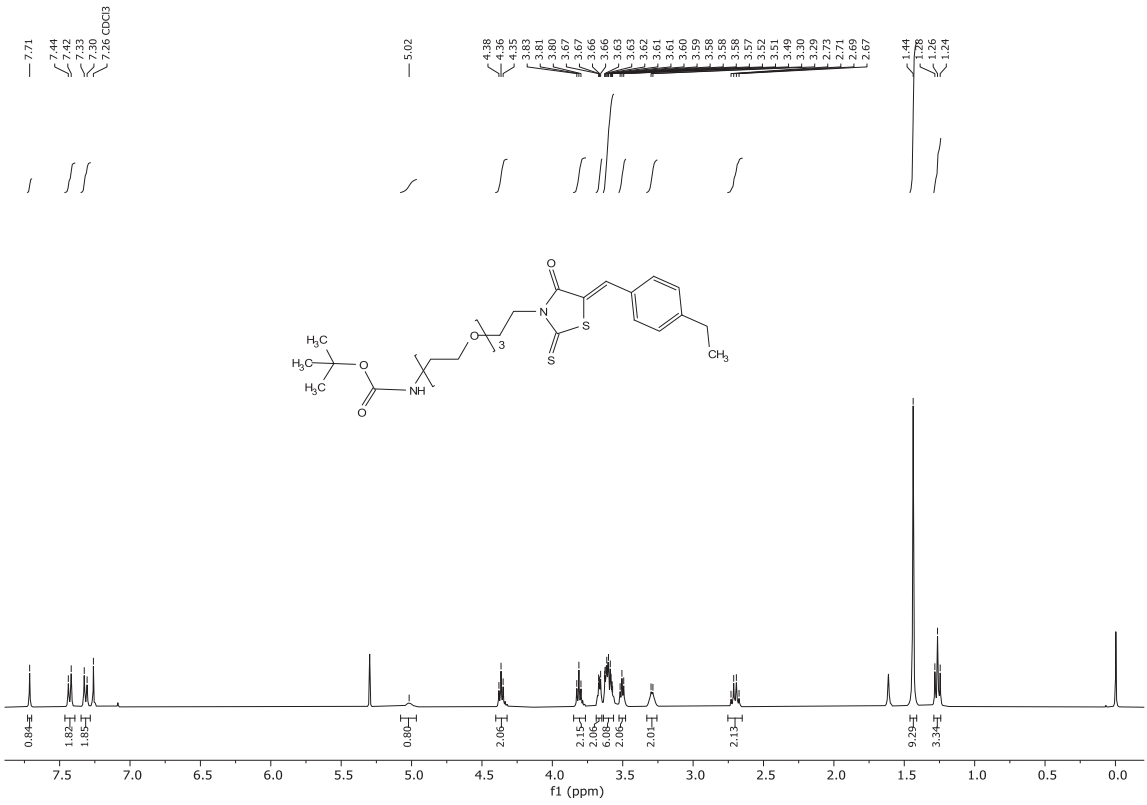

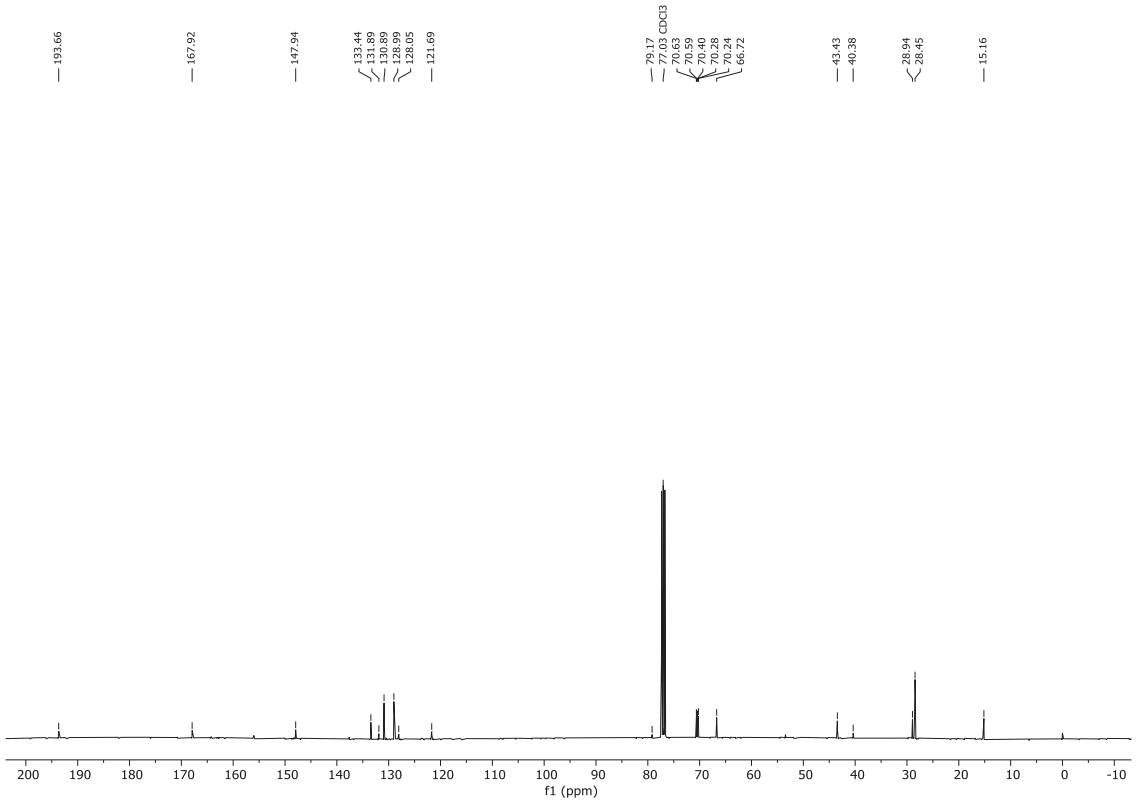

(*Z*)-2-(2,6-Dioxopiperidin-3-yl)-*N*-(8-(5-(4-isopropylbenzylidene)-4-oxo-2-thioxothiazolidin-3-yl)octyl)-1,3-dioxoisoindoline-5-carboxamide (ASA_MDEG-541)

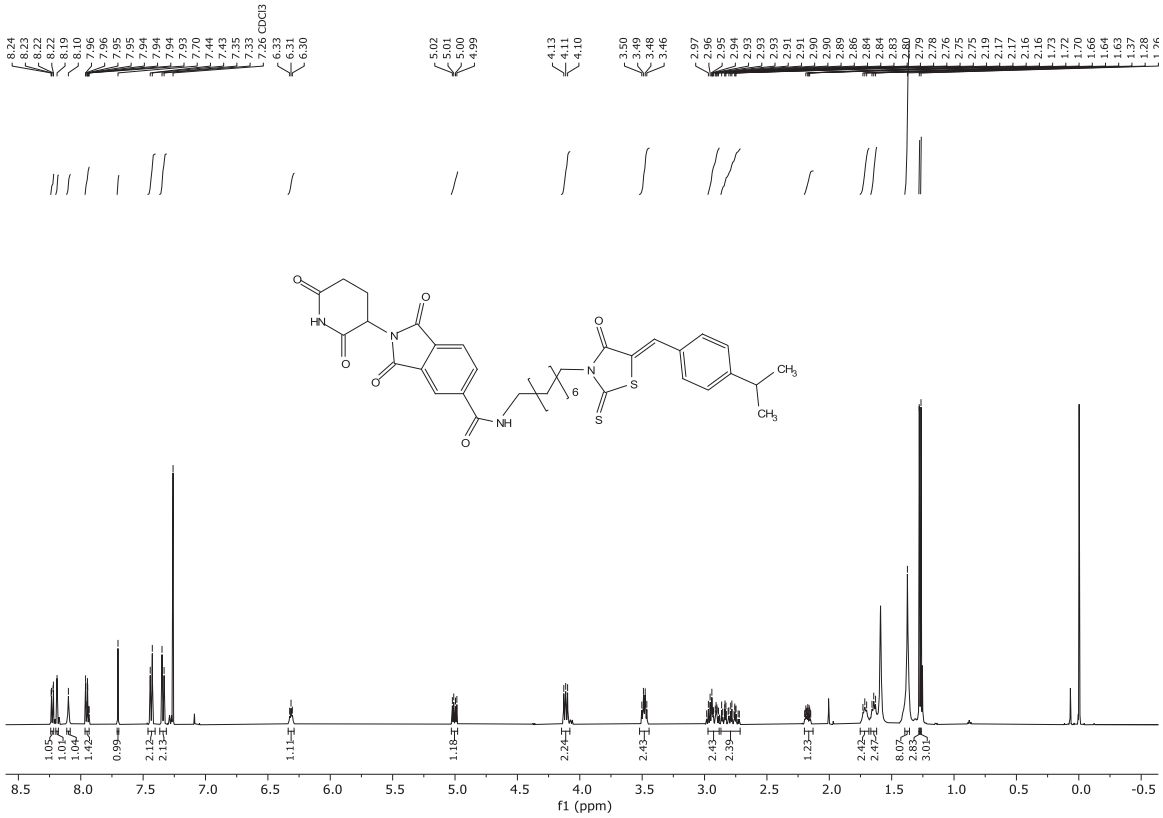

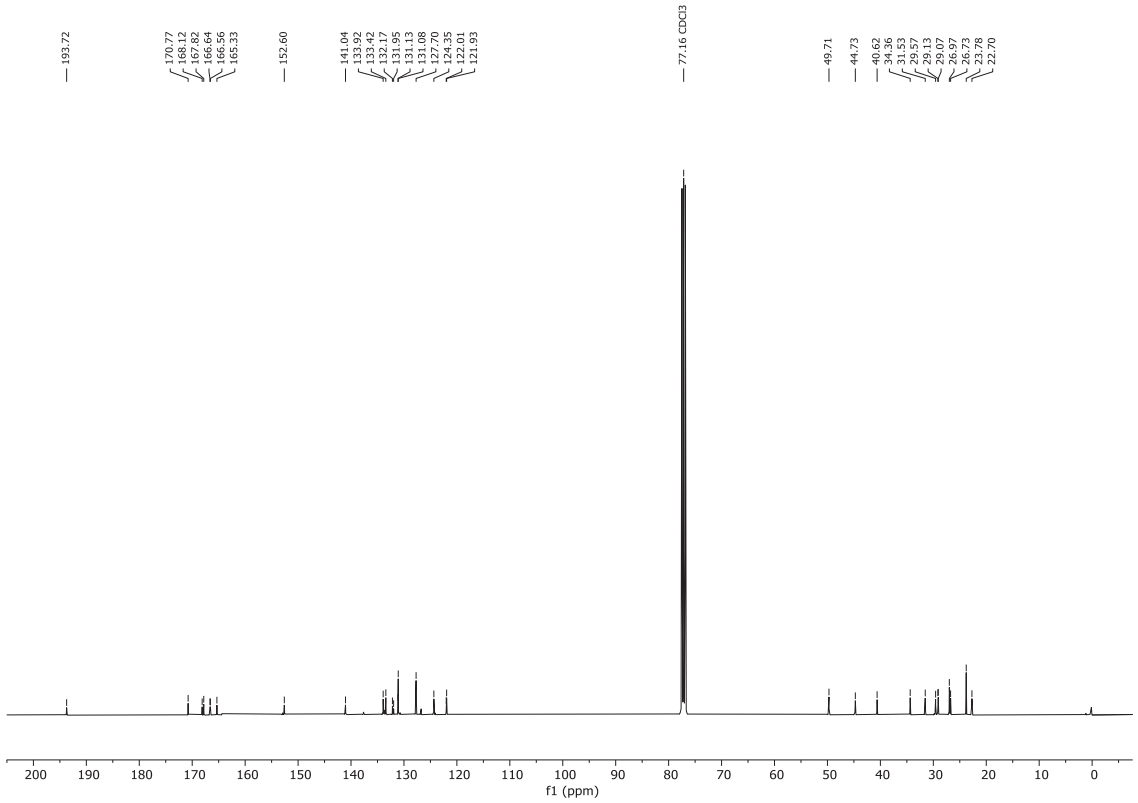

HPLC / MS ASA_MDEG-541

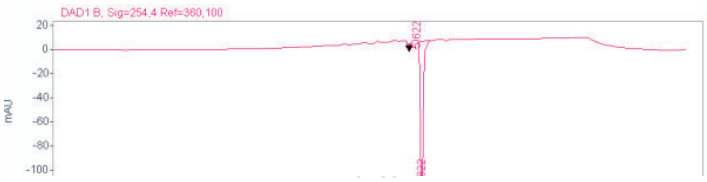

Signal: DAD1 B, Sig=254,4 Ref=360,100

RT [min]	Type	Width [min]	Area	Height	Area%	Name
5.622	PP N	0.0346	13.4834	6.4979	3.3384	
5.822	PM N	0.0503	390.4046	129.3104	96.6616	
		Sum	403.8880			

(*Z*)-2-(2,6-Dioxopiperidin-3-yl)-*N*-(8-(5-(4-ethylbenzylidene)-4-oxo-2-thioxothiazolidin-3-yl)octyl)-1,3-dioxoisoindoline-5-carboxamide (ASA_MDEG-542)

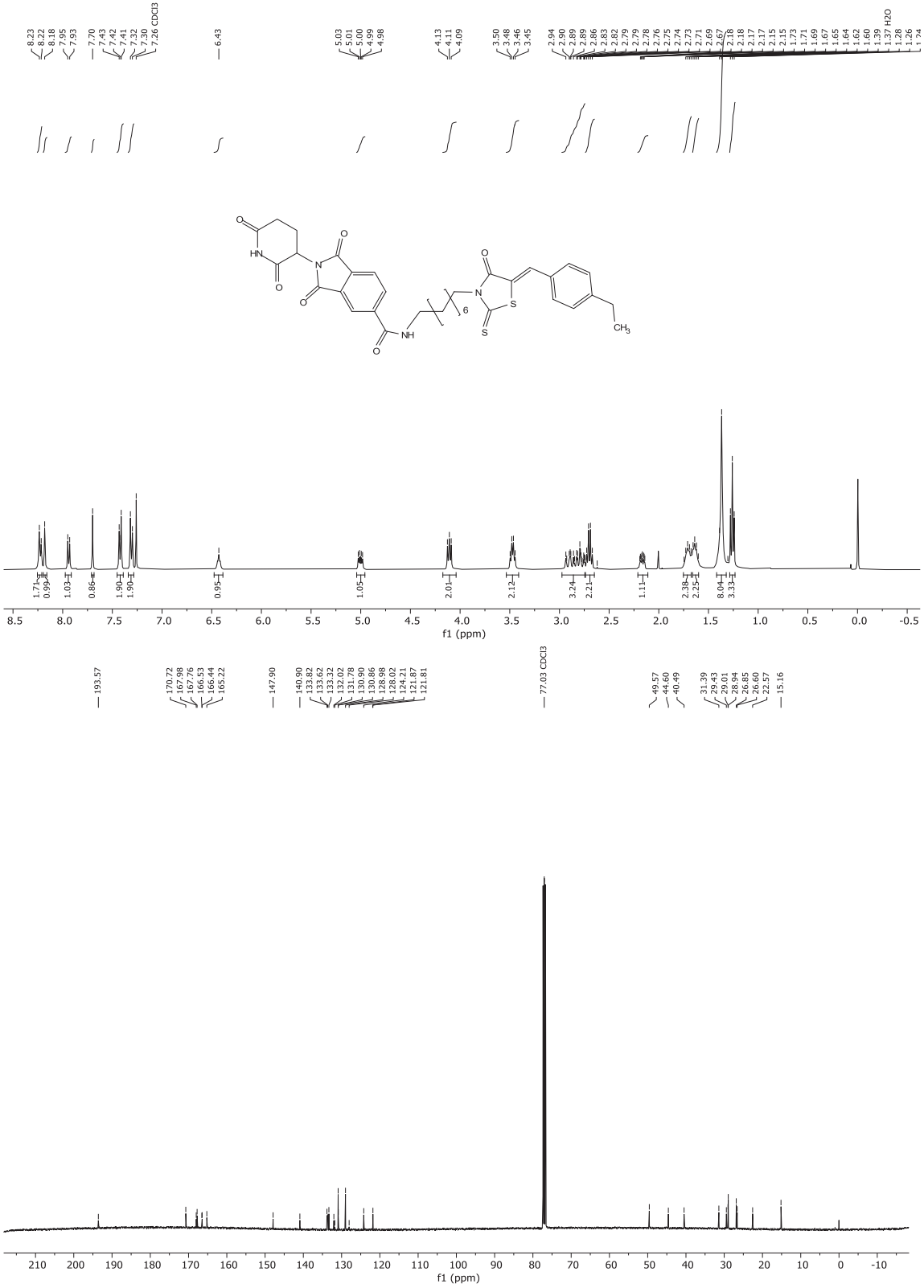

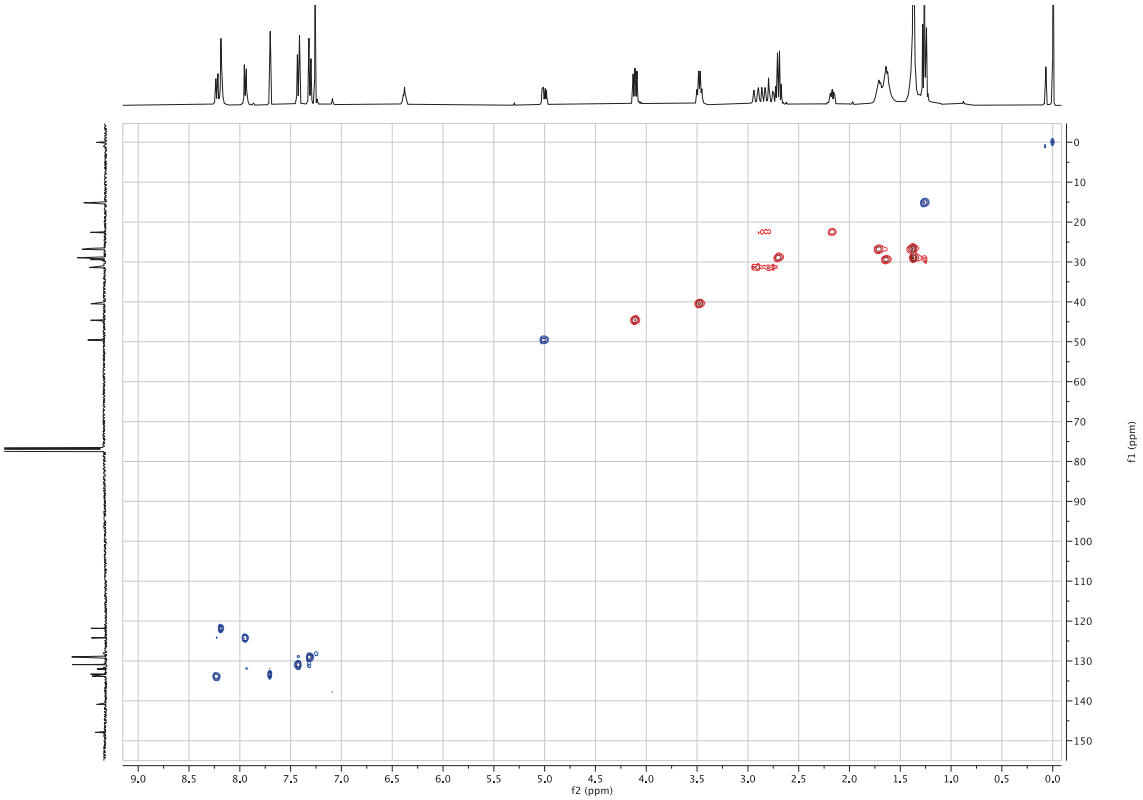
f2 (ppm)
f1 (ppm)

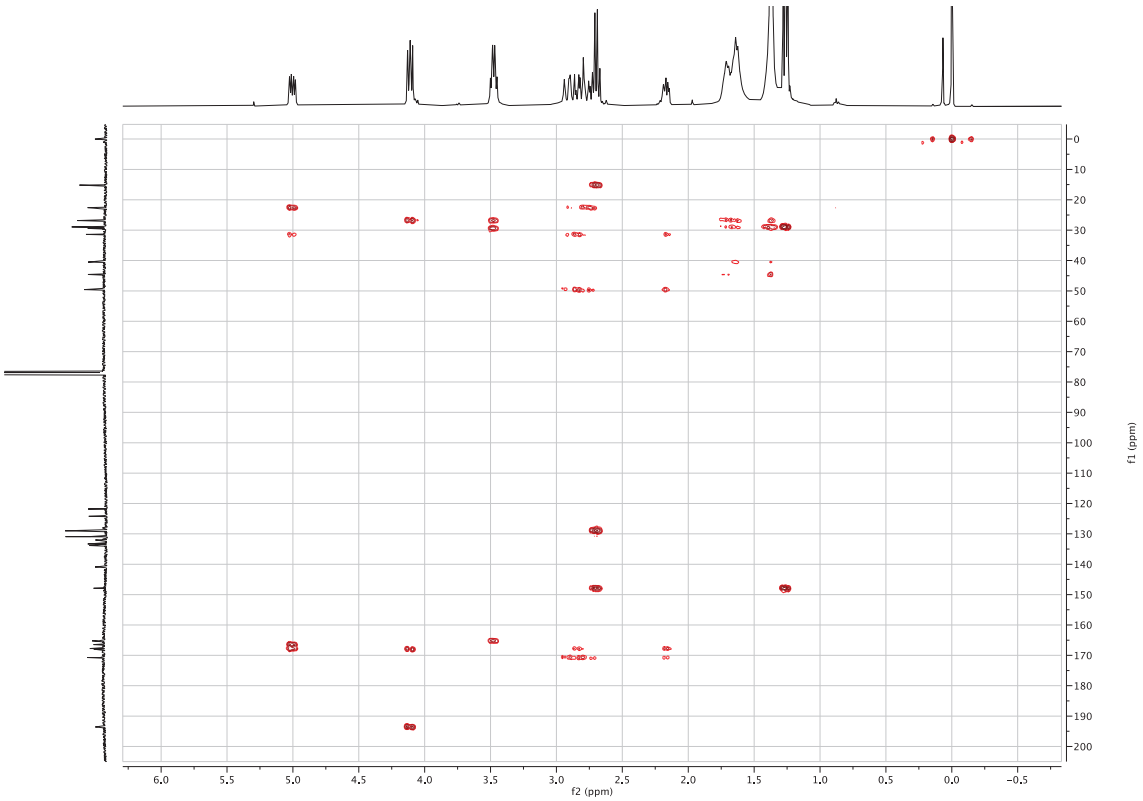
f2 (ppm)
f1 (ppm)

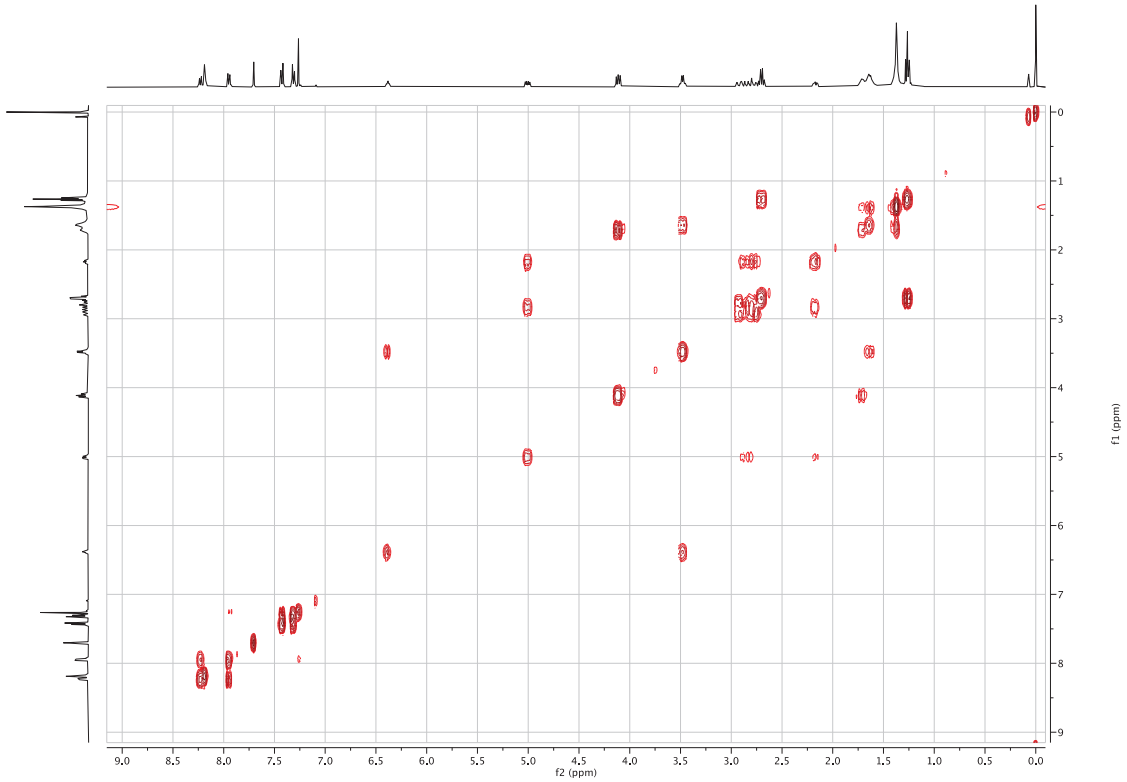

HPLC / MS ASA_MDEG-542

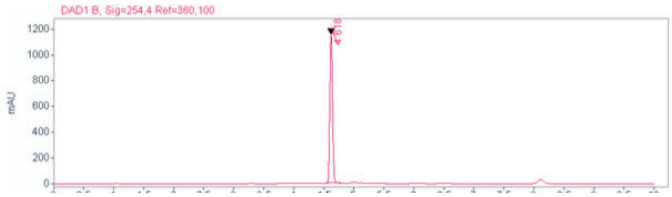

Signal: DAD1 B, Sig=254,4 Ref=360,100

RT [min]	Type	Width [min]	Area	Height	Area%	Name
4.618	BB	0.0487	3654.4199	1162.3351	100.0000	
		Sum	3654.4199			

(*Z*)-2-(2,6-Dioxopiperidin-3-yl)-*N*-(2-(2-(2-(5-(4-isopropylbenzylidene)-4-oxo-2-thioxothiazolidin-3-yl)ethoxy)ethoxy)ethyl)-1,3-dioxoisoindoline-5-carboxamide (ASA_MDEG-543)

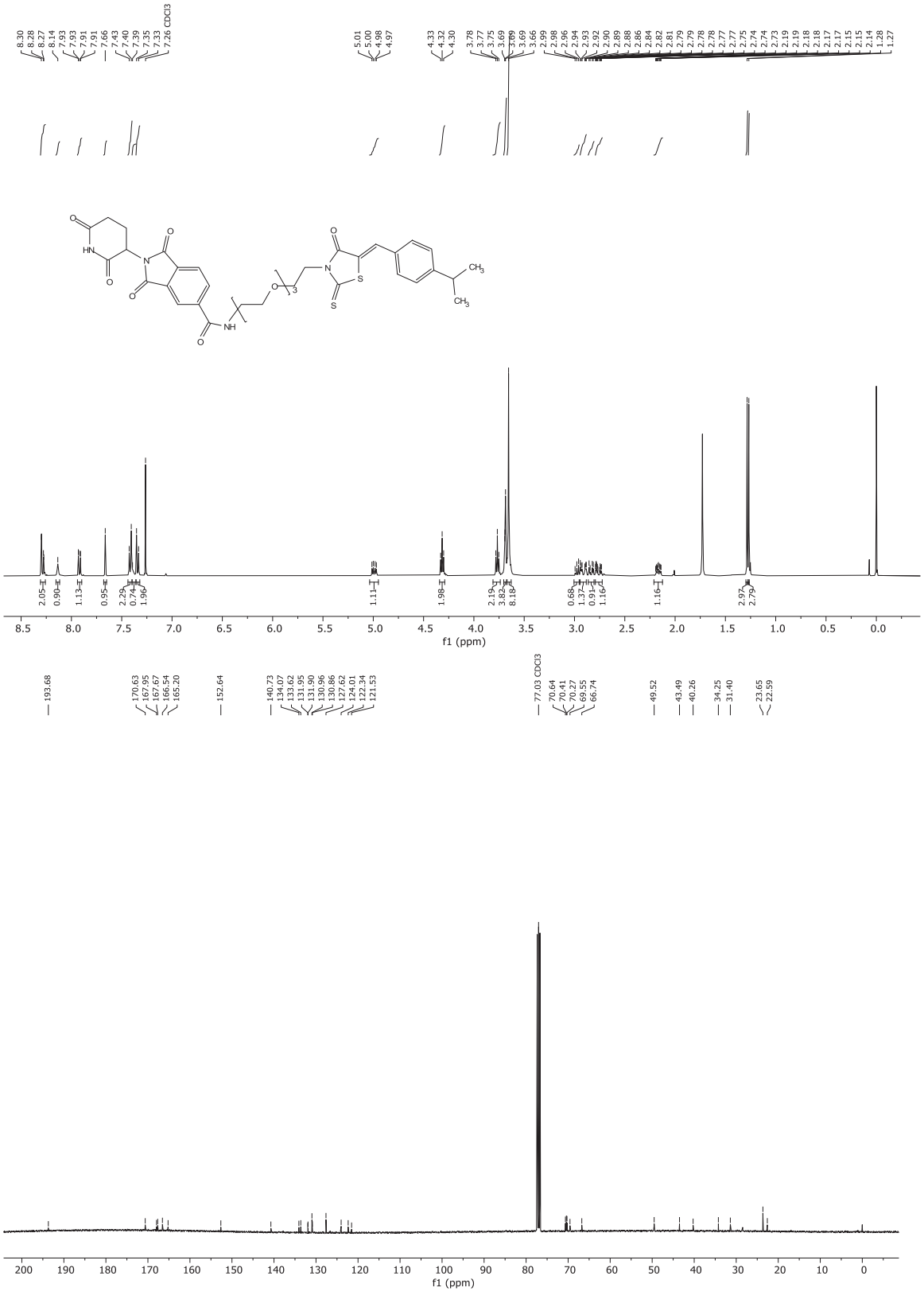

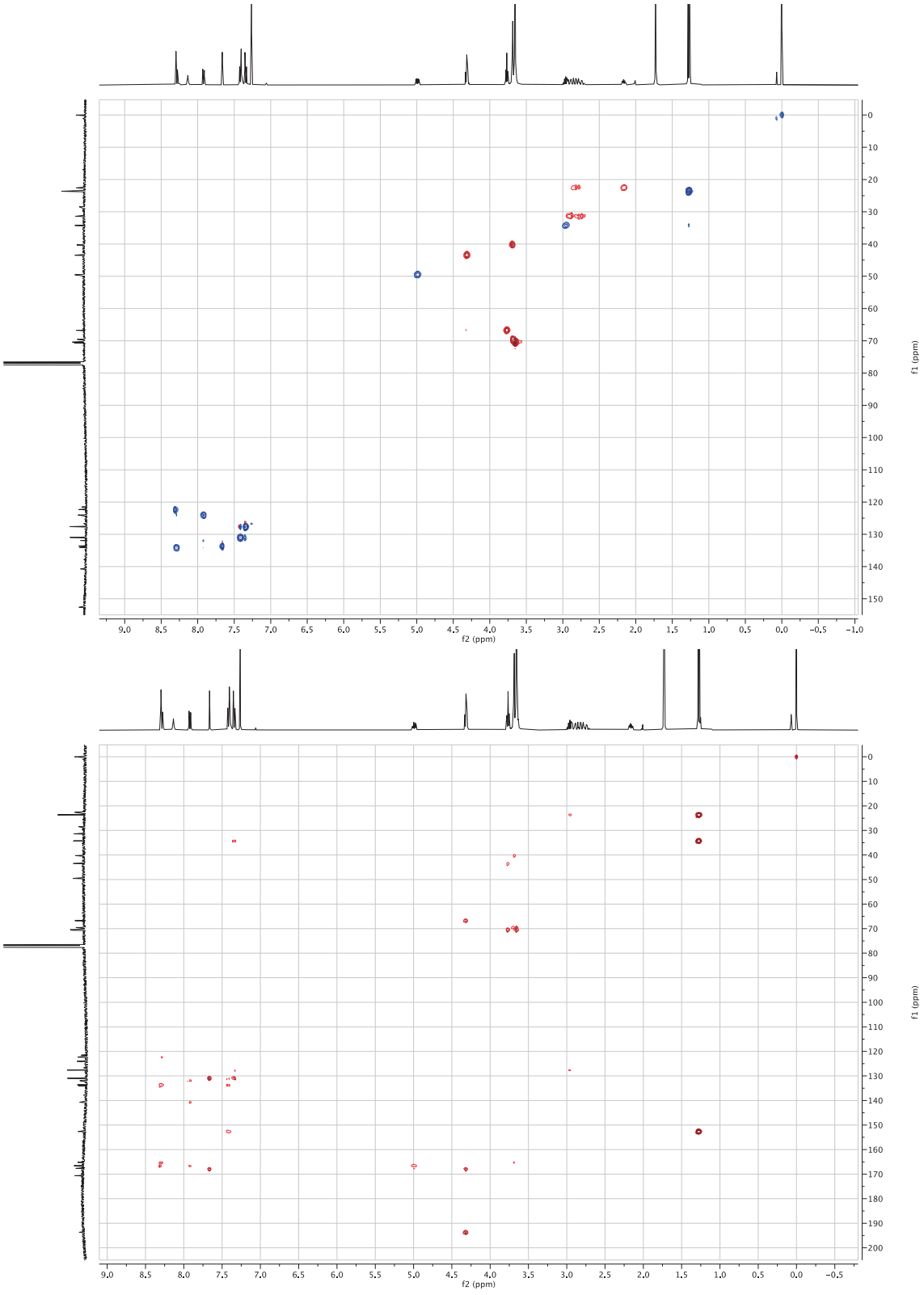
f2 (ppm)
f1 (ppm)
f2 (ppm)
f1 (ppm)

HPLC / MS ASA_MDEG-543

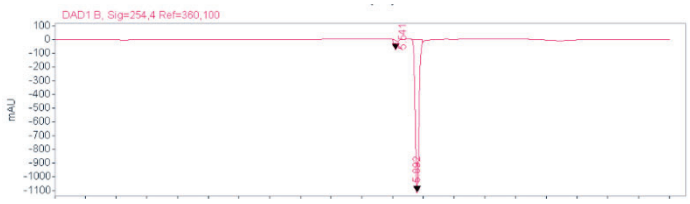

Signal: DAD1 B, Sig=254,4 Ref=360,100

RT [min]	Type	Width [min]	Area	Height	Area%	Name
5.541	MP N	0.0478	191.9436	66.8956	4.1023	
5.892	PM N	0.0666	4487.0381	1122.0549	95.8977	
		Sum	4678.9817			

(*Z*)-2-(2,6-Dioxopiperidin-3-yl)-*N*-(2-(2-(2-(2-(5-(4-ethylbenzylidene)-4-oxo-2-thioxothiazolidin-3-yl)ethoxy)ethoxy)ethoxy)ethyl)-1,3-dioxoisoindoline-5-carboxamide (ASA_MDEG-544)

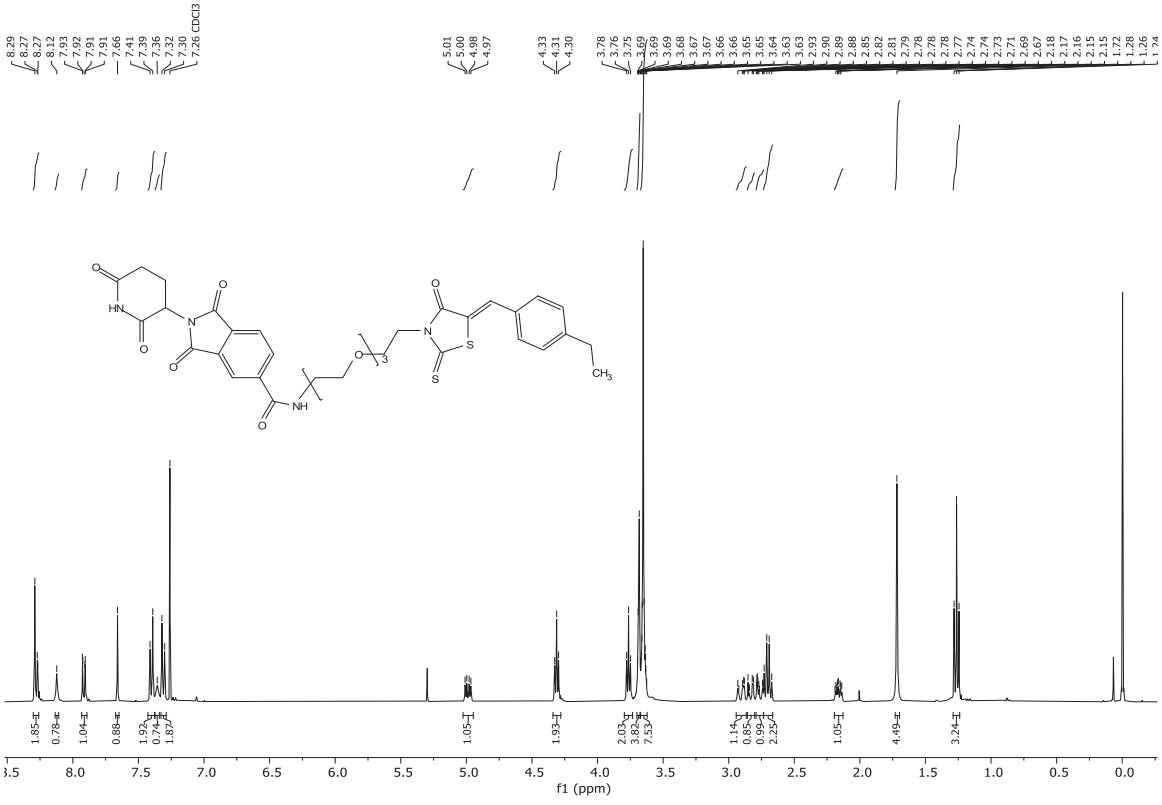

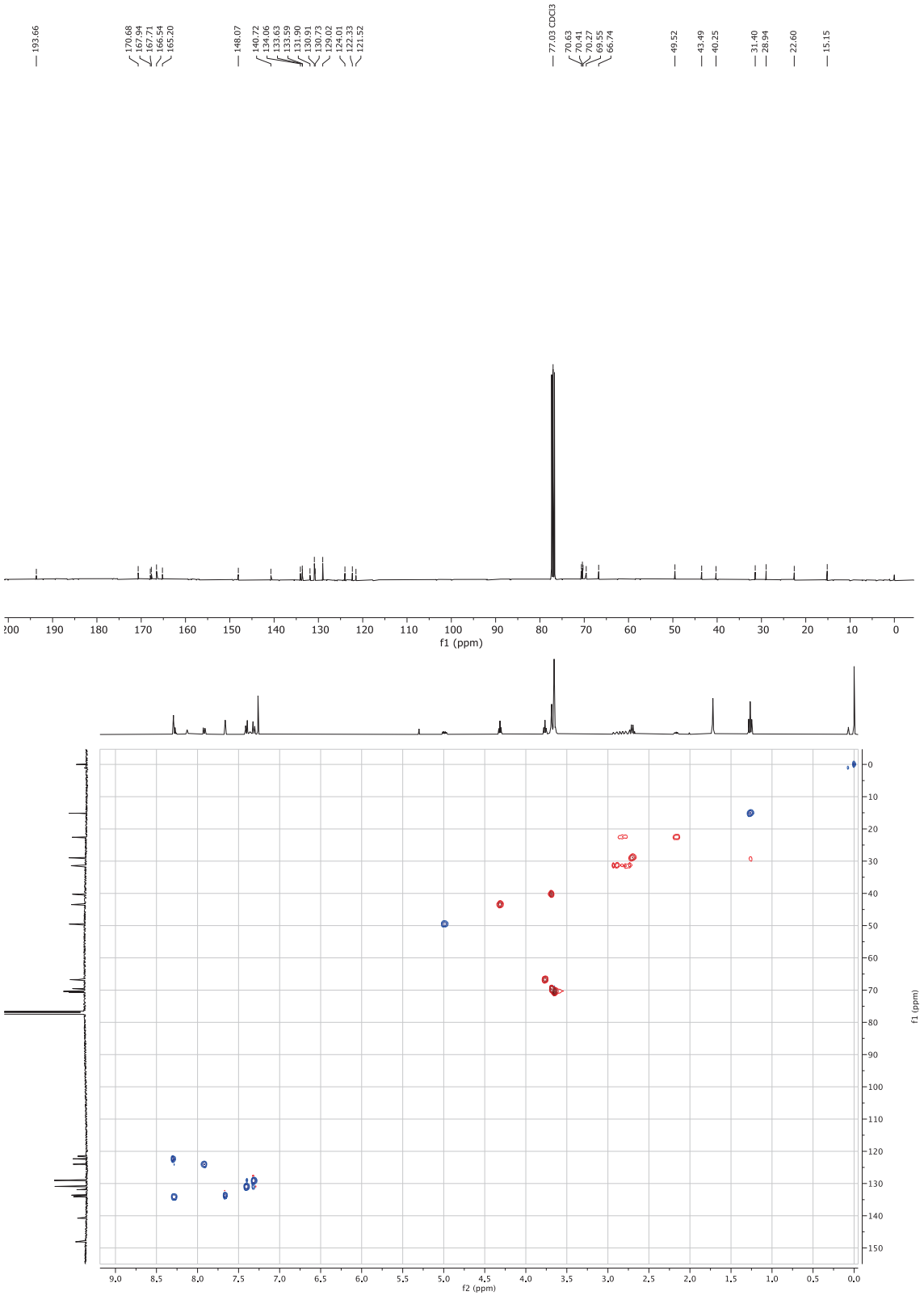
193.66
170.68
167.94
167.71
166.54
165.20
148.07
140.72
134.06
133.63
133.59
131.90
130.91
130.23
129.02
124.01
122.33
121.52
77.03 CDCl3
70.63
70.41
70.27
69.55
65.74
49.52
43.49
40.25
31.40
28.94
22.60
15.15
f1 (ppm)
f2 (ppm)

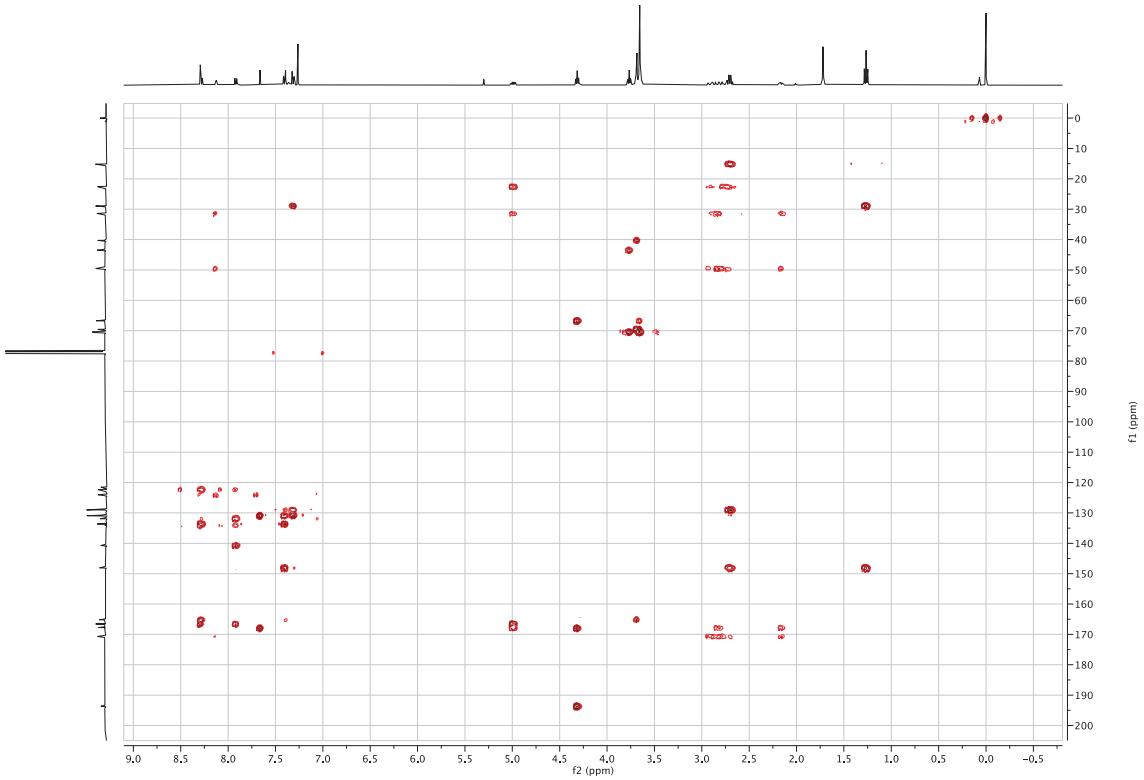
f2 (ppm)
f1 (ppm)

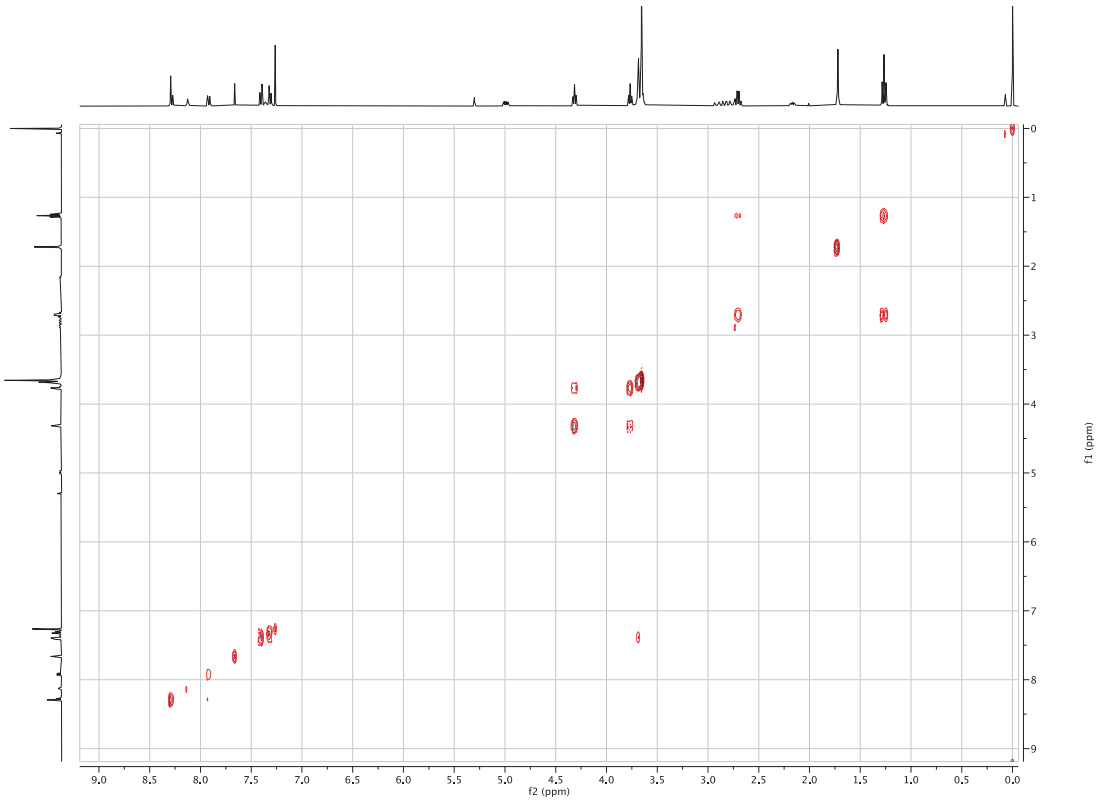
f2 (ppm)
f1 (ppm)

HPLC / MS ASA_MDEG-544

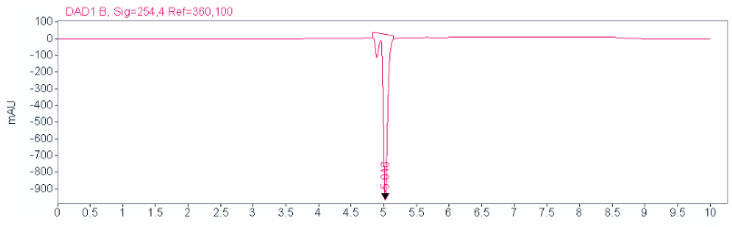

Signal: DAD1 B, Sig=254,4 Ref=360,100

RT [min]	Type	Width [min]	Area	Height	Area%	Name
5.016	MM N	0.0838	5029.5088	999.7067	100.0000	
		Sum	5029.5088			

Significant ^{1}H and ^{13}C NMR data of ASA-5 and ASA-6

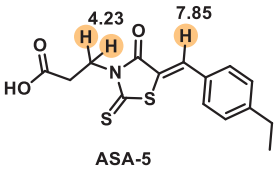

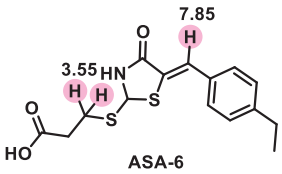

A)

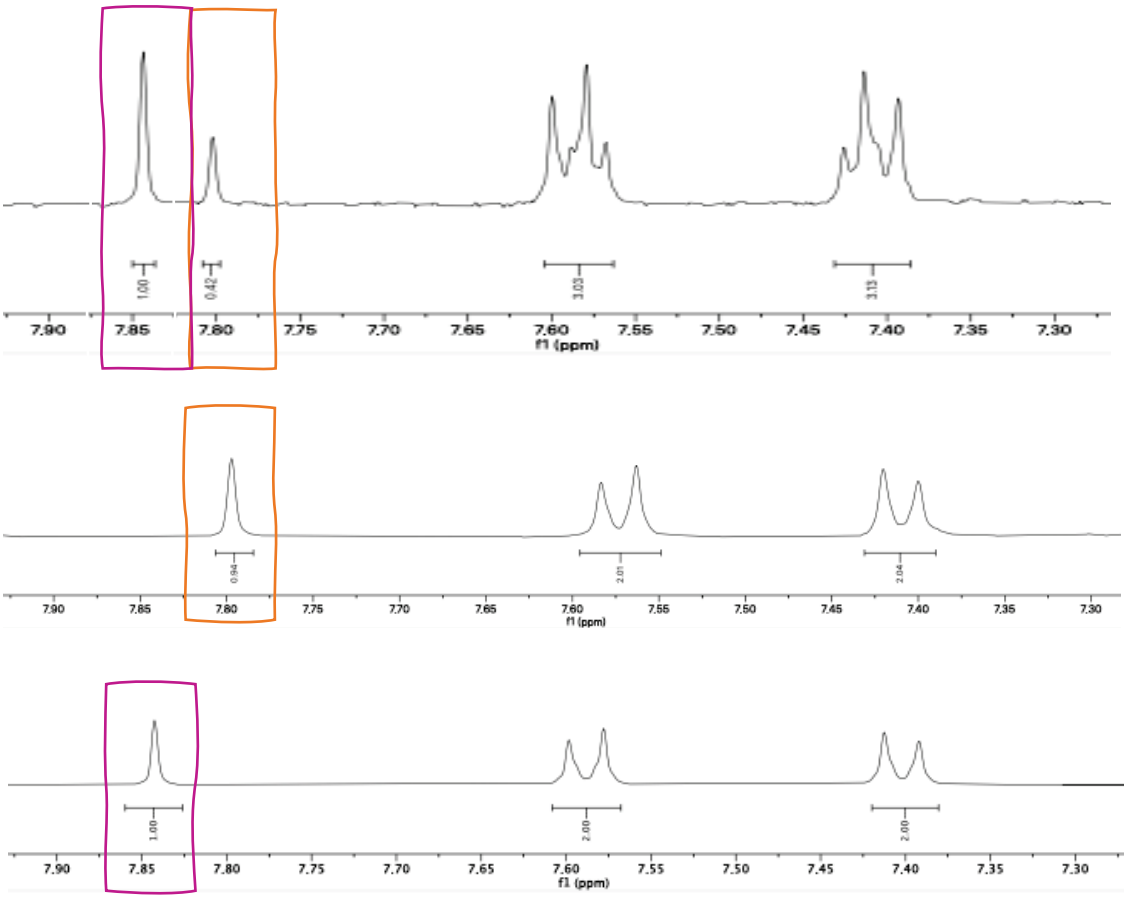

B)

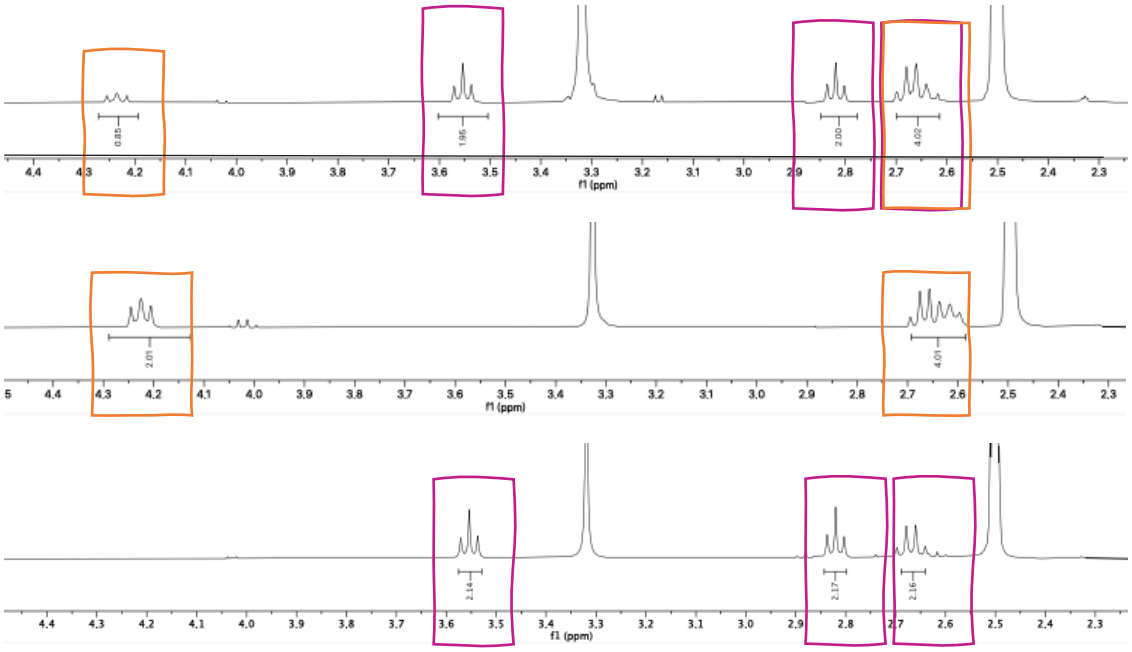

C)

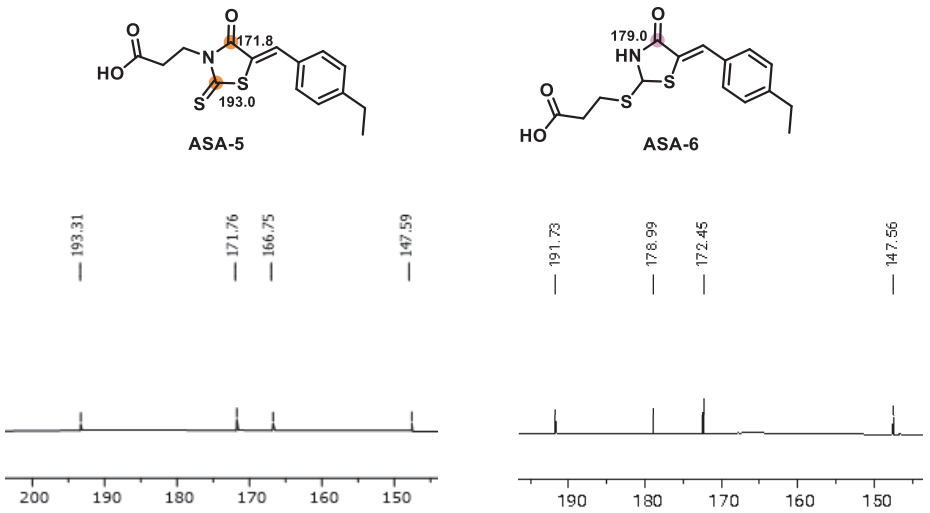

Figure 47: ^{1}H NMR spectra of both ASA-5 (orange) and ASA-6 (pink) present in the crude mixture and isolated respectively, in the aromatic (A) and alkyl chain regions (B). ^{13}C NMR spectra of both isolated ASA-5 (orange) and ASA-6 (C).

6.1.1.3 X- Ray Structure Studies

Crystals of 10058-F4, 6, 5 and ASA-5 were obtained from slow evaporation of methanol solutions. The single crystal X- Ray diffraction data set was collected at 294 K up to a max 2θ of ca. 57° on a Bruker Smart APEX II diffractometer, using mono- chromatic MoKα radiation λ = 0.71073 A and 0.3° separation between frames. Data integration was performed using SAINT V6.45A and SORTAV (Blessing, 1995) in the diffractometer package. The structures were solved by direct methods using SHELXT-2014 and Fourier's difference methods and refined by least squares on F2 using SHELXL-2014/7 inside the WinGX program environment. [251, 252] Anisotropic displacement parameters were used for non-H atoms and the H-atoms were positioned in calculated positions and refined riding on their parent atoms. This study was performed at Institut de Ciència de Materials de Barcelona (ICMAB-CSIC), Campus UAB (Cerdanyola, Spain) by Prof. Elies Molins.

6.1.2 Cellular and biology techniques

All cell culture and treatment procedures were carried out at the Scientific and Technical Services of the University of Barcelona (CCTiUB), specifically within the Cytometry Unit at the Barcelona Science Park (PCB).

6.1.2.1 Cell culture

The cell lines used in this thesis were kidney cells HEK 293 (from ATCC) and MYC-amplified colon cancer cells HCT 116 (from Cultek). The HEK 293 cells were cultured with DMEM while HCT 116 cells were in RPMI-1640 media, both supplemented with 10% Fetal Bovine Serum (FBS), 100 U ml−1 penicillin-streptomycin and 2 mM L-Glutamine in a humidified incubator at 37 °C and 5 % CO_2.

6.1.2.2 Cell treatment

HEK 293 and HCT-116 cells were plated in 6-well plates at 60-70 % confluency and left overnight prior to compound treatment in a humidified incubator at 37 °C and 5 % CO_2. The cells were treated for 6 or 24 hours with the different compound concentrations. Stock solutions of compounds were prepared in DMSO at a concentration of 10 mM or 50 mM, depending on the experiment set up, and stored at -20 °C. Working dilutions were made fresh using DMEM media and added dropwise to 6-well plates. For co-treatment assays, cells were pre-treated with inhibitors 10 µM MG-132 (Merck) or 1 µM MLN-4924 (Merck) for 1 hour, before treating the different PROTAC compound.

6.1.2.3 Cell collection and lysis

For cell collection, cells were washed once with ice-cold PBS 1X followed by clearance *via* centrifugation for 15 minutes at 14000 rpm at 4 ºC, before lysis incubation for 10 minutes on ice with RIPA lysis buffer (Thermo Fisher) and Protease Inhibitor cocktail (Thermo Fisher) and followed by clearance centrifugation for 15 minutes at 14000 rpm at 4 ºC. The lysates were collected in Eppendorf tubes and stored at -20 ºC.

6.1.2.4 BCA quantification

Protein concentration of lysates was quantified using the Pierce BCA Protein Assay (Thermo Fisher). The standard curve is obtained using eight BSA protein standards, which are prepared following the manufacturer's instructions. 25 mL of the sample, previously diluted with MQW (1:10 *v/v* at final volume of 60 mL), is added to the 96-well plate prior to the addition of the BCA working reagent (1:8 *v/v* at final volume of 200 mL). Then, the plates are incubated for 30 minutes at 37 ºC. The measurement is performed in an AmyloidTech microplate reader (BMG LabTech) at 562 nm. 20- 30 mg of lysate is prepared using 4xLDS sample buffer with 50 mM of dithiothreitol (DTT) and MQW.

6.1.2.5 Western blot

After sample preparation according to BCA protein quantification, 20 mg of protein is loaded into 10% Tris/Gly/SDS gels and resolved at constant intensity (25 mA / gel). Proteins are transferred to PVDF membranes with iBlot2 system (Invitrogen), blocked for 1 hour in 5% non -fat dry milk TBS-T 1X at room temperature, before incubating with primary antibodies overnight at 4ºC. The following antibodies are used: cMyc (1:1000 in TBS-T 1X, no. Ab32072, Abcam) and α-vinculin (1:1000 in TBS-T 1X, no. Ab128002, Abcam). Membranes are washed with TBST-T 1X and incubated with the secondary antibody Goat Anti-Rabbit IgG (H+L), HRP (1:2000, no.111-035-003, Jackson Immunoresearch) for 1 hour at room temperature, before further washes and chemiluminescent detection. Chemiluminescence (ECL) western blotting substrate (Thermo Fisher Scientific) is used to detect the HRP conjugates on the membrane with Amersham Imager 680 System (Cytiva). Western Blots are quantified using Image Lab software (v6.1 build 7). The statistical analysis is conducted using GraphPad Prism software (v10.1.1). One-way ANOVA was implemented to assess the differences when comparing more than two groups. Differences were considered statistically significant when $P<0.05$. P-values were denoted by asterisks as follows: (*) P- value<0.05; (**) P-value<0.01; (***) P-value<0.001; (****) P-value<0.0001.

6.2 Chapter 4: Degrading Cyclin E/CDK2 with a novel dual PROTAC approach

6.2.1 Chemistry Section

General Information

Followed as described in Chapter 6.1.1.1.

Data Analysis

Followed as described in Chapter 6.1.1.2.

6.2.1.1 Synthetic Procedures and Characterization Data

Synthesis of 1st series of Cyclin E / CDK2- based PROTACs

2-(2-(2-Aminoethoxy)ethoxy)-*N*-(2-(2,6-dioxopiperidin-3-yl)-1-oxoisoindolin-4-yl)acetamide 2,2,2-trifluoroacetate (11a)

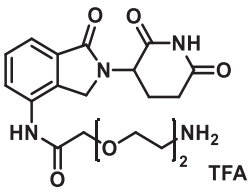

11a

2,2-Dimethyl-4-oxo-3,8,11-trioxa-5-azatridecan-13-oic acid (9a; 183 mg, 0.69 mmol, 1.2 eq) was added to a stirring solution of lenalidomide (8, 150 mg, 0.58 mmol, 1 eq) and DIPEA (0.3 mL, 1.74 mmol, 3 eq) in dry DMF (3.5 mL). After 15 min, HATU (264 mg, 0.69 mmol, 1.2 eq) was added and the reaction mixture was allowed to stir at room temperature for 12 h. Upon completion of the reaction as determined by HPLC / MS, the organic layer was washed with AcOEt and water, dried over Na_2SO_4, filtered, and concentrated. The crude was purified with reverse-phase column chromatography (31 % CH_3CN in 0.1 % aq. HCO_2H) to give 10a as a white solid (228 mg, 78 %). [52] HRMS m/z calc. for $C_{24}H_{32}N_4O_8$ $[M+H]^+$ 505.2220, found 505.2297.Then, *tert*-butyl (2-(2-(2-((2-(2,6-dioxopiperidin-3-yl)-1-oxoisoindolin-4-yl)amino)-2-oxoethoxy)ethoxy) ethyl)carbamate (10a; 100 mg, 0.20 mmol, 1 eq) was dissolved in dry DCM (0.8 mL, 0.25 M), and TFA (0.8 mL) was slowly added. The mixture was stirred for 30 min upon completion as determined by TLC. After removal of the volatiles, the oily residue was dried further under high vacuum to give 11a as TFA salt [52] without further purification in quantitative yield that matched the reported spectral data. [157]

2-(2-(2-Aminoethoxy)ethoxy)-*N*-(2-(2,6-dioxopiperidin-3-yl)-1-oxoisoindolin-4-yl)acetamide 2,2,2-trifluoroacetate (11b)

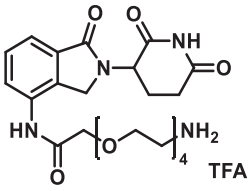

11b

2,2-Dimethyl-4-oxo-3,8,11,14,17-pentaoxa-5-azanonadecan-19-oic acid (**9b**; 244 mg, 0.69 mmol, 1.2 eq) was added to a stirring solution of **lenalidomide** (**8**; 150 mg, 0.58 mmol, 1 eq) and DIPEA (0.3 mL, 1.74 mmol, 3 eq) in dry DMF (3.4 mL, 0.17 M). After 15 min, HATU (264 mg, 0.69 mmol, 1.2 eq) was added and the reaction mixture was allowed to stir at room temperature for 12 h. Upon completion of the reaction as determined by HPLC / MS, the organic layer was washed with AcOEt and water, dried over Na_2SO_4, filtered, and concentrated. The crude was purified with reverse-phase column chromatography (40 % CH_3CN in 0.1 % aq. HCO_2H) to give **10b** as a white solid (282 mg, **82 %**). [52] **HRMS** m/z calc. for $C_{28}H_{40}N_4O_{10}$ $[M+H]^+$ 593.2740, found 593.2816. Then, *tert*-butyl (14-((2-(2,6-dioxopiperidin-3-yl)-1-oxoisoindolin-4-yl)amino)-14-oxo-3,6,9,12-tetraoxatetradecyl)carbamate (**19b**; 90 mg, 0.15 mmol, 1 eq) was dissolved in dry DCM (0.6 mL, 0.25 M), and TFA (0.6 mL) was slowly added. The mixture was stirred for 30 min upon completion as determined by TLC. After removal of the volatiles, the oily residue was dried further under high vacuum to give **11b** as TFA salt, [52] without further purification in quantitative yield that matched the reported spectral data. [157]

20-Amino-*N*-(2-(2,6-dioxopiperidin-3-yl)-1-oxoisoindolin-4-yl)-3,6,9,12,15,18-hexaoxaicosanamide 2,2,2-trifluoroacetate (11c)

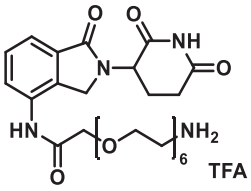

11c

2,2-Dimethyl-4-oxo-3,8,11,14,17,20,23-heptaoxa-5-azapentacosan-25-oic acid (**9c**; 163 mg, 0.37 mmol, 1.2 eq) was added to a stirring solution of **lenalidomide** (**8**; 80 mg, 0.31 mmol, 1 eq) and DIPEA (0.2 mL, 0.93 mmol, 3 eq) in dry DMF (1.8 mL, 0.17 M). After 15 min, HATU (264 mg, 0.69 mmol, 1.2 eq) was added and the reaction mixture was allowed to stir at room temperature for 12 h. Upon completion of the reaction as determined by HPLC / MS, the organic layer was washed with AcOEt and water, dried over Na_2SO_4, filtered, and concentrated. The crude was purified with reverse-phase column chromatography (43 % CH_3CN in 0.1 % aq. HCO_2H) to give **10c** as a white solid (158 mg, **75 %**). [52] **^{1}H NMR** (400 MHz, $CDCl_3$) δ 1.43 (s, 9H), 2.18 – 2.26 (m, 1H), 2.38 (qd, *J* = 5.1, 13.1 Hz, 1H), 2.75 – 2.94 (m, 2H), 3.26 – 3.32 (m, 2H), 3.51 – 3.53 (m, 4H), 3.57 – 3.60 (m, 8H), 3.64 – 3.70 (m, 5H), 3.71 – 3.75 (m, 3H), 3.77 – 3.81 (m, 2H), 4.16 (d, *J* = 4.5 Hz, 2H), 4.46 (s, 2H), 5.11 (s, 1H), 5.22 (dd, *J* = 5.2, 13.3 Hz, 1H), 7.49 (t, *J* = 7.7 Hz, 1H), 7.75 (t, *J* = 8.0 Hz, 2H), 8.42 (s, 1H), 9.00 (s, 1H). **^{13}C NMR** (101 MHz, $CDCl_3$) δ 23.4, 28.4, 31.6, 46.4, 51.8, 70.1, 70.1, 70.2, 70.2, 70.4, 70.4, 70.4, 70.5, 70.6, 71.3, 77.0, 79.2, 121.4, 126.2, 129.1, 132.1, 132.8, 134.4, 156.1, 168.5, 168.9, 169.6, 171.2. **HRMS** *m/z* calc. for $C_{32}H_{48}N_4O_{12}$ $[M+H]^+$ 681.3270, found 681.3338. Then, tert-butyl (20-((2-(2,6-dioxopiperidin-3-yl)-1-oxoisoindolin-4-yl)amino)-20-oxo-3,6,9,12,15,18-hexaoxaicosyl) carbamate (**10c**; 146 mg, 0.21 mmol, 1 eq) was dissolved in dry DCM (1 mL, 0.25 M), and TFA (1 mL) was slowly added. The mixture was stirred for 30 min upon completion as determined by TLC. After removal of the volatiles, the oily residue was dried further under high vacuum to give **11c** as TFA salt, [52] without further purification in quantitative yield.

(2*S*,4*R*)-1-((*S*)-2-(2-(2-Aminoethoxy)acetamido)-3,3-dimethylbutanoyl)-4-hydroxy-*N*-(4-(4-methylthiazol-5-yl)benzyl)pyrrolidine-2-carboxamide 2,2,2-trifluoroacetate (23a)

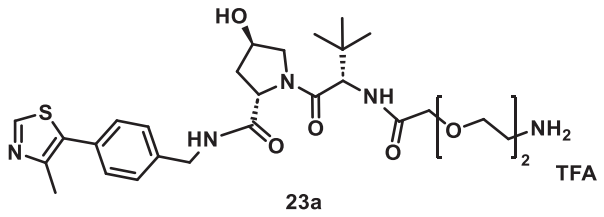

23a

2,2-Dimethyl-4-oxo-3,8,11-trioxa-5-azatridecan-13-oic acid (**19a**; 120 mg, 0.46 mmol, 1.2 eq) was added to a stirring solution of **VH032** as HCl salt (**39**; 177 mg, 0.38 mmol, 1 eq) and DIPEA (0.4 mL, 2.28 mmol, 6 eq) in dry DMF (2 mL, 0.17 M). After 15 min, HATU (173 mg, 0.46 mmol, 1.2 eq) was added and the reaction mixture was allowed to stir at room temperature for 12 h. Upon completion of the reaction as determined by HPLC / MS, the organic layer was washed with AcOEt and water, dried over Na_2SO_4, filtered, and concentrated. The crude was purified with reverse-phase column chromatography (52 % CH_3CN in 0.1 % aq. HCO_2H) to give **22a** as a white solid (181 mg, **70 %**) [52] that matched the reported spectral data. [166] **HRMS** m/z calc. for $C_{33}H_{49}N_5O_8S$ $[M+H]^+$ 676.3375, found 676.3370. Then, *tert*-butyl (2-(2-(((*S*)-1-((2*S*,4*R*)-4-hydroxy-2-((4-(4-methylthiazol-5-yl)benzyl)carbamoyl)pyrrolidin-1-yl)-3,3-dimethyl-1-oxobutan-2-yl)amino)-2-oxoethoxy)ethyl)carbamate (**22a;** 181 mg, 0.27 mmol, 1 eq) was dissolved in dry DCM (1 mL, 0.3 M) and TFA (0.3 mL) was slowly added. The mixture was stirred for 30 min upon completion as determined by TLC. After removal of the volatiles, the oily residue was dried further under high vacuum to give **23b** as TFA salt, [52] without further purification in quantitative yield.

(2*S*,4*R*)-1-((*S*)-2-(2-(2-Aminoethoxy)acetamido)-3,3-dimethylbutanoyl)-4-hydroxy-*N*-(4-(4-methylthiazol-5-yl)benzyl)pyrrolidine-2-carboxamide 2,2,2-trifluoroacetate (23b)

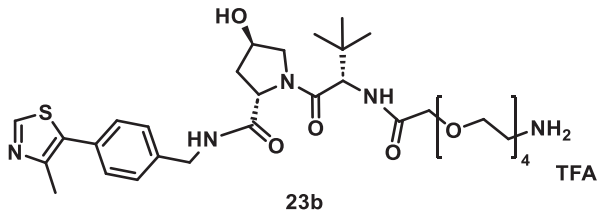

23b

2,2-Dimethyl-4-oxo-3,8,11,14,17-pentaoxa-5-azanonadecan-19-oic acid (**9b**; 90 mg, 0.26 mmol, 1.2 eq) was added to a stirring solution of **VH032** as HCl salt (**39**; 100 mg, 0.21 mmol, 1 eq) and DIPEA (0.2 mL, 1.29 mmol, 6 eq) in dry DMF (1.3 mL, 0.17 M). After 15 min, HATU (98 mg, 0.26 mmol, 1.2 eq) was added and the reaction mixture was allowed to stir at room temperature for 12 h. Upon completion of the reaction as determined by HPLC / MS, the organic layer was washed with AcOEt and water, dried over Na_2SO_4, filtered, and concentrated. The crude was purified with reverse-phase column chromatography (39 % CH_3CN in 0.1 % aq. HCO_2H) to give **20b** as a white solid (134 mg, **82 %**). [52] **HRMS** m/z calc. for $C_{37}H_{57}N_5O_{10}S$ $[M+H]^+$ 764.3830, found 764.3893. Then, *tert*-butyl (2-(2-(((*S*)-1-((2*S*,4*R*)-4-hydroxy-2-((4-(4-methylthiazol-5-yl)benzyl)carbamoyl) pyrrolidin-1-yl)-3,3-dimethyl-1-oxobutan-2-yl)amino)-2-oxoethoxy)ethyl)carbamate (**20b**; 100 mg, 0.13 mmol, 1 eq) was dissolved in dry DCM (0.5 mL, 0.25 M) and TFA (0.5 mL) was slowly added. The mixture was stirred for 30 min upon completion as determined by TLC. After removal of the volatiles, the oily residue was dried further under high vacuum to give **23b** as TFA salt, [52] without further purification in quantitative yield that matched the reported spectral data. [167]

(2*S*,4*R*)-1-((*S*)-2-(2-(2-Aminoethoxy)acetamido)-3,3-dimethylbutanoyl)-4-hydroxy-N-(4-(4-methylthiazol-5-yl)benzyl)pyrrolidine-2-carboxamide 2,2,2-trifluoroacetate
(23c)

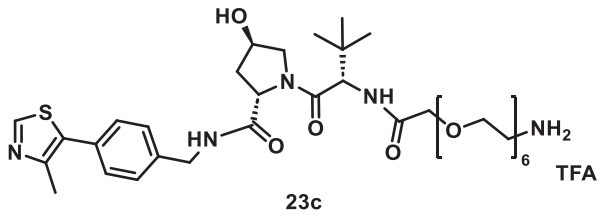

23c

2,2-Dimethyl-4-oxo-3,8,11,14,17,20,23-heptaoxa-5-azapentacosan-25-oic acid (**9c**; 113 mg, 0.26 mmol, 1.2 eq) was added to a stirring solution of **VH032** as HCl salt (**39**; 100 mg, 0.21 mmol, 1 eq) and DIPEA (0.2 mL, 1.29 mmol, 6 eq) in dry DMF (1.3 mL, 0.17 M). After 15 min, HATU (98 mg, 0.26 mmol, 1.2 eq) was added and the reaction mixture was allowed to stir at room temperature for 12 h. Upon completion of the reaction as determined by HPLC / MS, the organic layer was washed with AcOEt and water, dried over Na_2SO_4, filtered, and concentrated. The crude was purified with reverse-phase column chromatography (41 % CH_3CN in 0.1 % aq. HCO_2H) to give **22c** as a white solid (134 mg, **73 %**), [52] that matched the reported spectral data [185]. **HRMS** m/z calc. for $C_{41}H_{65}N_5O_{12}S$ $[M+H]^+$ 852.435, found 852.4414. Then, *tert*-butyl (2-(2-(((*S*)-1-((2*S*,4*R*)-4-hydroxy-2-((4-(4-methylthiazol-5-yl)benzyl)carbamoyl) pyrrolidin-1-yl)-3,3-dimethyl-1-oxobutan-2-yl)amino)-2-oxoethoxy)ethyl)carbamate (**22c**; 129 mg, 0.15 mmol, 1 eq) was dissolved in dry DCM (0.6 mL, 0.25 M) and TFA (0.6 mL) was slowly added. The mixture was stirred for 30 min upon completion as determined by TLC. After removal of the volatiles, the oily residue was dried further under high vacuum to give **23c** as TFA salt, [52] without further purification in quantitative yield that matched the reported spectral data [185].

N-(2-(2-(2-((2-(2,6-Dioxopiperidin-3-yl)-1-oxoisoindolin-4-yl)amino)-2-oxoethoxy)ethoxy)ethyl)-2-(((4-oxo-1-phenyl-4,5-dihydro-1*H*-pyrazolo[3,4-*d*]pyrimidin-6-yl)methyl)thio)-1*H*-benzo[*d*]imidazole-6-carboxamide (CYC-1)

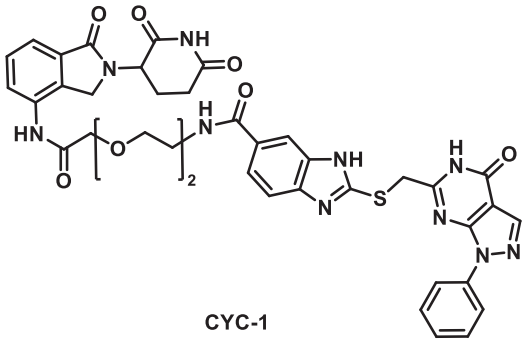

CYC-1

2-(2-(2-Aminoethoxy)ethoxy)-*N*-(2-(2,6-dioxopiperidin-3-yl)-1-oxoisoindolin-4-yl)acetamide 2,2,2-trifluoroacetate (**11a**; 55 mg, 0.11 mmol, 1 eq) was added to a stirring solution of **ARG-91** (53 mg, 0.13 mmol, 1.2 eq) and DIPEA (0.1 mL, 0.64 mmol, 6 eq) in dry DMF (0.6 mL, 0.17 M). After 15 min, HATU (48 mg, 0.13 mmol, 1.2 eq) and the reaction mixture was allowed to stir at room temperature for 12 h. Upon completion of the reaction as determined by HPLC / MS, the organic layer was washed with AcOEt and water, dried over Na_2SO_4, filtered, and concentrated. The crude was purified with reverse-phase column chromatography (30 % CH_3CN in 0.1 % aq. HCO_2H) to give **CYC-1** as a white solid (28 mg, **33 %**). [52] **^{1}H NMR** (400 MHz, DMSO) δ 1.96 – 2.04 (m, 1H), 2.30 – 2.39 (m, 1H), 2.54 – 2.63 (m, 1H), 2.84 – 2.94 (m, 1H), 3.44 (q, 4H), 3.59 (t, *J* = 6.1 Hz, 2H), 3.63 – 3.67 (m, 2H), 3.68 – 3.72 (m, 2H), 4.14 (s, 2H), 4.36 (d, *J* = 6.5 Hz, 2H), 4.58 (s, 2H), 5.13 (dd, *J* = 5.1, 13.3 Hz, 1H), 7.27 – 7.36 (m, 3H), 7.46 – 7.51 (m, 2H), 7.55 (dd, *J* = 1.2, 7.5 Hz, 1H), 7.68 – 7.74 (m, 2H), 7.83 – 7.86 (m, 2H), 8.00 (s, 1H), 8.29 (s, 1H), 8.48 (t, *J* = 5.6 Hz, 1H), 9.70 (s, 1H), 11.00 (s, 1H). **^{13}C NMR** (101 MHz, DMSO) δ 23.0, 31.7, 35.0, 40.0, 46.9, 52.0, 69.5, 69.9, 70.5, 70.8, 106.6, 120.2, 121.7, 121.8, 126.8, 127.3, 128.5, 129.1, 129.5, 133.2, 133.4, 135.3, 136.5, 138.7, 151.8, 152.3, 158.3, 167.1, 168.2, 168.9, 171.5, 173.3. **HRMS** *m/z* calc. for $C_{39}H_{36}N_{10}O_8S$ $[M+H]^+$ = 805.2440, found 805.2520.

N-(14-((2-(2,6-Dioxopiperidin-3-yl)-1-oxoisoindolin-4-yl)amino)-14-oxo-3,6,9,12-tetraoxatetradecyl)-2-(((4-oxo-1-phenyl-4,5-dihydro-1*H*-pyrazolo[3,4-*d*]pyrimidin-6-yl)methyl)thio)-1*H*-benzo[*d*]imidazole-6-carboxamide (CYC-2)

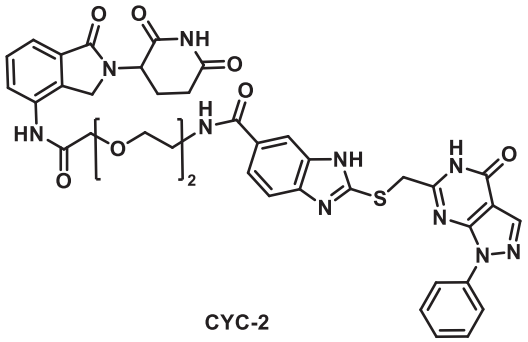

CYC-2

2-(2-(2-Aminoethoxy)ethoxy)-*N*-(2-(2,6-dioxopiperidin-3-yl)-1-oxoisoindolin-4-yl)acetamide 2,2,2-trifluoroacetate (**11b**; 64 mg, 0.11 mmol, 1 eq) was added to a stirring solution of **ARG-91** (53 mg, 0.13 mmol, 1.2 eq) and DIPEA (0.1 mL, 0.64 mmol, 6 eq) in dry DMF (0.6 mL, 0.17 M). After 15 min, HATU (48 mg, 0.13 mmol, 1.2 eq) and the reaction mixture was allowed to stir at room temperature for 12 h. Upon completion of the reaction as determined by HPLC / MS, the organic layer was washed with AcOEt and water, dried over Na_2SO_4, filtered, and concentrated. The crude was purified with reverse-phase column chromatography (30 % CH_3CN in 0.1 % aq. HCO_2H) to give **CYC-2** as a white solid (41 mg, **43 %**). [52] **^{1}H NMR** (400 MHz, DMSO) δ 1.96 – 2.04 (m, 1H), 2.29 – 2.41 (m, 1H), 2.56 – 2.64 (m, 1H), 2.85 – 2.96 (m, 1H), 3.41 (q, *J* = 6.1 Hz, 4H), 3.48 – 3.52 (m, 8H), 3.57 – 3.60 (m, 2H), 3.65 – 3.68 (m, 2H), 4.12 (s, 2H), 4.37 (d, *J* = 10.9 Hz, 2H), 4.58 (s, 2H), 5.14 (dd, *J* = 5.1, 13.3 Hz, 1H), 7.28 – 7.36 (m, 3H), 7.48 – 7.53 (m, 2H), 7.56 (dd, *J* = 1.2, 7.5 Hz, 1H), 7.69 – 7.75 (m, 2H), 7.82 – 7.87 (m, 2H), 8.01 (s, 1H), 8.29 (s, 1H), 8.46 (t, *J* = 5.6 Hz, 1H), 9.67 (s, 1H), 11.00 (s, 1H). **^{13}C NMR** (101 MHz, DMSO) δ 22.0, 30.6, 33.9, 38.9, 45.8, 50.9, 68.4, 69.0, 69.0, 69.1, 69.2, 69.3, 69.8, 105.5, 119.1, 120.6, 125.8, 126.2, 127.5, 128.0, 128.4, 132.1, 132.3, 134.3, 135.4, 137.6, 151.2, 157.2, 165.9, 167.2, 167.8, 170.4, 172.2. **HRMS** *m/z* calc. for $C_{43}H_{44}N_{10}O_{10}S$ $[M+H]^+$ = 893.2960, found 893.3029.

N-(20-((2-(2,6-Dioxopiperidin-3-yl)-1-oxoisoindolin-4-yl)amino)-20-oxo-3,6,9,12,15,18-hexaoxaicosyl)-2-(((4-oxo-1-phenyl-4,5-dihydro-1*H*-pyrazolo[3,4-*d*]pyrimidin-6-yl)methyl)thio)-1*H*-benzo[*d*]imidazole-6-carboxamide (CYC-3)

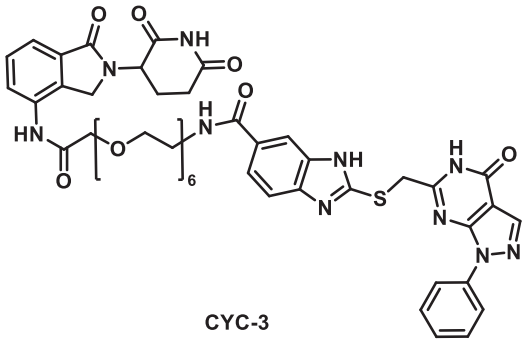

CYC-3

20-Amino-*N*-(2-(2,6-dioxopiperidin-3-yl)-1-oxoisoindolin-4-yl)-3,6,9,12,15,18-hexaoxaicosanamide 2,2,2-trifluoroacetate (**11c**; 70 mg, 0.10 mmol, 1 eq) was added to a stirring solution of **ARG-91** (50 mg, 0.12 mmol, 1.2 eq) and DIPEA (0.11 mL, 0.60 mmol, 6 eq) in dry DMF (0.6 mL, 0.17 M). After 15 min, HATU (46 mg, 0.12 mmol, 1.2 eq) and the reaction mixture was allowed to stir at room temperature for 12 h. Upon completion of the reaction as determined by HPLC / MS, the organic layer was washed with AcOEt and water, dried over Na_2SO_4, filtered, and concentrated. The crude was purified with reverse-phase column chromatography (37 % CH_3CN in 0.1 % aq. HCO_2H) to give **CYC-3** as a white solid (40 mg, **41 %**). [52] **^{1}H NMR** (400 MHz, DMSO) δ 1.96 – 2.04 (m, 1H), 2.29 – 2.41 (m, 1H), 2.55 – 2.63 (m, 1H), 2.85 – 2.96 (m, 1H), 3.42 (s, 6H), 3.44 – 3.45 (m, 2H), 3.46 – 3.49 (m, 6H), 3.50 – 3.55 (m, 8H), 3.58 – 3.62 (m, 2H), 3.66 – 3.70 (m, 2H), 4.13 (s, 2H), 4.37 (d, *J* = 11.1 Hz, 2H), 4.59 (s, 2H), 5.14 (dd, *J* = 5.1, 13.3 Hz, 1H), 7.28 – 7.36 (m, 3H), 7.47 – 7.53 (m, 2H), 7.56 (dd, *J* = 1.2, 7.5 Hz, 1H), 7.69 – 7.77 (m, 2H), 7.80 – 7.86 (m, 2H), 8.01 (s, 1H), 8.30 (s, 1H), 8.47 (t, *J* = 5.6 Hz, 1H), 9.66 (s, 1H), 11.00 (s, 1H). **^{13}C NMR** (101 MHz, DMSO) δ 23.0, 31.7, 34.9, 40.0, 46.9, 52.0, 69.5, 70.1, 70.2, 70.2, 70.3, 70.4, 70.9, 106.6, 120.2, 121.7, 126.8, 127.3, 128.6, 129.1, 129.5, 133.2, 133.4, 135.3, 136.5, 138.6, 152.2, 158.1, 167.0, 168.2, 168.9, 171.5, 173.3. **HRMS** *m/z* calc. for $C_{47}H_{52}N_{10}O_{12}S$ $[M+H]^+$ 981.3490, found 981.3568.

N-(2-(2-(2-(((*R*)-1-((2*R*,4*S*)-4-Hydroxy-2-((4-(4-methylthiazol-5-yl)benzyl)carbamoyl) pyrrolidin-1-yl)-3,3-dimethyl-1-oxobutan-2-yl)amino)-2-oxoethoxy)ethoxy)ethyl)-2-(((4-oxo-1-phenyl-4,5-dihydro-1*H*-pyrazolo[3,4-*d*]pyrimidin-6-yl)methyl)thio)-1*H*-benzo [*d*]imidazole-6-carboxamide (CYC-10)

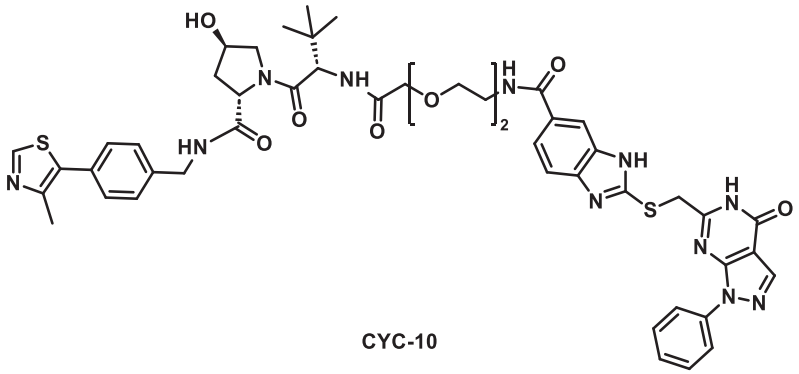

CYC-10

(2*S*,4*R*)-1-((*S*)-2-(2-(2-Aminoethoxy)acetamido)-3,3-dimethylbutanoyl)-4-hydroxy-*N*-(4-(4-methylthiazol-5-yl)benzyl)pyrrolidine-2-carboxamide 2,2,2-trifluoroacetate (**23a**; 55 mg, 0.08 mmol, 1 eq) was added to a stirring solution of **ARG-91** (40 mg, 0.10 mmol, 1.2 eq) and DIPEA (0.1 mL, 0.48 mmol, 6 eq) in dry DMF (0.5 mL, 0.17 M). After 15 min, HATU (36 mg, 0.10 mmol, 1.2 eq) and the reaction mixture was allowed to stir at room temperature for 12 h. Upon completion of the reaction as determined by HPLC / MS, the organic layer was washed with AcOEt and water, dried over Na_2SO_4, filtered, and concentrated. The crude was purified with reverse-phase column chromatography (30 % CH_3CN in 0.1 % aq. HCO_2H) to give **CYC-10** as a white solid (27 mg, **35 %**). [52] **^{1}H NMR** (400 MHz, DMSO) δ 0.93 (s, 9H), 1.85 – 1.95 (m, 1H), 2.02 – 2.10 (m, 1H), 2.42 (s, 3H), 3.42 – 3.48 (m, 4H), 3.55 – 3.70 (m, 10H), 3.96 (s, 2H), 4.21 – 4.27 (m, 1H), 4.35 (d, *J* = 6.0 Hz, 2H), 4.46 (t, *J* = 8.2 Hz, 1H), 4.58 (s, 2H), 7.27 – 7.33 (m, 3H), 7.37 (s, 4H), 7.44 (d, *J* = 10.0 Hz, 1H), 7.50 (d, *J* = 8.4 Hz, 1H), 7.70 (dd, *J* = 1.6, 8.5 Hz, 1H), 7.82 – 7.85 (m, 2H), 8.01 (s, 1H), 8.29 (s, 1H), 8.47 (t, *J* = 5.6 Hz, 1H), 8.63 (t, *J* = 6.0 Hz, 1H), 8.95 (s, 1H). **^{13}C NMR** (101 MHz, DMSO) δ 16.0, 26.2, 34.5, 35.8, 38.0, 39.5, 41.8, 55.8, 56.7, 58.8, 68.9, 69.2, 69.4, 69.6, 70.5, 106.2, 121.2, 121.4, 126.9, 127.5, 128.1, 128.2, 128.7, 128.9, 129.1, 129.8, 131.2, 136.1, 138.2, 139.4, 147.8, 151.5, 151.9, 157.8, 157.9, 166.7, 168.8, 169.3, 171.8. **HRMS** m/z calc. for $C_{48}H_{53}N_{11}O_8S_2$ $[M+H]^+$ 976.3520, found 976.3594.

N-((*R*)-16-((2*R*,4*S*)-4-Hydroxy-2-((4-(4-methylthiazol-5-yl)benzyl)carbamoyl)pyrrolidine-1-carbonyl)-17,17-dimethyl-14-oxo-3,6,9,12-tetraoxa-15-azaoctadecyl)-2-(((4-oxo-1-phenyl-4,5-dihydro-1*H*-pyrazolo[3,4-*d*]pyrimidin-6-yl)methyl)thio)-1*H*-benzo[*d*]imidazole-6-carboxamide (CYC-11)

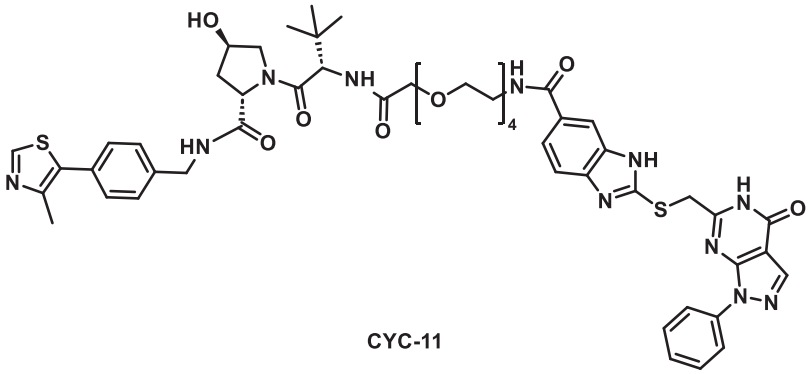

CYC-11

(2*S*,4*R*)-1-((*S*)-2-(2-(2-Aminoethoxy)acetamido)-3,3-dimethylbutanoyl)-4-hydroxy-*N*-(4-(4-methylthiazol-5-yl)benzyl)pyrrolidine-2-carboxamide 2,2,2-trifluoroacetate (**23b**; 104 mg, 0.13 mmol, 1 eq) was added to a stirring solution of **ARG-91** (67 mg, 0.16 mmol, 1.2 eq) and DIPEA (0.1 mL, 0.80 mmol, 6 eq) in dry DMF (0.8 mL, 0.17 M). After 15 min, HATU (61 mg, 0.16 mmol, 1.2 eq) and the reaction mixture was allowed to stir at room temperature for 12 h. Upon completion of the reaction as determined by HPLC / MS, the organic layer was washed with AcOEt (x3) and water, dried over Na_2SO_4, filtered, and concentrated. The crude was purified with reverse-phase column chromatography (36.00 % CH_3CN in 0.1 % aq. HCO_2H) to give **CYC-11** as a white solid (8 mg, **6 %**). [52] **^{1}H NMR** (400 MHz, DMSO) δ 0.93 (s, 9H), 1.86 – 1.92 (m, 1H), 1.98 – 2.02 (m, 1H), 2.43 (s, 3H), 3.39 – 3.44 (m, 4H), 3.48 – 3.55 (m, 12H), 3.55 – 3.70 (m, 3H), 3.95 (s, 2H), 4.20 – 4.28 (m, 2H), 4.32 – 4.38 (m, 2H), 4.41 – 4.47 (m, 2H), 4.56 (s, 2H), 5.32 (t, *J* = 4.7 Hz, 1H), 7.28 – 7.35 (m, 3H), 7.39 (s, 4H), 7.41 (d, *J* = 9.8 Hz, 1H), 7.49 (d, *J* = 8.4 Hz, 1H), 7.70 (d, *J* = 8.4 Hz, 1H), 7.86 (d, *J* = 7.8 Hz, 2H), 8.01 (s, 1H), 8.28 (s, 1H), 8.46 (t, *J* = 5.5 Hz, 1H), 8.59 (t, *J* = 6.1 Hz, 1H), 8.97 (s, 1H). **^{13}C NMR** (101 MHz, DMSO) δ 16.0, 26.2, 35.8, 38.0, 41.7, 55.8, 56.6, 58.8, 68.9, 69.6, 69.8, 70.5, 106.2, 121.2, 125.6, 126.9, 127.5, 128.0, 128.7, 129.1, 129.7, 131.2, 136.0, 139.5, 141.4, 147.8, 151.5, 156.2, 158.2, 166.7, 168.7, 169.2, 171.9. **HRMS** *m/z* calc. for $C_{52}H_{61}N_{11}O_{10}S_2$ $[M+H]^+$ 1064.4040, found 1064.4118.

*The ^{13}C NMR spectra of **CYC-11** was not acquired due to low yield and small quantity obtained from the reaction, and it will be assessed in the future.*

N-((*R*)-16-((2*R*,4*S*)-4-Hydroxy-2-((4-(4-methylthiazol-5-yl)benzyl)carbamoyl)pyrrolidine-1-carbonyl)-17,17-dimethyl-14-oxo-3,6,9,12-tetraoxa-15-azaoctadecyl)-2-(((4-oxo-1-phenyl-4,5-dihydro-1*H*-pyrazolo[3,4-*d*]pyrimidin-6-yl)methyl)thio)-1*H*-benzo[*d*]imidazole-6-carboxamide (CYC-12)

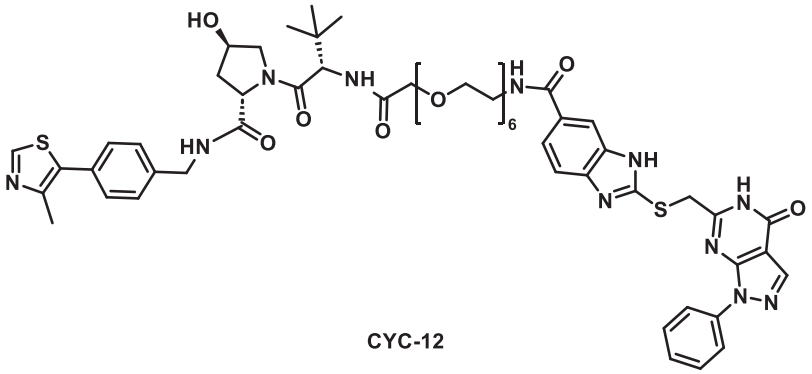

CYC-12

(2*S*,4*R*)-1-((*S*)-2-(2-(2-Aminoethoxy)acetamido)-3,3-dimethylbutanoyl)-4-hydroxy-N-(4-(4-methylthiazol-5-yl)benzyl)pyrrolidine-2-carboxamide 2,2,2-trifluoroacetate (**23c**; 65 mg, 0.08 mmol, 1 eq) was added to a stirring solution of **ARG-91** (38 mg, 0.09 mmol, 1.2 eq) and DIPEA (0.1 mL, 0.45 mmol, 6 eq) in dry DMF (0.4 mL, 0.17 M). After 15 min, HATU (34 mg, 0.09 mmol, 1.2 eq) and the reaction mixture was allowed to stir at room temperature for 12 h. Upon completion of the reaction as determined by HPLC / MS, the organic layer was washed with AcOEt and water, dried over Na_2SO_4, filtered, and concentrated. The crude was purified with reverse-phase column chromatography (36% CH_3CN in 0.1 % aq. HCO_2H) to give **CYC-12** as a white solid (13 mg, **15 %**). [52] **^{1}H NMR** (400 MHz, DMSO) δ 0.94 (s, 9H), 1.86 – 1.94 (m, 1H), 1.98 – 2.09 (m, 1H), 2.43 (s, 3H), 3.42 (d, *J* = 5.8 Hz, 4H), 3.44 (s, 4H), 3.45 – 3.50 (m, 8H), 3.50 – 3.56 (m, 10H), 3.58 – 3.62 (m, 3H), 3.96 (s, 2H), 4.21 – 4.28 (m, 1H), 4.32 – 4.39 (m, 2H), 4.40 – 4.47 (m, 2H), 4.56 (s, 2H), 7.28 – 7.35 (m, 3H), 7.39 (s, 4H), 7.42 (d, *J* = 9.7 Hz, 1H), 7.49 (d, *J* = 8.5 Hz, 1H), 7.70 (dd, *J* = 1.7, 8.4 Hz, 1H), 7.87 (d, *J* = 7.7 Hz, 2H), 8.01 (d, *J* = 1.8 Hz, 1H), 8.27 (s, 1H), 8.46 (t, *J* = 5.6 Hz, 1H), 8.59 (t, *J* = 6.1 Hz, 1H), 8.97 (s, 1H). **^{13}C NMR** (101 MHz, DMSO) δ 15.9, 26.2, 34.5, 35.7, 37.9, 41.7, 47.6, 55.7, 56.6, 58.8, 68.9, 69.0, 69.6, 69.6, 69.7, 69.8, 69.8, 70.5, 106.2, 121.2, 126.9, 127.1, 127.5, 128.1, 128.4, 128.7, 129.1, 129.7, 131.2, 136.0, 138.2, 139.5, 147.8, 151.5, 151.8, 157.7, 166.5, 168.6, 169.1, 171.8. **HRMS** *m/z* calc. for $C_{56}H_{69}N_{11}O_{12}S_2$ $[M+H]^+$ 1152.4570, found 1152.4639.

6.2.1.2 NMR Spectra and HPLC / MS Report of Selected Compounds

tert-Butyl (1-((2-(2,6-dioxopiperidin-3-yl)-1-oxoisoindolin-4-yl)amino)-1-oxo-3,6,9,12,15,18-hexaoxaicosan-5-yl)carbamate (11c)

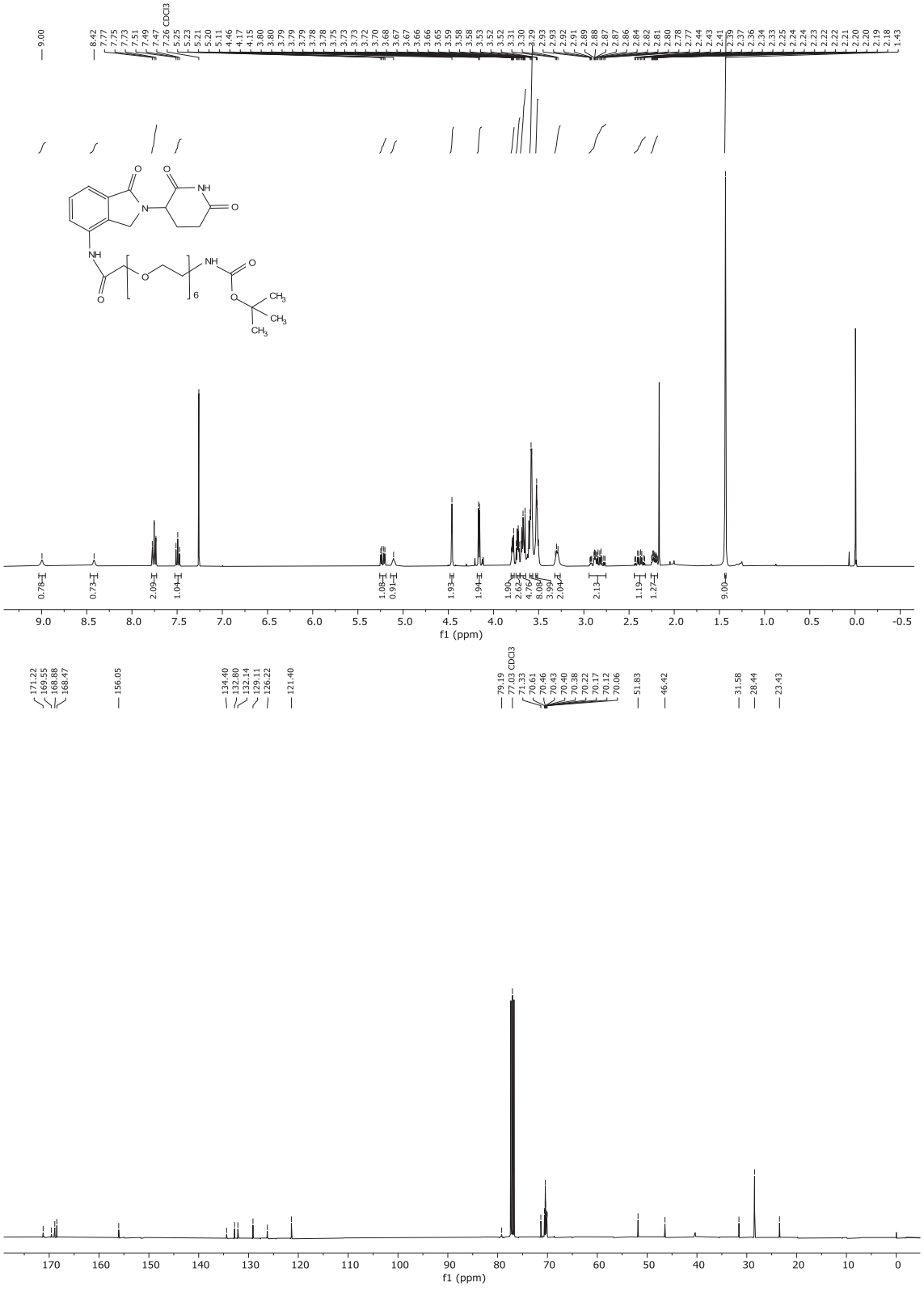

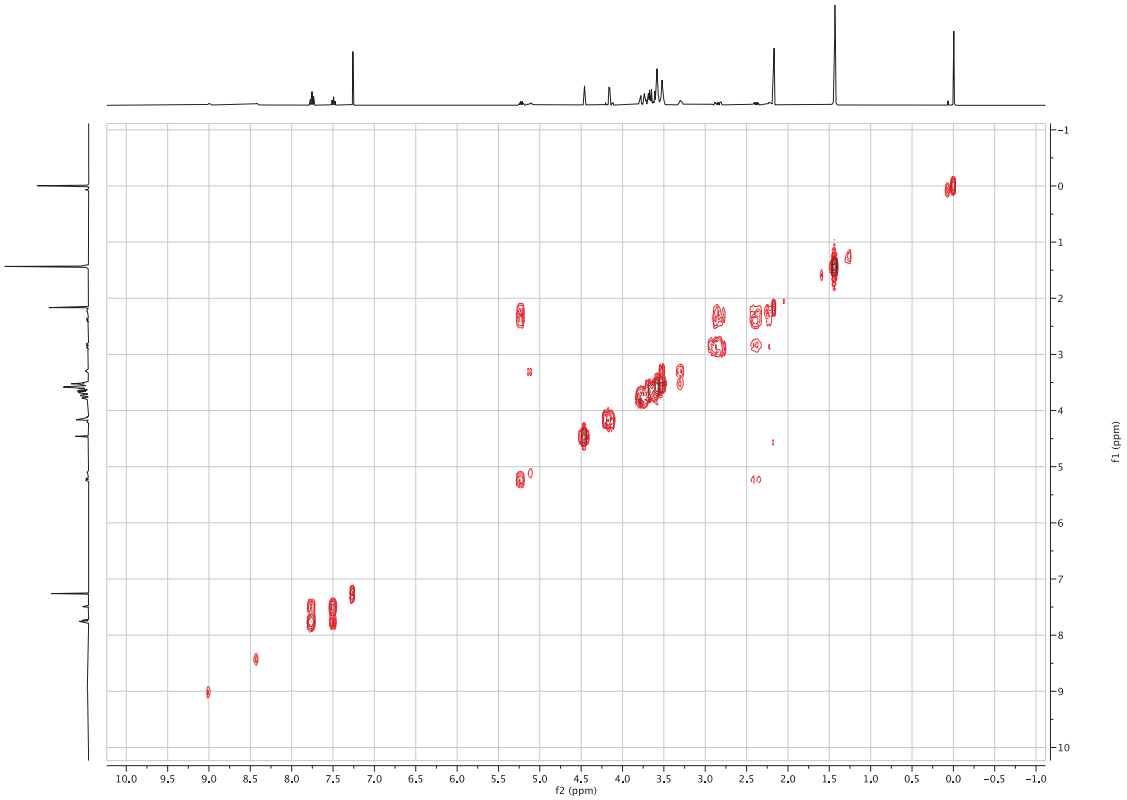

N-(2-(2-(2-((2-(2,6-Dioxopiperidin-3-yl)-1-oxoisoindolin-4-yl)amino)-2-oxoethoxy)ethoxy)ethyl)-2-(((4-oxo-1-phenyl-4,5-dihydro-1*H*-pyrazolo[3,4-*d*]pyrimidin-6-yl)methyl)thio)-1*H*-benzo[*d*]imidazole-6-carboxamide (CYC-1)

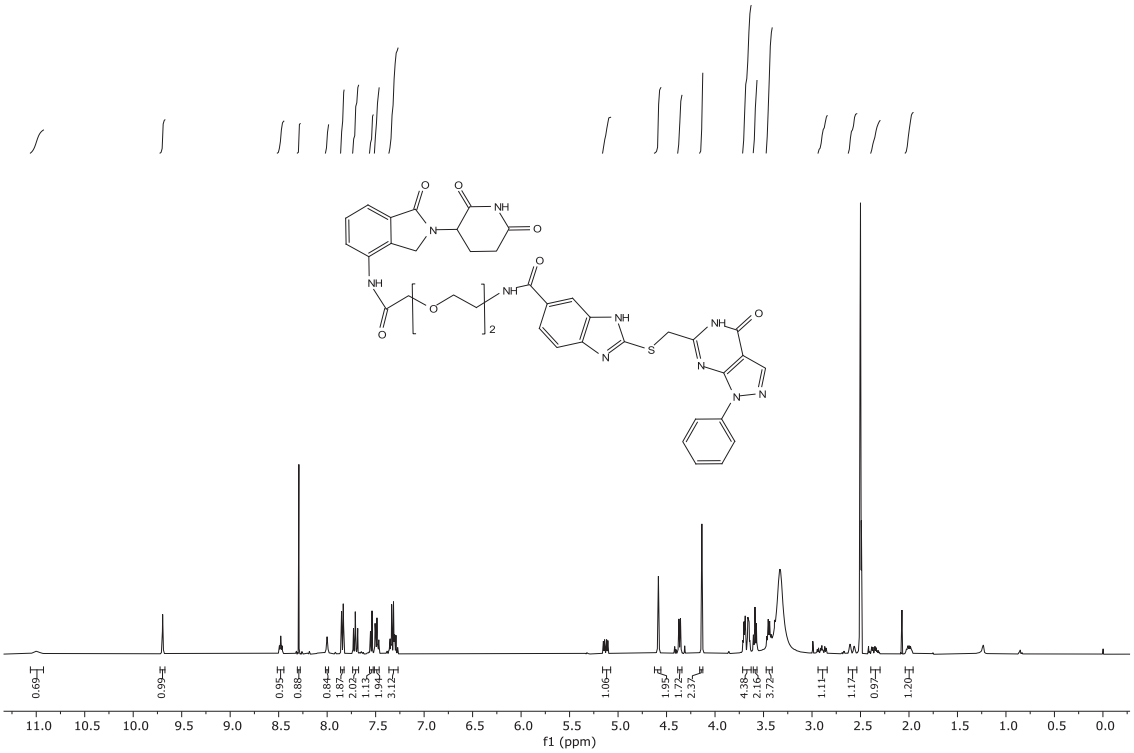

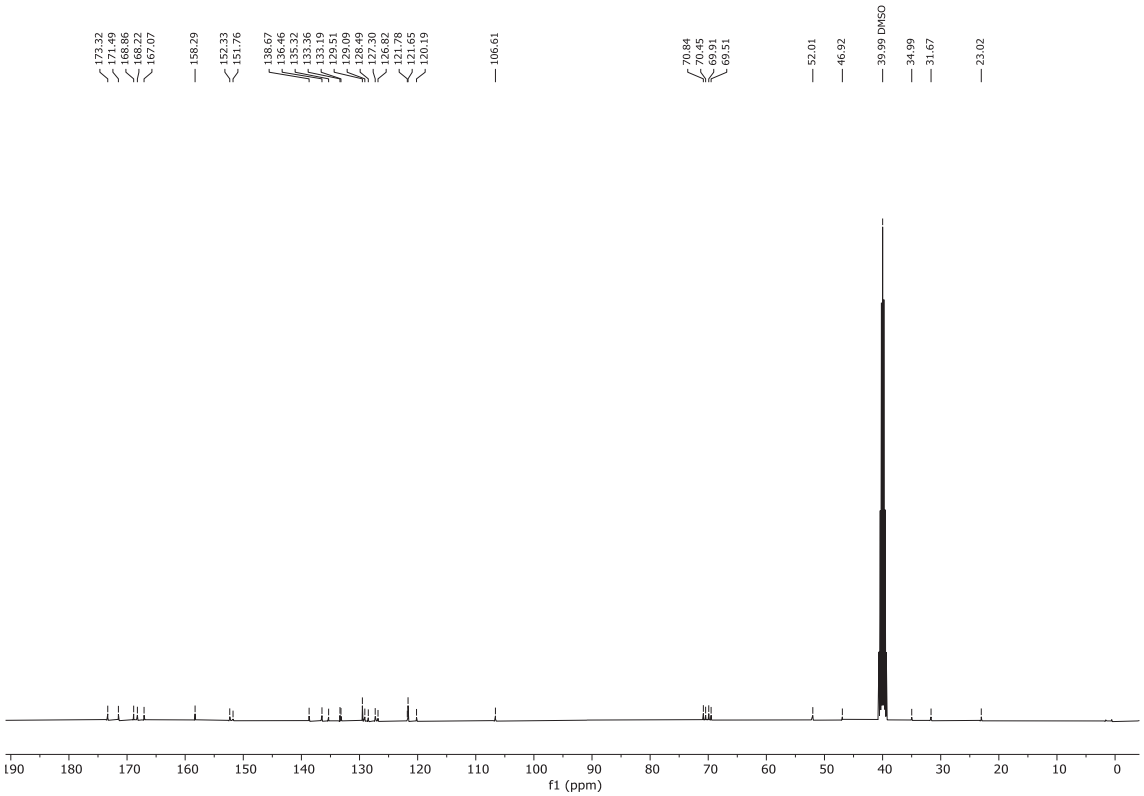

HPLC / MS CYC-1

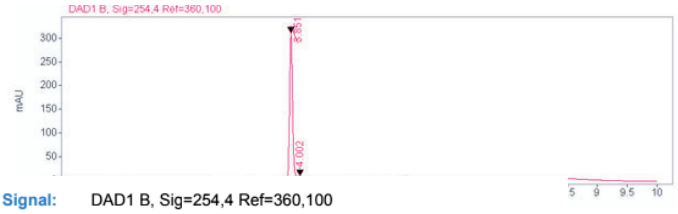

Signal: DAD1 B, Sig=254,4 Ref=360,100

RT [min]	Type	Width [min]	Area	Height	Area%	Name
3.851	BB	0.0531	1031.4883	308.0310	98.8230	
4.002	BB	0.0464	12.2855	4.1625	1.1770	
		Sum	1043.7737			

N-(14-((2-(2,6-Dioxopiperidin-3-yl)-1-oxoisoindolin-4-yl)amino)-14-oxo-3,6,9,12-tetraoxatetradecyl)-2-(((4-oxo-1-phenyl-4,5-dihydro-1*H*-pyrazolo[3,4-*d*]pyrimidin-6-yl)methyl)thio)-1*H*-benzo[*d*]imidazole-6-carboxamide (CYC-2)

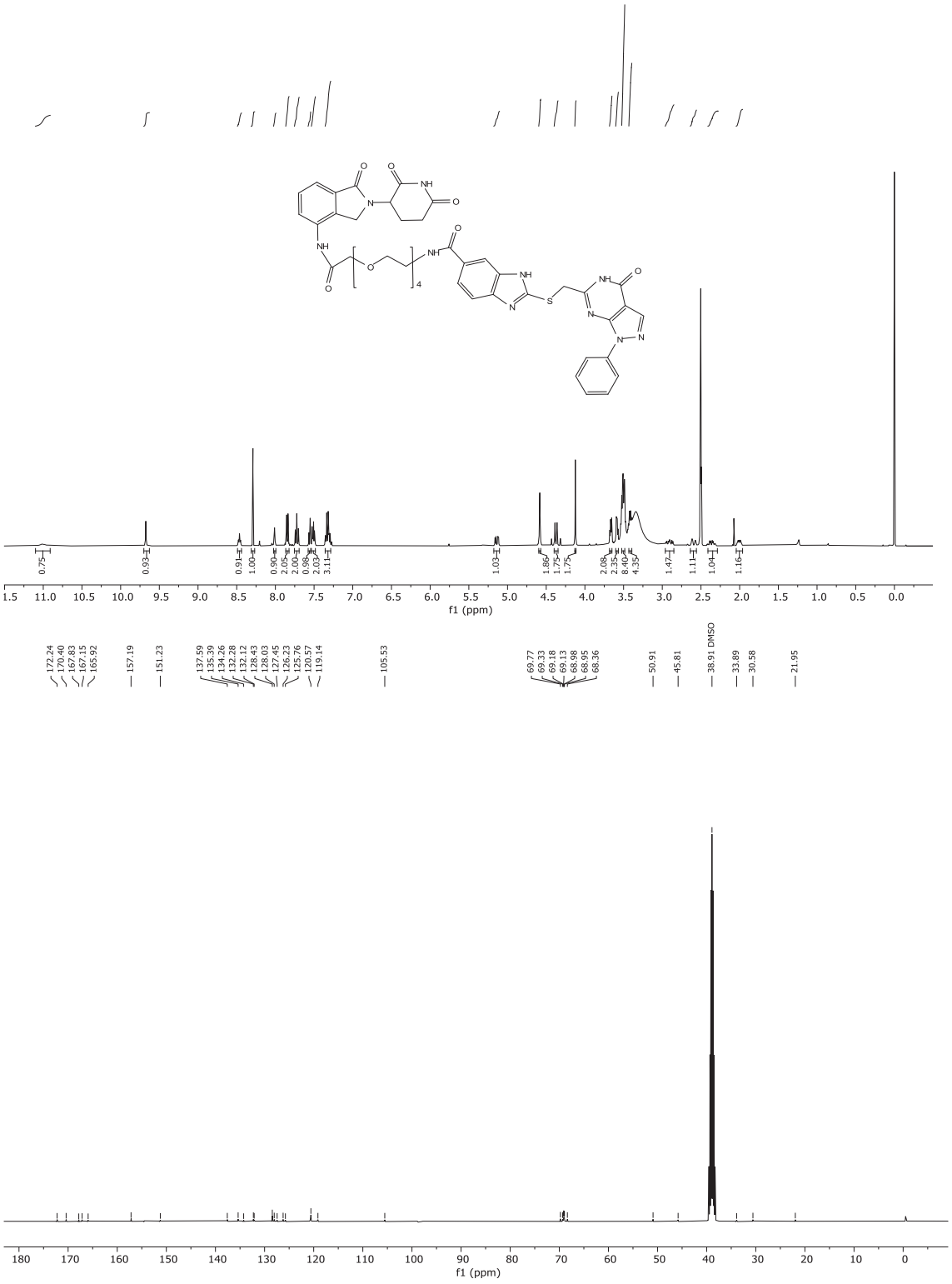

HPLC / MS CYC-2

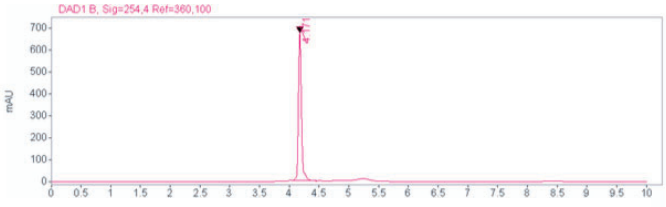

Signal: DAD1 B, Sig=254,4 Ref=360,100

RT [min]	Type	Width [min]	Area	Height	Area%	Name
4.171	BB	0.0532	2392.1250	677.6882	100.0000	
		Sum	2392.1250			

N-(20-((2-(2,6-Dioxopiperidin-3-yl)-1-oxoisoindolin-4-yl)amino)-20-oxo-3,6,9,12,15,18-hexaoxaicosyl)-2-(((4-oxo-1-phenyl-4,5-dihydro-1*H*-pyrazolo[3,4-*d*]pyrimidin-6-yl) methyl)thio)-1*H*-benzo[*d*]imidazole-6-carboxamide (CYC-3)

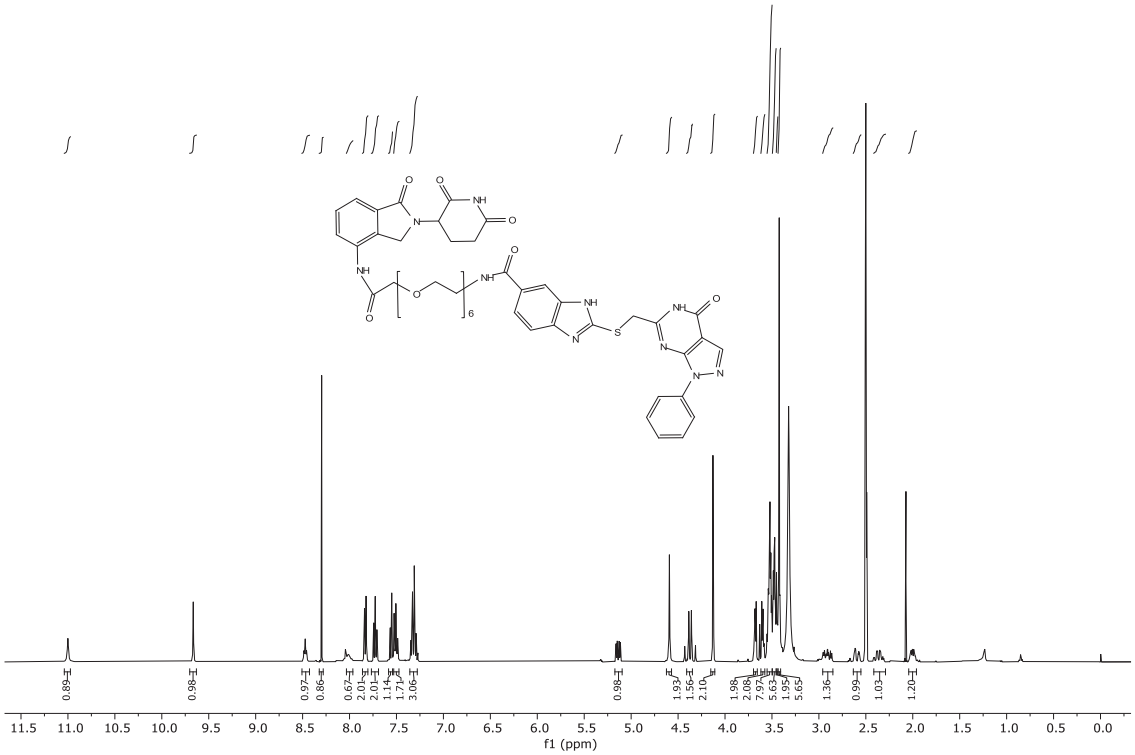

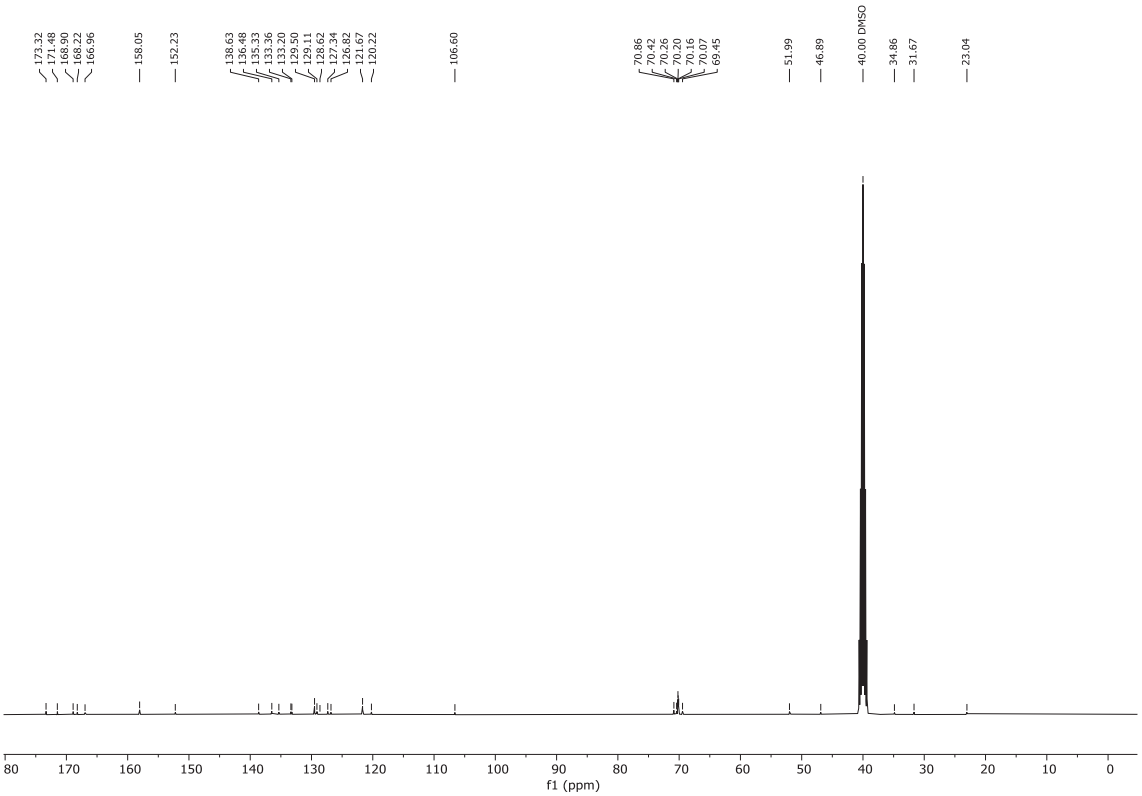

HPLC / MS CYC-3

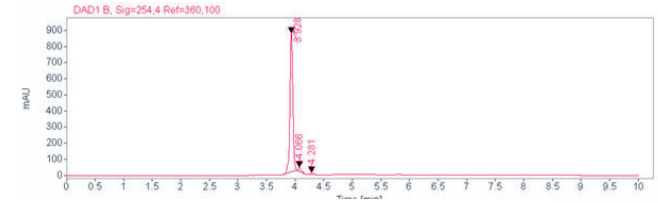

Signal: DAD1 B, Sig=254,4 Ref=360,100

RT [min]	Type	Width [min]	Area	Height	Area%	Name
3.928	BB	0.0548	3051.7478	872.8716	95.6162	
4.066	BB	0.0519	94.0313	27.5260	2.9462	
4.281	BB	0.0519	45.8860	14.1240	1.4377	
		Sum	3191.6651			

N-(2-(2-(2-(((*R*)-1-((2*R*,4*S*)-4-Hydroxy-2-((4-(4-methylthiazol-5-yl)benzyl)carbamoyl) pyrrolidin-1-yl)-3,3-dimethyl-1-oxobutan-2-yl)amino)-2-oxoethoxy)ethoxy)ethyl)-2-(((4-oxo-1-phenyl-4,5-dihydro-1*H*-pyrazolo[3,4-*d*]pyrimidin-6-yl)methyl)thio)-1*H*-benzo[*d*]imidazole-6-carboxamide (CYC-10)

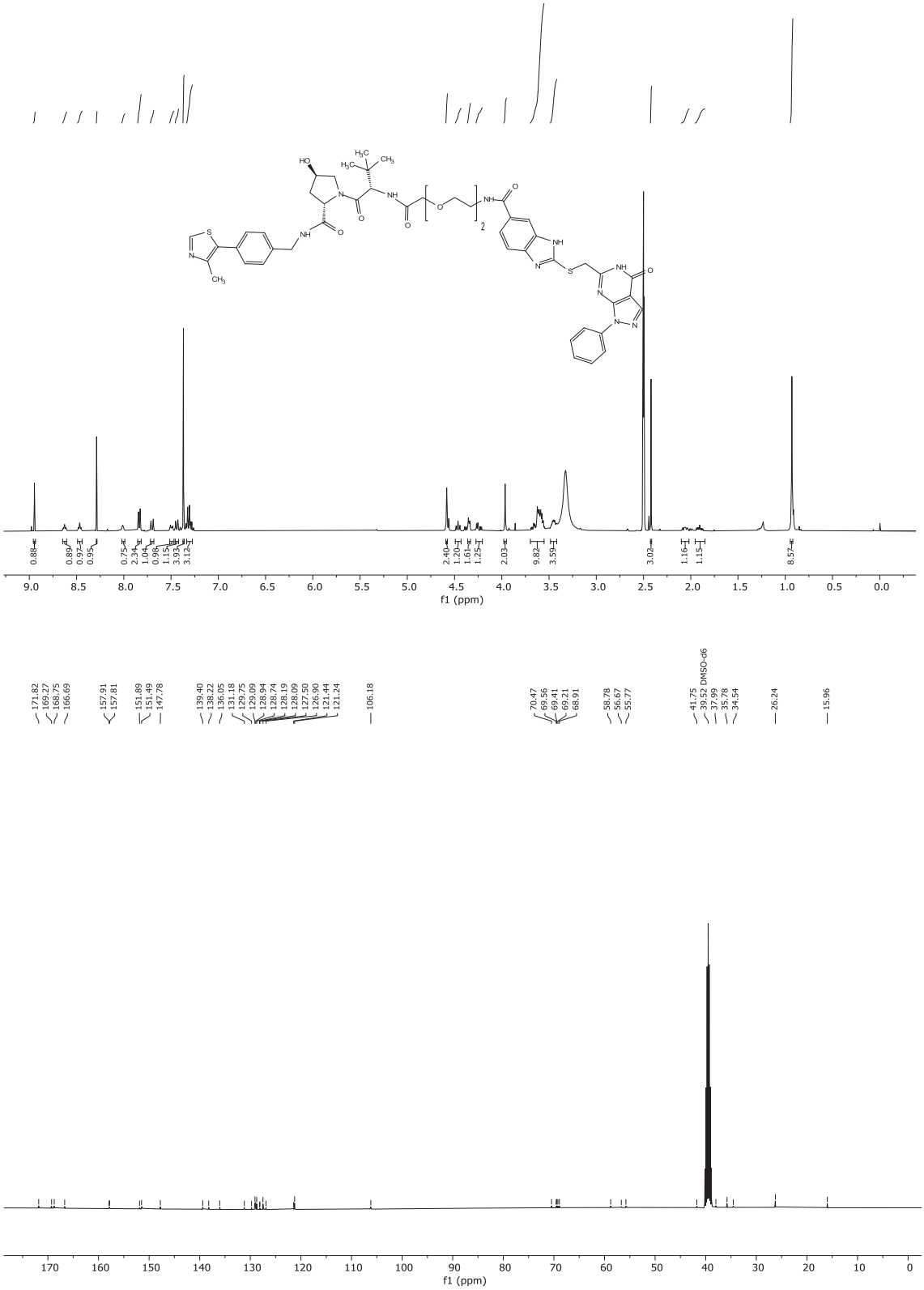

HPLC / MS CYC-10

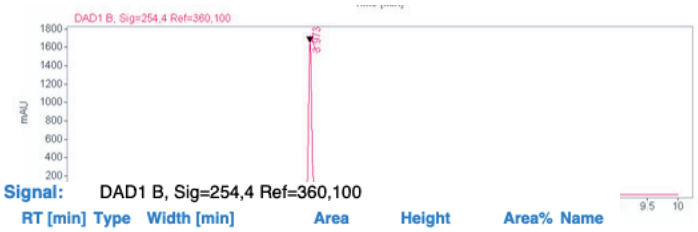

N-((*R*)-16-((2*R*,4*S*)-4-Hydroxy-2-((4-(4-methylthiazol-5-yl)benzyl)carbamoyl)pyrrolidine-1-carbonyl)-17,17-dimethyl-14-oxo-3,6,9,12-tetraoxa-15-azaoctadecyl)-2-(((4-oxo-1-phenyl-4,5-dihydro-1*H*-pyrazolo[3,4-*d*]pyrimidin-6-yl)methyl)thio)-1*H*-benzo[*d*]imidazole-6-carboxamide (CYC-11)

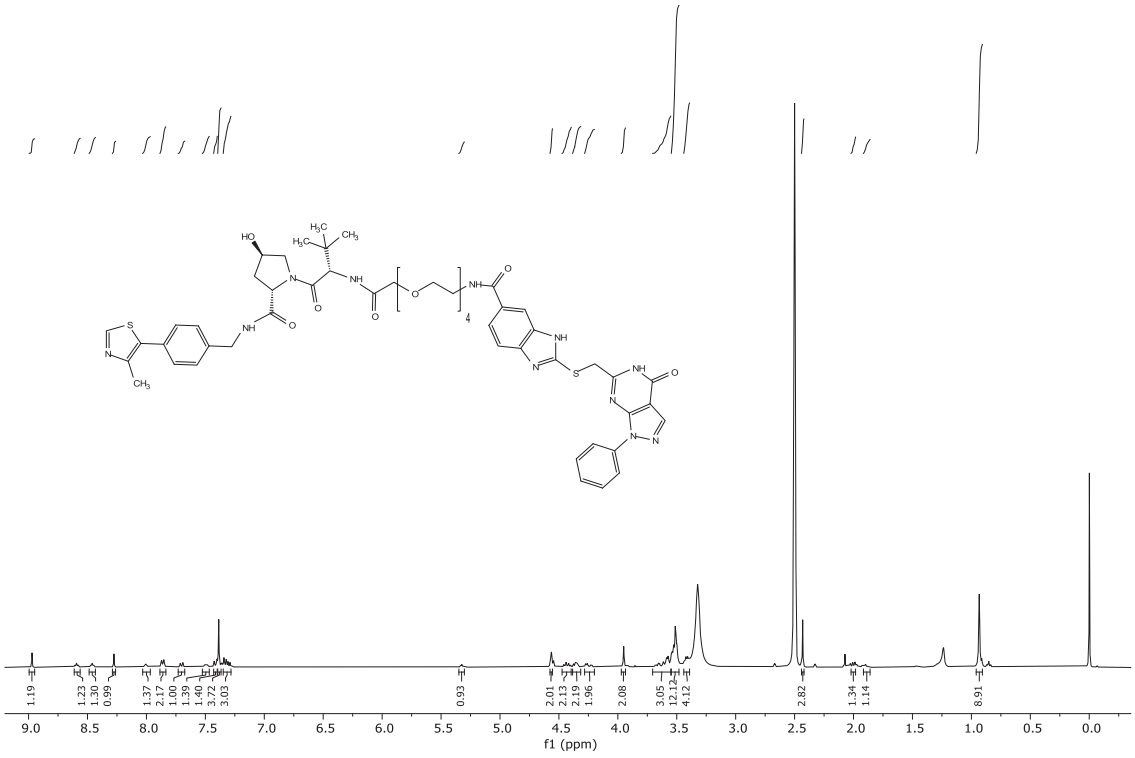

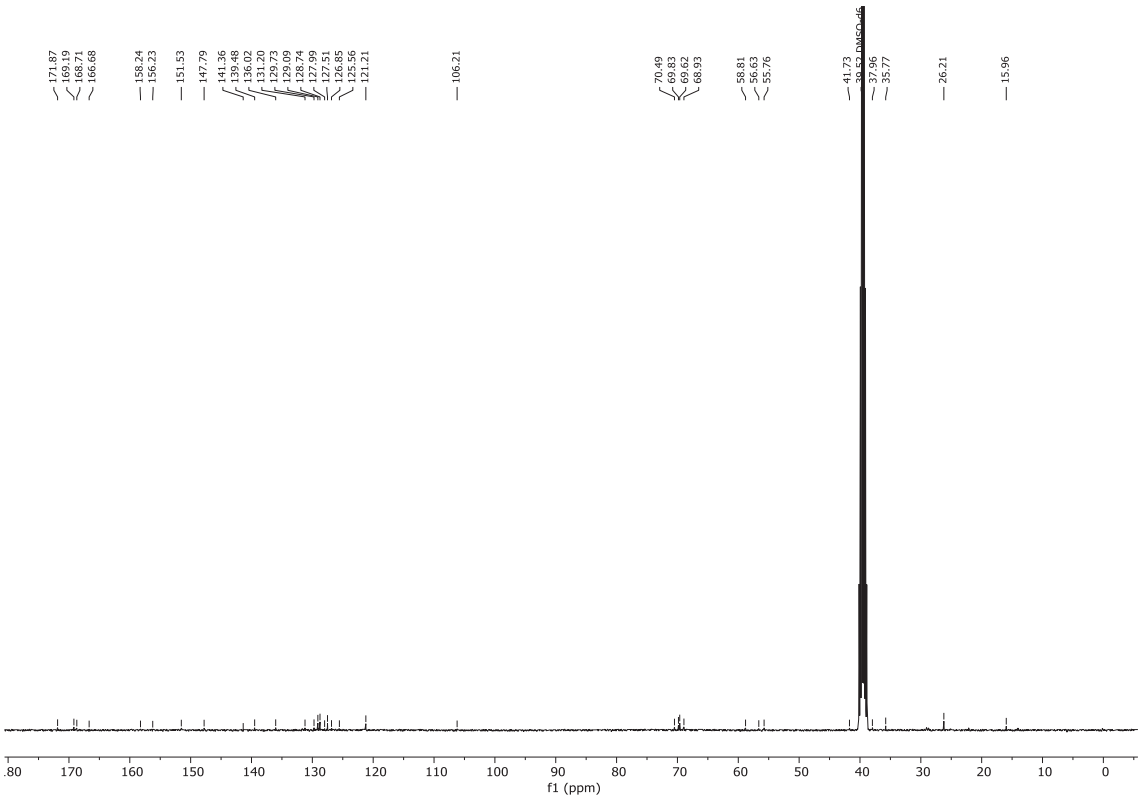

HPLC / MS CYC-11

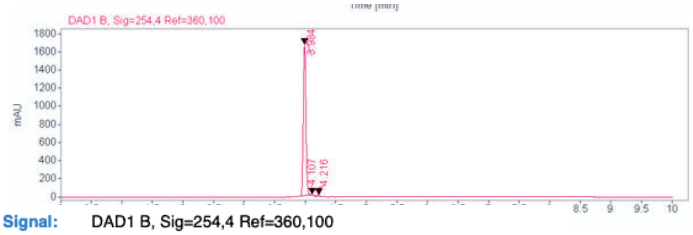

Signal: DAD1 B, Sig=254,4 Ref=360,100

RT [min]	Type	Width [min]	Area	Height	Area%	Name
3.984	BB	0.0468	4983.5483	1672.3290	98.0029	
4.107	BB	0.0408	39.5407	16.0202	0.7776	
4.216	BB	0.0441	62.0126	22.5437	1.2195	
		Sum	5085.1016			

N-((*R*)-16-((2*R*,4*S*)-4-Hydroxy-2-((4-(4-methylthiazol-5-yl)benzyl)carbamoyl)pyrrolidine-1-carbonyl)-17,17-dimethyl-14-oxo-3,6,9,12-tetraoxa-15-azaoctadecyl)-2-(((4-oxo-1-phenyl-4,5-dihydro-1*H*-pyrazolo[3,4-*d*]pyrimidin-6-yl)methyl)thio)-1*H*-benzo[*d*]imidazole-6-carboxamide (CYC-12)

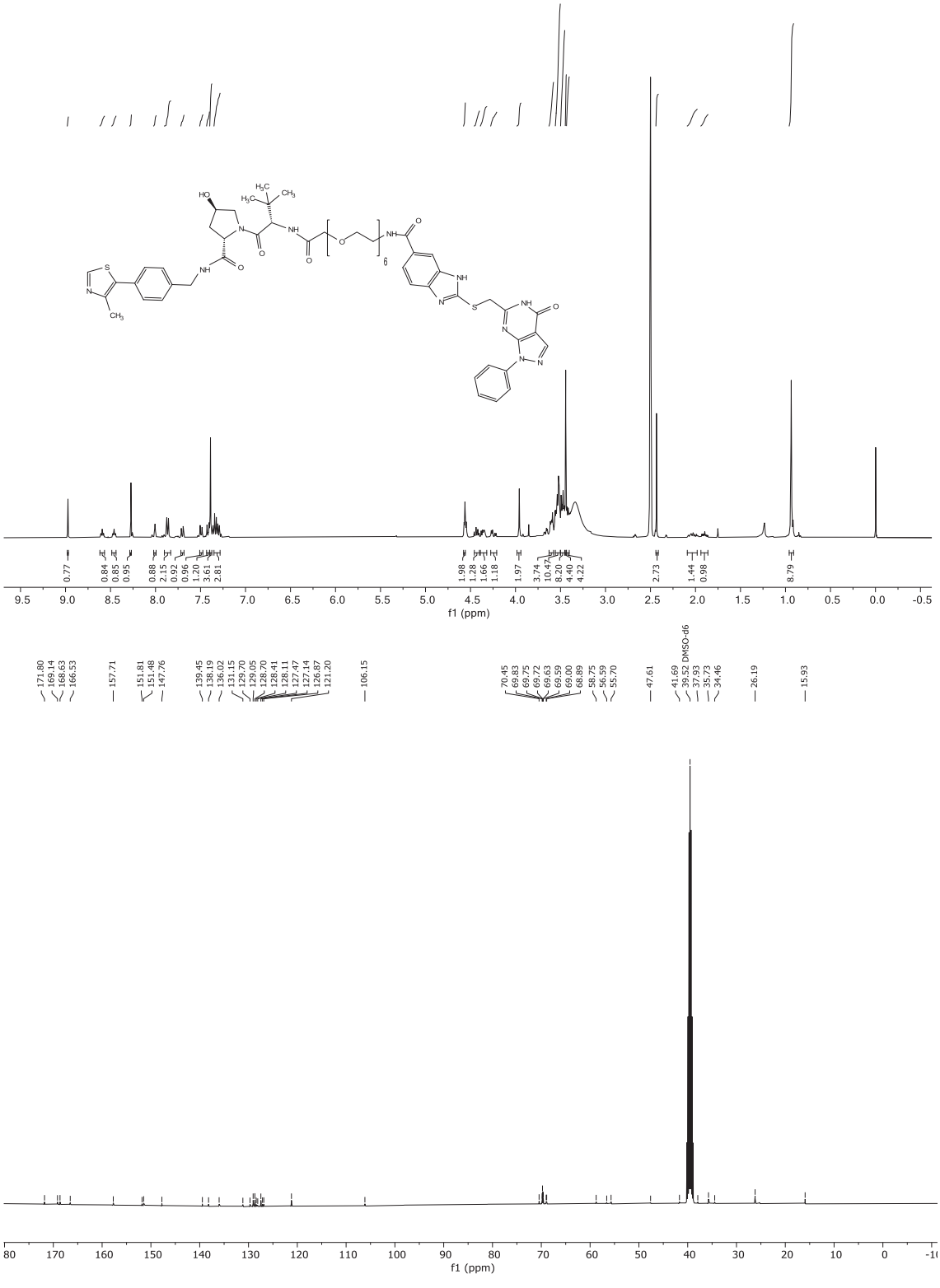

HPLC / MS CYC-12

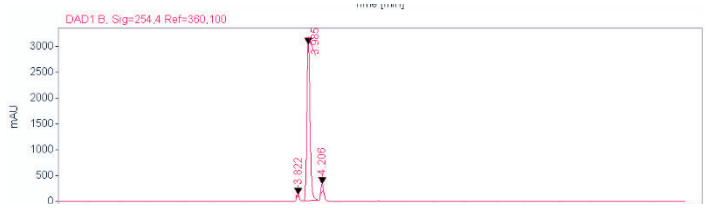

Signal: DAD1 B, Sig=254,4 Ref=360,100

RT [min]	Type	Width [min]	Area	Height	Area%	Name
3.822	MM	0.0265	81.2533	51.0536	0.7104	
3.985	BB	0.0578	10979.8633	3066.8208	95.9921	
4.206	MM	0.0334	377.1794	188.3308	3.2975	
		Sum	11438.2960			

6.2.2 Cellular and biology techniques

The following assays are performed at the Centre for Targeted Protein Degradation, School of Life Sciences, University of Dundee (Dundee, Scotland) during the 3-months STSM internship stay.

6.2.2.1 Cell culture

HEK 293 cells, originally soured from ATCC, are provided by the MRC PPU reagents facility at the University of Dundee and cultured with DMEM (Gibco) supplemented with 10% fetal bovine serum (FBS; Thermo Fisher), 100 U ml−1 penicillin-streptomycin (Thermo Fisher) and 2 mM L-glutamine (Thermo Fisher). The cell line is grown in a humidified incubator at 37 °C and 5% CO_2 and routinely tested for mycoplasma contamination. The cell line is authenticated by short tandem repeat profiling.

6.2.2.2 Cell treatment

Cells were seeded at 80-90 % confluency and attached overnight prior to compound treatment in a humidified atmosphere of 5% CO_2. Then, the cells were treated for 6 or 24 hours with different compound concentrations. The co-treatments with the different inhibitors were added 1 hour before compound treatment. MG-132, proteasome inhibitor (from Merck) was added at 10 µM; and MLN-4924, NAE inhibitor (from Merck) was added at 1 µM.

6.2.2.3 Cell collection and lysis

HEK 293 cells are plated in 6-well plates at varying densities (0.5 to 0.7 × 10^6 cells per mL), depending on experimental setup, and left overnight prior to compound treatment in a humidified incubator at 37 °C and 5 % CO_2. The cells are treated for 6, 14 or 24 hours with different compound concentrations. Stock solutions of compounds are prepared in DMSO at a concentration of 10 mM and stored at -20 °C. Working dilutions are made fresh using DMEM media and added dropwise to 6-well plates. For co-treatment assays, cells were pre-treated with inhibitors 10 µM MG-132 or 1 µM MLN-4924 for 1 hour, before treating with different PROTAC compound.

6.2.2.4 BCA quantification

Protein concentration of lysates was quantified using the Pierce BCA Protein Assay (23225, Thermo Fisher). The standard curve is obtained using eight BSA protein standards in ddH_2O for concentration of 2, 1, 0.5, 0.25 and 0.125 mg/mL (ThermoFisher). 25 mL of

the sample, previously diluted with ddH_2O (1:10 *v/v* at final volume of 60 mL), is added to the 96-well plate prior to the addition of the BCA working reagent (1:8 *v/v* at final volume of 200 mL). Then, the plates are incubated for 30 minutes at 37 ºC. The measurement is performed in an PHERAstar (BMG LabTech). 20- 30 mg of lysate is prepared using 4xLDS sample buffer with 50 mM of dithiothreitol (DTT) and ddH_2O.

6.2.2.5 Western blot

After sample preparation according to BCA protein quantification, 20 mg of protein is loaded on NuPAGE 12% bis-tris gels (ThermoFisher) and resolved at constant intensity (25 mA / gel). Proteins are transferred to nitrocellulose membranes, blocked for 1 hour in 5% non -fat dry milk TBS-T 1X at room temperature, before incubating with primary antibodies overnight at 4ºC. The following antibodies are used: Cyclin E1 (1:1000 in 5% milk-TBS-T 1X, no. Ab33911, Abcam), CDK2 (1:1000 in 5% milk-TBS-T 1X, no. Ab32147, Abcam) and α-tubulin (1:500, DM1A, T9026, Sigma-Aldrich). Membranes are washed with TBST-T 1X and incubated with the fluorescent- conjugated secondary antibody for 1 hour at room temperature, before further washes and imaging on a ChemiDoc Touch imaging system (Bio-Rad) operated on Image Lab software (v2.4.0.03). Secondary antibodies used are IRDye 800CW donkey anti-rabbit (1:5,000, 926-32211, Li-Cor) and hFABTM rhodamine anti-tubulin (1:5,000, 12004165, Bio-Rad). Western Blots are quantified using Image Lab software (v6.1 build 7).

6.2.2.6 Cell-cycle arrest

Cell proliferation is a highly regulated process, key for the growth and development of any organism. The eukaryotic cell cycle comprises five phases with the following sequential transition: [G_0] -> G_1 -> S -> G_2 -> M]). Cell synchronization is a technique that aligns cultured cells at various phases of the cell cycle to the same stage, allowing them to progress through the cycle as a uniform cohort. This method facilitates the study and understanding of the changes that occur during a specific phase.

Different strategies have been employed to synchronize the cell cycle, which can be categorized into physical and chemical methods. In this case, we will focus on the chemical ones, which involve the use of pharmacological agents to block the progression of the cells at a specific phase (Table 6). Cell cycle progression is regulated by a family of CDKs that associate with their respective Cyclin regulatory subunits, which oscillations levels determine CDK activity and control of cell cycle transition. In this case, our proteins of interest are Cyclin E in complex with CDK2, which controls G1 / S phase transition and S phase progression. Thus, thymidine blockade is used to study the effect of our degraders, as it synchronizes the cells at the G1 / S phase, where Cyclin E / CDK2 complex is more abundant.

Chemical inhibitor	*Cell cycle synchronized stage*	*Cyclin and Kinase expression profile*	*MoA*
Lovastatin	G_0 / G_1	D CDK4, CDK6	HMG-CoA reductase inhibitor that depletes mevalonate and acts as an antimitogenic agent [253]
Thymidine	G_1 / S	E, A CDK2	Pyrimidine nucleoside blocks DNA replication by interfering in the deoxynucleotide-metabolism pathway at high concentrations [254]
Nocodazole	G_2 / M	A, B – cdc2	Benzimidazole inhibitor of microtubule polymerization that forms the mitotic spindle [255]

Table 6: Chemical methods for cell-cycle synchronization. CDK, cell-dependent kinase; cdc, Cyclin-dependent kinase. [256]

Protocol

In order to synchronize cells in G_1 / S interphase with the double- thymidine blockade, [257] HEK 293 cells are plated in 20-30 % confluency in 10 cm- well plates ($1.5x10^6$) cells/ dish) containing 5 mL of complete DMEM media* and left overnight in a humidified incubator at 37 ºC and 5 % CO_2. Next day, 60 µL of thymidine blocking solution (prepared by dissolving thymidine (Thermo Fisher) in ddH_2O to a final 2mM concentration) for each 1 mL of culture media, are added in each well and left incubating for 16 hours. For the asynchronic wells, 60 µL of ddH_2O are added as vehicle control. After incubation, the cells are released from thymidine by washing twice with 10mL pre- warmed 1X PBS. Subsequently, 5 mL of fresh DMEM media* are added and left incubating for 9 hours. For the second blockade, 60 µL of thymidine (to a final concentration of 2 mM) are added and left incubating for another 14 hours. The treated wells also contain 0.6µL of the PROTAC compound (dissolved in pure DMSO at a final concentration of 5 µM) for each 1mL of culture media. At this point, the cells are now arrested at the G_1 / S interphase. Finally, cells are released at selected times by washing twice with 1X PBS, followed by the addition of 1mL of fresh complete DMEM* in control wells and 0.6 µL of PROTAC compound in treated wells for each 1mL of culture media. Cells are collected at 0 (G_1 fraction), 4 hours (S fraction), 6 (G_2 fraction) and 10 hours (M fraction) after release, following the procedure explained in Cell collection and lysis (Figure 47).

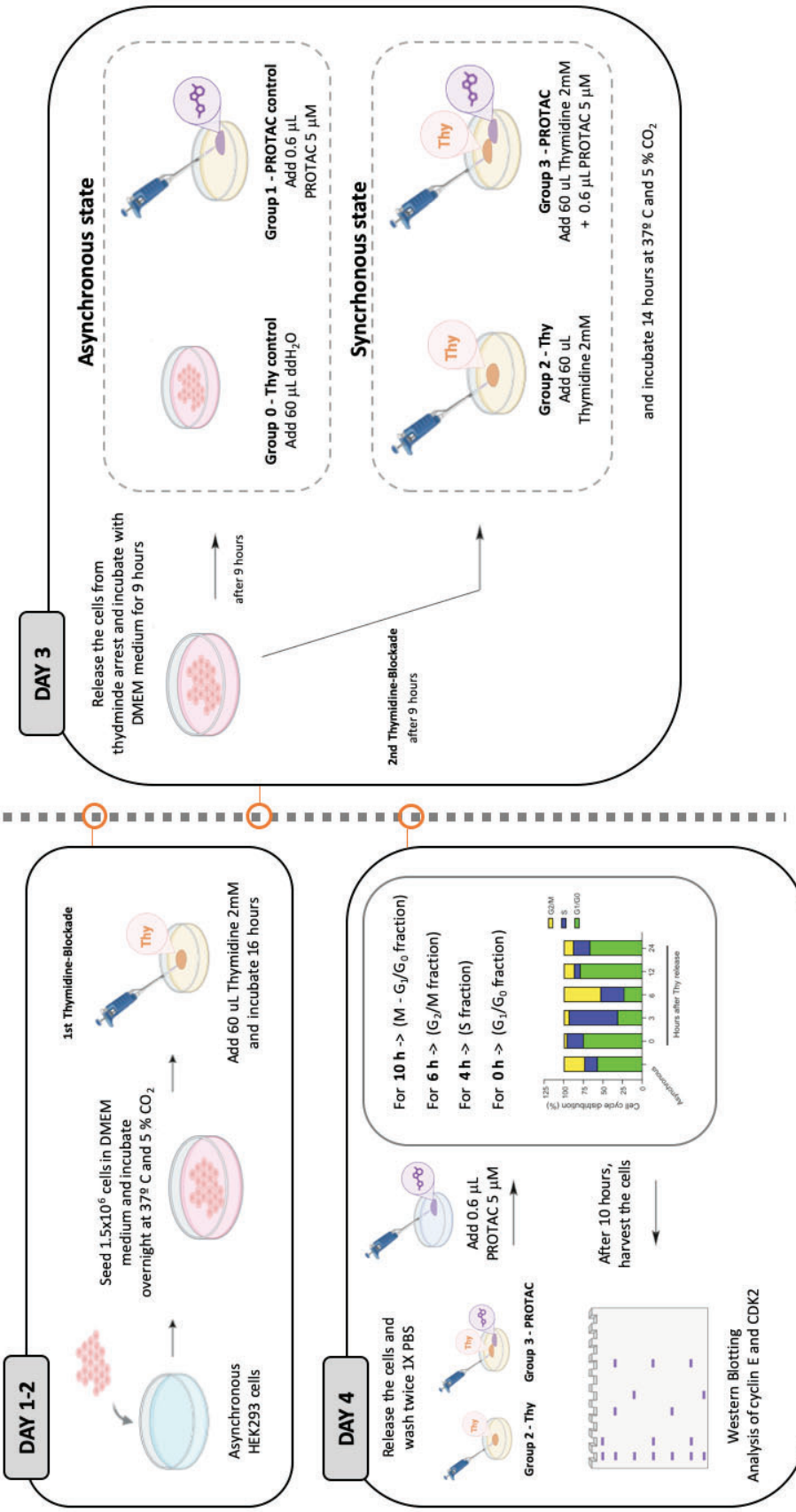

Figure 47: Workflow of the cell cycle arrest assay (created with BioRender.com). Percentage of cells in each phase of the cell cycle at different time points are shown. [258]

6.2.3 Biophysical techniques

6.2.3.1 NanoBRET Target Engagement Intracellular E3 ligase assay

The initial steps of protein degradation *via* PROTACs involve entry of the small molecule degrader compound into the cell, followed by binding to the E3 ubiquitin ligase and protein target. Hence, we use the biophysical NanoBRET® Target Engagement (TE) Intracellular E3 Ligase technique (**Box 3**) to study the CRBN- based PROTACs binding affinity for CRBN protein as well as their permeability properties.

Box 3: Principle of the NanoBRET Target Engagement Assay

Target engagement describes the interaction or binding of a chemical compound with its target protein in a living system. Promega has developed a novel cell- based approach, called NanoBRET® TE Intracellular E3 Ligase Assay, that provides live- cell measurement of test compound affinity as well as compound permeability for a target protein *via* bioluminescence resonance energy transfer (BRET). This energy transfer is based on the cellular expression of the NanoLuc® luciferase-tagged target protein and a cell-permeable fluorescent NanoBRET® tracer, which reversibly engages the target protein of interest. When the fluorescent tracer binds to the target-NanoLuc® fusion protein in live cells, the tracer is in close proximity to NanoLuc® Luciferase and results in a BRET signal. Thus, the test compounds that bind to the target protein compete with the tracer and result in loss of NanoBRET® signal.

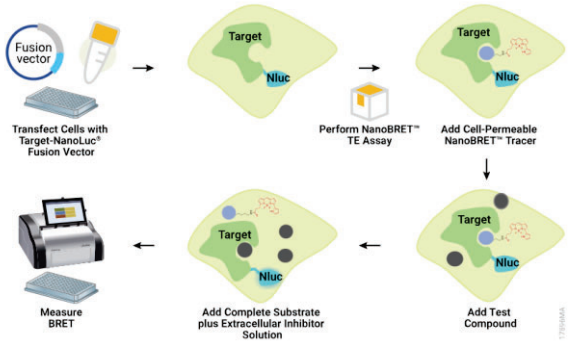

NanoBRET® TE Workflow (from Promega).

Protocol

Target engagement and intracellular availability for CRBN degraders are assessed using the NanoBRET TE Intracellular E3 ligase assay (Promega N274A). HEK 293 cells are transfected with CRBN-NanoLuc® fusion constructs using FuGENE HD (Promega) according to manufacturer's protocol. In brief, Briefly, CRBN- NanoLuc® construct is diluted into Transfection Carrier DNA (Promega) at a mass ratio of 1:9 (w/w), after which FuGENE HD is added at a ratio of 1:3 (µg DNA: µL FuGENE HD). FuGENE HD complex thus formed is combined with HEK 293 cells suspended at a density of 2 × 105 cells/mL,

transferred to a tissue-culture treated flask (T-75), and incubated at 37 °C and 5 % CO2 in a humidified atmosphere for 20 hours. The following day, cells are washed, harvested by trypsinization, and resuspended in phenol red- free OptiMEM (Gibco). BRET assays are performed in white, 96- well non- binding surface plates (Corning #3600) at a density of 2 × 105 cells / well. All chemical compounds are prepared serially diluted at 1000X final concentrated stock solutions in DMSO (Sigma-Aldrich) and diluted in Opti-MEM (unless otherwise noted) to prepare 10X final concentration stocks, in triplicates. For measurement of intracellular affinity for CRBN- based degraders, live cells are equilibrated for 4 hours with test compounds and the last 2 hours, also with CRBN tracer prior to BRET measurements. CRBN tracer is prepared as a 100X intermediate stock at 50 µM in pure DMSO and subsequently diluted to a working concentration of 20X in tracer dilution buffer (TDB; 12.5 mM HEPES, 31.25% PEG-400, pH 7.5). CRBN tracer is added to live cells at a final concentration of 10 µM from the 20X working stock.

For measurement of intrinsic affinity for CRBN- based degraders, the NanoBRET TE assay is applied as described above, with some changes: the cells are permeabilized by adding digitonin to a final concentration of 50 µg/mL, the CRBN tracer is prepared as a 100X intermediate stock at 25 µM in pure DMSO and subsequently diluted to 20X with TDB , the permeabilized cells are incubated with tracer and test compound for 10 minutes at room temperature, and the Extracellular NanoLuc Inhibitor is omitted from the NanoGlo substrate solution.

To measure BRET, NanoBRET NanoGlo Substrate and Extracellular NanoLuc Inhibitor (Promega) are added according to the manufacturer's recommended protocol, and filtered luminescence is measured on a Pherastar equipped with 450 nm BP filter (donor) and 610 nm LP filter (acceptor), using 1s integration time. Milli-BRET units (mBU) are calculated by multiplying the raw BRET values by 1000. Competitive displacement data are plotted with GraphPad Prism software (v10.1.1) and IC_{50} values are determined using the [inhibitor] vs response – variable slope (four parameters). For this experiment, NanoBRET ratios are normalized to background correction and expressed in %.

6.3 Chapter 5: Design and Synthesis of novel Brd4- targeting molecules with computer assisted FBDD

6.3.1 Chemistry Section

General Information

Followed as described in Chapter 6.1.1.1.

Data Analysis

Followed as described in Chapter 6.1.1.2.

6.3.1.1 Synthetic Procedures and Characterization Data

Synthesis of SSR4- and SSR12- intermediate derivatives

4-(3-Bromophenyl)-2-hydrazineylthiazole (*m*-1)

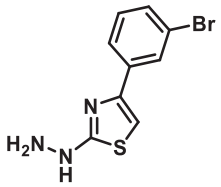

***m*-1**

A solution of a thiosemicarbazide (**45**; 607 mg, 6.61 mmol, 1 eq) and 2-bromo-1-(3-bromophenyl)ethan-1-one (**46**; 1851 mg, 6.61 mmol, 1 eq) in dioxane (12 mL) was stirred at room temperature overnight. The precipitate of hydrobromide salt was filtered and washed with cold dioxane and, basified with 2N Na_2CO_3 to give ***m*-1**. The product was filtered, washed with ddH_2O, dried and brought to the next step without further purification. [237] HRMS *m/z* calc. for $C_9H_8BrN_3S$ $[M+H]^+$ = 269.9620, found 269.9698.

N'-(4-(3-Bromophenyl)thiazol-2-yl)propionohydrazide (*m*-2)

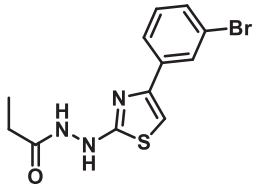

***m*-2**

To a cooled solution (0 ºC) of 4-(3-bromophenyl)-2-hydrazineylthiazole (***m*-1;** 1230 mg, 4.55 mmol, 1 eq) in THF (6.5 mL) was added dropwise a solution of propionyl chloride (**41**; 0.5 mL, 5.15 mmol, 1.1 eq) in THF (6.5 mL). The reaction mixture was stirred at 0 °C for 45 min and the precipitate formed was collected by filtration and washed with cold

water to give ***m*-2** as a white solid. The product was brought to the next reaction without further purification. [249] **HRMS** *m/z* calc. for $C_{12}H_{12}BrN_3OS$ $[M+H]^+$ = 325. 325.9957, found 325.9955.

5-(3-Bromophenyl)-3-ethylthiazolo[2,3-*c*][1,2,4]triazole (AS-10)

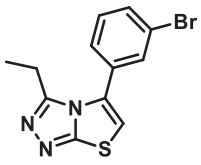

AS-10

A mixture of *N*'-(4-(3-bromophenyl)thiazol-2-yl)propionohydrazide (***m*-2;** 1209 mg, 3.71 mmol, 1 eq) in xylene (12 mL) and phosphoryl chloride (6 mL, 66.53 mmol, 18 eq) was heated at 130 ºC overnight. The mixture was cooled to room temperature and quenched with crushed ice and cold water. Then, the organic layer was washed with AcOEt and water, dried over Na_2SO_4, filtered, and concentrated. The crude was purified with reverse-phase column chromatography (37 % CH_3CN in 0.1 % aq. HCO_2H) to give **AS-10** as a brown solid (650 mg, **19 %** overall yield). [240] **HRMS** *m/z* calc. for $C_{12}H_{10}BrN_3S$ $[M+H]^+$ = 307.9780, found 307.9852. **^{1}H NMR** (400 MHz, $CDCl_3$) δ 1.15 (t, *J* = 7.5 Hz, 3H), 2.59 (q, *J* = 7.5 Hz, 2H), 6.77 (s, 1H), 7.39 – 7.42 (m, 2H), 7.65 (s, 1H), 7.68 – 7.71 (m, 1H). **^{13}C NMR** (101 MHz, $CDCl_3$) δ 11.4, 20.2, 114.7, 122.8, 127.9, 129.3, 130.3, 130.4, 132.3, 133.5, 149.5, 157.6.

4-(2-Bromophenyl)-2-hydrazineylthiazole (*o*-1)

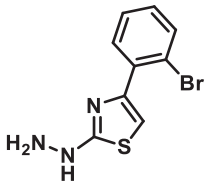

***o*-1**

A solution of a thiosemicarbazide (**45**; 295 mg, 3.24 mmol, 1.5 eq) and 2-bromo-1-(2-bromophenyl)ethan-1-one (**47**; 600 mg, 2.16 mmol, 1 eq) in anhydrous methanol (4 mL) was pre-stirred in a sealed vessel for 5 min under argon atmosphere and then heated up by microwave irradiation at 90 ºC for 20 min. The reaction mixture was cooled down and the solvent was reduced under vacuum to give compound ***o*-1** as a brown solid. [238] The product was brought to the next reaction without further purification and matched with the reported spectra data. [259] **HRMS** *m/z* calc. for $C_9H_8BrN_3S$ $[M+H]^+$ = 269.9620, found 269.9698.

N'-(4-(2-Bromophenyl)thiazol-2-yl)propionohydrazide (*o*-2)

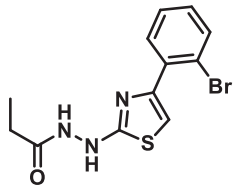

***o*-2**

To a cooled solution (0 ºC) of 4-(2-bromophenyl)-2-hydrazineylthiazole (***o*-1**; 683 mg, 2.53 mmol, 1 eq) in THF (3.6 mL) was added dropwise a solution of propionyl chloride (**41**; 0.3 mL, 2.86 mmol, 1.1 eq) in THF (3.6 mL). The reaction mixture was stirred at 0 ºC for 30 min and the precipitate formed was collected by filtration and washed with cold water to give ***o*-2** as a white solid. [249] The product was brought to the next reaction without further purification.

5-(2-Bromophenyl)-3-ethylthiazolo[2,3-*c*][1,2,4]triazole (AS-11)

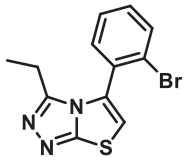

AS-11

A mixture of *N*'-(4-(2-bromophenyl)thiazol-2-yl)propionohydrazide (***o*-2**; 853 mg, 2.61 mmol) and phosphoryl chloride (4.3 mL, 46.91 mmol, 18 eq) was heated under microwave irradiation at 150 ºC for 150 min. The mixture was cooled to room temperature and quenched with crushed ice and cold water. Then, the organic layer was washed with AcOEt and water, dried over Na_2SO_4, filtered, and concentrated. The crude was purified with reverse-phase column chromatography (35 % CH_3CN in 0.1 % aq. HCO_2H), to give **AS-11** as a brown solid (251 mg, **16 %** overall yield). [241] **HRMS** *m/z* calc. for $C_{12}H_{10}BrN_3S$ [M+H]+ = 307.9852, found 307.9846. **^{1}H NMR** (400 MHz, $CDCl_3$) δ 1.14 (t, *J* = 7.5 Hz, 3H), 2.30 (q, *J* = 7.8 Hz, 1H), 2.57 (q, *J* = 7.9 Hz, 1H), 6.79 (s, 1H), 7.44 – 7.49 (m, 3H), 7.74 (d, *J* = 6.5 Hz, 1H). **^{13}C NMR** (101 MHz, $CDCl_3$) δ 12.2, 19.1, 118.1, 125.0, 129.3, 129.4, 129.8, 133.6, 133.8, 134.1, 150.3, 157.8.

4-(3-Bromo-5-methylphenyl)-2-hydrazineylthiazole (*m*-3)

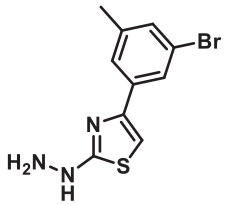

***m*-3**

A solution of a thiosemicarbazide (**45**; 250 mg, 2.74 mmol, 1 eq) and 2-bromo-1-(3-bromo-5-methylphenyl)ethan-1-one (**48**; 801 mg, 2.74 mmol, 1 eq) in dioxane (5 mL) stirred at room temperature overnight. The precipitate of hydrobromide salt was filtered and washed with cold dioxane and, basified with 2N Na_2CO_3 to give ***m*-3**. The product was filtered, washed with ddH_2O, dried and brought to the next step without further purification. [237]

N'-(4-(3-Bromo-5-methylphenyl)thiazol-2-yl)propionohydrazide (*m*-4)

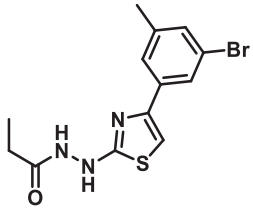

***m*-4**

To a cooled solution (0 ºC) of 4-(3-bromo-5-methylphenyl)-2-hydrazineylthiazole (***m*-3**; 596 mg, 2.10 mmol, 1 eq) in THF (3 mL) was added dropwise a solution of propionyl chloride (**41**; 0.2 mL, 2.38 mmol, 1.13 eq) in THF (3 mL). The reaction mixture was stirred at 0 ºC for 45 min and the precipitate formed was collected by filtration and washed with cold water to give ***m*-4** as a white solid. [249] The product was brought to the next reaction without further purification.

5-(3-Bromo-5-methylphenyl)-3-ethylthiazolo[2,3-*c*][1,2,4]triazole (AS-12)

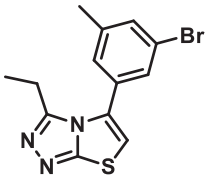

AS-12

A mixture of *N*'-(4-(3-bromo-5-methylphenyl)thiazol-2-yl)propionohydrazide (***m*-4; 160** mg, 0.47 mmol, 1 eq) in xylene (1.6 mL) and phosphoryl chloride (0.8 mL, 8.44 mmol, 18 eq) was heated at 130 ºC overnight. The mixture was cooled to room temperature and quenched with crushed ice and cold water. Then, the organic layer was washed with

AcOEt and water, dried over Na_2SO_4, filtered, and concentrated. The crude was purified with reverse-phase column chromatography (48 % CH_3CN in 0.1 % aq. HCO_2H) to give **AS-12** as a brown solid (43 mg, **10 %** overall yield). [240] **HRMS** *m/z* calc. for $C_{13}H_{12}BrN_3S$ $[M+H]^+$ = 322.0008, found 322.0012. **^{1}H NMR** (400 MHz, $CDCl_3$) δ 1.16 (t, *J* = 7.5 Hz, 3H), 2.42 (s, 3H), 2.59 (q, *J* = 7.5 Hz, 2H), 6.74 (s, 1H), 7.21 (s, 1H), 7.44 (s, 1H), 7.52 (s, 1H).

The ^{13}C NMR spectra of **AS-12** *was not acquired due to low yield and small quantity obtained from the reaction, and it will be assessed in the future.*

4-(5-Bromo-2-chlorophenyl)-2-hydrazineylthiazole (*o*-3)

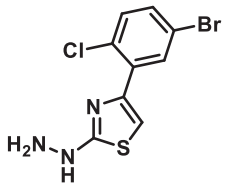

***o*-3**

A solution of a thiosemicarbazide (**45**; 193 mg, 2.11 mmol, 1 eq) and 2-bromo-1-(5-bromo-2-chlorophenyl)ethan-1-one (**49**; 660 mg, 2.11 mmol, 1 eq) in dioxane (4 mL) was stirred at room temperature overnight. The precipitate of hydrobromide salt was filtered and washed with cold dioxane and basified with 2N Na_2CO_3 to give ***o*-3**. The product was filtered, washed with ddH_2O, dried and brought to the next step without further purification. [237] **HRMS** *m/z* calc. for $C_9H_7BrClN_3S$ $[M+H]^+$ = 303.9305, found 303.9301.

N'-(4-(5-Bromo-2-chlorophenyl)thiazol-2-yl)propionohydrazide (*o*-4)

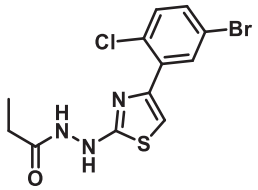

***o*-4**

To a cooled solution (0 ºC) of 4-(5-bromo-2-chlorophenyl)-2-hydrazineylthiazole (***o*-3**; 560 mg, 1.84 mmol, 1 eq) in THF (3.3 mL) was added dropwise a solution of propionyl chloride (**41**; 0.2 mL, 2.08 mmol, 1.1 eq) in THF (2 mL). The reaction mixture was stirred at 0 ºC for 45 min and the precipitate formed was collected by filtration and washed with cold water to give ***o*-4** as a white solid. [249] The product was brought to the next reaction without further purification. **HRMS** *m/z* calc. for $C_{12}H_{11}BrClN_3OS$ $[M+H]^+$ 359.9567; found 359.9576.

5-(5-Bromo-2-chlorophenyl)-3-ethylthiazolo[2,3-*c*][1,2,4]triazole (AS-13)

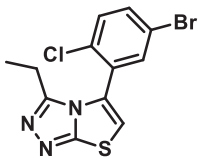

AS-13

A mixture of *N*'-(4-(5-bromo-2-chlorophenyl)thiazol-2-yl)propionohydrazide (***o*-4**; 587 mg, 1.72 mmol, 1 eq) and phosphoryl chloride (2.7 mL, 29.21 mmol, 18 eq) was heated under microwave irradiation at 150 ºC for 150 min. The mixture was cooled to room temperature and quenched with crushed ice and cold water. Then, the organic layer was washed with AcOEt and water, dried over Na_2SO_4, filtered, and concentrated. The crude was purified with reverse-phase column chromatography (51 % CH_3CN in 0.1 % aq. HCO_2H) to give **AS-13** as a brown solid (29 mg, **4 %** overall yield). [241] **HRMS** *m/z* calc. for $C_{12}H_9BrClN_3S$ $[M+H]^+$ = 341.9462, found 341.9465. **^{1}H NMR** (400 MHz, $CDCl_3$) δ 1.19 (t, *J* = 7.5 Hz, 3H), 2.33 – 2.65 (m, 2H), 6.84 (s, 1H), 7.44 (d, *J* = 8.4 Hz, 1H), 7.62 – 7.68 (m, 2H).**^{13}C NMR** (101 MHz, $CDCl_3$) δ 11.4, 19.0, 116.5, 120.9, 126.2, 129.7, 131.5, 134.3, 135.2, 135.3, 149.6, 157.2.

Synthesis of SSR4 and SSR12 amine- derivatives

General procedure for amine-derivatives AS-1, AS-5 and SSR12

A solution of **AS-10** (1 eq), Cs_2CO_3 (2 eq) and the amine (1.5 eq) in dry DMF (0.32 M) in a 5 mL Pyrex microwave process vial, were degassed by bubbling argon through the mixture for 15 min. Then, XantPhos (0.1 eq) and Pd_2dba_3 (0.05 eq) were added, and the mixture was kept under argon for 15 more minutes. Afterwards, the mixture was heated at 153 ºC for 150 min under microwave conditions or left overnight. Then, the organic layer was washed with AcOEt and water, dried over Na_2SO_4, filtered, and concentrated. All compounds were purified by reverse-phase column chromatography. [248]

N-[2-(Difluoromethoxy)phenyl]-3-{3-ethyl-[1,2,4]triazolo[3,4-*b*][1,3]thiazol-5-yl}aniline (SSR12)

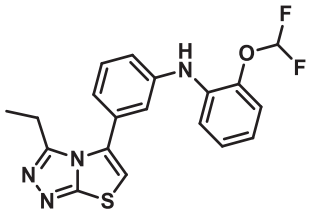

SSR12

Following the general procedure, a solution of 5-(3-bromophenyl)-3-ethylthiazolo[2,3-*c*][1,2,4]triazole (**AS-10**; 149.00 mg, 0.48 mmol, 1 eq), Cs_2CO_3 (315 mg, 0.97 mmol, 2 eq), 2-(difluoromethoxy)aniline (**MN12**; 0.1 mL, 0.73 mmol, 1.5 eq) in DMF (1.5 mL, 0.32 M). Then, XantPhos (28 mg, 0.05 mmol, 0.1 eq) and Pd_2dba_3 (22 mg, 0.02 mmol, 0.05 eq) were added and it was heated to 153 ºC for 150 min under microwave conditions. The crude was purified with reverse- phase column chromatography (56 % CH_3CN in 0.1 % aq. HCO_2H) to give **SSR12** as a brown solid (17 mg, **9 %**). **HRMS** *m/z* calc. for $C_{19}H_{16}F_2N_4OS$ $[M+H]^+$ = 387.1086, found = 387.1095. **^{1}H NMR** (400 MHz, $CDCl_3$) δ 1.15 (t, *J* = 7.5 Hz, 3H), 2.64 (q, *J* = 7.5 Hz, 2H), 6.11 (bs, 1H), 6.54 (s, 1H), 6.73 (s, 1H), 6.96 (t, *J* = 7.8 Hz, 1H), 7.04 (d, *J* = 7.5 Hz, 1H), 7.13 – 7.20 (m, 3H), 7.27 (s, 1H), 7.35 (d, *J* = 8.0 Hz, 1H), 7.42 (t, *J* = 7.9 Hz, 1H). **^{13}C NMR** (101 MHz, $CDCl_3$) δ 11.7, 21.6, 113.9, 115.9, 116.6, 118.0, 120.4, 120.9, 121.8, 123.4, 126.4, 129.5, 131.2, 134.6, 140.3, 141.0, 143.0, 149.8, 157.7.

3-{3-Ethyl-[1,2,4]triazolo[3,4-b][1,3]thiazol-5-yl}-N-[2-(pyridin-2-yl)ethyl]aniline (AS-1)

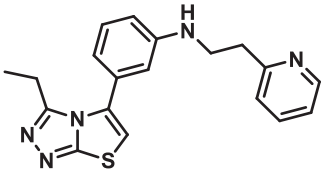

AS-1

Following the general procedure, a solution of 5-(3-bromophenyl)-3-ethylthiazolo[2,3-*c*][1,2,4]triazole (**AS-10**; 150 mg, 0.49 mmol, 1 eq), Cs_2CO_3 (317 mg, 0.97 mmol, 2 eq), 2-(pyridin-2-yl)ethan-1-amine (**MN1**; 0.1 mL, 0.73 mmol, 1.5 eq) in DMF (1.5 mL, 0.32 M). Then, XantPhos (28 mg, 0.05 mmol, 0.1 eq) and Pd_2dba_3 (22.00 mg, 0.02 mmol, 0.05 eq) were added and it was heated to 153 ºC for 150 min under microwave conditions. The crude was purified with reverse- phase column chromatography (60 % CH_3CN in 0.1 % aq. HCO_2H) to give **AS-1** as a brown solid (13 mg, **8 %**). **HRMS** *m/z* calc. for $C_{19}H_{19}N_5S$ $[M+H]^+$ = 350.1434, found 350.1439. **^{1}H NMR** (400 MHz, $CDCl_3$) δ 1.11 (t, *J* = 7.5 Hz, 3H), 2.63 (q, *J* = 7.5 Hz, 2H), 3.11 (t, *J* = 6.5 Hz, 2H), 3.55 (t, *J* = 6.6 Hz, 2H), 6.62 – 6.65 (m, 1H), 6.67 (s, 1H), 6.72 (d, *J* = 7.4 Hz, 1H), 6.76 (dd, *J* = 2.4, 8.3 Hz, 1H), 7.15 – 7.20 (m, 3H), 7.26 (d, *J* = 7.4 Hz, 1H), 7.60 – 7.65 (m, 1H), 8.56 (d, *J* = 4.9 Hz, 1H).

The 13C NMR spectra of AS-12 *is not acquired due to low yield and small quantity obtained from the reaction, and it will be assessed in the future.*

N-[2-(Difluoromethoxy)phenyl]-3-{3-ethyl-[1,2,4]triazolo[3,4-b][1,3]thiazol-5-yl}-5-methylaniline (AS-5)

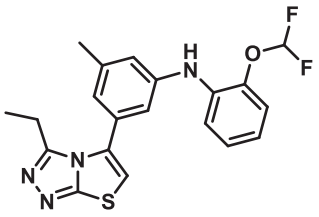

AS-5

Following the general procedure, a solution of 5-(3-bromo-5-methylphenyl)-3-ethylthiazolo[2,3-*c*][1,2,4]triazole (AS-12; 86 mg, 0.27 mmol, 1 eq), Cs_2CO_3 (173 mg, 0.53 mmol, 2 eq), 2-(difluoromethoxy)aniline (MN12; 0.1 mL, 0.40 mmol, 1.5 eq) in DMF (0.8 mL, 0.32 M). Then, XantPhos (15 mg, 0.03 mmol, 0.1 eq) and Pd_2dba_3 (12 mg, 0.01 mmol, 0.05 eq) were added and it was heated to 153 ºC for 150 min under microwave conditions. The crude was purified with reverse- phase column chromatography (60 % CH_3CN in 0.1 % aq. HCO_2H) to give AS-5 as a brown solid (10 mg, 9 %). HRMS *m/z* calc. for $C_{20}H_{18}F_2N_4OS$ $[M+H]^+$ = 401.1242, found 401.1243. ^{1}H NMR (400 MHz, $CDCl_3$) δ 1.16 (t, *J* = 7.5 Hz, 3H), 2.39 (s, 3H), 2.64 (q, *J* = 7.5 Hz, 2H), 6.06 (s, 1H), 6.53 (s, 1H), 6.70 (s, 1H), 6.86 (s, 1H), 6.92 – 6.97 (m, 1H), 6.98 (s, 1H), 7.07 (s, 1H), 7.12 – 7.18 (m, 2H), 7.33 (dd, *J* = 1.4, 7.2 Hz, 1H). ^{13}C NMR (101 MHz, $CDCl_3$) δ 11.7, 20.2, 21.6, 113.6, 114.0, 116.0, 116.6, 118.0, 119.2, 120.4, 120.9, 121.7, 123.4, 126.4, 129.6, 131.1, 134.7, 140.3, 140.9, 142.9.

6.3.1.2 NMR Spectra and HPLC / MS Report

5-(3-Bromophenyl)-3-ethylthiazolo[2,3-*c*][1,2,4]triazole (AS-10)

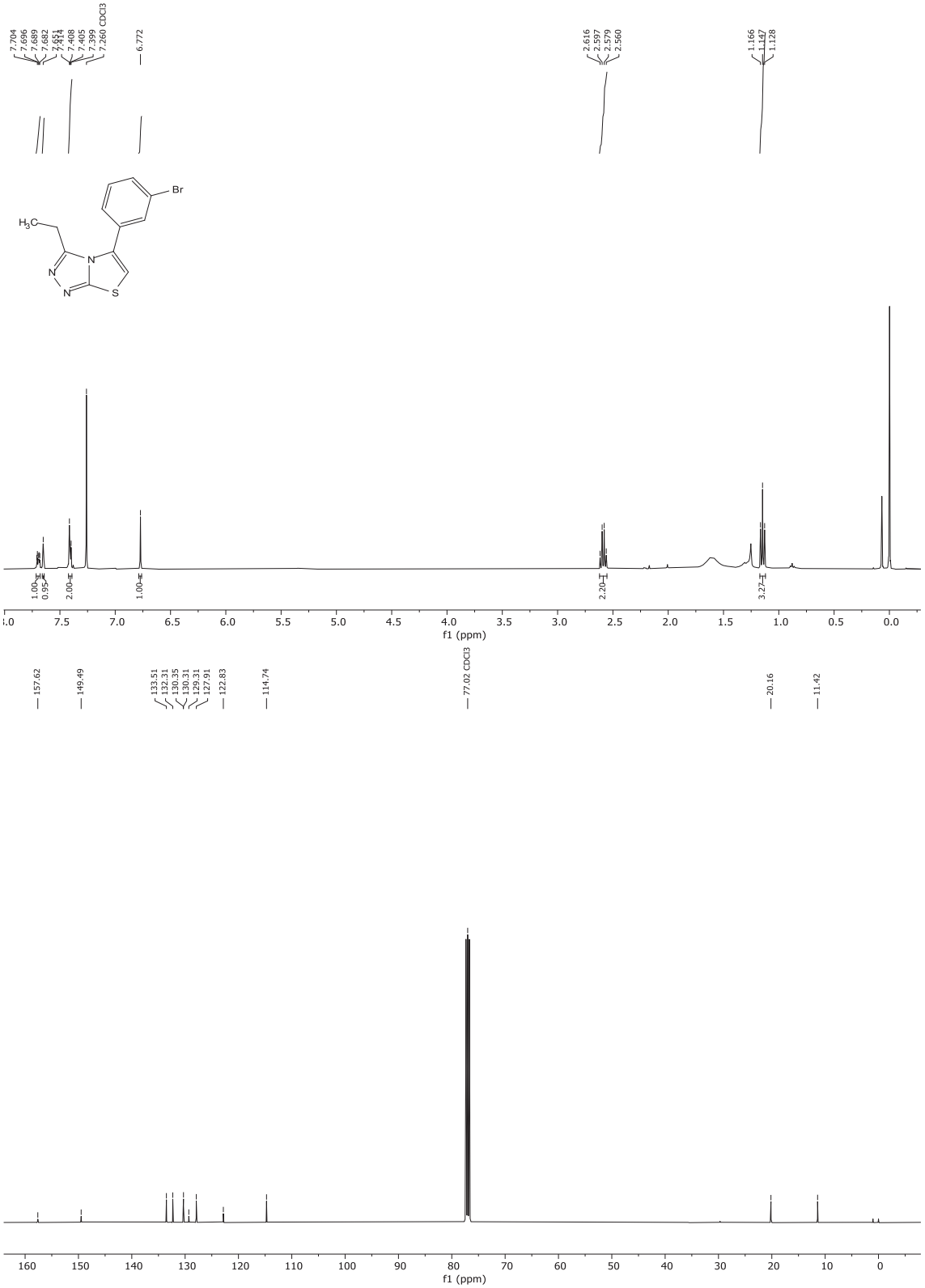

HPLC / MS AS-10

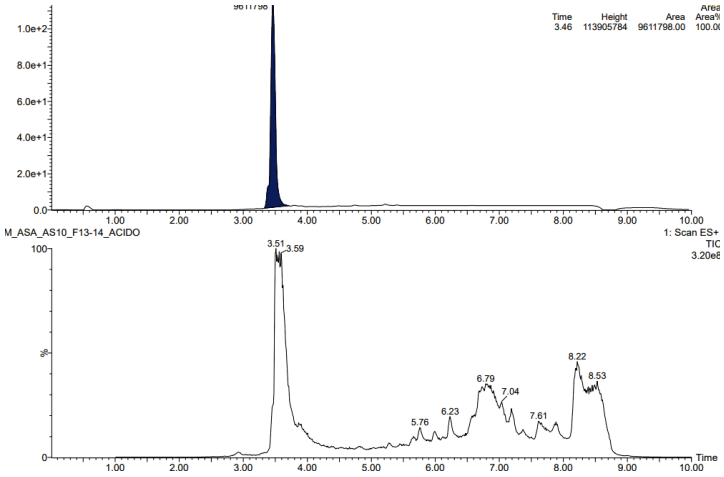

5-(2-Bromophenyl)-3-ethylthiazolo[2,3-*c*][1,2,4]triazole (AS-11)

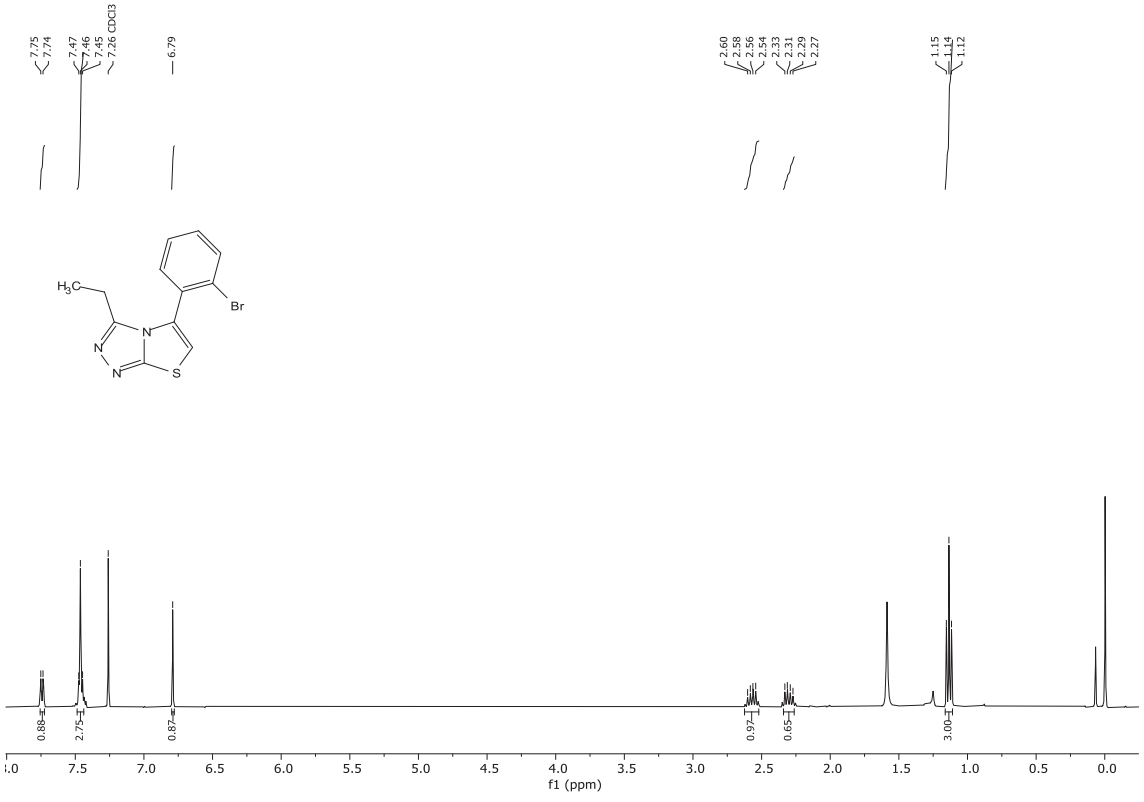

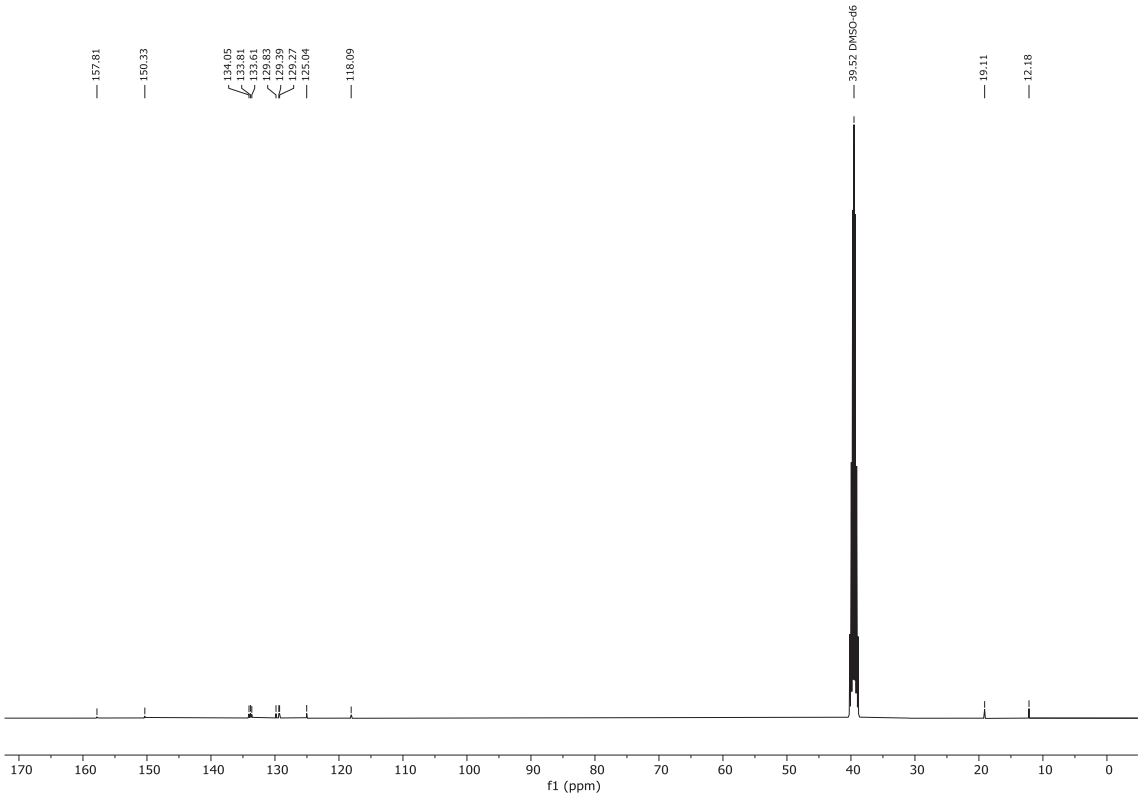
157.81
150.33
134.05
133.81
133.61
129.83
129.39
129.27
125.04
118.09
39.52 DMSO-d6
19.11
12.18
170 160 150 140 130 120 110 100 90 80 70 60 50 40 30 20 10 0
f1 (ppm)

HPLC / MS AS-11

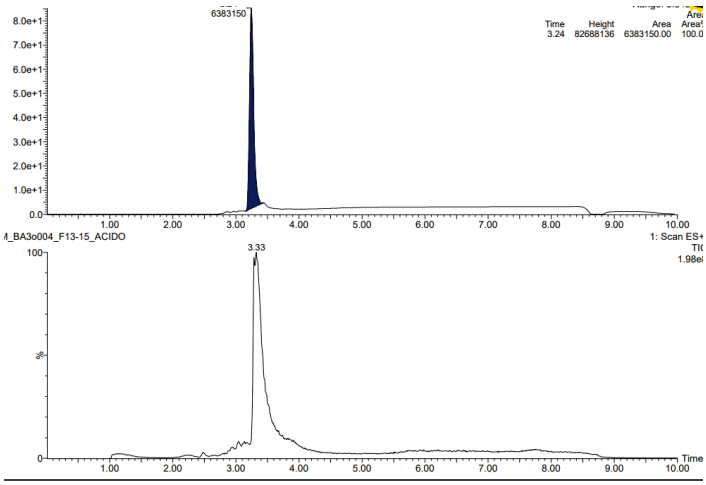
6383150
Time Height Area
3.24 82688136 6383150.00
1: Scan ES+
3.33
Time

5-(3-Bromo-5-methylphenyl)-3-ethylthiazolo[2,3-*c*][1,2,4]triazole (AS-12)

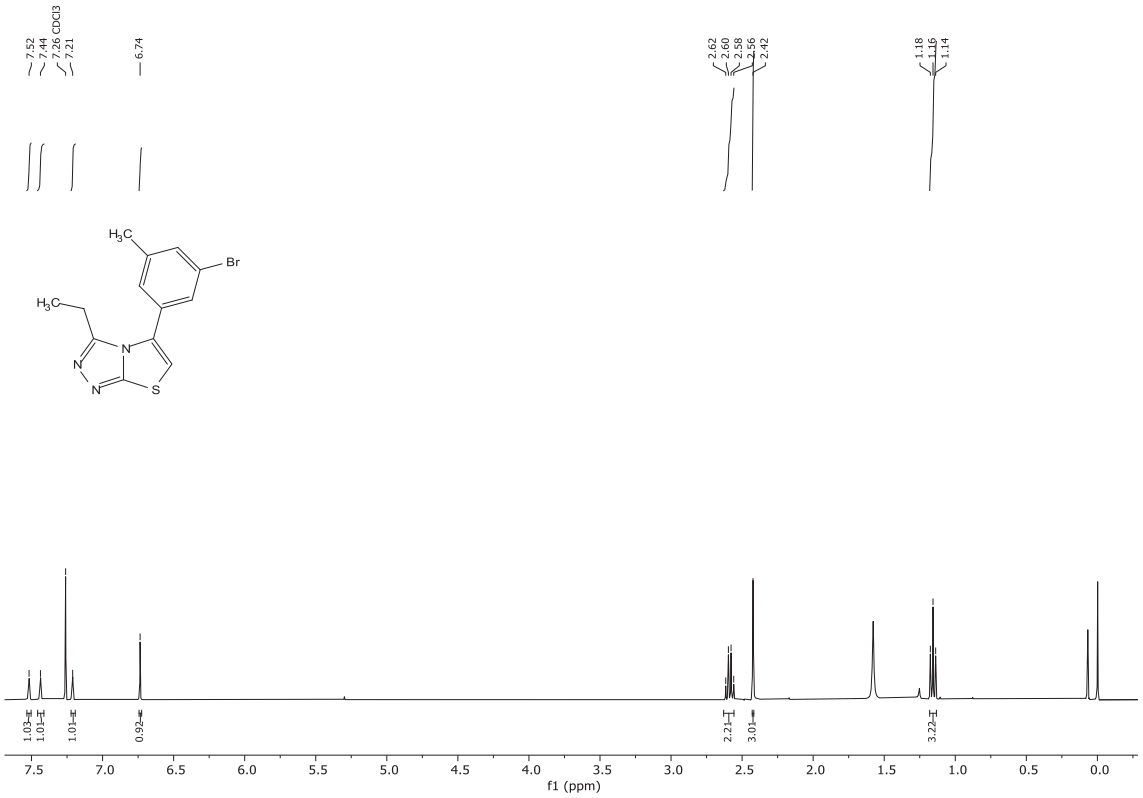

HPLC / MS AS-12

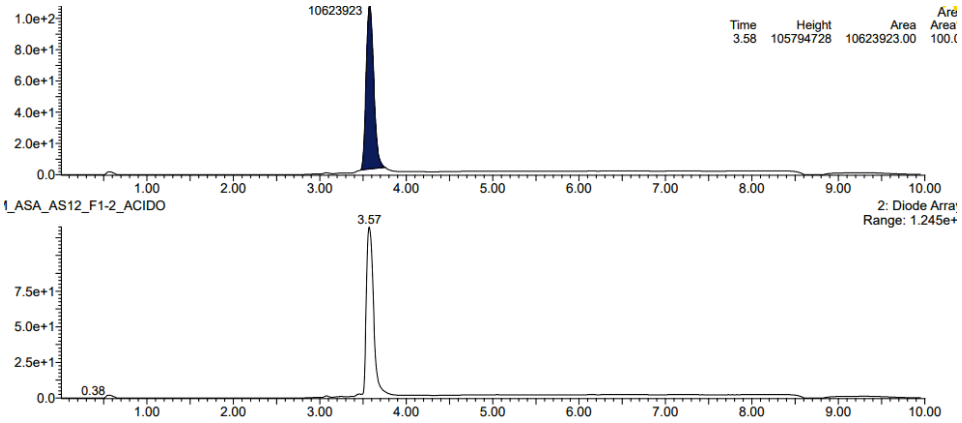

5-(5-Bromo-2-chlorophenyl)-3-ethylthiazolo[2,3-*c*][1,2,4]triazole (AS-13)

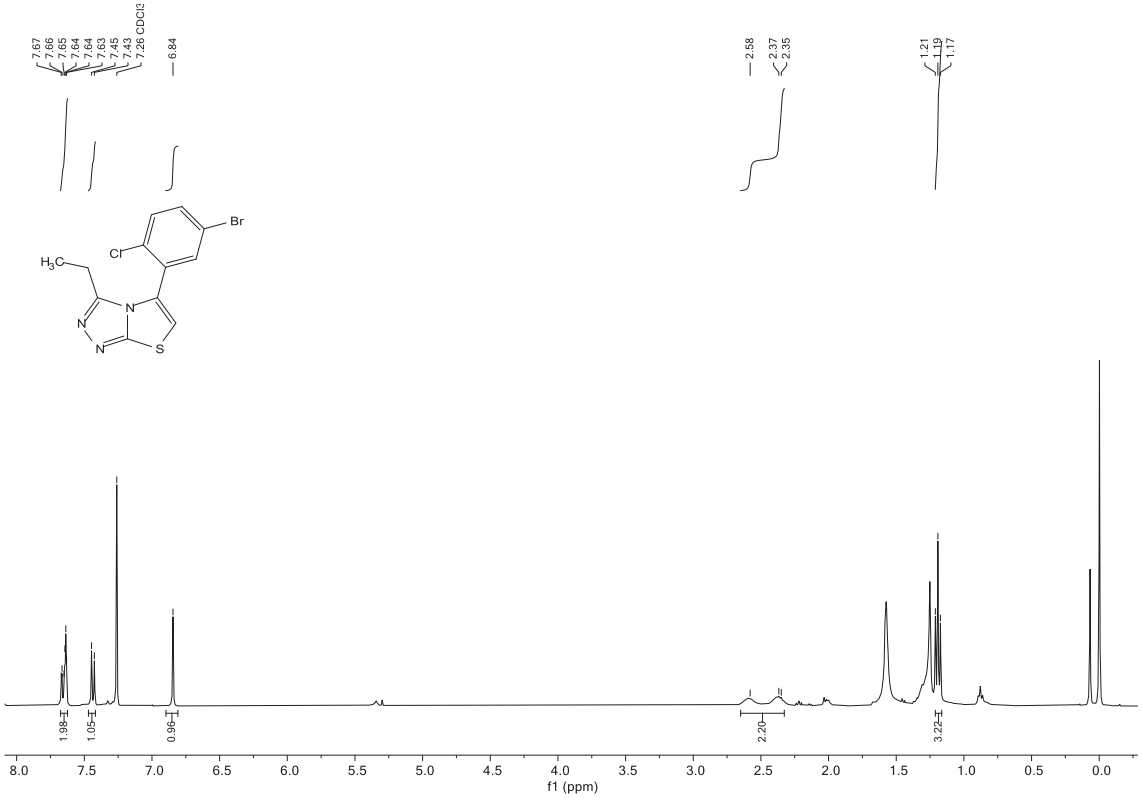

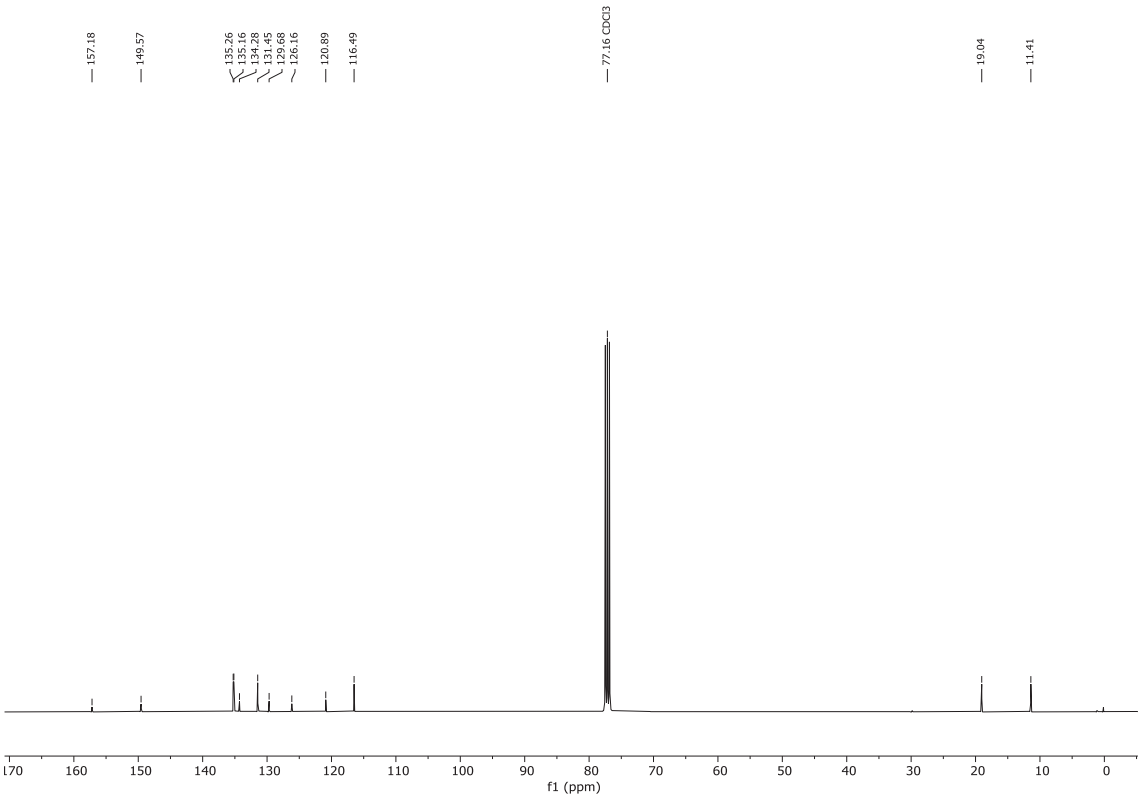

HPLC / MS AS-13

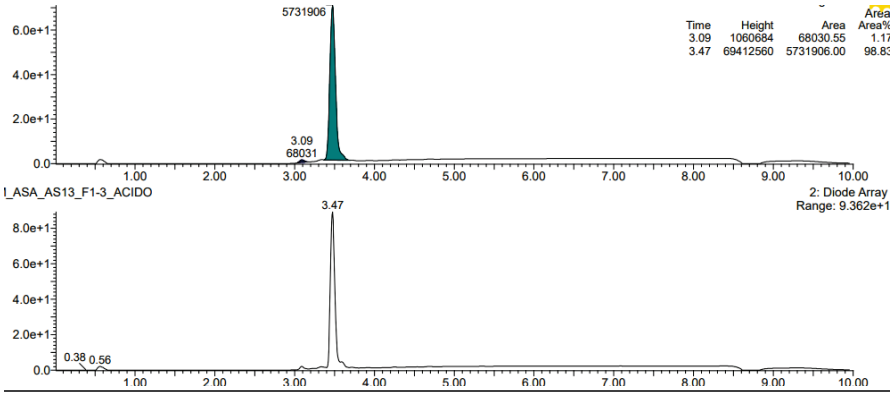

N-[2-(Difluoromethoxy)phenyl]-3-{3-ethyl-[1,2,4]triazolo[3,4-*b*][1,3]thiazol-5-yl}aniline (SSR12)

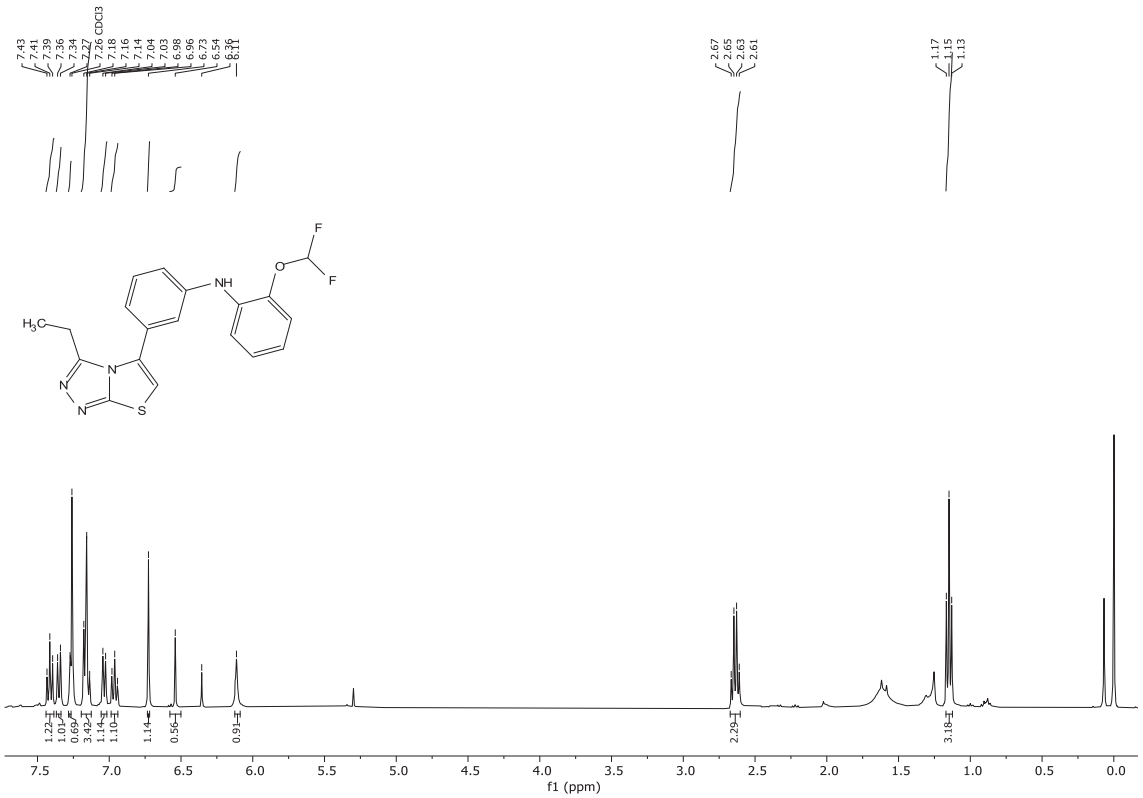

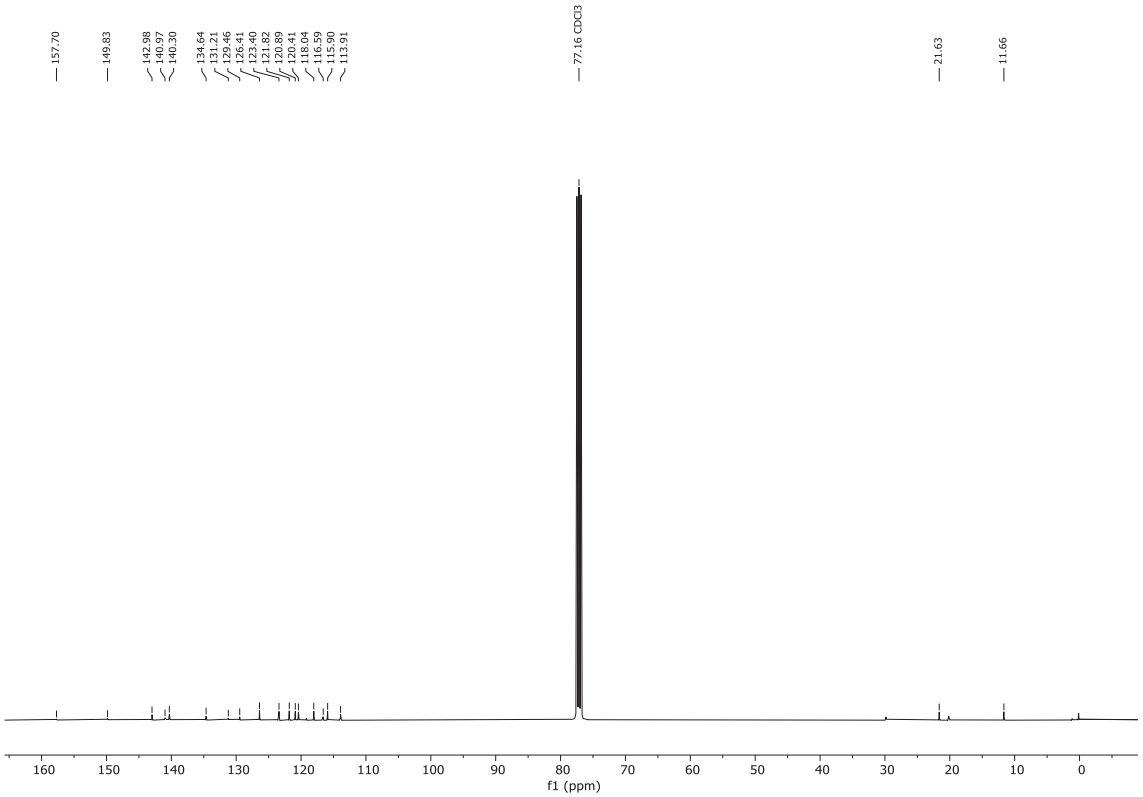

HPLC / MS SSR12

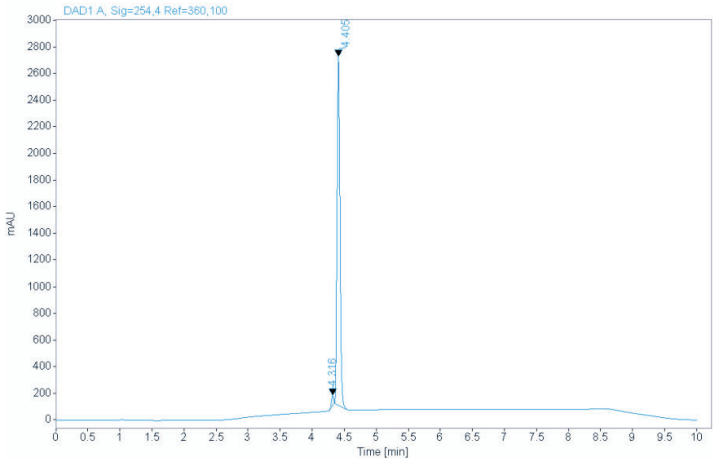

Signal: DAD1 A, Sig=254,4 Ref=360,100

RT [min]	Type	Width [min]	Area	Height	Area%	Name
4.316	BB	0.0394	198.9458	84.6337	2.3262	
4.405	BB	0.0511	8353.2686	2624.2983	97.6738	
		Sum	8552.2143			

3-{3-Ethyl-[1,2,4]triazolo[3,4-b][1,3]thiazol-5-yl}-N-[2-(pyridin-2-yl)ethyl]aniline (AS-1)

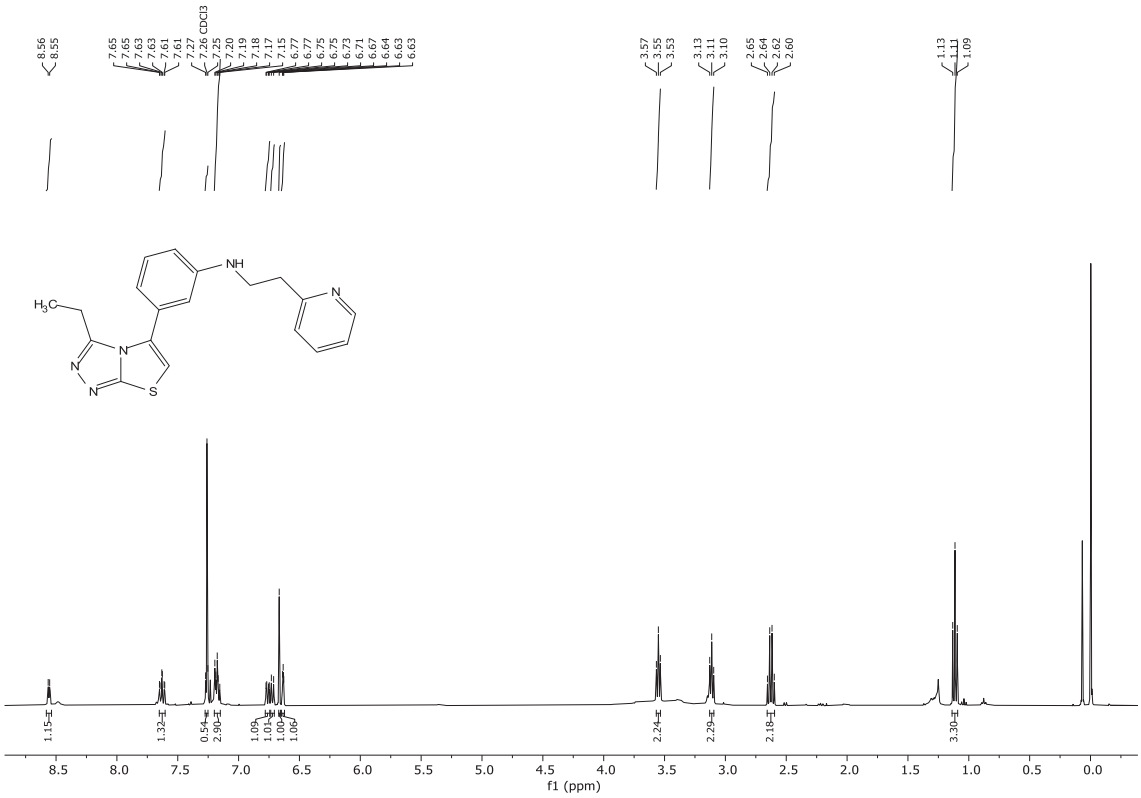

HPLC / MS AS-1

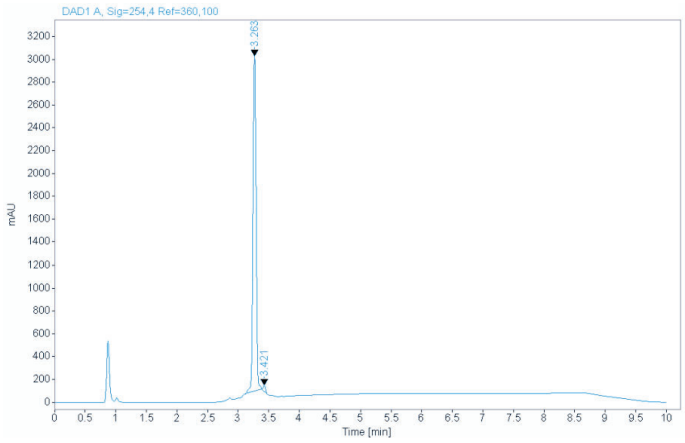

Signal: DAD1 A, Sig=254,4 Ref=360,100

RT [min]	Type	Width [min]	Area	Height	Area%	Name
3.263	BB	0.0573	10490.0010	2963.1140	98.7346	
3.421	BB	0.0423	134.4469	51.8100	1.2654	
		Sum	10624.4479			

N-[2-(Difluoromethoxy)phenyl]-3-{3-ethyl-[1,2,4]triazolo[3,4-b][1,3]thiazol-5-yl}-5-methylaniline (AS-5)

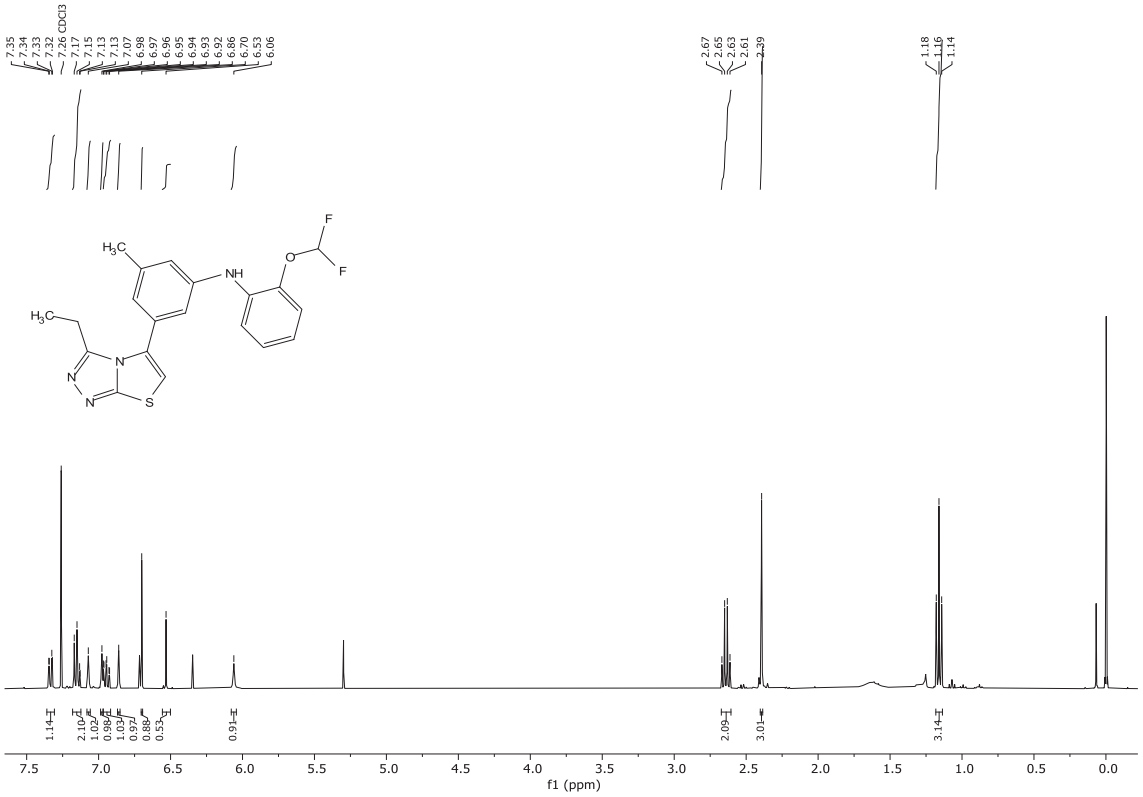

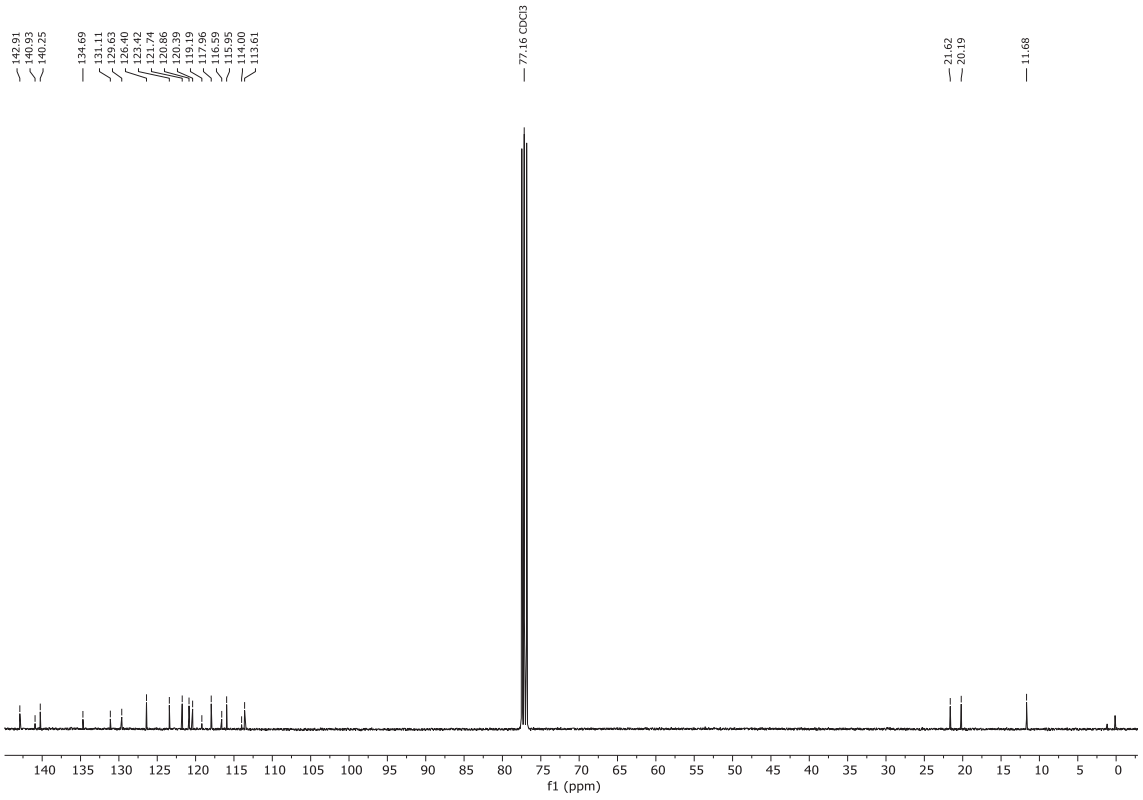

HPLC / MS AS-5

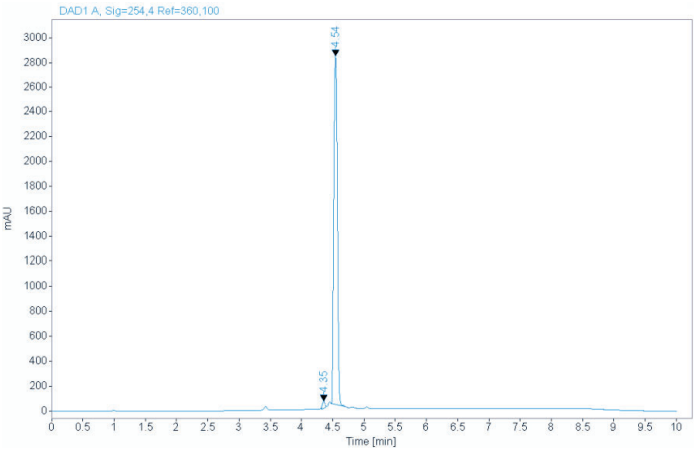

Signal: DAD1 A, Sig=254,4 Ref=360,100

RT [min]	Type	Width [min]	Area	Height	Area%	Name
4.350	MM	0.0454	170.0798	62.3799	1.4944	
4.540	BB	0.0664	11210.7559	2816.4949	98.5056	
		Sum	11380.8357			

6.3.2 Biophysical techniques

6.3.2.1 Time Resolved- Förster Resonance Energy Transfer (TR-FRET) Assay

The TR-FRET competitive binding assay (**Box 4**) is used to measure the disruption of the interaction between Brd4(BD1) and an acetylated [Lys(Ac)5/8/12/16]-Histone H4 (1-21)-GGK(Biotin) (Eurogentec) with the synthesized compounds. FRET is often referred to as a "molecular ruler" because it provides a simple yet precise way to measure nanometer-scale distances and conformational changes within or between macromolecules. This makes it particularly useful for studying protein-protein interactions and structural dynamics. TR-FRET is frequently used in drug discovery due to its robustness, medium throughput, and ability to provide detailed insights into ligand-receptor binding and protein interactions. [260, 261]

Box 4: Principle of TR-FRET Assay

Fluorescence Resonance Energy Transfer (FRET) is a powerful technique widely used to investigate dynamic interactions between proteins and various biochemical signaling events using specialized biosensors. The method relies on the non-radiative transfer of energy from an excited donor fluorophore to an acceptor fluorophore. This energy transfer results in the emission of fluorescence from the acceptor, which is measured to provide information about molecular interaction. For energy transfer to occur in FRET, the donor and acceptor fluorophores must be in close proximity, typically within 10 nm, as the efficiency of FRET is inversely proportional to the sixth power of the distance between them. Additionally, the relative orientation of the fluorophores must permit dipole-dipole coupling. A parallel alignment allows for maximum transfer efficiency (100%), while a perpendicular alignment results in no energy transfer.

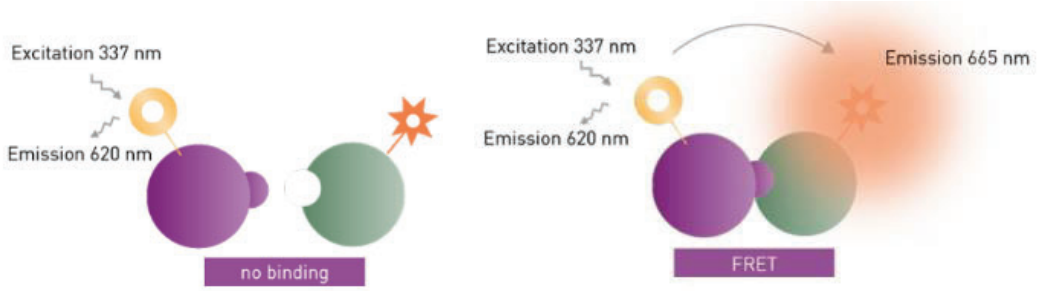

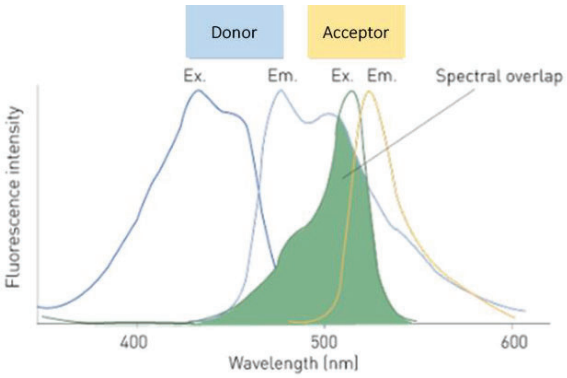

Schematic representation of FRET: in case of no- binding and binding (TR-FRET takes place, the acceptor emits light at a different wavelength and the emission intensity of the donor is quenched). Optical spectra of donor emission spectrum which overlaps with the acceptor excitation spectrum (spectral overlap).

TR-FRET (Time-Resolved FRET) is a variation of FRET that improves signal sensitivity and reduces background noise by introducing a time delay before fluorescence measurement. This technique uses lanthanide- based donors, such as europium or terbium complexes, which have long-lived excited states. The delayed measurement ensures that only signals from the donor-acceptor pairs are detected, excluding short-lived background fluorescence. [258, 259]

Protocol

The TR-FRET experiments were performed using a CLARIOstar (BMG Labtech) plate reader using the homogeneous time-resolved fluorescence module (excitation, 337 nm with 200 flashes; emission, 620 and 665 nm). The compound screening is carried out in 384- well, white, round bottom, small volume plates (CORNING) in a final volume of 20 µL of 52 mM HEPES (pH 7.4), 52 mM NaCl, 400 mM KF (Sigma), 0.5 mM CHAPS (Sigma) and 0.05 % BSA (Sigma). The His-tagged Brd4(BD1) (100 nM) is mixed with the biotin-labeled histone peptide (Eurogentec) (200 nM) and incubated for 10 min at RT. The labeled anti-His6-XL665 antibody (CisBio) (10 nM) is added to the mixture and incubated for 15 min at RT. Then, the Eu^{3+} cryptate-conjugated streptavidin (2 nM) (CisBio) is added and incubated for 15 min at room temperature. Compounds are titrated at 16 different serial dilution concentrations (from 0.1 nM to 10 mM) by duplicate. They are prepared in 250 mM Hepes (pH= 7.4), 250 mM NaCl, 1 % BSA at 20 % DMSO and added to the solution to a final concentration of 1 % DMSO in a total well volume of 20 µl and incubated for 90 minutes. Inhibition (%) is calculated with the following formula:

$$100 \times \left[1 - \frac{competitor\ FRET\ ratio\ \frac{665}{620} - FRET\ ratio\ \frac{665}{620}\ of\ the\ negative\ control}{FRET\ ratio\ \frac{665}{620}\ of\ the\ positive\ control - FRET\ ratio\ \frac{665}{620}\ of\ the\ negative\ control}\right]$$

where negative control is run without Brd4(BD1) and compound (inhibitor) and positive control without compound to give the bottom signal and top signal, respectively. The titration of (+)-JQ1 is used as a positive control for each experiment. The 665 nm / 620 nm ratios are converted to % normalized TR-FRET ratio (top signal equals 100 % and bottom signal equals 0 %). Compounds' concentrations are plotted against the mean normalized response data. IC_{50} values are calculated by plotting the log [competitor/compound] *vs* mean normalized response data from a single experiment measured in duplicates and fitting to an equation with standard Hill slope using GraphPad Prism software (v10.1.1).

CHAPTER 7
Bibliography

7. CHAPTER 7: BIBLIOGRAPHY

1. Rosa AC, Mio M, Andreadou I, Sumbayev VV. The challenge of new therapeutic approaches for unmet therapeutic needs. *Front Pharmacol*. 2020;*11*:1341.
2. Kola I, Landis J. Can the pharmaceutical industry reduce attrition rates? *Nat Rev Drug Discov*. 2004;*3*:711–5.
3. Singh N, et al. Drug discovery and development: introduction to the general public and patient groups. *Front Drug Discov*. 2023;*3*.
4. Hughes JP, Rees S, Kalindjian SB, Philpott KL. Principles of early drug discovery. *Br J Pharmacol*. 2010;*162*:1239–49.
5. Macarron R, et al. Impact of high-throughput screening in biomedical research. *Nat Rev Drug Discov*. 2011;*10*:188–95.
6. Congreve M, et al. Recent developments in fragment-based drug discovery. *J Med Chem*. 2008;*51*:3661–80.
7. Vemula D, et al. CADD, AI and ML in drug discovery: A comprehensive review. *Eur J Pharm Sci*. 2023;*181*:106324.
8. Keseru GM, Makara GM. Hit discovery and hit-to-lead approaches. *Drug Discov Today*. 2006;*11*:741–8.
9. Mohs RC, Greig NH. Drug discovery and development: Role of basic biological research. *Alzheimers Dement (N Y)*. 2017;*3*:651–7.
10. Kandi V, Vadakedath S. Clinical trials and clinical research: A comprehensive review. *Cureus*. 2023;*15*:e35077.
11. Kana O, Brylinski M. Elucidating the druggability of the human proteome with eFindSite. *J Comput Aided Mol Des*. 2019;*33*:509–19.
12. Lander ES, Linton LM, Birren B, et al. Initial sequencing and analysis of the human genome. *Nature*. 2001;*409*:860–921.
13. Hopkins AL, Groom CR. The druggable genome. *Nat Rev Drug Discov*. 2002;*1*:727–30.
14. Brown D, Superti-Furga G. Rediscovering the sweet spot in drug discovery. *Drug Discov Today*. 2003;*8*:1067–77.
15. Bohacek RS, McMartin C, Guida WC. The art and practice of structure-based drug design: a molecular modeling perspective. *Med Res Rev*. 1996;*16*:3–50.
16. Luttens A, Vo DD, Scaletti ER, et al. *Nat Commun*. 2025;*16*(1):1741.
17. Lipinski CA, Lombardo F, Dominy BW, Feeney PJ. Experimental and computational approaches to estimate solubility and permeability in drug discovery and development settings. *Adv Drug Deliv Rev*. 2001;*46*:3–26.
18. Abi Hussein, H., Geneix, C., Petitjean, M., Borrel, A., Flatters, D. & Camproux, A. C. Global vision of druggability issues: applications and perspectives. *Drug Discov Today*. 2017;*22*:404–15.
19. Doak, B. C., Over, B., Giordanetto, F. & Kihlberg, J. Oral druggable space beyond the rule of 5: Insights from drugs and clinical candidates. *Chem. Biol.* 2014; *21*:1115–1142.

20. Egbert, M., Whitty, A., Keserű, G. M. & Vajda, S. Why Some Targets Benefit from beyond Rule of Five Drugs. *J. Med. Chem.* 2019; *62*:10005–10025.
21. Doak, B. C., Zheng, J., Dobritzsch, D. & Kihlberg, J. How beyond Rule of 5 drugs and clinical candidates bind to their targets. *J. Med. Chem.* 2016; *59*:2312–2327.
22. Edfeldt FNB, Folmer RH, Breeze AL. Fragment screening to predict druggability (ligandability) and lead discovery success. *Drug Discov Today*. 2011;*16*:284–7.
23. Verdine GL, Walensky LD. The challenge of drugging undruggable targets in cancer: lessons learned from targeting BCL-2 family members. *Clin Cancer Res*. 2007;*13*:7264–70.
24. Dang CV, Reddy EP, Shokat KM, Soucek L. Drugging the 'undruggable' cancer targets. *Nat Rev Cancer*. 2017;*17*:502–8.
25. Huang L, et al. KRAS mutation: from undruggable to druggable in cancer. *Signal Transduct Target Ther*. 2021;*6*:386.
26. Oprea TI, et al. Unexplored therapeutic opportunities in the human genome. *Nat Rev Drug Discov*. 2018;*17*:317–32.
27. Xie X, Yu T, Li X, et al. Recent advances in targeting the "undruggable" proteins: from drug discovery to clinical trials. *Signal Transduct Target Ther*. 2023;*8*:335.
28. Lazo JS, Sharlow ER. Drugging undruggable molecular cancer targets. *Annu Rev Pharmacol Toxicol*. 2016;*56*:23–40.
29. Blair HA. Sotorasib: first approval. *Drugs*. 2021;*81*:1573–9.
30. Varmus HE. Oncogenes and transcriptional control. *Science*. 1987;*238*:1337–9.
31. Brivanlou AH, Darnell JE. Signal transduction and the control of gene expression. *Science*. 2002;*295*:813–8.
32. Lambert SA, et al. The human transcription factors. *Cell*. 2018;*172*:650–65.
33. Lee TI, Young RA. Transcriptional regulation and its misregulation in disease. *Cell*. 2013;*152*:1237–51.
34. Darnell JE. Transcription factors as targets for cancer therapy. *Nat Rev Cancer*. 2002;*2*:740–9.
35. Liu J, et al. Intrinsic disorder in transcription factors. *Biochemistry*. 2006;*45*:6873–88.
36. Voss TC, Hager GL. Dynamic regulation of transcriptional states by chromatin and transcription factors. *Nat Rev Genet*. 2014;*15*:69–81
37. Ptashne M, Gann A. Transcriptional activation by recruitment. *Nature*. 1997;*386*:569–77.
38. Vaquerizas JM, Kummerfeld SK, Teichmann SA, Luscombe NM. A census of human transcription factors: function, expression and evolution. *Nat Rev Genet*. 2009;*10*:252–63.
39. Loh CY, et al. Signal transducer and activator of transcription (STATs) proteins in cancer and inflammation: functions and therapeutic implication. *Front Oncol*. 2019;*9*:48

40. McEwan IJ. In: McEwan IJ, editor. The Nuclear Receptor Superfamily. Vol. *1443*. Humana; 2016. p. 3–9.
41. Jones S. An overview of the basic helix–loop–helix proteins. *Genome Biol*. 2004;*5*:226.
42. Boija A, et al. Transcription factors activate genes through the phase-separation capacity of their activation domains. *Cell*. 2018;*175*:1842–56.e16
43. Henley MJ, Koehler AN. Advances in targeting 'undruggable' transcription factors with small molecules. *Nat Rev Drug Discov*. 2021;*20*:669–88.
44. Sabari BR, et al. Coactivator condensation at super-enhancers links phase separation and gene control. *Science*. 2018;*361*:eaar3958.
45. Goldstein I, Hager GL. Dynamic enhancer function in the chromatin context: dynamic mechanism for enhancer activation. *Wiley Interdiscip Rev Syst Biol Med*. 2018;*10*:e1390.
46. Darnell JE Jr. Transcription factors as targets for cancer therapy. *Nat Rev Cancer*. 2002;*2*:740–9.
47. Downward J. Targeting RAS signalling pathways in cancer therapy. *Nat Rev Cancer*. 2003;*3*:11–22.
48. Cardenas MG, et al. The expanding role of the BCL6 oncoprotein as a cancer therapeutic target. *Clin Cancer Res*. 2017;*23*:885–93
49. Bradner JE, Hnisz D, Young RA. Transcriptional addiction in cancer. *Cell*. 2017;*168*:629–43.
50. Schuijers J, et al. Transcriptional dysregulation of MYC reveals common enhancer-docking mechanism. *Cell Rep*. 2018;*23*:349–360.
51. Tsherniak A, et al. Defining a cancer dependency map. *Cell*. 2017;*170*:564–576.e16.
52. Galdeano, C., Gadd, M. S., Soares, P., Scaffidi, S., Van Molle, I., Birced, I., Hewitt, S., Dias, D. M. & Ciulli. Structure-guided design and optimization of small molecules targeting the protein-protein interaction between the von Hippel–Lindau (VHL) E3 ubiquitin ligase and the hypoxia-inducible factor (HIF) alpha subunit with in vitro nanomolar affinities. *J Med Chem*. 2014;*57*:8657–8663.
53. Gronemeyer H, Gustafsson J-Å, Laudet V. Principles for modulation of the nuclear receptor superfamily. *Nat Rev Drug Discov*. 2004;*3*:950–964.
54. Wang DJ, et al. New generation of selective androgen receptor degraders: our initial design, synthesis, and biological evaluation of new compounds with enzalutamide-resistant prostate cancer activity. *N Engl J Med*. 2014;*371*:1028–1038.
55. Leung CH, et al. DNA-binding small molecules as inhibitors of transcription factors. *Med Res Rev*. 2013;*33*:823–846.
56. Li H, Ban F, Dalal K, Leblanc E, Frewin K, Ma D, et al. Discovery of small-molecule inhibitors selectively targeting the DNA-binding domain of the human androgen receptor. *J Med Chem*. 2014;*57*:6458–6467.

57. Huang W, Dong Z, Wang F, Peng H, Liu JY, Zhang JT. A small molecule compound targeting STAT3 DNA-binding domain inhibits cancer cell proliferation, migration, and invasion. *ACS Chem Biol*. 2014;*9*:1188–1196.
58. Cheng SS, et al. The design and development of covalent protein-protein interaction inhibitors for cancer treatment. *J Hematol Oncol*. 2020;*13*:26.
59. Geppert T, et al. Context-based identification of protein-protein interfaces and "hot-spot" residues. *Chem Biol*. 2011;*18*:344–353.
60. Miklossy G, Hilliard TS, Turkson J. Therapeutic modulators of STAT signalling for human diseases. *Nat Rev Drug Discov*. 2013;*12*:611–629.
61. Struntz NB, et al. Stabilization of the Max homodimer with a small molecule attenuates Myc-driven transcription. *Cell Chem Biol*. 2019;*26*:711–723.e14.
62. Illendula A, et al. A small-molecule inhibitor of the aberrant transcription factor CBFβ–SMMHC delays leukemia in mice. *Science*. 2015;*347*:779–784.
63. Scheuermann TH, et al. Allosteric inhibition of hypoxia inducible factor-2 with small molecules. *Nat Chem Biol*. 2013;*9*:271–276.
64. Estrada-Ortiz N, Neochoritis CG, Dömling A. How to design a successful p53-MDM2/X interaction inhibitor: a thorough overview based on crystal structures. *ChemMedChem*. 2016;*11*:757–772.
65. Faivre EJ, et al. Selective inhibition of the BD2 bromodomain of BET proteins in prostate cancer. *Nature*. 2020;*578*:306–310.
66. Fowler T, et al. Regulation of MYC expression and differential JQ1 sensitivity in cancer cells. *PLoS One*. 2014;*9*:e87003.
67. Chipumuro E, et al. CDK7 inhibition suppresses super-enhancer-linked oncogenic transcription in MYCN-driven cancer. *Cell*. 2014;*159*:1126–1139.
68. Richters A, et al. Modulating androgen receptor-driven transcription in prostate cancer with selective CDK9 inhibitors. *Cell Chem Biol*. 2021;*28*:134–147.e14.
69. Lasko LM, et al. Discovery of a selective catalytic p300/CBP inhibitor that targets lineage-specific tumours. *Nature*. 2017;*550*:128–132.
70. Schick S, et al. Acute BAF perturbation causes immediate changes in chromatin accessibility. *Nat Genet*. 2021;*53*:269–278.
71. Wang F, et al. Advances in CRISPR-Cas systems for RNA targeting, tracking and editing. *Biotechnol. Adv.* 2019; *37*:708–729.
72. Xue Y, et al. Noncoding RNA: from dark matter to bright star. *Sci. China Life Sci.* 2020; *63*:463–468.
73. Ross SJ, et al. Targeting KRAS-dependent tumors with AZD4785, a high-affinity therapeutic antisense oligonucleotide inhibitor of KRAS. *Sci. Transl. Med.* 2017; *9*:eaal5253.
74. Thielmann M, et al. Teprasiran, a small interfering RNA, for the prevention of acute kidney injury in high-risk patients undergoing cardiac surgery: a randomized clinical study. *Circulation.* 2021; *144*:1133–1144.

75. McAndrews KM, et al. Exosome-mediated delivery of CRISPR/Cas9 for targeting of oncogenic Kras(G12D) in pancreatic cancer. *Life Sci Alliance.* 2021; *4*:e202000875.
76. Hershko A, Ciechanover A. THE UBIQUITIN SYSTEM. *Annu. Rev. Biochem.* 1998; *67*:425–79.
77. Bouvier C, Lawrence R, Cavallo F, Xolalpa W, Jordan A, Hjerpe R, Rodriguez MS. Breaking bad proteins—Discovery approaches and the road to clinic for degraders. *Cells.* 2024; *13*:578.
78. Burslem GM, Crews CM. Small-Molecule Modulation of Protein Homeostasis. *Chem. Rev.* 2017; *117*:11269–11301.
79. Krönke J, et al. Lenalidomide causes selective degradation of IKZF1 and IKZF3 in multiple myeloma cells. *Science*. 2014;*343*:301–305.
80. Lu G, et al. The myeloma drug lenalidomide promotes the cereblon-dependent destruction of Ikaros proteins. *Science*. 2014;*343*:305–309.
81. Lopez-Girona A, et al. Cereblon is a direct protein target for immunomodulatory and antiproliferative activities of lenalidomide and pomalidomide. *Leukemia.* 2012; *26*:2326–2335.
82. Chamberlain PP, et al. Structure of the human Cereblon–DDB1–lenalidomide complex reveals basis for responsiveness to thalidomide analogs. *Nat. Struct. Mol. Biol.* 2014; *21*:803–809.
83. Huang X, Dixit VM. Drugging the undruggables: exploring the ubiquitin system for drug development. *Cell Res.* 2016; *26*:484–498.
84. Sakamoto KM, et al. Protacs: Chimeric molecules that target proteins to the Skp1–Cullin–F box complex for ubiquitination and degradation. *Proc. Natl. Acad. Sci.* 2001; *98*:8554–8559.
85. Buckley DL, et al. Targeting the von Hippel–Lindau E3 Ubiquitin Ligase Using Small Molecules To Disrupt the VHL/HIF-1α Interaction. *J. Am. Chem. Soc.* 2012; *134*:4465–4468.
86. Buckley DL, et al. Small-Molecule Inhibitors of the Interaction between the E3 Ligase VHL and HIF1α. *Angew. Chem. Int. Ed.* 2012; *51*:11463–11467.
87. Zengerle, M., Chan, K.-H. & Ciulli, A. Selective Small Molecule Induced Degradation of the BET Bromodomain Protein BRD4. *ACS Chem. Biol.* 2015; *10*:1770–1777.
88. Winter, G. E. et al. Phthalimide conjugation as a strategy for in vivo target protein degradation. *Science.* 2015; *348*:1376–1381.
89. Bondeson, D. P. et al. Catalytic in vivo protein knockdown by small-molecule PROTACs. *Nat. Chem. Biol.* 2015; *11*:611–617.
90. Neklesa, T.; Snyder, L. B.; Willard, R. R.; Vitale, N.; Pizzano, J.; Gordon, D. A.; Bookbinder, M.; Macaluso, J.; Dong, H.; Ferraro, C.; Wang, G.; Wang, J.; Crews, C. M.; Houston, J.; Crew, A. P.; Taylor, I. ARV-110: an oral androgen receptor PROTAC degrader for prostate cancer; *ASCO-GU: San Francisco, California, USA*, 14−16 (2019).

91. Flanagan, J. J.; Qian, Y.; Gough, S. M.; Andreoli, M.; Bookbinder, M.; Cadelina, G.; Bradley, J.; Rousseau, E.; Chandler, J.; Willard, R.; Pizzano, J.; Crews, C. M.; Crew, A. P.; Taylor, I.; Houston, J. ARV-471, an oral estrogen receptor PROTAC protein degrader for breast cancer; *SABCS: San Antonio, Texas, USA* 4–8 (2018).
92. Mullard, A. First targeted protein degrader hits the clinic. *Nat. Rev. Drug Discov.* 2019; *18*:237–239.
93. Degorce, S. L. et al. Discovery of proteolysis-targeting chimera molecules that selectively degrade the IRAK3 pseudokinase. *J. Med. Chem.* 2020; *63*:10460–10473.
94. Donovan, K. A. et al. Mapping the degradable kinome provides a resource for expedited degrader development. *Cell.* 2020; *183*:1714–1731.e10.
95. Imaide, S. et al. Trivalent PROTACs enhance protein degradation via combined avidity and cooperativity. *Nat. Chem. Biol.* 2021; *17*:1157–1167.
96. Gadd, M. S. et al. Structural basis of PROTAC cooperative recognition for selective protein degradation. *Nat. Chem. Biol.* 2017; *13*:514–521.
97. Riching, K. M., Caine, E. A., Urh, M. & Daniels, D. L. The importance of cellular degradation kinetics for understanding mechanisms in targeted protein degradation. *Chem. Soc. Rev.* 2022; *51*:6210–6221.
98. Mares, A. et al. Extended pharmacodynamic responses observed upon PROTAC-mediated degradation of RIPK2. *Commun. Biol.* 2020; *3*:140.
99. Burslem, G. M. et al. The advantages of targeted protein degradation over inhibition: an RTK case study. *Cell Chem. Biol.* 2018; *25*:67–77. e3.
100. Popow, J. et al. Targeting cancer with small molecule pan-KRAS degraders. *Science.* 2024; *385*:6715.
101. Schreiber SL. The rise of molecular glues. *Cell*. 2021;*184*:3–9.
102. Hanan EJ, et al. Monomeric targeted protein degraders. *J Med Chem*. 2020;*63*:11330–11361.
103. Ohoka N, Misawa T, Kurihara M, Demizu Y, Naito M. Development of a peptide-based inducer of protein degradation targeting NOTCH1. *Bioorg Med Chem Lett*. 2017;*27*:4985–4988.
104. Słabicki M, et al. Small-molecule-induced polymerization triggers degradation of BCL6. *Nature*. 2020;*588*:164–168.
105. Dauvois S, Danielian PS, White R, Parker MG. Antiestrogen ICI 164,384 reduces cellular estrogen receptor content by increasing its turnover. *Proc Natl Acad Sci USA*. 1992;*89*:4037–4041.
106. Kaelin WG Jr. The von Hippel–Lindau tumour suppressor protein: O2 sensing and cancer. *Nat Rev Cancer*. 2008;*8*:865–873.
107. Ettmayer P, Ciulli A, et al. Targeting cancer with small-molecule pan-KRAS degraders. *Science*. 2024;*385*:1338–1347.
108. Li Y, Yang J, Aguilar A, McEachern D, Przybranowski S, Liu L, Yang CY, Wang M, Han X, Wang S. Discovery of MD-224 as a first-in-class, highly potent, and efficacious

proteolysis targeting chimera murine double minute 2 degrader capable of achieving complete and durable tumor regression. *J Med Chem*. 2019;*62*:448–66.

109. Bai L, Zhou H, Xu R, Zhao Y, Chinnaswamy K, McEachern D, Chen J, Yang CY, Liu Z, Wang M, Liu L, Sun D, Wang S. A potent and selective small-molecule degrader of STAT3 achieves complete tumor regression by promoting the degradation of oncogenic transcription factor STAT3. *J Med Chem*. 2018;*61*:4646–4660.
110. Liao, H. et al. A PROTAC peptide induces durable β-catenin degradation and suppresses Wnt-dependent intestinal cancer. *Cell Discov.* 2020; *6*:35.
111. Marei, H. et al. Antibody targeting of E3 ubiquitin ligases for receptor degradation. *Nature.* 2022; *610*:182–189.
112. Foley, K. P. et al. Abstract 971: Chaperone-mediated protein degradation (CHAMP): a novel technology for tumor-targeted protein degradation. *Cancer Res.* 2021; *81*:971–971.
113. Li, X. et al. Application of novel degraders employing autophagy for expediting medicinal research. *J. Med. Chem.* 2023; *66*:1700–1711.
114. Takahashi, D. et al. AUTACs: cargo-specific degraders using selective autophagy. *Mol. Cell.* 2019; *76*:797–810.e10.
115. Whitworth, C., & Ciulli, A. New class of molecule targets proteins outside cells for degradation. *Nature.* 2020; *584*:193-194.
116. Pei, J. et al. Targeting lysosomal degradation pathways: new strategies and techniques for drug discovery. *J. Med. Chem.* 2021; *64*:3493–3507.
117. Banik, S. M. et al. Lysosome-targeting chimaeras for degradation of extracellular proteins. *Nature.* 2020; *584*:291–297.
118. Shen, F., & Dassama, L.M.K. Opportunities and challenges of protein-based targeted protein degradation. *Chem. Sci.* 2023; *14*:8433–8447.
119. Henning, N. J. et al. Deubiquitinase-targeting chimeras for targeted protein stabilization. *Nat. Chem. Biol.* 2022; *18*:412–421.
120. Liu, J. et al. TF-DUBTACs stabilize tumor suppressor transcription factors. *J. Am. Chem. Soc.* 2022; *144*:12934–12941.
121. Dhanasekaran R, et al. The MYC oncogene — the grand orchestrator of cancer growth and immune evasion. *Nat Rev Clin Oncol*. 2022;*19*:23–36.
122. Vennstrom B, Sheiness D, Zabielski J, Bishop JM. Isolation and characterization of c-myc, a cellular homolog of the oncogene (v-myc) of avian myelocytomatosis virus strain 29. *J Virol*. 1982;*42*:773–9.
123. Blackwood EM, Eisenman RN. Max: A Helix-Loop-Helix Zipper Protein That Forms a Sequence-Specific DNA-Binding Complex with Myc. *Science*. 1991;*251*:1211–7.
124. Kim SY, Herbst A, Tworkowski KA, Salghetti SE, Tansey WP. Skp2 regulates Myc protein stability and activity. *Mol Cell*. 2003;*11*:1177–88.
125. Welcker M, Clurman BE. FBW7 ubiquitin ligase: a tumour suppressor at the crossroads of cell division, growth and differentiation. *Nat Rev Cancer*. 2008;*8*:83–93.

126. Yada M, et al. Phosphorylation-dependent degradation of c-Myc is mediated by the F-box protein Fbw7. *EMBO J*. 2004;*101*:9085–90.
127. Garralda E, et al. MYC targeting by OMO-103 in solid tumors: a phase 1 trial. *Nat Med*. 2024;*30*:762–71.
128. Madden SK, De Araujo AD, Gerhardt M, Fairlie DP, Mason JM. Taking the Myc out of cancer: toward therapeutic strategies to directly inhibit c-Myc. *Mol Cancer*. 2021;*20*:3.
129. Fletcher S, Prochownik EV. Small-molecule inhibitors of the Myc oncoprotein. *Biochim Biophys Acta BBA - Gene Regul Mech*. 2015;*1849*:525–43.
130. Berg T, Cohen SB, Desharnais J, Sonderegger C, Maslyar DJ, Goldberg J, Boger DL, Vogt PK. Small-molecule antagonists of Myc/Max dimerization inhibit Myc-induced transformation of chicken embryo fibroblasts. *Proc Natl Acad Sci U S A*. 2002;*99*:3830–5.
131. Shi J, Stover JS, Whitby LR, Vogt PK, Boger DL. Small molecule inhibitors of Myc/Max dimerization and Myc-induced cell transformation. *Bioorg Med Chem Lett*. 2009;*19*:6038–41.
132. Xu Y, Shi J, Yamamoto N, Moss JA, Vogt PK, Janda KD. A credit-card library approach for disrupting protein-protein interactions. *Bioorg Med Chem*. 2006;*14*:2660–73.
133. Kiessling A, Sperl B, Hollis A, Eick D, Berg T. Selective inhibition of c-Myc/Max dimerization and DNA binding by small molecules. *Chem Biol*. 2006;*13*:745–51.
134. Yin X, Giap C, Lazo JS, Prochownik EV. Low molecular weight inhibitors of Myc–Max interaction and function. *Oncogene*. 2003;*22*:6151–9.
135. Wang H, Chauhan J, Hu A, Pendleton K, Yap JL, Sabato PE, Jones JW, Perri J, Cione E, Kane MA, Fletcher S, Prochownik EV. Disruption of Myc–Max heterodimerization with improved cell-penetrating analogs of the small molecule 10074-G5. *Oncotarget*. 2013;*4*:936–47.
136. Hart JR, et al. Inhibitor of MYC identified in a Kröhnke pyridine library. *Proc Natl Acad Sci*. 2014;*111*:12556–61.
137. Wang H, et al. Improved low molecular weight Myc-Max inhibitors. *Mol Cancer Ther*. 2007;*6*:2399–408.
138. Follis AV, Hammoudeh DI, Wang H, Prochownik EV, Metallo SJ. Structural rationale for the coupled binding and unfolding of the c-Myc oncoprotein by small molecules. *Chem Biol*. 2008;*15*:1149–55.
139. Follis AV, Hammoudeh DI, Daab AT, Metallo SJ. Small-molecule perturbation of competing interactions between c-Myc and Max. *Bioorg Med Chem Lett*. 2009;*19*:807–10.
140. Cuchillo R, Michel J. Mechanisms of small-molecule binding to intrinsically disordered proteins. *Biochem Soc Trans*. 2012;*40*:1004–8.

141. Michel J, Cuchillo R. The impact of small molecule binding on the energy landscape of the intrinsically disordered protein c-Myc. *PLoS ONE*. 2012;*7*:e41070.
142. Available in https://clinicaltrials.gov/study/NCT05908409#study-plan. Last access: May 2025.
143. Wu S, et al. BRD4 PROTAC degrader ARV-825 inhibits T-cell acute lymphoblastic leukemia by targeting 'undruggable' Myc-pathway genes. *Cancer Cell Int*. 2021;*21*:230.
144. Raina K, et al. PROTAC-induced BET protein degradation as a therapy for castration-resistant prostate cancer. *Proc Natl Acad Sci USA*. 2016;*113*:7124–9.
145. Ishida T, Ciulli A. E3 Ligase Ligands for PROTACs: How They Were Found and How to Discover New Ones. *SLAS Discov*. 2021;*26*:484–502.
146. Roy MJ, et al. SPR-Measured Dissociation Kinetics of PROTAC Ternary Complexes Influence Target Degradation Rate. *ACS Chem Biol*. 2019;*14*:361–8.
147. Troup RI, Fallan C, Baud MGJ. Current strategies for the design of PROTAC linkers: a critical review. *Explor Target Anti-Tumor Ther*. 2020;*1*:273–312.
148. Knoevenagel E. Condensation von Malonsäure mit aromatischen Aldehyden durch Ammoniak und Amine. *Ber Deutsche Chem Gesellschaft*. 1894;*27*:2345–6.
149. Khodair AI. A convenient synthesis of 2-Arylidene-5 H -thiazolo[2,3- b]quinazo-line-3,5[2 H]-diones and their benzoquinazoline derivatives. *J Heterocycl Chem*. 2002;*39*:1153–60.
150. Alizadeh M, Keshavarzipour F, Tavakol H. *ACS Omega*. 2024;*9*(16):16321–29.
151. Khodair AI, et al. Design, synthesis, molecular modelling and antitumor evaluation of S -glucosylated rhodanines through topo II inhibition and DNA intercalation. *J Enzyme Inhib Med Chem*. 2023;*38*:2163996.
152. Makki MST, Abdel-Rahman RM, Alshammari NAH. Synthesis of Novel Fluorine Compounds Substituted-4-thiazolidinones Derived from Rhodanine Drug as Highly Bioactive Probes. *Curr Org Synth*. 2019;*16*:413–22.
153. Metallo S, Prochownik EV, Follis AV. Patent: US 2012/0015989. 2012.
154. Coulibaly WK, Montoya-Castilla S, Boucherle B, Gornitzka H, Nepveu F. Synthesis of New N,N'-Bis(5-arylidene-4-oxo-4,5-dihydrothiazolin-2-yl)piperazine Derivatives under Microwave Irradiation and Preliminary Biological Evaluation. *Sci Pharm*. 2012;*80*:825–36.
155. Matiichuk U, et al. Synthesis and biological activity of rhodanine-furan conjugates: A review. *Curr Chem Lett*. 2024;*13*:287–302.
156. Liang D, et al. Structure-based design and biological evaluation of inhibitors of the pseudomonas aeruginosa heme oxygenase (pa-HemO). *Bioorg Med Chem Lett*. 2018;*28*:1024–9.
157. Sasmal S, Samajdar S, Mukherjee S, Abbineni C. WO2019/207538. 2019.
158. Pansare DN, Shelke RN, Pawar CD. Microwave Assisted and Efficient Synthesis of Substituted Thiazole Acid Derivatives. *Lett Org Chem*. 2017;*14*:517–24.

159. Steinebach C, et al. A facile synthesis of ligands for the von Hippel–Lindau E3 ligase. *Synthesis*. 2020;*52*:2521–7.
160. Han X, et al. Discovery of ARD-69 as a Highly Potent Proteolysis Targeting Chimera (PROTAC) Degrader of Androgen Receptor (AR) for the Treatment of Prostate Cancer. *J Med Chem*. 2019;*62*:941–64.
161. Nan J, Nello M, Matthew W. 2020;2020010210.
162. Yan W, Pan B-S, Shao J, Lin H, Li H. Feasible Column Chromatography-Free, Multi-Gram Scale Synthetic Process of VH032 Amine, Which Could Enable Rapid PROTAC Library Construction. *ACS Omega*. 2022;*7*:26015–21.
163. Mizoroki T, Mori K, Ozaki A. Arylation of olefin with aryl iodide catalyzed by palladium. *Bull Chem Soc Jpn*. 1971;*44*:581.
164. Buckley DL, et al. Small molecule inhibitors of the interaction between the E3 ligase VHL and HIF1α. *Angew Chem Int Ed*. 2012;*51*:11463–7.
165. Frost J, et al. Potent and selective chemical probe of hypoxic signalling downstream of HIF-α hydroxylation via VHL inhibition. *Nat Commun*. 2016;*7*:13312.
166. Zhao Z-Y, et al. Discovery of potent PROTACs targeting EGFR mutants through optimization of covalent EGFR ligand. *J Med Chem*. 2022;*65*:4709–26.
167. Mainolfi N, Ji N, Kluge AF, Weiss MM, Zhang Y. US 2019/0192668. 2019.
168. Paul I, Ahmed SF, Bhowmik A, Deb S, Ghosh MK. The ubiquitin ligase CHIP regulates c-Myc stability and transcriptional activity. *Oncogene*. 2013;*32*:1284–95.
169. Boyd SR, Chamakuri S, Trostle AJ, Chen H, Liu Z, Jian A, Wang J, Malovannaya A, Young DW. MYC-Targeting PROTACs lead to bimodal degradation and N-terminal truncation. *ACS Chem Biol*. 2025;*20*(4):896–906.
170. Lier S, Sellmer A, Orben F, Heinzlmeir S, Krauß L, Schneeweis C, Hassan Z, Schneider C, Schäfer APG, Pongratz H, Engleitner T, Öllinger R, Kuisl A, Bassermann F, Schlag C, Kong B, Dove S, Kuster B, Rad R, Reichert M, Wirth M, Saur D, Mahboobi S, Schneider G. A novel Cereblon E3 ligase modulator with antitumor activity in gastrointestinal cancer. *Bioorg Chem*. 2022;*119*:105505.
171. N'ta Ambeu C, et al. Microwave synthesis of new 3-(3-aminopropyl)-5-arylidene-2-thioxo-1,3-thiazolidine-4-ones as potential Ser/Thr protein kinase inhibitors. *Med Chem Res*. 2016;*25*:2940–58.
172. Coulibaly WK, et al. Prospective study directed to the synthesis of unsymmetrical linked bis-5-arylidene rhodanine derivatives via "one-pot two steps" reactions under microwave irradiation with their antitumor activity. *Med Chem Res*. 2015;*24*:1653–61.
173. Matsson P, Kihlberg J. How Big Is Too Big for Cell Permeability? *J Med Chem*. 2017;*60*:1662–4.
174. García Jiménez D, et al. Designing Soluble PROTACs: Strategies and Preliminary Guidelines. *J Med Chem*. 2022;*65*:12639–49.

175. Klein VG, Bond AG, Craigon C, Lokey RS, Ciulli A. Amide-to-Ester Substitution as a Strategy for Optimizing PROTAC Permeability and Cellular Activity. *J Med Chem*. 2021;*64*:18082–101.
176. Klein VG, et al. Understanding and Improving the Membrane Permeability of VH032-Based PROTACs. *ACS Med Chem Lett*. 2020;*11*:1732–8.
177. Daina A, Michielin O, Zoete V. SwissADME: a free web tool to evaluate pharmacokinetics, drug-likeness and medicinal chemistry friendliness of small molecules. *Sci Rep*. 2017;*7*:42717.
178. Matthews HK, Bertoli C, De Bruin RAM. Cell cycle control in cancer. *Nat Rev Mol Cell Biol*. 2022;*23*:74–88.
179. Chu C, Geng Y, Zhou Y, Sicinski P. Cyclin E in normal physiology and disease states. *Trends Cell Biol*. 2021;*31*:732–46.
180. Hwang HC, Clurman BE. Cyclin E in normal and neoplastic cell cycles. *Oncogene*. 2005;*24*:2776–86.
181. Xiong Y, et al. Bridged Proteolysis Targeting Chimera (PROTAC) Enables Degradation of Undruggable Targets. *J Am Chem Soc*. 2022;*144*:22622–32.
182. Tadesse S, et al. Targeting CDK2 in cancer: challenges and opportunities for therapy. *Drug Discov Today*. 2020;*25*:406–13.
183. Milletti G, Colicchia V, Cecconi F. Cyclers' kinases in cell division: from molecules to cancer therapy. *Cell Death Differ*. 2023;*30*:2035–52.
184. Fagundes R, Teixeira LK. Cyclin E/CDK2: DNA Replication, Replication Stress and Genomic Instability. *Front Cell Dev Biol*. 2021;*9*:774845.
185. Qian Y, et al. WO2017030814A1. 2017.
186. Winter GE, et al. BET Bromodomain Proteins Function as Master Transcription Elongation Factors Independent of CDK9 Recruitment. *Mol Cell*. 2017;*67*:5–18.
187. Gehling VS, et al. Discovery, design, and optimization of isoxazole azepine BET inhibitors. *ACS Med Chem Lett*. 2013;*4*:835–40.
188. Piticchio SG, Martínez-Cartró M, Scaffidi S, Rachman M, Rodriguez-Arevalo S, Sanchez-Arfelis A, Escolano C, Picaud S, Krojer T, Filippakopoulos P, von Delft F, Galdeano C, Barril X. Discovery of novel BRD4 ligand scaffolds by automated navigation of the fragment chemical space. *J Med Chem*. 2021;*64*:17887–900.
189. Baker M. Fragment-based phenotypic screening is a hit. *Nat Rev Drug Discov*. 2017;*16*:225–6.
190. Parker CG, et al. Ligand and target discovery by fragment-based screening in human cells. *Cell*. 2017;*168*:527–41.
191. Scott DE, Coyne AG, Hudson SA, Abell C. Fragment-based approaches in drug discovery and chemical biology. *Biochemistry*. 2012;*51*:4990–5003.
192. Erlanson DA, Fesik SW, Hubbard RE, Jahnke W, Jhoti H. Twenty years on: The impact of fragments on drug discovery. *Nat Rev Drug Discov*. 2016;*15*:605–19.

193. Bohacek RS, McMartin C, Guida WC. The art and practice of structure-based drug design: A molecular modeling perspective. *Med Res Rev*. 1996;*16*:3–50.
194. Van Montfort RLM, Workman P, Lamoree B, Hubbard RE. Current perspectives in fragment-based lead discovery (FBLD). *Essays Biochem*. 2017;*61*:453–64.
195. Goldberg AD, Allis CD, Bernstein E. Epigenetics: A landscape takes shape. *Cell*. 2007;*128*:635–8.
196. Kouzarides T. Chromatin modifications and their function. *Cell*. 2007;*128*:693–705.
197. Strahl BD, Allis CD. The language of covalent histone modifications. *Nature*. 2000;*403*:414–5.
198. Arrowsmith CH, et al. Epigenetic protein families: A new frontier for drug discovery. *Nat Rev Drug Discov*. 2012;*11*:384–400.
199. Yang X-J, Seto E. Lysine acetylation: Codified crosstalk with other posttranslational modifications. *Mol Cell*. 2008;*31*:449–46.
200. Kuo MH, Allis CD. Roles of histone acetyltransferases and deacetylases in gene regulation. *Bioessays*. 1998;*20*:615–26.
201. Morinière J, et al. Cooperative binding of two acetylation marks on a histone tail by a single bromodomain. *Nature*. 2009;*461*:664–8.
202. Sanchez R, Meslamani J, Zhou MM. The bromodomain: From epigenome reader to druggable target. *Biochim Biophys Acta*. 2014;*1839*:676–85.
203. Fu LL, et al. Inhibition of BET bromodomains as a therapeutic strategy for cancer drug discovery. *Oncotarget*. 2015;*6*:5501–16.
204. Mujtaba S, Zeng L, Zhou MM. Structure and acetyl-lysine recognition of the bromodomain. *Oncogene*. 2007;*26*:5521–7.
205. Galdeano C, Ciulli A. Selectivity on-target of bromodomain chemical probes by structure-guided medicinal chemistry and chemical biology. *Future Med Chem*. 2016;*8*:1655–80.
206. Marchand JR, Caflisch A. Binding mode of acetylated histones to bromodomains: Variations on a common motif. *ChemMedChem*. 2015;*10*:1327–33.
207. Romero FA, et al. Disrupting acetyl-lysine recognition: Progress in the development of bromodomain inhibitors. *J Med Chem*. 2016;*59*:1271–98.
208. Chung CW, et al. Fragment-based discovery of bromodomain inhibitors part 1: Inhibitor binding modes and implications for lead discovery. *J Med Chem*. 2012;*55*:576–86.
209. Filippakopoulos P, Knapp S. Targeting bromodomains: Epigenetic readers of lysine acetylation. *Nat Rev Drug Discov*. 2014;*13*:337–56.
210. Cochran AG, Conery AR, Sims RJ. Bromodomains: A new target class for drug development. *Nat Rev Drug Discov*. 2019;*18*:609–28.
211. Filippakopoulos P, et al. Selective inhibition of BET bromodomains. *Nature*. 2010;*468*:1067–73.

212. Nicodeme E, et al. Suppression of inflammation by a synthetic histone mimic. *Nature*. 2010;*468*:1119–23.
213. Pérez-Salvia M, Esteller M. Bromodomain inhibitors and cancer therapy: From structures to applications. *Epigenetics*. 2017;*12*:323–39.
214. Zuber J, et al. RNAi screen identifies Brd4 as a therapeutic target in acute myeloid leukaemia. *Nature*. 2011;*478*:524–8.
215. Baratta MG, et al. An in-tumor genetic screen reveals that the BET bromodomain protein, BRD4, is a potential therapeutic target in ovarian carcinoma. *Proc Natl Acad Sci U S A*. 2015;*112*:232–7.
216. Chung CW, et al. Discovery and characterization of small molecule inhibitors of the BET family bromodomains. *J Med Chem*. 2011;*54*:3827–38.
217. Zhou XL, et al. A comprehensive review of BET-targeting PROTACs for cancer therapy. *Bioorg Med Chem*. 2022;*73*:117033.
218. Saenz D, et al. Novel BET protein proteolysis-targeting chimera exerts superior lethal activity than bromodomain inhibitor (BETi) against post-myeloproliferative neoplasm secondary (s) AML cells. *Leukemia*. 2017;*31*:1951–61.
219. Kotekar A, Singh AK, Devaiah BN. BRD4 and MYC: Power couple in transcription and disease. *FEBS J*. 2023;*290*:4820–42.
220. Coudé MM, et al. BET inhibitor OTX015 targets BRD2 and BRD4 and decreases c-MYC in acute leukemia cells. *Oncotarget*. 2015;*6*:17698–711.
221. Delmore JE, et al. BET bromodomain inhibition as a therapeutic strategy to target c-Myc. *Cell*. 2011;*146*:904–17.
222. Scott DE, Coyne AG, Hudson SA, Abell C. Fragment-based approaches in drug discovery and chemical biology. *Biochemistry*. 2012;*51*:4990–5003.
223. Pearlman DA, Murcko MA. CONCERTS: dynamic connection of fragments as an approach to de novo ligand design. *J Med Chem*. 1996;*39*:1651–63.
224. Nishibata Y, Itai A. Confirmation of usefulness of a structure construction program based on three-dimensional receptor structure for rational lead generation. *J Med Chem*. 1993;*36*:2921–8
225. Böhm H. The computer program LUDI: a new method for the de novo design of enzyme inhibitors. *J Comput Mol Des*. 1992;*6*:61–78.
226. DeWitte RS, Shakhnovich E. SMoG: de novo design method based on simple, fast, and accurate free energy estimates. 1. Methodology and supporting evidence. *J Am Chem Soc*. 1996;*118*:11733–44.
227. Hartenfeller M, Zettl H, Walter M, Rupp M, Reisen F, Proschak E, et al. Dogs: reaction-driven de novo design of bioactive compounds. *PLoS Comput Biol*. 2012;*8*:e1002542.
228. Wolber G, Langer T. LigandScout: 3-D pharmacophores derived from protein-bound ligands and their use as virtual screening filters. *J Chem Inf Model*. 2005;*45*:160–9.

229. Kutchukian PS, Shakhnovich EI. De novo design: balancing novelty and confined chemical space. *Expert Opin Drug Discov*. 2010;*5*:789–812.
230. Schneider G, Lee ML, Stahl M, Schneider P. De novo design of molecular architectures by evolutionary assembly of drug-derived building blocks. *J Comput Aided Mol Des*. 2000;*14*:487–94.
231. Vinkers HM, de Jonge MR, Daeyaert FF, et al. SYNOPSIS: SYNthesize and OPtimize System in Silico. *J Med Chem*. 2003;*46*:2765–73.
232. Schneider G, Fechner U. Computer-based de novo design of drug-like molecules. *Nat Rev Drug Discov*. 2005;*4*:649–63.
233. Dey F, Caflisch A. Fragment-based de novo ligand design by multiobjective evolutionary optimization. *J Chem Inf Model*. 2008;*48*:679–90.
234. Schneider G, Hartenfeller M, Reutlinger M, et al. Voyages to the (un)known: adaptive design of bioactive compounds. *Trends Biotechnol*. 2009;*27*:18–26.
235. Boda K, Seidel T, Gasteiger J. Structure and reaction-based evaluation of synthetic accessibility. *J Comput Aided Mol Des*. 2007;*21*:311–25.
236. Sommer K, Flachsenberg F, Rarey M. NAOMInext: synthetically feasible fragment growing in a structure-based design context. *Eur J Med Chem*. 2019;*163*:747–62.
237. Wagner S, et al. Regulation of protein synthesis. *US 2010/0144805 A1*. 2010.
238. Carradori S, et al. Evaluation of a large library of (thiazol-2-yl)hydrazones and analogues as histone acetyltransferase inhibitors: enzyme and cellular studies. *Eur J Med Chem*. 2014;*80*:569–78.
239. El-Sherif HA, Mahmoud AM, Sarhan AAO, Hozien ZA, Habib OMA. One pot synthesis of novel thiazolo[3,2-b][1,2,4]triazoles: A useful synthetic application of the acidified acetic acid method. *J Sulfur Chem*. 2006;*27*:65–85.
240. Furuyama H, et al. Inhibitors of AKT activity. *WO 2009148916*. 2009.
241. Kumar P, Kumar A, Makrandi JK. Synthesis and evaluation of bioactivity of thiazolo[3,2-b]-[1,2,4]-triazoles and isomeric thiazolo[2,3-c]-[1,2,4]-triazoles. *J Heterocycl Chem*. 2013;*50*:1141–8.
242. Sambiagio C, et al. Copper-catalysed Ullmann type chemistry: From mechanistic aspects to modern development. *Chem Soc Rev*. 2014;*43*:3525–50.
243. Kwong FY, Buchwald SL. Mild and efficient copper-catalyzed amination of aryl bromides with primary alkylamines. *Org Lett*. 2003;*5*:793–6.
244. Altman RA, Anderson KW, Buchwald SL. Pyrrole-2-carboxylic acid as a ligand for the Cu-catalyzed reactions of primary anilines with aryl halides. *J Org Chem*. 2008;*73*:5167–9.
245. Heravi MM, et al. Buchwald-Hartwig reaction: An overview. *J Organomet Chem*. 2018;*861*:17–104.
246. Ruiz-Castillo P, Buchwald SL. Applications of palladium-catalyzed C–N cross-coupling reactions. *Chem Rev*. 2016;*116*:12564–649.

247. Salome C, et al. Buchwald–Hartwig reactions in water using surfactants. *Tetrahedron*. 2014;*70*:3413–21.
248. Copin C, et al. SNAr versus Buchwald–Hartwig amination/amidation in the imidazo[2,1-*b*][1,3,4]thiadiazole series. *Eur J Org Chem*. 2015;*17*:6932–42.
249. Peet NP, Sunder S, Barbuch RJ. Synthesis of thiazolotriazepinones. *J Heterocycl Chem*. 1982;*19*:747–52.
250. Chung CW, et al. Discovery and characterization of small-molecule inhibitors of the BET family bromodomains. *J Med Chem*. 2011;*54*:3827–38.
251. Sheldrick GM. Crystal structure refinement with SHELXL. *Acta Cryst*. 2015;*71*:3–8.
252. Farrugia LJ. WinGX and ORTEP for Windows: an update. *J Appl Cryst*. 2012;*45*:849–54.
253. Downs JR, Clearfield M, Weis S, et al. Primary prevention of acute coronary events with lovastatin in men and women with average cholesterol levels: results of AFCAPS/TexCAPS. Air Force/Texas Coronary Atherosclerosis Prevention Study. *JAMA*. 1998;*279*:1615–22.
254. Bjursell G, Reichard P. Effects of thymidine on deoxyribonucleoside triphosphate pools and deoxyribonucleic acid synthesis in Chinese hamster ovary cells. *J Biol Chem*. 1973;*248*:3904–9.
255. Samaké S, Smith LC. Synchronization of cell division in eight-cell bovine embryos produced in vitro: effects of Nocodazole. *Mol Reprod Dev*. 1996;*44*:486–92.
256. Jackman J, O'Connor PM. Methods for synchronizing cells at specific stages of the cell cycle. *Curr Protoc Cell Biol*. 1998;*8*:3.1–3.20.
257. Chen G, Deng X. Cell Synchronization by Double Thymidine Block. *Bio Protoc*. 2018;*8*.
258. Surani AA, Colombo SL, Barlow G, Foulds GA, Montiel-Duarte C. Optimizing cell synchronization using nocodazole or double thymidine block. In: Coutts AS, Weston L, editors. Cell Cycle Oscillators. *Methods in Molecular Biology*, vol. 2329, 111–121. Humana: New York, NY; 2021.
259. Qazi SU, et al. Semicarbazones, thiosemicarbazone, thiazole and oxazole analogues as monoamine oxidase inhibitors: Synthesis, characterization, biological evaluation, molecular docking, and kinetic studies. *Bioorganic Chemistry*. 2021;*115*:105209.
260. Stryer L, Haugland RP. Energy transfer: a spectroscopic ruler. *Proc Natl Acad Sci U S A*. 1967;*58*:719–26.
261. Algar WR, et al. FRET as a biomolecular research tool — understanding its potential while avoiding pitfalls. *Nat Methods*. 2019;*16*:815–29.
262. Comley J. TR-FRET-based assays – getting better with age. *Drug Discov World*. 2006;*6*:22–37.
263. Förster T. Energy migration and fluorescence. *J Biomed Opt*. 2012;*17*:1.